CHEMICAL REVIEWS

pubs.acs.org/CR Review

Flexible and Stretchable Light-Emitting Diodes and Photodetectors for Human-Centric Optoelectronics

Published as part of Chemical Reviews virtual special issue "Wearable Devices".

Sehui Chang,† Ja Hoon Koo,† Jisu Yoo,† Min Seok Kim, Moon Kee Choi,* Dae-Hyeong Kim,* and Young Min Song*

Cite This: https://doi.org/10.1021/acs.chemrev.3c00548 Read Online

ACCESS | Metrics & More | Article Recommendations

ABSTRACT: Optoelectronic devices with unconventional form factors, such as flexible and stretchable light-emitting or photoresponsive devices, are core elements for the next-generation human-centric optoelectronics. For instance, these deformable devices can be utilized as closely fitted wearable sensors to acquire precise biosignals that are subsequently uploaded to the cloud for immediate examination and diagnosis, and also can be used for vision systems for human-interactive robotics. Their inception was propelled by breakthroughs in novel optoelectronic material technologies and device blueprinting methodologies, endowing flexibility and mechanical resilience to conventional rigid optoelectronic devices. This paper reviews the advancements in such soft optoelectronic device technologies, honing in on various materials, manufacturing techniques, and device design strategies. We will first highlight the general approaches for flexible and stretchable device fabrication, including the appropriate material selection for the substrate, electrodes, and insulation layers. We will then focus on the materials for flexible and stretchable light-emitting diodes, their device integration strategies, and representative application examples. Next, we will move on to the materials for flexible and stretchable photodetectors, highlighting the state-of-the-art materials and device fabrication methods, followed by their representative application examples. At the end, a brief summary will be given, and the potential challenges for further development of functional devices will be discussed as a conclusion.

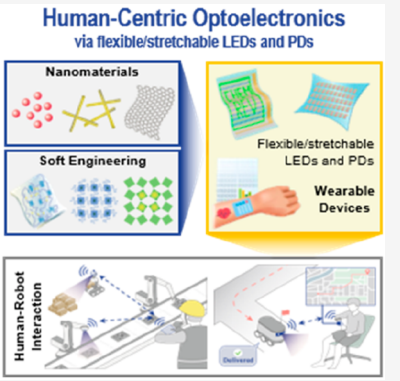

CONTENTS

Received: July 31, 2023
Revised: November 16, 2023
Accepted: December 19, 2023

1. INTRODUCTION

The invention of a transistor in December 1947 marked a significant milestone in the field of electronics and laid the foundation for modern electronic devices and integrated circuits.[1] The first generation of electronic devices utilized vacuum tubes as the primary component for amplification and switching, which were large, power-consuming, and generated significant heat. Transistors were smaller, more reliable, and consumed less power than the vacuum tubes, and combining multiple transistors and other components onto a single semiconductor chip enabled the miniaturization of electronic devices, along with improved performance, reliability, and efficiency. The second generation of electronic devices thus became more popularized, greatly improving people's quality of life at home and work. The third generation of electronic devices encompasses the present era of electronics, characterized by advancements in digital technology, microprocessors, and the proliferation of personal, portable devices such as laptops and smartphones. The development of wireless communication technology provided unprecedented connectivity between users, and enabled novel applications such as Internet of Things.

The development of electronic devices can also be interpreted in viewpoint of inputs and outputs (Figure 1A). The inputs and outputs of the first generation of electronic devices, which can be classified as analog devices, are simple. The electronic devices each have their unique functionalities, and they operate as stand-alone devices. The second generation of electronic devices can be classified as digital devices, and they exhibit superior performances in terms of faster inputs and outputs. But still, the devices are unconnected. The third generation of electronic devices, which can be categorized as mobile devices, are known for their "smart" and "personalized (or customized)" operations. It became more convenient for the users to provide inputs and receive outputs from the electronic devices, and the unprecedented connectivity between the users and also between the electronic devices have enabled various functionalities that promote the user experience and proliferate our daily lives. The fourth generation of electronic devices is expected to become more human-centric by maximizing the device-to-user interactivity, such as those that can be worn on or implanted in the human body without any discomfort. Owing to their unique physical features, these electronic devices will be used to provide futuristic functionalities that are impossible by using conventional rigid electronic devices.

Specifically, novel applications have been readily demonstrated by the advancements in light-emitting devices and photodetectors (PDs) with unconventional form factors (Figure 1B). For instance, displays have been made wearable by integration into smart glasses, adding information alongside or to what the user is seeing. The leading companies in the field of electronic devices are increasingly investigating in, and have demonstrated wearable devices for augmented and virtual realities. The flexible and stretchable optoelectronic devices have also been used in various healthcare devices, such as smart watches or rings which are capable of detecting the changes in biosignals, wearable glucose monitors, or wearable thermo-devices that help reduce anxiety and ease hot flashes using thermal treatments.

As such, there is a significant interest in developing advanced optoelectronic devices that may enable future human-centric applications (Figure 2). These devices may be integrated into a contact lens to diagnose various diseases such as glaucoma and diabetes[2−5] or provide augmented/virtual reality vision.[6−10] Flexible and stretchable PDs with high resolution can realize various curvy-shaped retinas in natural eyes, which can be implemented in artificial vision for mobile robotics or visual prostheses to provide/restore vision.[11−18] Fully mimicked, bioinspired artificial imagers can provide user-friendly preprocessed images, minimizing the computational cost for refining the raw data.[19−23] Wearable and implantable devices can be used to detect activities in the brain, heart, and muscles, blood pressure, and other vital signs.[24−36] The collected data can be transmitted to the cloud for real-time analysis to assist in predictive diagnostics or provide proper treatment, including but not limited to drug delivery and therapy based on thermal, electrical, and ultrasound stimulation.[37−46] These soft sensors and actuators can also be applied to various prosthetics or human-machine interfaces (HMIs) to restore senses or major functionalities of the human body.[47−55] In conjunction with the artificial intelligence (AI) technology, the human-centric devices with flexible and stretchable form factors are expected to bring a change of paradigm in medicine from treatment to diagnosis, prevention, and restoration, transitioning to personalized precision medicine. Through the utilization of

https://doi.org/10.1021/acs.chemrev.3c00548
Chem. Rev. XXXX, XXX, XXX−XXX

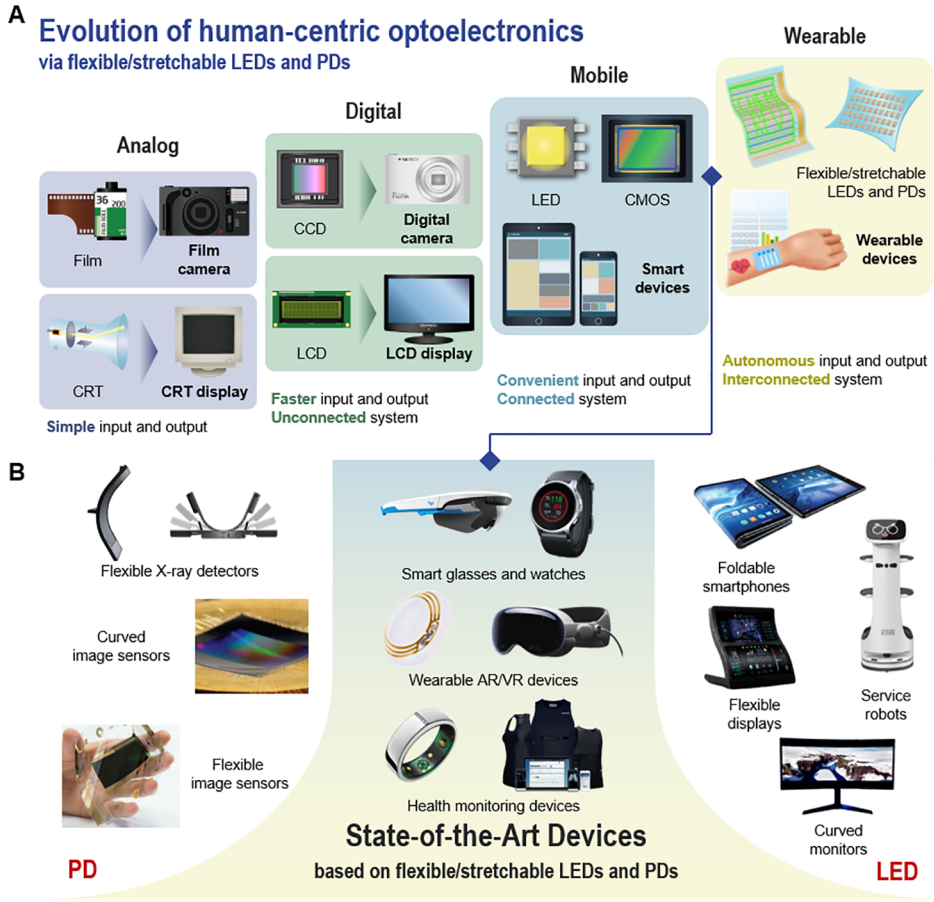

Figure 1. (A) Evolution of human-centric optoelectronic devices, in viewpoint of user-interactivity. (B) State-of-the-art electronic devices with human-centric applications, based on deformable optoelectronic technologies. Reproduced with permission from ref 920. Copyright 2023 DRTECH. Reproduced with permission from ref 14. Copyright 2017 John Wiley & Sons, Inc. Reproduced with permission from ref 921. Copyright 2018 Society for Information Display. Reproduced with permission from ref 922. Copyright 2022 John Wiley & Sons, Inc. Reproduced with permission from ref 4. Copyright 2021 John Wiley & Sons, Inc. Reproduced with permission from ref 923. Copyright 2023 Springer Nature. Reproduced with permission from ref 924. Copyright 2021 Springer Nature. Reproduced with permission from ref 925. Copyright 2023 John Wiley & Sons, Inc. Reproduced with permission from ref 371. Copyright 2021 John Wiley & Sons, Inc. Reproduced with permission from ref 926. Copyright 2022 MDPI. Reproduced with permission from ref 927. Copyright 2020 MDPI.

medical big data, AI can impact various areas of healthcare, including prediction, diagnosis, treatment, and rehabilitation.

The perception of flexible and stretchable optoelectronic devices in healthcare and human-friendly robotics is becoming more widespread,[56−70] and to meet the growing demand, extensive research efforts are being devoted to the development of such soft devices from both academia and industry. The focus is on high accuracy and reliable data collection, and thus significant progress has been achieved in sensor accuracy-related technologies. The key idea is to minimize the mismatch in mechanical properties between the human body and electronic devices by making the devices flexible and stretchable.[71−75] This way, conformal integration of the biomedical devices onto the target tissues or organs can be realized, which in turn results in a maximized signal-to-noise ratio (SNR) and biocompatibility, as well as minimized impedance and side effects.[76−80] However, conventional materials and device designs used to construct biomedical wearables and implants are rigid and bulky in size, significantly differing from the mechanical properties of soft human tissues and organs. In specific, the elastic modulus of biological tissues, such as the brain, heart, and skin, are less than a few MPa, whereas those of the materials used in modern electronic devices usually exhibit few hundreds of GPa.[25,55,81,82] Such discrepancy in mechanical properties impedes the seamless integration of soft devices with the human body, preventing a unified and cohesive fit. This can lead to diverse side effects, especially in cases where large, inflexible devices are required to be implanted or come into contact with specific tissues or organs over an extended period of time.

To overcome the mismatch present at the biotic-abiotic interface, tremendous research efforts have been devoted to developing functional devices that exhibit mechanical properties analogous to the target biological tissues.[83−95] Specifically, optoelectronic devices that mimic the mechanical properties of human tissues and organs have been extensively investigated, owing to the possibility of realizing versatile and practical applications. These include artificial vision systems,[23,96−99] HMIs,[100−102] soft prosthetics,[103−105] and biometric authentication systems.[106,107] Several optoelectronic devices with flexible and stretchable features have been readily demonstrated, showing excellent elastic properties and operational durability under mechanical deformation.[108−118] These optoelectronic devices engaged with users to consistently and precisely monitor their physiological conditions without imposing limitations based on the users' location. The

https://doi.org/10.1021/acs.chemrev.3c00548
Chem. Rev. XXXX, XXX, XXX−XXX

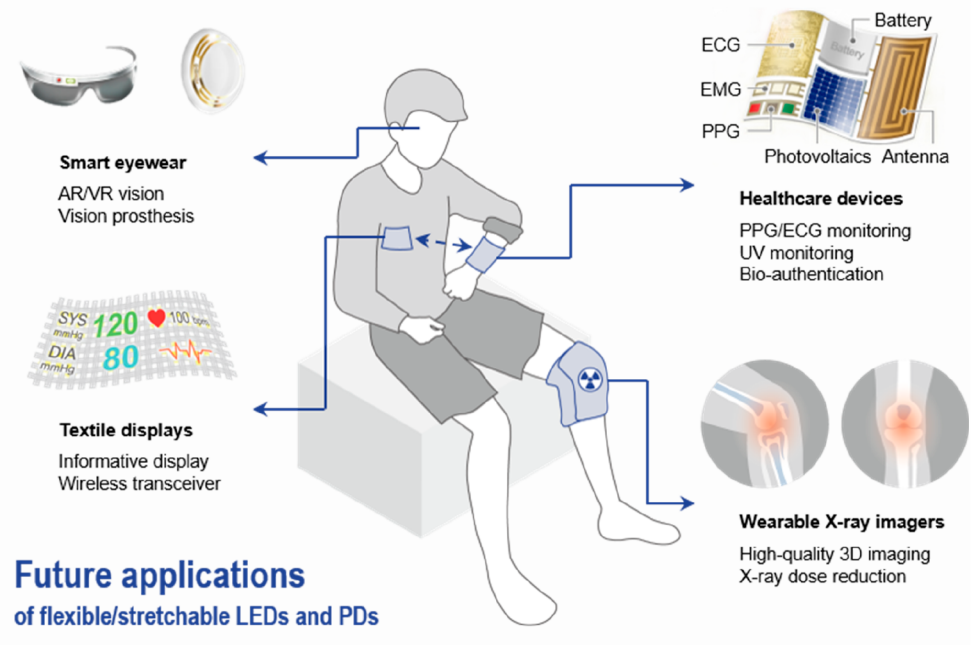

Figure 2. Perspective on future applications of flexible and stretchable light-emitting devices and PDs for human-centric electronics.

advancements in these devices were mainly achieved by the development of novel flexible and stretchable photoactive materials, along with device design and integration strategies.

In this review, we summarize the recent technological advances in flexible and stretchable optoelectronic devices with enhanced user-interactivity. We first focus on explaining the basics of mechanics for flexible and stretchable device fabrication based on the engineering of electronic materials in terms of geometry, structural engineering of electronic devices, and use of soft electronic materials. Then, the materials used for the fabrication of flexible and stretchable optoelectronic devices are reviewed, with the classification of substrates, electrodes, and insulators—the basic components of the optoelectronic devices, besides the photoactive layers. Next, we review the materials and fabrication strategies for flexible and stretchable light-emitting diodes (LEDs), explaining their working principles and the state-of-the-art technologies for materials synthesis, processing, and device integration. Representative examples of these soft LEDs in biomedical applications are also discussed. We then move on to the materials and fabrication strategies for flexible and stretchable PDs. After briefly reviewing the working principles, the materials and according processing techniques for device fabrication are presented, followed by representative examples of how these soft PDs have been used in biomedical applications. There are several comprehensive reviews and literature available on flexible and stretchable electronic and optoelectronic devices, encompassing transistors, actuators, memory, and sensors;[13,16−18,24−27,35−37] this work focuses on delivering a timely review addressing the progress of flexible and stretchable optoelectronic devices and their applications in human-centric biomedical electronics. Lastly, we conclude this article with a brief summary of the work and analysis of remaining challenges for fully functional human-centric electronic systems.

2. STRATEGIES FOR FLEXIBLE AND STRETCHABLE DEVICE FABRICATIONS

In the field of flexible and stretchable optoelectronics, significant advancements have been accomplished in terms of materials engineering, device design engineering for enhanced mechanical capabilities, and integration of different functional electronic components for practical applications in human-machine interactions, such as mobile health monitoring,[119−125] and closed-loop bioelectronic systems.[126−130] The primary goal of these flexible and stretchable devices is to maintain reliable and high-performance, even when subjected to repeated mechanical deformations. To accomplish the goal, the following strategies have been proposed. For flexible devices, the materials that constitute the optoelectronic devices have been engineered to exhibit ultrathin form factors, which resulted in reducing the flexural rigidity, or they have been replaced with those that exhibit intrinsic flexibility such as organic, polymeric, or composites based on nanomaterials and elastomers.[131−134] The strain induced in the flexible devices could also be accommodated by positioning them at a neutral-mechanical plane. Similarly, stretchability has been rendered to the optoelectronic device by structural engineering of the device designs,[135−137] and by adopting intrinsically stretchable materials for the device fabrication.[138−141] In this section, these strategies will be closely reviewed to provide fundamental knowledge about the mechanical properties of materials and device architecture.

2.1. Flexible Device Fabrication

When characterizing the deformability of the fabricated optoelectronic devices, two important mechanical parameters should be assessed, which are flexural rigidity and the Young's modulus. The flexural rigidity can be calculated using the following equation:[142]

$$D = \frac{Et^3}{12(1-\nu^2)} \quad (1)$$

https://doi.org/10.1021/acs.chemrev.3c00548
Chem. Rev. XXXX, XXX, XXX−XXX

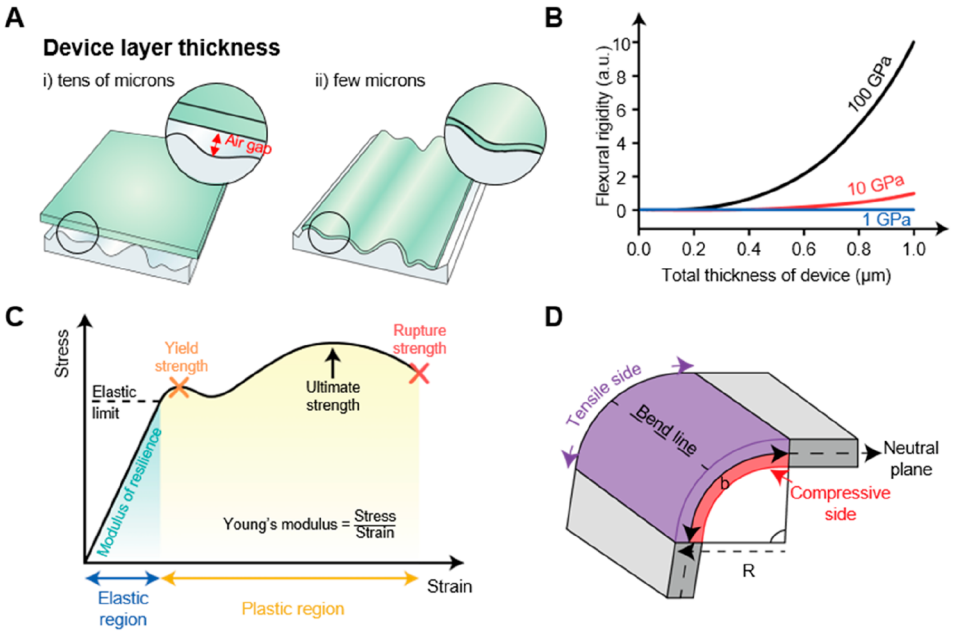

Figure 3. Flexural rigidity of soft electronic/optoelectronic devices. (A) Schematic image showing the importance of device layer thickness for conformal integration on surface with dynamic topologies. (B) Change in flexural rigidity as a function of total thickness of a soft device, for different Young's modulus. (C) Typical stress−strain curve of materials experiencing mechanical deformation. (D) Schematic illustration describing the neutral-mechanical plane layout for minimizing the strain experienced by the device.

where E, t, and v represent the Young's modulus, thickness of the device, and Poisson's ratio of the material, respectively. Here, the Young's modulus E can be calculated as[143]

$$E = \frac{\sigma(\varepsilon)}{\varepsilon} = \frac{F/A_0}{\Delta L/L_0} \tag{2}$$

where σ is the ratio between the force and effective area of the device, ε is the ratio between the elongated device length as compared to the original length, F is the force applied on the device during mechanical deformation, A_0 is the initial cross-sectional area of the device, and ΔL and L_0 are the change in the length of the device and the original length, respectively. From eq 1, the flexural rigidity can be most conveniently reduced by lowering the thickness of the device since D is proportional to the cube of t. Fabrication of optoelectronic devices with minimized flexural rigidity has been known to be beneficial in terms of forming conformal contact with biological tissues (Figure 3A).[144−147] However, although scaling down the total device thickness can significantly enhance the softness of the device regardless of the Young's modulus (Figure 3B), the materials processing and handling of the device after fabrication becomes extremely difficult. Furthermore, many of the tissues and organs in the human body are subject to dynamic motions such as contraction, expansion, and even distortion, and ultrathin flexible devices with thicknesses below a few micrometers cannot withstand the applied strain and can easily be ruptured. Thus, careful consideration of the final thickness of the flexible optoelectronic device is required for their integration onto biological surfaces.

In this regard, the Young's modulus, which is related to the stiffness of the material, should also be considered deliberately. Figure 3C shows the typical stress−strain curve of a material, whose Young's modulus can be estimated using eq 2. Owing to the different materials constituting the optoelectronic devices in multilayered structures, including conductors, dielectrics, and photonic layers (semiconductors), the devices exhibit varying Young's modulus and yield strengths at which plastic deformations occur. To ensure optimal device performance under the applied stresses, the overall stiffness of the fabricated devices should be carefully managed, taking into account the intrinsic properties of each layer. It is generally desirable to choose soft materials with lower Young's modulus than the target biological tissue for the device biointegration, which enables the retention of high functional capabilities while facilitating unrestricted movements, thus achieving a user-friendly interface.

The strain applied to the flexible devices under mechanical deformation can also be engineered using a neutral-mechanical plane layout.[148−151] In specific, the applied strain can be effectively dissipated by placing the fabricated device in the neutral-mechanical plane of a multilayer structure (Figure 3D), where the neutral-mechanical plane position b can be calculated using the following equation:[152]

$$b = \frac{\sum_{i=1}^{n} E_i t_i \left[\sum_{j=1}^{i} t_j - \frac{t_j}{2}\right]}{\sum_{i=1}^{n} E_i t_i} \tag{3}$$

Here E_i is the Young's modulus, and t_i is the thickness of each layer, respectively. The bending strain ε of the other layers that are not positioned in the neutral-mechanical plane b can be calculated according to the following equation:[153]

$$\varepsilon = \frac{r - b}{R + b} \tag{4}$$

where r is the distance of the layer from the neutral-mechanical plane and R is the bending radius of the layer. By considering the aforementioned correlations, the strains experienced by the device during bending can be minimized, which in turn enhances the cyclic durability at a specific bending radius or

https://doi.org/10.1021/acs.chemrev.3c00548
Chem. Rev. XXXX, XXX, XXX−XXX

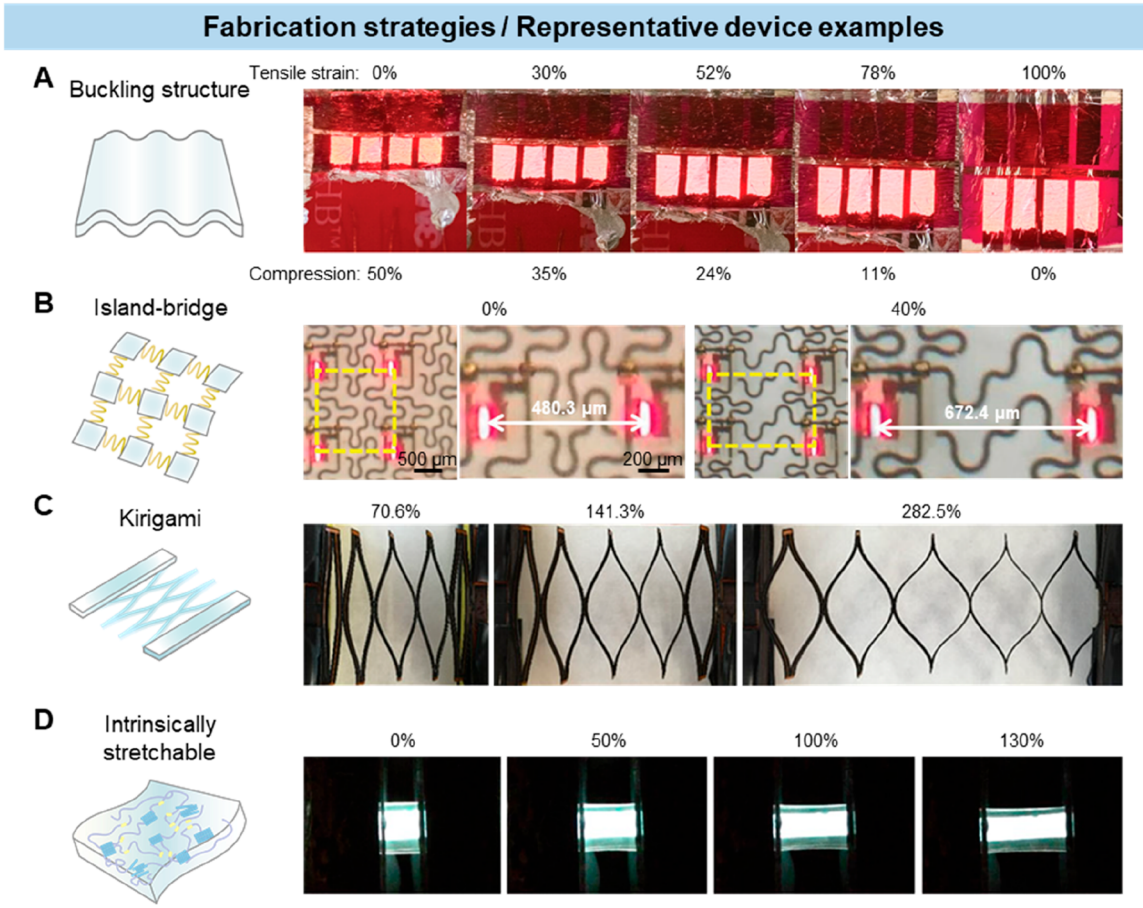

Figure 4. Different strategies for stretchable device fabrication and their representative examples. (A) Prestrained approach (left) and stretchable PLEDs fabricated on prestrained substrate (right). Reproduced with permission from ref 170. Copyright 2013 Springer Nature. (B) Island-bridge configuration (left) and stretchable micro-LEDs adopting the island-bridge approach (right). Reproduced with permission from ref 177. Copyright 2017 John Wiley & Sons, Inc. (C) Kirigami-inspired device approach (left) and stretchable supercapacitors incorporating kirigami design (right). Reproduced with permission from ref 183. Copyright 2018 Springer Nature. (D) Intrinsically stretchable approach (left) and stretchable PLEDs based on intrinsically stretchable materials (right). Reproduced with permission from ref 184. Copyright 2014 American Chemical Society.

angle, leading to improved operational stability even under severe mechanical deformations.

2.2. Stretchable Device Fabrication

As briefly mentioned, flexible optoelectronic devices may not be adequate for biointegration on tissues and organs that exhibit dynamic micromotions. In the case of implantable devices, mechanical failure of the device may result in unwanted immune or inflammatory responses from surrounding biological environments, which may require immediate surgery for their removal and replacement. As such, stretchable devices that can conform to the complex morphologies of the biological tissues and their activities are required to promote the user experience.[154−159] To impart stretchability to the optoelectronic devices, several strategies have been explored and proposed to minimize the stress under mechanical deformations, and they can be classified according to the types of materials they employ—rigid or soft ones. The strategies incorporating rigid materials are the prestrained approach,[160−162] island-bridge configuration,[163−165] and kirigami-inspired device design.[166−168] As a common factor, these approaches utilize rigid crystalline materials with ultrathin form factors (i.e., nanomembranes) to take advantage of the high electronic and optoelectronic material performances, along with geometrical engineering of the device structures. The soft materials approach utilizes materials with intrinsic stretchability, such as elastomeric composites incorporating various nanomaterials as functional electronic and optoelectronic fillers.[58,138,169] Facile manipulation of their mechanical properties (of which the details will be discussed in section 2.4) makes them the perfect candidate for developing target-specific biomedical optoelectronic devices. Figure 4A−D depicts the different strategies as mentioned above, which will be described in detail through this section.

Reducing the device thickness to the submicrometer level results in a drastic reduction in flexural rigidity and improved mechanical properties of the device. Such ultraflexible devices can be made more compatible with human physiology by employing buckling structures, which allows these devices to stretch within the prestretched strains of their supporting elastomeric substrates (Figure 4A, left). White et al. first demonstrated the fabrication of a stretchable polymer LED (PLED) using this method, where ultrathin (2 μm) red and orange PLEDs were adhered to prestrained (100%) elastomer tape. Upon the full release of the prestrain, the PLEDs were wrinkled due to the applied compression (50%), and they exhibited stable operation during the application of a tensile strain of 100% (Figure 4A, right).[170] Since then, various

https://doi.org/10.1021/acs.chemrev.3c00548
Chem. Rev. XXXX, XXX, XXX−XXX

Table 1. Properties of Commonly Used Substrate Materials for Flexible and Stretchable Substrates

Name	Glass transition temp. (°C)	Coefficient of thermal expansion (ppm °C^{-1})	Solvent resistance	Transmittance (%, at 550 nm)	Ultimate elongation (%)	Surface roughness (scale)
Ecoflex	−33	11−335	Good	46.45[185]	300−1,500	Micrometer
PC	145	75	Poor	88[187]	1−2	Nanometer
PDMS	−125	310	Poor	100[185]	50−500	Nanometer
PEN	120−155	20	Good	∼100[191]	85	Nanometer
PET	70−110	15−33	Good	∼86.5[193]	90	Nanometer
Polyurethane	80	153	Good	∼91[198]	300−800	Nanometer
Polyimide	155−360	8−20	Good	∼80[195]	80	Nanometer
SEBS	−35	150	Poor	88.4[200]	2,500	Nanometer

functional stretchable optoelectronic devices based on this strategy have been reported, including ultrathin solar devices that can be worn as electronic skins,[171,172] photonic skins capable of measuring and displaying photoplethysmogram (PPG) signals,[173,174] and self-powered soft optoelectronic devices for measuring biosignals.[175,176]

The island-bridge configuration approach involves placing rigid and functional electronic devices on a stretchable substrate, in which the devices are made into an island array connected with also rigid conductors, but with stretchable designs (i.e., serpentine, noncoplanar arc-shaped structure, etc.) (Figure 4B, left). The stretchable designs of the conductors enable effective dissipation of strain applied to the entire system, with less than 1% of the strain being experienced by the devices fabricated on the islands. Since high-quality inorganic materials with crystallinity can be used to develop stretchable devices using this island-bridge approach, the performance of the stretchable devices is comparable to those of the rigid ones. For instance, Choi et al. developed stretchable inorganic LEDs, whereby the micro-LEDs connected using serpentine-shaped metal interconnects could stably operate under the tensile strain of 40%, with light emission properties of wafer quality (Figure 4B, right).[177] Such an island-bridge design approach has been widely adopted to enable applications that require high stretchability and device performance at the same time, including hemispherical electronic eye cameras,[164,178] biomedical patches,[179,180] and wearable memory modules.[181,182] However, limitations with regard to the low device density that originate from the inevitable use of stretchable interconnects prohibit its use for applications that require high resolution and maximized device packing.

The kirigami-inspired device design approach offers a means to maximize stretchability and compressibility of devices built on elastic substrates (Figure 4C, left). By strategically opening formations in thin elastic sheets, the desired kirigami structure can be achieved. The mechanical strain applied to the active device components are effectively minimized by bending and torsional deformation of the entire system, achieved by the kirigami structures. Various wearable electronic devices have been developed using the kirigami technique, including but not limited to skin-mounted and implantable sensors, stretchable antenna, and stretchable heaters. In 2018, Xu et al. reported on the fabrication of highly stretchable supercapacitors that incorporated the kirigami-inspired design, which exhibited less than 2% change in capacitance after being elongated to 382.5% of its initial length (Figure 4C, right).[183] Despite the high stretchability attainable, the same limitation with regards to the device density exists, in addition to challenges associated with precise fabrication. Further research and exploration are necessary to address these aspects and pave the way for advancements and commercialization in this field.

Lastly, the soft materials approach utilizes materials with intrinsic stretchability to develop stretchable optoelectronic devices. Materials with intrinsic stretchability are generally synthesized by introducing functional fillers into elastomeric matrices, resulting in a stretchable composite (Figure 4D, left). As a good example, Liang et al. reported on the fabrication of an intrinsically stretchable PLED that can stretch up to 130% for the first time, using graphene oxide (GO)-soldered Ag nanowires (NWs)/polyurethane acrylate (PUA) composite as an intrinsically stretchable transparent conductor (Figure 4D, right).[184] The physical properties of these composite can be manipulated by controlling the amount of rigid backbones and side chains incorporated as matrices, as well as noncovalent cross-linkers that affect to the energy dissipation during strain. In addition, self-healing properties can be included by combining amorphous oligomers composed of similar or identical repeating units.

Despite these significant advancements, the mobilities of these materials remain limited and lower than those of single-crystalline-based inorganics and even organic materials. This is generally because stretchability is constrained by the crystallinity of the functional fillers and effective conjugation length.[24,25] This trade-off between stretchability and mobility poses challenges. Furthermore, developing intrinsically stretchable, light-sensitive semiconductor composites becomes even more challenging when considering their optoelectronic properties under mechanical deformations.[58] The monolithic device integration of stretchable composites with different electronic and optoelectronic properties is another challenge, as diversity in the materials properties and their deposition methods usually result in unstable interfaces at the junctions.[281] Although several limitations still exist, much research effort is being directed to solve these issues to enhance the performance and functionality of stretchable optoelectronic devices.

2.3. Materials for Flexible and Stretchable Substrates and Insulators

When fabricating a flexible and stretchable optoelectronic device, the first task is to choose the adequate material for the substrate, based on the target device functionality. Normally, physical properties such as toughness, stretchability, and thickness should be carefully considered to ensure operational stability under stress conditions. It is highly desirable that the substrate layer does not crack when stretched unless specifically engineered. Optical properties such as transparency should also be regarded, to allow efficient photoabsorption and emission, depending on the device type. Since additional layers are to be stacked vertically to construct the stretchable device,

https://doi.org/10.1021/acs.chemrev.3c00548
Chem. Rev. XXXX, XXX, XXX−XXX

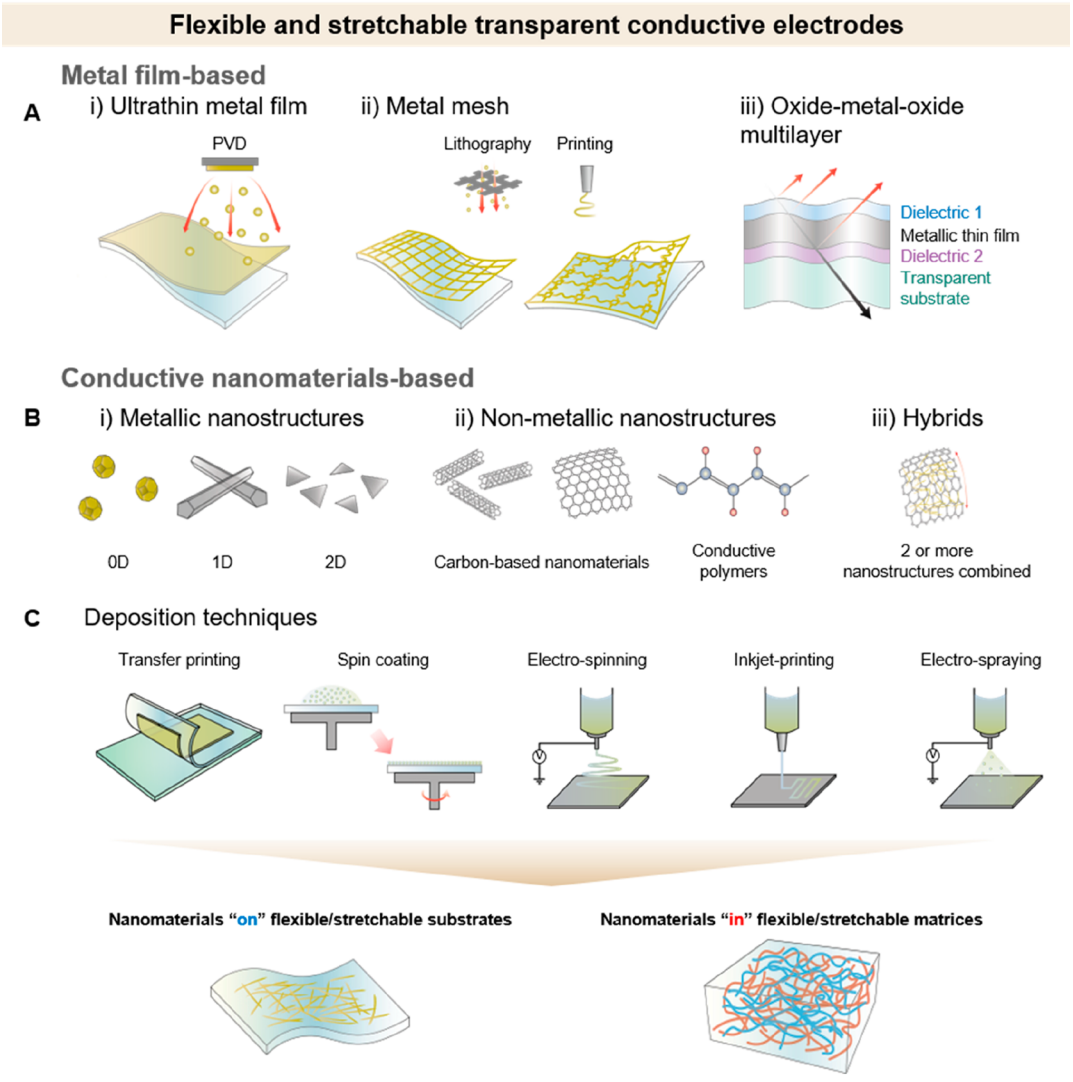

Figure 5. Different types of flexible and stretchable transparent conductive electrodes for soft optoelectronic applications. (A) Metal film-based approaches for fabrication of flexible and stretchable transparent electrodes (TEs), consisting (i) ultrathin metal film approach, (ii) metal mesh approach, and (iii) oxide-metal-oxide multilayer approach. (B) Conductive nanomaterials-based flexible and transparent electrodes, whereby soft composites are formed either by forming percolations of (i) metallic nanostructures, or (ii) nonmetallic nanostructures, or (iii) hybrids of two or more nanostructures "on" or "in" elastomeric matrices.

the compatibility with other stretchable layers should also be considered, to maintain a tight interface and functionality under repetitive mechanical deformation. Thus, surface energy of the material is important to achieve a high-quality smooth and uniform surface for consequent film deposition. Considering these attributes, the common materials choice for the flexible and stretchable substrates are Ecoflex,[185,186] polycarbonate (PC),[187,188] polydimethylsiloxane (PDMS),[189,190] polyethylene naphthalate (PEN),[191,192] polyethylene terephthalate (PET),[193,194] polyimide (PI),[195,196] polyurethane (PU),[197,198] and poly(styrene-ehtylene-butylene-styrene) (SEBS).[199,200] These substrate materials exhibit thicknesses of more than hundreds of micrometers, high mechanical durability, and excellent transparency in the visible regions. Several properties of the different substrates are summarized in Table 1.[185,187,191,193,195,198,200−203]

The thick elastic materials listed in Table 1 are generally employed as substrate materials, but some of them can also be utilized as stretchable dielectric layers in a thinner format for stretchable field-effect transistors (FETs)[204−207] and phototransistors (pTrs).[209,210] Although using the same material base as the substrate and dielectric layers may be beneficial in terms of processing compatibility and junction interface quality, most of these elastic materials can only be processed using solution processes, and thinning down their thicknesses via spin-coating has limitations. Moreover, they exhibit low density and low dielectric constants ($k \approx 2-3$), resulting in high leakage current (especially during mechanical deformation) and poor gate controllability, which is directly related to power consumption issues. Considering their use in biomedical applications, the operation voltage range should be maintained within a few volts, but typical stretchable devices employing the solution-processed elastic layers as dielectrics exhibit one to two orders higher operation voltage ranges. Applying excessive voltages directly on biological surfaces can be extremely harmful and thus, application of stretchable FETs and pTrs require significant advancements to engineer the

https://doi.org/10.1021/acs.chemrev.3c00548
Chem. Rev. XXXX, XXX, XXX−XXX

Table 2. Characteristics of Flexible and Stretchable TEs, According to the Different Material and Structure Types

Type	Materials	Transmittance (%)	R_s ($\Omega\ \square^{-1}$)	Maximum mechanical deformability	Durability (cyclic test number)	Ref.
Ultrathin metal film	Ni-doped Cu/PET	84	<20	Bending at bending radius of 2.5 mm	–	222
	Ag/epoxy	~55	18.2	Bending at bending radius of 1 mm	3,000 (bending at bending radius of 5 mm)	244
	Ca-doped Ag/PET	~95	27.1	Bending at bending radius of 5 mm	800 (bending at bending radius of 5 mm)	245
	ZnS-Ag-ZnS/PET	74.22	9.74	–	10,000 (bending at bending radius of 5 mm)	249
	Ag-PEI/PEN	>95	<10	Bending at bending radius of 5 mm	100,000 (bending at bending radius of 5 mm)	251
	Au-alucone/PET	77.8	~30	Bending at bending radius of 6 mm	1,500 (bending at bending radius of 6 mm)	254
	Ni-doped Ag/PET	80	<20	Bending at bending radius of 0.25 in.	1,200 (bending at bending radius of 0.25 in.)	257
	O-doped Ag/PET	91	20	Bending at bending radius of 1.1 mm	–	260
Metal mesh	Ni/PET	90	0.036	Bending at bending radius of 3 mm	1,000 (bending at bending radius of 3 mm)	262
	Ag/PEN	80.35	6.85	–	–	263
	Ag/PET	~80	13.26	Bending at bending radius of 5 mm	500 (bending at bending radius of 5 mm)	264
	Ag/PDMS	85.79	6	60% strain	1,000 (stretching at 60%)	264
	Cu/P(METAC-*co*-MPTS)	83	0.9	Bending at bending radius of 1 mm	1,000 (bending at bending radius of 1 mm)	267
	Au/PDMS	82.5	21	160% strain	1,000 (stretching at 50%)	272
	Au/PI	97	20	–	–	273
	Ag/PET	96	3	Bending at bending radius of 1 mm	50 (bending at bending radius of 1 mm)	274
Oxide-metal-oxide multilayer	NiO-Ag-NiO/PET	~82	7.6	Bending at bending angle of 90°	2,000 (bending at bending angle of 90°)	248
	Epoxy-Cu-ITO/PI	~92.5	50	Bending at bending radius of 3 mm	1,000 (bending at bending radius of 3 mm)	275
	Al:ZnO-Ag-Al:ZnO/CPI	96	8.5	Bending at bending radius of 5 mm	5,000 (bending at bending radius of 5 mm)	276
	MoO_3-Au-MoO_3/3M elastomer	70–80	~20	100% strain	100 (stretching @ 100%)	277
	ZnO-Cu-ZnO/PET	80.9	30.4	Bending at bending radius of 6 mm	1,000 (bending at bending radius of 8 mm)	278

dielectric materials and device operation before their use in biomedical systems.

Recently, Koo et al. developed a novel stretchable dielectric material which can be deposited using vacuum-based deposition technique, thus providing thickness controllability.[211] By copolymerizing two monomers with different mechanical properties through an initiated chemical vapor deposition process with an optimal ratio, high-quality nanometer-scale layers that exhibit both stretchability and insulation properties could be developed. In specific, the deposited polymeric film showed a trade-off relationship between its stretchability and final thickness, where 40% stretchability could be achieved at thickness of ~200 nm. Wafer-scale fabrication of stretchable transistors employing this stretchable dielectric with ~200 nm thickness exhibited high uniformity in terms of electrical performance, and significantly reduced operation voltage range (−5 to 5 V for logic gates) as compared to those employing solution-processed stretchable dielectrics. Although the biomedical application of stretchable devices employing the vacuum-deposited stretchable dielectric has not been demonstrated yet, it marks a significant advancement toward the development of functional electronic and optoelectronic circuits for use in future biomedical systems.

2.4. Materials for Flexible and Stretchable Transparent Electrodes

Thin film electrodes with optical transparency and mechanical deformability play a vital role in developing large-area flexible and stretchable optoelectronic devices. To be effective, these electrodes must withstand substantial strain (surpassing the fractural strain of electronic materials, approximately 1%) without noticeable alterations in their electrical and optical properties. In specific, both high optical transparency of above 90% and sheet resistance lower than 10 $\Omega\ \square^{-1}$ should be maintained, which is comparable to the conventional indium tin oxide (ITO) electrode used in industry for rigid devices. Research efforts have thus been devoted to achieving these characteristics, focusing on enhancing the mechanical performance of transparent electrodes (TEs) while meeting the required optoelectronic properties. Consequently, two strategies have emerged as effective approaches. One approach involves engineering the dimensional and structural configurations using established materials (i.e., ultrathin films of metal and oxide) to confer transparency and mechanical deformability (Figure 5A).[212,213] This metal film-based approach, as we name it, is beneficial in terms of high electrical conductivity and potential to achieve high optical transparency, while attaining a reasonable mechanical deformability. As such, homogeneous metal films (i.e., Ag,[214−216]

https://doi.org/10.1021/acs.chemrev.3c00548
Chem. Rev. XXXX, XXX, XXX−XXX

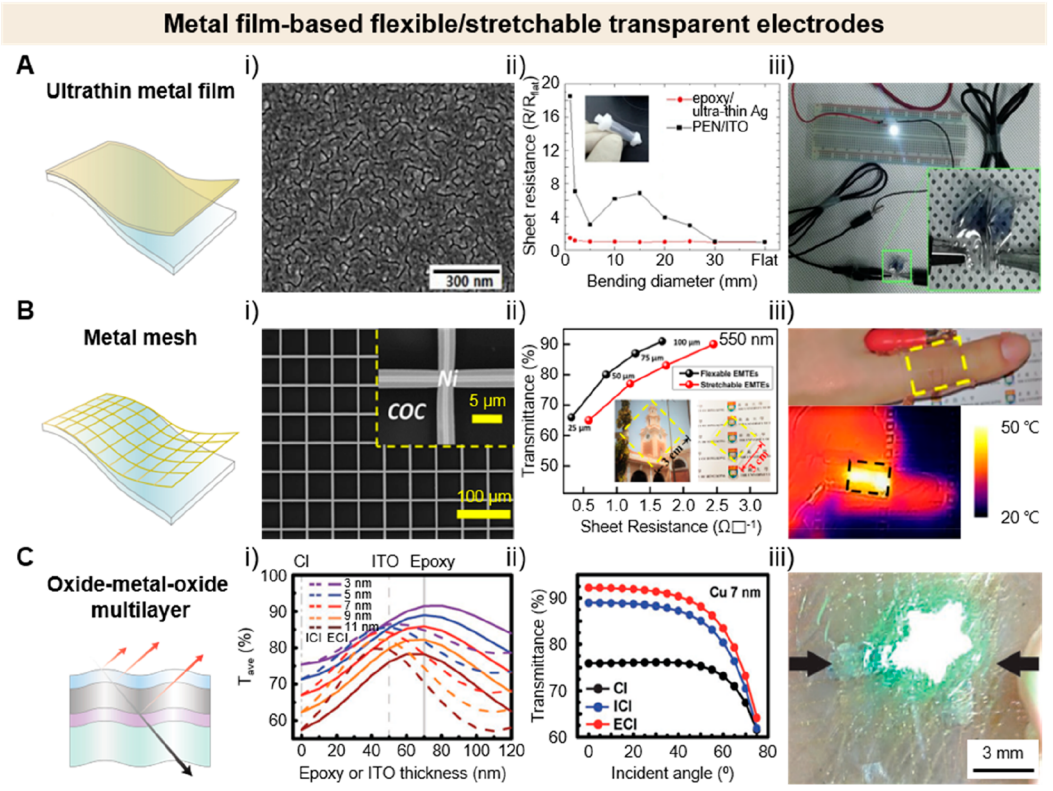

Figure 6. Metal film-based flexible and stretchable TEs. (A) From left to right, schematic image of an ultrathin metal film, (i) an SEM image showing the surface morphology of ultrathin metal, (ii) stability of the flexible TE during bending, and (iii) an LED maintaining its performance during crumpling of the electrode, respectively. Reproduced with permission from ref 244. Copyright 2020 Elsevier. (B) From left to right, schematic image of a metal mesh electrode, (i) an SEM image showing the grid pattern, (ii) relationship between sheet resistance and transmittance of a grid electrode, and (iii) stretchable transparent metal grid electrode applied as a heater, respectively. Reproduced with permission from ref 262. Copyright 2019 John Wiley & Sons, Inc. (C) From left to right, schematic image of an OMO multilayer, (i) relationship between bottom ITO thickness and transmittance, (ii) effect of incident angle on transmittance, and (iii) wearable QLED based on the OMO electrodes, respectively. Reproduced with permission from ref 275. Copyright 2017 John Wiley & Sons, Inc.

Al,[217] Au,[218−220] or Cu[221−223]) with a thickness of 10−20 nm exhibit good electrical conductivity and optical transparency. Utilizing their ultrathin nature and through structural engineering, flexible and stretchable TEs with high performance can be developed. However, these electrodes cannot recover their functionalities once experiencing mechanical breakdown, and owing to their brittle ultrathin nature, they are not suitable for applications that require extreme deformability. Furthermore, structural engineering of these ultrathin metal films complicates their fabrication, requiring high cost and time for their manufacture.

In this regard, the second approach, which involves fabrication of transparent stretchable conductive composites based on creating electrically percolative networks of the conductive nanomaterials on or within elastomeric or hydrogel matrices (Figure 5B), can provide a hopeful solution. Thin composite films composed of metallic nanostructures,[224−226] nonmetallic nanostructures such as carbon nanotubes (CNTs),[227−229] graphene,[230−232] conducting polymers,[233−235] and hybrid of two or more nanostructures[236−238] offer superior mechanical durability compared to the ultrathin metal film-based ones and potential for scalable manufacturing. However, a common drawback of stretchable TEs made using these materials is their relatively lower electrical conductivity. Among conducting polymers, poly(3,4-ethylenedioxythiophene)-poly(styrenesulfonate) (PEDOT:PSS) is widely used due to its low cost and facile processing.[239,240] However, PEDOT:PSS has limitations in terms of low intrinsic conductivity, poor environmental stability (especially under high temperature, high humidity, or UV irradiation), and self-emission of a blue/green tinge, which restrict its applications in flexible and stretchable optoelectronics. On the other hand, metallic NWs and carbon nanomaterials like CNTs and graphene can exhibit excellent conductivity. However, thin films comprising a multijunction assembly of these nanomaterials often suffer from high contact resistance at the junctions. Additionally, the presence of surface defects and polycrystallinity in carbon materials, which are challenging to eliminate, further reduces their conductivity. As such, the choice of materials and approaches for the fabrication of flexible and stretchable TEs must be carefully selected to meet the performance requirements of targeted application. In the following, the two approaches will be reviewed with detail, focusing on the material type and fabrication methods.

2.4.1. Flexible and Stretchable Transparent Electrodes Based on Metal Films. For flexible and stretchable TE applications, thin solid films must fulfill two fundamental requirements: high electrical conductivity and transparency. While metals exhibit the highest electrical conductivity compared to other materials, uniform metallic layers also exhibit high reflectivity, which results in low optical transmittance. Hence, numerous strategies have been developed to

https://doi.org/10.1021/acs.chemrev.3c00548
Chem. Rev. XXXX, XXX, XXX−XXX

improve the transparency of metal-based electrodes for use in optoelectronic applications, and among them, three strategies have been reported to be readily applicable for the fabrication of flexible and stretchable TEs. The first is reducing the thickness of the metals, which is beneficial in terms of both flexural rigidity and optical transparency of the TEs.[212] Adjusting the transparency by using noncontinuous metal films, such as metal mesh with different geometries and aspect ratios, is another widely adopted strategy for developing TEs.[241] Lastly, TEs fabricated by inserting ultrathin metal film between transparent oxide films, also known as oxide/metal/oxide (OMO) structures, have been reported to exhibit both high transparency and conductivity with mechanical flexibility.[242] Table 2 summarizes the representative properties of flexible and stretchable TEs based on metal films, with different materials and structures. In the following, each method will be reviewed comprehensively, focusing on the performance metrics of the flexible and stretchable TEs as well as integration strategies for flexible and stretchable optoelectronic device fabrication.

2.4.1.1. Ultrathin Metal Film-Based Flexible and Stretchable Transparent Electrodes. Ultrathin metal films can be deposited directly onto flexible and stretchable substrates using physical vapor deposition (PVD) techniques. The most frequently used materials for flexible and stretchable TEs based on ultrathin metal films are Ag and Cu, owing to their high intrinsic conductivity, with Ag being the most electrically conductive element, i.e., 6.30×10^7 S/cm at 20 °C. Cu exhibit similar level of conductivity, but is a much more cost-effective material. Generally, the deposition of thin metal films by PVD techniques such as thermal evaporation and sputtering follows an island-like growth model, known as the Volmer−Weber growth model.[243] Below a critical thickness that typically ranges from 10 to 20 nm, the deposited metal atoms are agglomerated into isolate islands and form a noncontinuous film on a nonwettable substrate, thus exhibiting high sheet resistance due to electron scattering at the interfaces and grain boundaries. After reaching the percolation threshold, the sheet resistance can be lowered by further deposition of the metal, but the optical transparency is significantly sacrificed. Thus, the key strategy for developing flexible and stretchable TEs based on ultrathin metal films has been improving the wettability of metals on target substrates, thereby decreasing the percolation threshold.

One effective strategy to improve the wettability of the deposited metal layer is pre-evaporating a seed layer on the target substrate. The seeding layer serve as dense nucleation centers, thereby suppressing the growth of metal islands and lowering the percolation threshold. For example, Bae et al. reported on the fabrication of ultrathin (9 nm) Ag TEs, where a spin-coated polyethylenimine (PEI) layer was used as a seed layer to promote Ag deposition (Figure 6A).[244] specifically, amine groups in the PEI served as nucleation sites, and Ag atoms during the initial stage of deposition were immobilized and reacted over the entire surface to suppress random aggregation of Ag clusters (Figure 6A (i)). As a result, a continuous film of Ag could be deposited with a minimal thickness of 9 nm, which exhibited an initial conductivity of 6.11×10^4 S/cm and 4.16×10^4 S/cm at a bending radius of 1 mm (Figure 6A (ii)). The flexible TE could be used to turn on a white LED, and maintain its operation while the TE was being crumpled (Figure 6A (iii)). Besides the PEI seeding layer, various seeding materials have been reported including metals,[245−247] dielectrics,[248−250] polymer,[244,251,252] and organic monolayers.[253−255] Although different in the materials, the existence of a predeposited seeding layer effectively lowers the percolation threshold for forming a continuous film with smooth surface, thereby resulting in enhanced electrical conductivity and transparency with reduced thickness for enhanced mechanical flexibility.

Co-sputtering different materials as dopants, such as Al,[250,256] Ca,[245] Cu,[257,258] N,[222] Ni,[257] and O,[259,260] can also improve the wettability of the deposited metal by suppressing the formation of metal islands, thereby achieving a continuous film at reduced thickness. For instance, Gu et al. reported on the fabrication of an ultrasmooth and ultrathin Ag film, in which the percolation threshold was significantly reduced by introducing a small of Al during metal deposition.[261] As a result, a 6 nm-thick Al-doped-Ag film exhibited transmittance of 65% in the whole visible range (400−800 nm). The percolation threshold can be further decreased by combining the two strategies described. In a work by Zhao et al., a seeding layer of Ta_2O_5 was predeposited on a PET substrate, followed by codeposition of Ag and Al, which resulted in the deposition of a smooth continuous film with thickness of 4 nm.[250] Flexible organic solar cells developed using this ultrathin metal film exhibited comparable power conversion efficiency as those fabricated using ITO electrodes, but with enhanced mechanical capabilities.

However, challenges remain in terms of improving the optical transparency for adoption in flexible and stretchable TE applications. For fabrication of devices that does not support sequential vacuum-based layer deposition techniques, their transfer can be extremely difficult due to the ultrathin brittle nature. Increasing the layer thickness may increase the transfer yield, but in sacrifice of optical transparency which is already at a modest level with minimal thicknesses. Thus, further investigation is required before their practical use for flexible and stretchable optoelectronic device fabrication.

2.4.1.2. Metal Mesh-Based Flexible and Stretchable Transparent Electrodes. TEs based on periodically or randomly patterned metal meshes on flexible and stretchable substrates have been widely investigated.[241,242] This is mainly ascribed to the facile manipulation of the optical transparency and electrical conductivity by modifying the geometric parameters such as the line width, spacing (or pitch), and thickness under the same active area. For example, Khan et al. reported on the fabrication of a highly conductive (sheet resistance as low as 0.036 Ω $\square^{-1}$) and transparent (optical transmittance of 91% at 550 nm wavelength, Figure 6B (ii)) deformable TEs based on template-electrodeposited and imprint-transferred Ni mesh with a microscale line width (4 μm, Figure 6B (i)).[262] In specific, mesh patterns were first photolithographically formed on an ITO substrate using SU-8 film, followed by electrodeposition of Ni inside the trenches of the SU-8 template. Flexible TEs were fabricated by heating and pressing the metal mesh into a plastic film; stretchable TEs by pouring PDMS solution onto the electroplated SU-8 template and peeling off after curing the PDMS. The stretchable Ni mesh-based TE was applied as a heater and attached onto a human finger, showing no performance degradation during finger motions and under various tensile strains (Figure 6B (iii)).

Basically, there is a trade-off relationship between the conductivity and transparency. Increasing the line width and thickness results in higher conductivity due to enhanced carrier

https://doi.org/10.1021/acs.chemrev.3c00548
Chem. Rev. XXXX, XXX, XXX−XXX

path, but results in decreased transparency due to increased shadow area (the area beneath the metal mesh). Increasing the line spacing results in higher transparency due to decreased shadow area, but in decreased conductivity. The opposite effects are incurred by decreasing the line width, thickness, and spacing. The aspect-ratio (AR) of the mesh, which is defined as the line thickness divided by the width, also affect the TE performance. An increase in the AR of the metal mesh results in higher conductivity due to decreased lateral resistance of the TE, but results in higher surface roughness. This can be disadvantageous in terms of device fabrication, especially in subsequent deposition of a functional layer on top of the TE. Thus, the geometrical factors must be carefully planned for desired electrical and optical performance, and for followed processes for device fabrication.

The high cost and time-consuming fabrication processes, such as nanoimprint lithography, e-beam lithography, vacuum-based PVD, metal etching, and lift-off processes, are the major challenges for the commercialization of metal mesh-based flexible and stretchable TEs. In addition, the surface roughness issue must be resolved for scalable fabrication of flexible and stretchable optoelectronic devices and thus, research is directed at developing facile, high-throughput, low-cost, and scalable methods for fabrication of metal mesh-based flexible and stretchable TEs with low surface roughness. Yu et al. developed a vacuum-free method for fabricating Ag mesh TEs with low surface roughness of about 20 nm.[263] Combining a doctor blade method with roll-to-roll thermal-imprinting process, Ag mesh TEs with sheet resistance of 6.85 $\Omega\ \square^{-1}$ and transmittance of 80.35% were fabricated, which is fully compatible with the industrial roll-to-roll process. Kim et al. strategically used a PEDOT:PSS layer to reduced the surface roughness, after fabrication of Ag mesh-based TE via gravure-offset printing process.[264] After the gravure printing process using a UV-curable resin, the exposed Ag meshes were coated with a PEDOT:PSS layer, which minimized the surface roughness. Flexible solar cells were developed using such a smooth electrode, and they were reported to exhibit higher power conversion efficiency and mechanical durability as compared to ITO-based control devices.

Recently, Li et al. reported on the development of a facile fabrication method for metal mesh-based flexible and stretchable TEs, which were embedded in an elastomeric PDMS matrix for minimized surface roughness.[265] The fabrication process involved three main steps of 1) spin coating a liquid PDMS layer on a PET substrate, 2) Ag mesh printing using liquid substrate electric-field-driven (LS-EFD) microscale 3D printing, and 3) low temperature sintering. Their method could directly encapsulate the Ag mesh TE with high AR on a flexible substrate without any additional packaging processes. The metal mesh-based TE exhibited excellent electrical and optical performance (sheet resistance of 6 $\Omega\ \square^{-1}$ and transmittance of 85.70%, respectively), and stretchable strain sensors made using the Ag mesh TE could be successfully applied to different positions of the body to differentiate various facial expressions and distinguish joint movements. As such, the low surface roughness is beneficial for integration in a large range of devices, especially for thin film-based flexible and stretchable optoelectronic devices that require a smooth TE to avoid short-circuit.

Besides the periodically patterned metal meshes with rectangular shapes, metal meshes with other geometrical symmetries such as lines, triangular shapes, honeycomb structures, serpentine structures, brick-walls, and circular can be fabricated, based on various patterning techniques.[241] Nonperiodic and randomly patterned metal meshes can also be fabricated via low-cost processes, which include bioinspired template,[266,267] self-forming crack lithography,[268,269] coffee-ring lithography,[270,271] and grain boundary lithography.[272] For instance, Yu et al. reported on the fabrication of bioinspired flexible and stretchable TEs, whereby plant leaves were adopted as the template to create random mesh structures via chemical deposition of Cu.[267] The fabricated TEs displayed an exceptional conductivity and transmittance (0.9 $\Omega\ \square^{-1}$ at 83% transmittance), and also exhibited high mechanical durability under cyclic bending and stretching tests. Guo et al. used In_2O_3 islands as a mask to deposit Au nanomesh on Si wafers, which were then transferred onto elastomeric substrate for stretchable TE fabrication.[272] Despite the complicated fabrication process of In_2O_3 mask deposition, etching in diluted HNO_3 and HF for island formation, Au deposition, and final transferring, the fabricated stretchable Au nanomesh TE exhibited excellent mechanical stability with minimal degradation up to 50% tensile strain, and high transmittance of 82.5% at sheet resistance of ~20 $\Omega\ \square^{-1}$.

Direct deposition of metal meshes onto target substrates using printing techniques have been investigated as cost-efficient methods for the fabrication of flexible and stretchable TEs, since most of the metal materials are wasted in lithography-based techniques for metal mesh fabrication. Another advantage of this direct printing method is that TEs can be readily developed on surfaces with dynamic morphologies, and on elastomeric substrates with low thermal budgets. Examples include direct writing of metal meshes on flexible substrates using concentrated Ag nanoparticle inks and electrohydrodynamic printing of Ag and Au metal meshes with submicron line widths.[273,274] Owing to the maskless and etching-free patterning approach, metal meshes with high transmittance of over 90% could be fabricated on deformable substrates, which is highly desirable for flexible and stretchable optoelectronic applications.

In summary, metal mesh-based TEs on flexible and stretchable substrates are regarded a promising candidate for soft optoelectronic applications owing to their superior mechanical, electrical, and optical properties. Minimizing the surface roughness of these metal meshes is critical for followed device fabrication. In terms of fabrication, facile and scalable methods that support low cost, reproducibility, and homogeneity is required for mass production. Direct printing techniques with high precision control of mesh patterning are particularly of great interest. Technological advances have enabled the direct deposition of metal meshes with line widths in the submicrometer range, resulting in excellent optoelectrical performances. Depending on the target application, the selection of materials and fabrication techniques should be carefully chosen, which will be discussed in detail in the following sections.

2.4.1.3. Oxide-Metal-Oxide Multilayer-Based Flexible and Stretchable Transparent Electrodes. The OMO multilayer structures feature tunable high transparency and electrical conductivity, and great compatibility with other layers of soft optoelectronic devices in terms of charge injection and collection.[242] Owing to the bottom oxide layer, which serves as a seeding layer for metal thin film growth, the percolation threshold of the metal thin film can be greatly reduced to achieve a smooth and continuous film at a few nanometer

https://doi.org/10.1021/acs.chemrev.3c00548
Chem. Rev. XXXX, XXX, XXX−XXX

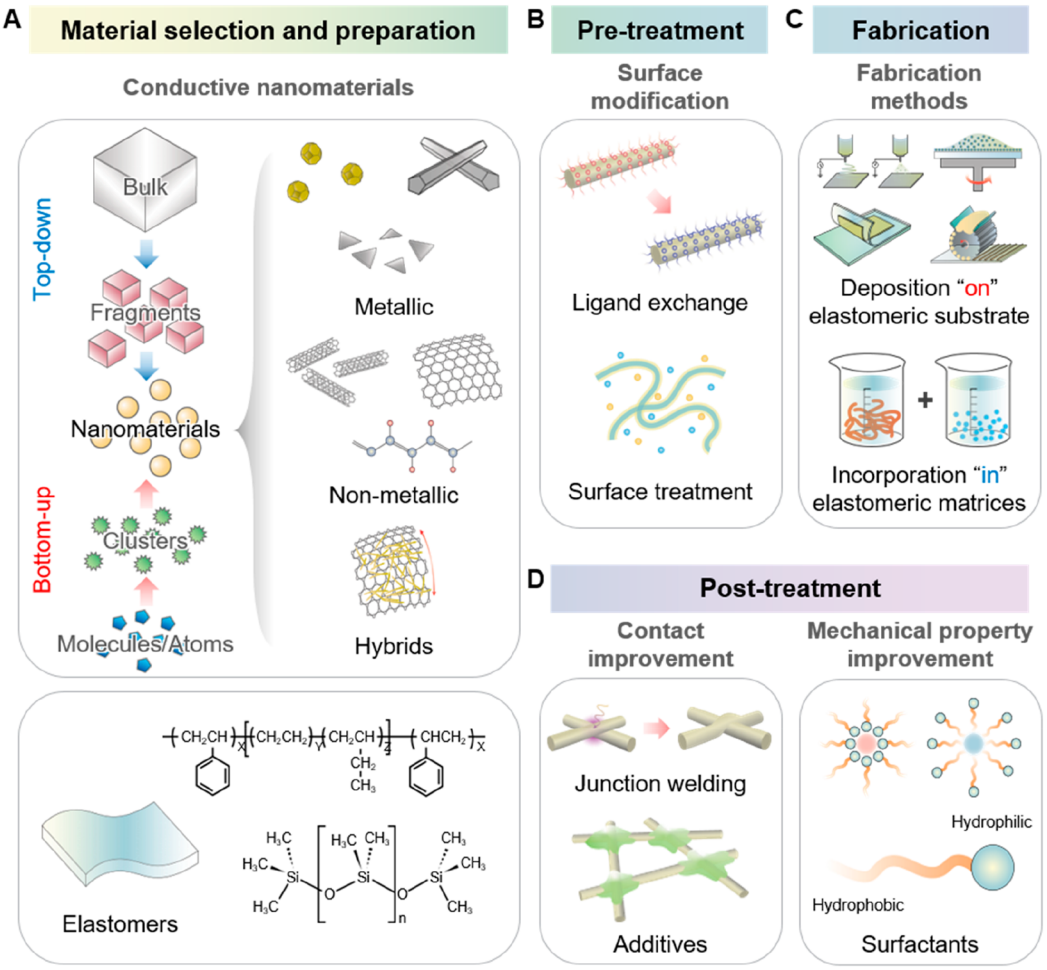

Figure 7. Schematic illustration describing the strategies for developing flexible and stretchable TEs based on conductive nanomaterials. First, (A) proper materials for the conductive nanomaterials and elastomeric matrices should be chosen, followed by (B) pretreatments for enhanced miscibility. (C) After the composite fabrication via different methods, (D) post-treatments can be performed for enhanced electrical and mechanical properties.

scale. The work function of the OMO multilayer can be deliberately controlled to form desired contact with the adjacent functional layers via appropriate selection of the oxide, or via doping. The problems associated with low transparency of the bare metal film can be solved by modulating the thickness of the oxide layers for an antireflective effect (Figure 6C). Song et al. reported on the fabrication of multilayered flexible and stretchable TEs using Cu as the metal, and epoxy/ITO as the top/bottom oxide layers, respectively.[275] Owing to the destructive interference induced by spin-coated epoxy layer with low refractive index, a high average transmittance of over 90% was achieved for epoxy/Cu/ITO multilayer structure, with Cu thickness of 7 nm (sheet resistance of 50 Ω $\square^{-1}$, (Figure 6C (i) and (ii)). By integrating geometrical engineered multilayer TE with ultra-thin quantum dot LEDs (QLEDs), stretchable QLEDs with a high brightness of 20,000 cd/m^2 at 9 V could maintain its operation after being mounted on skin and applying a compressive force (Figure 6C (iii)).

The enhancement of optical transmittance can be achieved by adopting the following design rules: 1) select a highly conductive metal thin film with low loss (Cu, Ag, Au, Al, and Pt in most cases), 2) for the bottom oxide, use high refractive index materials, and control its thickness to obtain a phase angle of $\pi/2$ at the metal/oxide interface, 3) optimize the refractive index and thickness of the top oxide layer for optimal broadband transmittance. Using this approach, Ji et al. demonstrated the fabrication of OMO multilayer TEs deposited on flexible PET substrates, whose transmittance (~88.4%) surpassed that of the original PET substrate (~81.4%), achieving a transmittance of ~100.3%.[258] In specific, Al_2O_3 was adopted as the top oxide layer, Cu-doped Ag as the metal film, and ZnO as the bottom oxide layer. The optimized thicknesses of 56 nm/6.5 nm/24 nm for the Al_2O_3/Cu-Ag alloy/ZnO, respectively, resulted in sheet resistance of 18.6 Ω $\square^{-1}$ and absolution transmittance of 88.4%. More recently, Kim et al. reported on the fabrication of flexible OMO multilayer TEs with less than 50 nm thickness, using nitrogen-doped Ag layers as the sandwiched metal.[276] The ~20 nm thick Al-doped ZnO was used as both the top and bottom oxide layers, and the thickness of the Ag film was 9 nm, owing to the doping effect of N_2 that substantially lowered the percolation threshold for film formation. The multilayered flexible TE exhibited a high transmittance of 96% at wavelength of 550 nm and low sheet resistance of 8.5 Ω $\square^{-1}$, and no significant changes in the sheet resistance was observed after 5,000 bending cycles.

https://doi.org/10.1021/acs.chemrev.3c00548
Chem. Rev. XXXX, XXX, XXX−XXX

The continuous and uniform, smooth features of the OMO multilayer flexible and stretchable TEs provide a distinct advantage when integrating them into photovoltaic or light-emitting devices. For instance, Choi et al. reported on the fabrication of stretchable organic LEDs (OLEDs) based on MoO_3/Au/MoO_3 multilayer TEs with less than 40 nm thickness.[277] The prestrained approach was adopted to impart stretchability to the OLED structure with overall thickness below 1 μm. A Norland Optical Adhesive 63 (NOA63) was used to transfer the ultrathin OLED layers onto prestrained 3M elastomer. The NOA63 also served as an encapsulation layer, and as optical-adhesive for enhanced light out-coupling after incorporation with SiO_2 nanoparticles. As a result, a high current efficiency of ~82.4 cd/A and an external quantum efficiency of ~22.3% were achieved with minimum efficiency roll-off during 100% stretching, owing to the efficient charge injection through the smooth-surfaced OMO multilayer TEs. Most recently, Li et al. demonstrated that the flexible solar cells fabricated using ZnO/Cu/ZnO multilayer TEs exhibited power conversion efficiency of 6.01%, which was nearly 2.5 times higher than that of ITO-based control device.[278] This was mainly attributed to the enhanced transmittance to effectively convert light, and to lower series resistance resulting from the low surface roughness compared to cells with ITO.

The continuous nature of the OMO multilayer with near micrometer thickness also offers benefits in terms of processing. Namely, mass production technologies such as roll-to-roll printing have been reported to be applicable to OMO multilayer TE fabrication on large commercial PET substrate. The performance of the OMO TEs is highly dependent on the maturity of film deposition technology. Practical routes for commercialization of the flexible and stretchable OMO TE technology thus lies in scalable and high throughput film deposition methods that support operation at low temperatures.

2.4.2. Intrinsically Soft Transparent Electrodes Based on Conductive Nanomaterials. Although flexible and stretchable TEs based on ultrathin metal films exhibit promising attributes for use in next-generation soft optoelectronic devices, in oftentimes their fabrication requires complex and time-consuming processes such as vacuum-based film deposition, patterning and etching of the deposited structures for enhancing the optical transparency, and transferring of the ultrathin and brittle functional materials onto target substrates which may be undesirable in terms of scalable fabrication. Furthermore, the electrical and optical performance of the ultrathin metal film-based flexible and stretchable TEs are subject to severe degradation at the onset of crack formation, limiting their use in diverse applications. For instance, the smooth and continuous morphology of the metal film is mechanically susceptible to stretching, where cracks are formed on the surfaces of the metal film. While electrical pathways may be preserved during stretching, the formation of cracks can alter the optical transmittance, as well as hinder efficient charge injection onto vertically stacked layers. As such, the ultrathin metal film-based and OMO multilayer-based TEs may not be suitable for fabrication of stretchable optoelectronic devices. While metal meshes with specific geometries, such as honeycomb structures, can tolerate certain amounts of applied strain, the mesh structures are particularly not suited for LED applications since vertical charge injection can only occur through the areas of the mesh, resulting in nonuniform light emission.

Structural engineering methods, such as the adoption of stretchable wavy designs, can be used to impart stretchability to the ultrathin metal film-based TEs, but significantly complicates their device integration. Moreover, these space-consuming designs are not desirable for applications that require high device density or resolution, such as wide field-of-view cameras (based on arrays of stretchable PDs) and stretchable active matrix displays. In this regard, intrinsically soft TEs based on composites of conductive nanomaterials and elastomeric matrices have gained increasing attentions. Figure 7 schematically illustrates the strategies for the fabrication of these TEs based on conductive nanomaterials. In general, the fabrication of intrinsically soft TEs involves the following sequential processes: 1) selection of appropriate conductive nanomaterials and elastomeric matrices for desired electrical, mechanical, and optical performance (Figure 7A); 2) pretreatment of the conductive nanomaterials to achieve homogeneous dispersion or mixture with the elastomeric matrices (Figure 7B); 3) fabrication of the intrinsically soft composite, via direct/indirect printing of conductive nanomaterials on the elastomers or mixing/embedding the nanomaterials in the elastomeric matrices (Figure 7C); and 4) post-treatment for achieving enhanced junction qualities of percolated nanomaterial networks or enhanced mechanical properties of the elastomeric matrices (Figure 7D).

In fact, these strategies are identical to those used for the fabrication of intrinsically soft electrodes in general, of which the details have been thoroughly reviewed in our previous review articles,[25,279−282] as well as in other literature.[283−285] We recommend referring to those articles for a comprehensive understanding on the overall strategies for the fabrication of intrinsically soft electrodes with desired properties, such as materials selection for conductive nanomaterials and elastomers, and also pre- and post-treatment methods for tunable electrode properties. In this review, we will focus on the strategies for materials and fabrication techniques used to develop intrinsically soft TEs in the form of nanocomposite films. The electrical, mechanical, and optical performance of these intrinsically stretchable TEs can be manipulated by controlling the quantity of conductive nanomaterials deposited on or incorporated into the elastomeric matrices. Generally, there is a trade-off relationship between the electrical performance and mechanical/optical performances: higher amounts of conductive nanomaterials enhance their percolation for improved electrical performance, in sacrifice of optical transparency and stretchability. Opposingly, minimal amounts of percolated nanomaterials result in enhanced mechanical freedom of the composite with high transmittance, but with low electrical performance. The physical properties of the conducive nanomaterials and elastomers are critical for achieving a homogeneous mixture, which in turn affect the final surface properties of the composite and their device integration strategies. In the following sections, the strategies for developing intrinsically soft TEs will be reviewed, with focus on the selection of appropriate materials and their fabrication techniques.

2.4.2.1. Intrinsically Soft Transparent Nanocomposite Electrodes Based on Metallic Nanostructures. When fabricating intrinsically soft TEs based on conductive nanomaterials, several factors must be thoroughly considered besides controlling the quantity of nanomaterials for obtaining the desired electrical, mechanical, and optical properties. These include 1) the dimension of the nanomaterials for achieving

https://doi.org/10.1021/acs.chemrev.3c00548
Chem. Rev. XXXX, XXX, XXX−XXX

Table 3. Characteristics of Intrinsically soft TEs, According to the Material Types

Type	Materials	Transmittance (%)	R_s (Ω $\square^{-1}$)	Maximum mechanical deformability	Durability (cyclic test number)	Ref.
Metallic 1D nanostructures	Ag NW/PDMS	~91.0	~20	50% strain	10,000 (stretching at 50%)	286
	Ag NW/chitosan	89.0 at 550 nm	8.4	50% strain	500 (bending at bending radius of ~4 mm); 100 (stretching at 30%)	287
	Ag NW/PDMS	78	~18	30% strain	500 (stretching at 30%)	288
	Ag NW/PET	–	0.72	–	–	289
	Ag nanotrough/PET	90	~2	50%	2,000 (bending at bending radius of 2 mm)	290
	Ag NW/PET	92	~10	Bending at bending radius of 1.5 mm	1,000 (bending at bending radius of 5 mm)	291
	Ag NW/PDMS	88	<20	100% strain	4,000 (bending at bending radius of 5 mm) 4,000 (stretching at 20%)	292
	Ag NW/PUA	76.4	10	Bending at bending radius of 1 mm	–	293
	Cu NW/PET	85	31	Bending at bending radius of 5 mm	1,000 (bending at bending radius of 5 mm)	294
	Cu NW/PU	86.7 at 550 nm	52	60% strain	200 (stretching at 60%)	295
Nonmetallic nanomaterials	CNT/PAA	84	60	100% strain	1 million (stretching at 40%)	296
	PDMS/CNT/PDMS	53.1 at 550 nm	–	100% strain	100 (stretching at 100%)	297
	CNT/PEN	90	98	Bending at bending radius of 7.5 mm	500 (bending at bending radius of 7.5 mm)	298
	Graphene/PET	97 at 550 nm	~350	Bending at bending radius of 2 mm	10,000 (bending at bending radius of 2 mm); 10,000 (stretching at 5%)	299
	Graphene/PDMS	90.8 at 550 nm	6	90% strain	10,000 (stretching at 60%)	300
	Graphene/PDMS	80.7 at 550 nm	~1,000	30% strain	1,000 (stretching at 30%)	301
	PEDOT:PSS/PET	93 at 550 nm	~90	Bending at bending radius of 4 mm	200 (bending at bending radius of 4 mm)	302
	PEDOT:PSS/ionogel	87 at 550 nm	50	Bending at bending radius of 3 mm	1,000 (bending at bending radius of 3 mm)	303
	PEDOT:PSS/ENIM TCB	91.5 at 550 nm	80	50% strain	80 (stretching at 40%)	304
	PEDOT:PSS/PEO	93.2 at 550 nm	130	80% strain	5,000 (stretching at 80%)	235
Nanomaterial hybrids	Ag NW@rGO/PDMS	91.1	3.3	40% strain	1,000 (stretching at 40%)	305
	Graphene/Ag NW-embedded SEBS	84	23.2	40% strain	500 (stretching at 40%)	306
	Ag NW@MXene/PMMA	83.8 at 550 nm	13.9	Bending at bending radius of 5 mm	1,000 (bending at bending radius of 5 mm)	307
	Ag NW-CNT/glass	83 at 550 nm	~30	–	–	308
	Ag NW-CNT/Ecoflex	<90	24–27	400% strain	10,000 (bending at bending radius of 2 mm)	309
	Ag NW-CNT/VHB	66.4	8.7	250% strain	1,000 (stretching at 50%)	310
	CNT-PEDOT:PSS/PDMS	84 at 550 nm	90	100% strain	1,000 (stretching at 50%)	311
	Ag NW-PEDOT:PSS/PET	96 at 550 nm	12	Bending	5,000 (bending)	312
	Graphene-Ag NW-embedded PEDOT:PSS/PDMS	78	58	~85% strain	50 (stretching at 80%)	313
	Ag NW/Mxene@PEDOT:PSS	97.6	17	100% strain	5,000 cycles (bending at bending radius of 2 mm)	314

low percolation threshold, 2) the quality of contacts within the percolated nanomaterials for enhanced conductivity, 3) surface chemistry of the nanomaterials to achieve homogeneous mixture and enhanced percolation quality, and 4) proper selection of the elastomeric matrix for desired mechanical properties. As such, the quality of the percolated network significantly impacts the electrical conductivity of the resulting intrinsically soft nanocomposite TEs as current is delivered through the percolated network of the nanomaterials. In addition, the intrinsic conductivity of the nanomaterials is also important. The most widely adopted conductive nanomaterials for the fabrication of intrinsically soft TEs are metallic nanostructures,[224−226] carbon-based nanostructures,[227−232] conducting polymers,[233−235] and their hybrids.[236−238] Table 3 summarizes the representative properties of recent intrinsically soft TEs fabricated using these nanomaterials, according to the material type.[286−314]

Among them, metallic nanostructures exhibit the highest electrical conductivity, and thus are most favorable for achieving high conductivity. However, most metallic nanostructures are opaque, and thus it is desirable to achieve a low percolation threshold for high optical transmittance. 1-dimensional (1D) nanostructures are beneficial in this purpose, because they can effectively form percolated networks with fewer quantity as compared to 0-dimensional (0D) and 2-dimensional (2D) nanostructures (Figure 8A). Furthermore, current can be dominantly conducted through the nanostructure itself rather than through the contacts between the nanostructures, which results in high conductivity since the contact resistance is much higher than the resistance of the

https://doi.org/10.1021/acs.chemrev.3c00548
Chem. Rev. XXXX, XXX, XXX−XXX

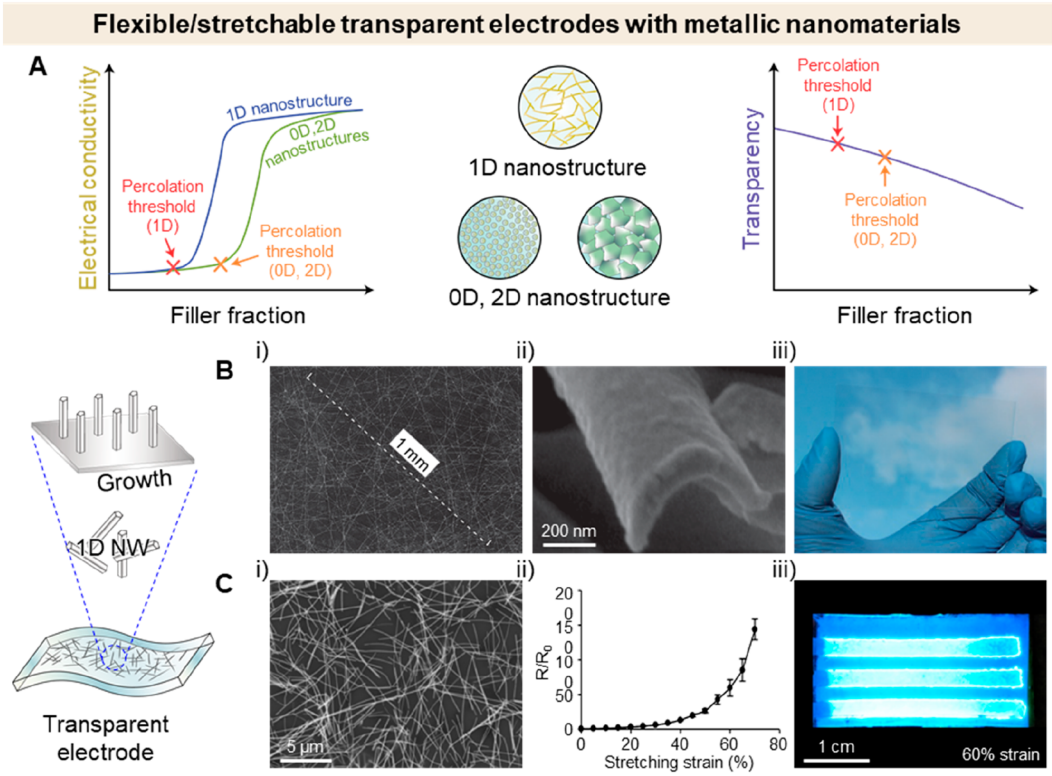

Figure 8. Intrinsically soft transparent nanocomposite electrodes based on metallic nanostructures. (A) Plots showing the relationship between the filler fraction and electrical conductivity/transparency of the fabricated soft TEs, based on the nanomaterial dimensions. Lower percolation threshold can be achieved using 1D nanostructures, and therefore their use is more beneficial in terms of achieving higher optical transparency. (B) From left to right, (i) a SEM image showing synthesis of ultralong Ag nanotroughs, (ii) a magnified image of the Ag nanotrough, and (iii) highly transparent nature of the Ag nanotrough-based electrode, respectively. Reproduced with permission from ref 290. Copyright 2013 Springer Nature. (C) From left to right, (i) a SEM image showing percolated Ag NWs, (ii) resistance change of Ag NW-based stretchable TE with respect to applied strain, and (iii) an image of intrinsically stretchable EL device, respectively. Reproduced with permission from ref 315. Copyright 2019 American Chemical Society.

nanostructure itself. Thus, both high electrical conductivity and optical transmittance can be obtained more easily when 1D metallic nanostructures are adopted to form percolation networks in intrinsically stretchable TEs.

Han et al. reported on the fabrication of intrinsically soft TEs based on the Ag NWs/PDMS composite, which exhibited a low sheet resistance of ~20 Ω $\square^{-1}$ and high transmittance of ~91%.[286] The authors strategically aligned the Ag NWs by a 2D ice-templating approach, whereby the Ag NWs were expelled and aligned by the ice crystals that were frozen at a certain speed and direction. The alignment of the Ag NWs resulted in minimized junction contacts, and even with a relatively low dosage of Ag NWs (4 $\mu g/cm^2$), a highly transparent and conductive stretchable TE was developed, with could maintain its electrode performance during stretching with 50% strain and after cyclic bending test for 10,000 cycles. In another work, Park et al. developed intrinsically soft TEs by embedding Ag NWs into biocompatible chitosan matrix.[287] The poor adhesion between the Ag NWs and chitosan matrix was modified by using an organic modifier, ethanolamine, which introduced polar groups to the surface of chitosan for improved bonding strength with the NWs. As a result, a low sheet resistance of 8.4 Ω $\square^{-1}$ and high transmittance of 89.0% at 500 nm was achieved. The fabricated Ag NW/chitosan TEs could conform to curved surface of human skin and maintain their electrical, mechanical, and optical robustness. As such, achieving strong bonding between the metallic nanostructure and the elastomeric matrix is vital for simultaneously obtaining high conductivity and mechanical stability. Gao et al. reported on the fabrication of intrinsically soft TEs by spray-coating Ag NWs on PDMS substrates.[288] Prior to the spray-coating, the PDMS substrates were treated with hexane to change the surface property from hydrophobic to hydrophilic, followed by oxygen plasma treatment. This ensured a good adhesion between the spray-coated Ag NW networks and PDMS, which was prestretched at 150% tensile strain for further improving the stretchability of the TE. The resulting stretchable TE exhibited a low sheet resistance of 18 Ω $\square^{-1}$ and transmittance of ~78%, and demonstrated minimal change in resistance after 500 cyclic stretching at 30% strain.

For the composites where the 1D metallic nanostructures are deposited on elastomeric substrates, post-treatment methods can be used to enhance the performance of the soft TEs. For instance, Li et al. adopted a series of post-treatment processes including water washing, plasma treatment, thermal annealing, and mechanical pressure to obtain highly conductive TEs based on screen-printed Ag NWs on flexible PET substrates.[289] The authors used Ag NW inks with a simple composition of distilled water, Ag NWs, and (hydroxypropyl)-methyl cellulose, which is a nonconductive polymer. Thus, charge transport was hindered by the nonconductive polymer portion after the Ag NW ink was printed. Through consecutive processes mentioned above, the polymer could be successfully removed and the Ag NWs were welded, resulting in an

https://doi.org/10.1021/acs.chemrev.3c00548
Chem. Rev. XXXX, XXX, XXX−XXX

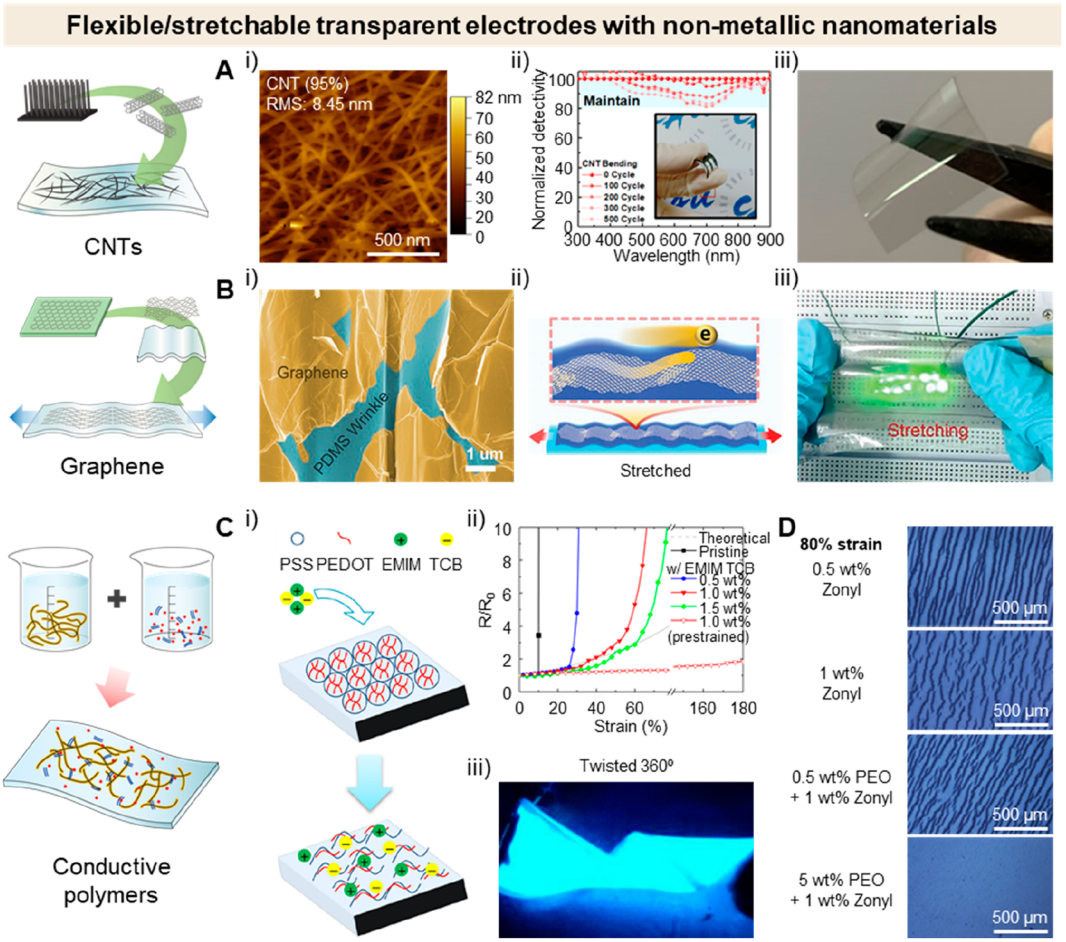

Figure 9. Intrinsically soft transparent nanocomposite electrodes based on nonmetallic nanostructures. (A) From left to right, (i) an AFM image showing low R_{RMS} of CNT networks, (ii) a plot showing the superb detectivity of PD based on CNT composite electrode, and (iii) an image of the flexible CNT composite electrode, respectively. Reproduced with permission from ref 298. Copyright 2021 Elsevier. (B) From left to right, (i) a SEM image of graphene/PDMS composite electrode, (ii) a schematic illustration describing charge transport in the stretched graphene/PDMS electrode, and (iii) an image showing stable operation of LEDs after stretching the graphene/PDMS electrodes, respectively. Reproduced with permission from ref 169. Copyright 2022 John Wiley & Sons, Inc. (C) Schematic illustrations showing (i) the morphological and compositional changes of PEDOT:PSS films after incorporation of ENIM TCB, and (ii), (iii) evidence of high mechanical stability of the PEDOT:PSS composite electrodes. Reproduced with permission from ref 303. Copyright 2017 American Chemical Society. (D) Optical microscopy images of stretched PEDOT:PSS composite electrodes with different PEO and Zonyl incorporation variations. Reproduced with permission from ref 304. Copyright 2020 John Wiley & Sons, Inc.

extremely low sheet resistance of 0.72 Ω $\square^{-1}$. On the other hand, Wu et al. used a different approach to minimize the junction contact resistance of the percolated 1D metallic nanostructures.[290] Their strategy involved the synthesis of ultralong (in millimeter-scale) 1D structured Ag nanotrough network, which could be easily transferred onto various flexible and stretchable substrates (Figure 8B). Specifically, the Ag nanotrough networks were fabricated by electrospinning polymer fibers into a web-like structure, followed by deposition of Ag and subsequent etching of the polymer fiber (SEM images shown in Figure 8B (i) and (ii)). Notably, the high junction resistance could be avoided owing to the continuous nature of the deposited Ag, which resulted in a low sheet resistance of below 10 Ω $\square^{-1}$ for the fabricated stretchable TEs. An excellent optical transmittance of over 90% was simultaneously achieved due to the spatially distributed Ag nanotroughs (Figure 8B (iii)). The mechanical stability of the Ag nanotrough networks was verified by connecting to a commercial LED and activating the LED while crushing and unfolding the fabricated electrode.

It is crucial that the soft TEs exhibit a smooth surface with minimized roughness, possibly within few nanometer scales, for compatibility with the followed device fabrication processes and scalable device integration. One simple yet effective method to achieve a smooth surface is by embedding the 1D metallic nanostructures into elastomeric matrices, rather than their deposition on the outer surface. Chen et al. reported on the fabrication of an intrinsically stretchable electroluminescent (EL) device based on nanocomposite films embedded with Ag NWs (Figure 8C (i)).[315] Ag NWs was first deposited on PDMS substrate with hydrophilic line patterns, resulting in their alignment in the hydrophilic regions. After recovering the hydrophobic property (leaving at ambient conditions for 24 h), the line-patterned Ag NW networks were transferred onto a stretchable substrate of Clear Flex 50 (CF, urethane rubber) by simply curing the CF and removing the PDMS template. The resulting stretchable TE exhibited sheet resistance of ∼15 Ω

https://doi.org/10.1021/acs.chemrev.3c00548
Chem. Rev. XXXX, XXX, XXX−XXX

$\square^{-1}$, optical transmittance of ∼85%, and low root-mean-square surface roughness (R_{rms}) of ∼22 nm. After consecutive layer depositions on the stretchable TE, a stretchable EL device was fabricated and showed stable operation at 60% stretching strain (Figure 8C (ii) and (iii)). In another work by Cui et al., stretchable TEs with extremely smooth R_{rms} was fabricated by embedding Ag NW networks into a bilayered structure of cross-linked poly(vinyl alcohol) (C-PVA)/PDMS.[292] C-PVA was deliberately chosen to enhance the chemical stability of PDMS and facilitate the device integration of the TE into a PD. The stretchable TE exhibited smooth surface with R_{rms} of 2.24 nm, a sheet resistance below 20 Ω $\square^{-1}$, and optical transmittance of >88%, all of which contributed to the stable operation of the fabricated PD at an extreme bending radius of 0.5 mm.

While 1D nanostructures based on Ag are most widely used, mainly owing to their good electrical conductivity, Cu NWs are being explored as a good substitute since they exhibit comparable electrical conductivity with much lower production cost and abundance.[316] However, their practical use has been hindered by the inevitable formation of byproducts (such as nanocubes and nanorods) which in turn affects the transmittance, and oxidation of the Cu NW surface that degrades the electrical conductivity significantly. Zhang et al. reported on a highly effective purification process of Cu NWs, which took advantage of the differences in the hydrophilicities of 1D and other nanostructures of Cu.[294] This resulted in their different adsorption affinities to otadecylamine (ODA)-based solution, and Cu NWs with extreme high purity could be obtained after a series of stirring and centrifugation with different solvent bases. Treating the purified Cu NWs with glacial acetic acid for a few minutes removed the oxides formed at Cu NW surfaces, and flexible TEs fabricated by filtering the highly purified Cu NWs exhibited a low sheet resistance of 31 Ω $\square^{-1}$ and high transmittance of 85%. Hu et al. fabricated stretchable TEs based on Cu NW/PU composite.[295] Prior to the composite formation, the oxides were removed by treating Cu NW film under forming gas (5% H_2 + 95% N_2) at 300 °C and chemically treated by 6-aminohexanoic acid to promote their bonding with PU matrix. Cu NW/PU TEs exhibited tunable sheet resistance of 8−52 Ω $\square^{-1}$ with transmittance of 70.7−86.7%, respectively, by controlling the amount of Cu NWs. The stretchable Cu NW/PU composite TE could endure tensile strains up to 60%, and remained functional after 200 cycles of stretching.

2.4.2.2. Intrinsically Soft Transparent Nanocomposite Electrodes Based on Nonmetallic Nanostructures. Carbon-based nanomaterials such as CNTs and graphene exhibit many attributes favorable for the fabrication of soft TEs in composite formats. These include excellent intrinsic electrical and mechanical properties and easy/well-established surface functionalization and doping methods that facilitate their homogeneous incorporation into elastomeric matrices with enhanced electrical performance. Other types of carbon-based nanomaterials, including fullerene and graphite, are considered less favorable for soft TE applications due to their high percolation threshold. In general, graphene has advantage over CNTs in terms of TE fabrication, because bundles of CNTs are semitransparent, cytotoxic, require additional processes to remove insulating dispersant in solution, and exhibit higher surface roughness when deposited onto elastomeric substrates. Despite these disadvantages, relentless efforts have been devoted by researchers toward investigating novel methods for soft TE fabrication based on CNT nanocomposites. For example, Zhou et al. reported on the development of highly durable and stretchable TEs based on poly(acrylic acid) (PAA)-wrapped CNTs.[296] Specifically, the authors devised a method where a monolayer of PAA partially wrapped individual CNTs in a helical structure, which displayed a significant enhancement effect of electrical conductivity as opposed to the intrinsically insulating nature of the PAA. The fabricated stretchable TEs exhibited highly durable features, with performance (a sheet resistance of 60 Ω $\square^{-1}$ at transmittance of 84%) remaining almost identical after 1 million cyclic stretching at applied strain of 100%.

Jang et al. reported on the fabrication of flexible CNT composite TEs, which played a vital role in suppressing the dark current of an organic PD with a fine detectivity of 2.07×10^{14} Jones.[298] First, CNT networks collected by filtering through microporous filters, featuring time-controlled transmittance and sheet resistance. After transferring the networks onto a PEN substrate, the CNT networks exhibited a smooth surface with R_{rms} of 8.45 nm, facilitating its integration with other layers of the organic PD (Figure 9A (i)). The optimized CNT composite TEs exhibited a sheet resistance of 98 Ω $\square^{-1}$ at transmittance of 90%. The flexible organic PD based on the CNT composite TEs could maintain its detectivity after cyclic bending of 500 cycles at bending radius of 7.5 mm (Figure 9 A (ii) and (iii)).

Graphene and its derivatives, GO and reduced GO (rGO), have been extensively researched for intrinsically soft TE applications owing to their single-atom-thickness-based high transparency, theoretically high electrical conductivity, and chemical/mechanical/thermal stabilities that facilitate their device integration.[317−319] As a good example, He et al. reported on the fabrication of soft TEs based on wrinkled graphene-elastomer composite, through a simple fabrication process of picking up nanosheets of graphene from water using prestrained PDMS (Figure 9B (i) and (ii)).[169] The stretchability of the TE could be optimized by controlling the amount of prestrain applied to the PDMS support. The TEs exhibited maximum stretchability of 100% (without performance degradation) using PDMS prestrained at 50%. LED lamps connected to the graphene/PDMS TEs were stably operated with respect to twisting and stretching of the TEs, thus showing a high durability (Figure 9B (iii)).

Roh et al. systematically compared the performance differences of single-crystalline graphene (SCG)-based stretchable TEs and polycrystalline graphene (PCG)-based stretchable TEs.[299] Both SCG and PCG were synthesized on Cu foils, which were transferred to PDMS substrates using a general wet-transfer method, by wet-etching Cu after coating poly(methyl methacrylate) (PMMA) and transferring to desired substrates. The TEs fabricated by transferring the graphene layers onto PDMS exhibited high transmittance of 97.6% and 97.1% for SCG and PCG electrodes, respectively. The SCG TE exhibited a slightly lower sheet resistance of ∼314 Ω $\square^{-1}$ as compared to ∼362 Ω $\square^{-1}$ of the PCG TE, of which the gap began to increase even when a small amount of strain was applied (>2%). These results implied that grain boundaries are important for stretchable TE fabrication, since cracks are more easily formed on PCG TEs from the grain boundaries and also from extrinsic defects due to the graphene transfer process. Also, from cyclic stretching tests, it was revealed that the resistance change was stabilized for SCG TEs after ∼1,000 cycles, which suggested that defects were not propagated

https://doi.org/10.1021/acs.chemrev.3c00548
Chem. Rev. XXXX, XXX, XXX−XXX

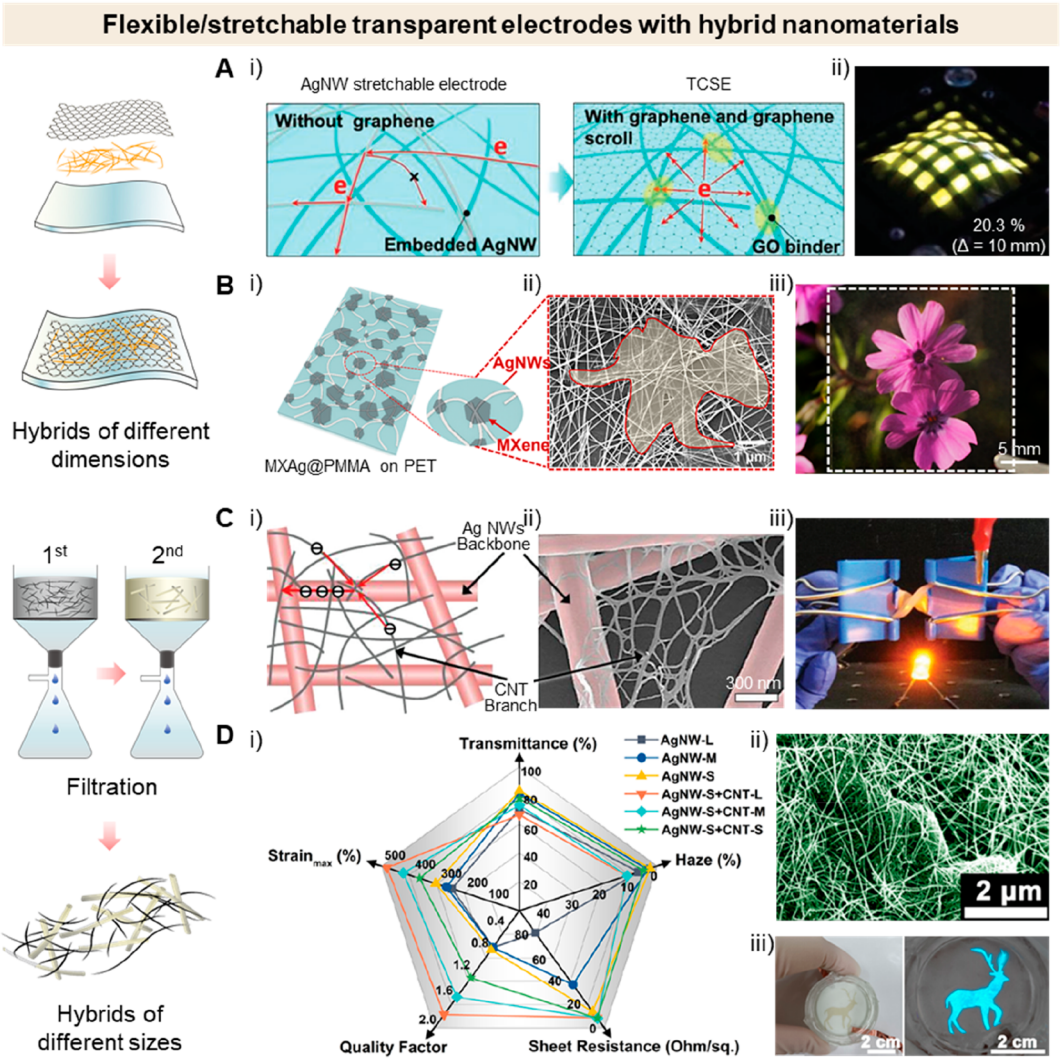

Figure 10. Intrinsically soft transparent nanocomposite electrodes based on hybrids of nanomaterials. (A) From left to right, (i) schematic illustrations explaining enhanced charge transport via hybrid structures of Ag NW and graphene, and (ii) operation of PM light-emitting device using the stretchable hybrid TEs, respectively. Reproduced with permission from ref 306. Copyright 2022 John Wiley & Sons, Inc. (B) From left to right, (i) a schematic illustration of hybrid Ag NW/Mxene electrode, (ii) a SEM image of their actual structure, and (iii) highly transparent nature of the Ag NW/Mxene composite electrode, respectively. Reproduced with permission from ref 307. Copyright 2022 American Chemical Society. (C) From left to right, (i) schematic illustration of Ag NW/CNT hybrid electrode structure, (ii) a SEM image showing its actual structure, and (iii) stable operation of a commercial LED during twisting of the Ag NW/CNT hybrid electrodes, respectively. Reproduced with permission from ref 309. Copyright 2014 John Wiley & Sons, Inc. (D) (i) A cobweb diagram of optoelectronic/mechanical performance of Ag NW/CNT hybrid electrodes with different variations, (ii) a SEM image of the hybrid structure, and (iii) images of a light-emitting device using patterned Ag NW/CNT hybrid electrodes before and after turning it on. Reproduced with permission from ref 310. Copyright 2022 American Chemical Society.

further. On the other hand, the PCG TE exhibited continuous increase in resistance during the cyclic stretching test. Thus, for stretchable TE fabrication, minimizing the surface defect as well as surface roughness is crucial to suppress crack formation and thereby, electrical performance degradation upon stretching.

To avoid unwanted damage caused to the graphene-based layers during their transferring, Han et al. devised a novel direct-growth method of multilayered graphene on elastomeric substrates.[300] The synthesis involved a two-step plasma-assisted thermal chemical vapor deposition (PATCVD), which enabled *in situ* growth of a Ti-buffer layer on the PDMS substrate and subsequent low-temperature growth of multilayer graphene on the Ti. A four-layered graphene multistack grown on PDMS substrate exhibited a low sheet resistance of ~6 Ω $\square^{-1}$ and high transmittance of 90.8% at wavelength of 550 nm. A remarkable mechanical stability was reported, whereby a normalized resistance change $((R - R_0)/R_0)$ at values of less than 10 was recorded for applied strains of up to 60%. This was an unprecedented figure for graphene-based stretchable TEs without any geometrical engineering, which might be the result of large domain size of the graphene layers (>260 μm) grown directly on the Ti-buffer layer and avoidance of a transfer process.

Although conducting polymers are not usually classified as conductive nanomaterials, they form nanofibril structures when mixed inside the elastomeric matrices.[25] Also, the smooth surface of composites that either incorporate the polymers inside the elastomers or form bilayer on the elastomers is beneficial for followed device fabrication. Elastomeric

https://doi.org/10.1021/acs.chemrev.3c00548
Chem. Rev. XXXX, XXX, XXX−XXX

composites based on transparent conducting polymers such as PEDOT:PSS,[320−322] polyaniline (PAni),[323,324] and polypyrrole (PPy)[325,326] have been extensively explored as intrinsically soft TEs. The focus of research has been on enhancing the electrical conductivity and stretchability of the TEs by incorporating ionic liquids, ionic salts, or surfactants as plasticizers. For instance, Preston et al. reported on the fabrication of intrinsically stretchable electrochromic display based on PEDOT:PSS/ionic liquid composite TEs.[327] An ionic liquid of 1-butyl-3-methylimidazolium octyl sulfate was strategically adopted to enhance both the conductivity and stretchability of the TE, of which the reported values were 288 S/cm and 176%, respectively. In another work by Ma et al., the conductivity and stretchability of PEDOT:PSS-based TEs were modified by combining PEDOT:PSS with poly(1-vinyl-3-ethylimidazolium dicyanamide) ionogel.[235] A sheet resistance of ∼50 Ω $\square^{-1}$ and trasmittance of 87% was achieved, along with a good mechanical strength.

Teo et al. successfully manipulated the conductivity and transmittance of PEDOT:PSS by incorporating an ionic liquid of 1-ethyl-3-methylimidazolium tetracyanoborate (ENIM TCB, (Figure 9C (i))).[303] A PEDOT:PSS/ENIM TCB TE exhibited sheet resistance of 80 Ω $\square^{-1}$ with a transmittance of 91.5% at 550 nm, owing to a strong dopant effect that forced a structural transformation of the PEDDOT:PSS, as well as increase in the free volume of PEDOT:PSS (Figure 9C). Addition of 1.0 wt % ENIM TCB resulted in enhanced mechanical durability up to applied tensile strain of 50%, with further stretchability achievable by using the prestrained approach (up to 180%, (Figure 9C (ii))). The PEDOT:PSS/ENIM TCB TEs were adopted as both the bottom and top electrodes of intrinsically stretchable alternating current EL devices, which operated with excellent stability at the applied strain of 50% and upon twisting the device (Figure 9C (iii)). Meanwhile, Dauzon et al. used a combination of poly(ethylene oxide) (PEO) network and surfactant Zonyl to enhance the electrical and mechanical performance of PEDOT:PSS-based TEs.[304] While the addition of Zonyl with insulating character improved the ductility of PEDOT:PSS at the sacrifice of conductivity, it could be compensated by the introduction of PEO that provided a 3D matrix for efficient charge transport. For an optimized mixing ratio of 1 wt % Zonyl with 5 wt % PEO, a sheet resistance of 130 Ω $\square^{-1}$ was achieved with transmittance of 93.2%, due to the smooth surface of PEDOT:PSS/PEO/Zonyl composite on PDMS (Figure 9D). The optimized TE could maintain its performance up to 80% tensile strain.

2.4.2.3. Intrinsically Soft Transparent Nanocomposite Electrodes Based on Nanostructure Hybrids. The combination of two or more types of conductive nanomaterials for the fabrication of intrinsically soft TEs results in enhanced electrical conductivities and mechanical tolerance of the soft composites without significantly affecting the optical performance. In general, two approaches have been reported as effective methods: 1) combining conductive nanomaterials with different dimensions and 2) combining conductive nanomaterials with same dimensions, but with different sizes or material types. In the former strategy, 1D nanostructures (i.e., metallic NWs and CNTs) are usually combined with 2D nanostructures (i.e., graphene and its derivatives).[284,328,329] The limited charge transport from high junction resistances in 1D nanostructure networks can be compensated by the addition of 2D nanostructure, which provide additional paths for charge transport. For example, Zhou et al. reported on the fabrication of stretchable TEs that incorporate a graphene layer on top of embedded Ag NWs in SEBS elastomer matrix.[306] The introduction of a graphene layer provided distinct functionalities of 1) modifying the work function of the TEs for efficient charge injection, for use in LED applications, 2) promoting efficient charge spreading for enhanced conductivity, and 3) passivating the surface against oxygen and moisture (Figure 10A (i)). As such, a reduction in sheet resistance from 38 to 24 Ω $\square^{-1}$ was observed after incorporating graphene layers on Ag NW-embedded TE by solution dipping. The transmittance remained at ∼89% with little change, owing to the highly transparent nature of the graphene layer with atomic thickness. The hybrid soft TEs were used to develop intrinsically stretchable 5 × 5 passive matrix (PM) OLEDs, which operated with high mechanical stability during convex stretching (∼20% linear strain, (Figure 10A (ii))).

While 2D nanostructures in large sizes can be used to cover the percolated networks of 1D nanostructures to promote efficient charge transfer, 2D nanosheets can be used for improving the wire-to-wire junction contacts, displaying similar effects as junction welding.[330−332] Jiang et al. developed flexible hybrid TEs based on Ag NWs and MXene flakes, whereby the presence of MXene flakes on the NW junctions significantly reduced the contact resistance (Figure 10B (i) and (ii)).[307] As a result, a low sheet resistance of 13.9 Ω $\square^{-1}$ and transmittance of 83.8% were achieved by TEs fabricated on PET supports (Figure 10B (iii)), which were then used to develop QLEDs with excellent bending stability. Notably, the work function of the flexible hybrid TEs could be tuned via controlling the amount of MXene flakes added, thus enhancing charge injection to the transport layers of the QLEDs.

Yang et al. reported on a different strategy for combining conductive nanomaterials with different dimensions, namely Ag NWs and rGO nanosheets.[305] In their work, rGO nanosheets conformally wrapped Ag NW networks, achieved via sequential processes of selective electrodeposition of GO nanosheets on Ag NWs and a pulsed laser irradiation treatment. Such a treatment successfully reduced the GO and welded the Ag NWs together through a surface plasmon resonance process, resulting in a low sheet resistance of 3.3 Ω $\square^{-1}$, transmittance of 91.1%, and good flexibility of the hybrid TEs. In another work by Shin et al., the mechanical durability of TEs was improved by embedding Ag NW networks in a PEDOT:PSS matrix, followed by lamination of graphene layers. The combination of 3 conductive elements with intrinsic soft features enabled the fabrication of mechanically robust TEs with a sheet resistance of 58 Ω $\square^{-1}$ and transmittance of 78%, which were used to fabricate alternating current EL devices composed of 8 × 8 PM arrays. The EL devices could withstand high levels of mechanical deformation such as bending, rolling, twisting, and stretching (with maximum stretching range of ∼80%).

The second strategy for developing intrinsically soft TEs based on hybrids of conductive nanomaterials is based on the combination of nanomaterials with same dimensions.[284,333,334] This strategy is aimed to improve the connectivity of the main base-material used to create percolation networks, which are subject to disconnection under external strains. For this purpose, the secondary additive nanomaterials usually exhibit higher mechanical softness such that alternative conduction pathways can be provided even when the percolation of the main nanomaterial is destroyed under stress. In viewpoint of

https://doi.org/10.1021/acs.chemrev.3c00548
Chem. Rev. XXXX, XXX, XXX−XXX

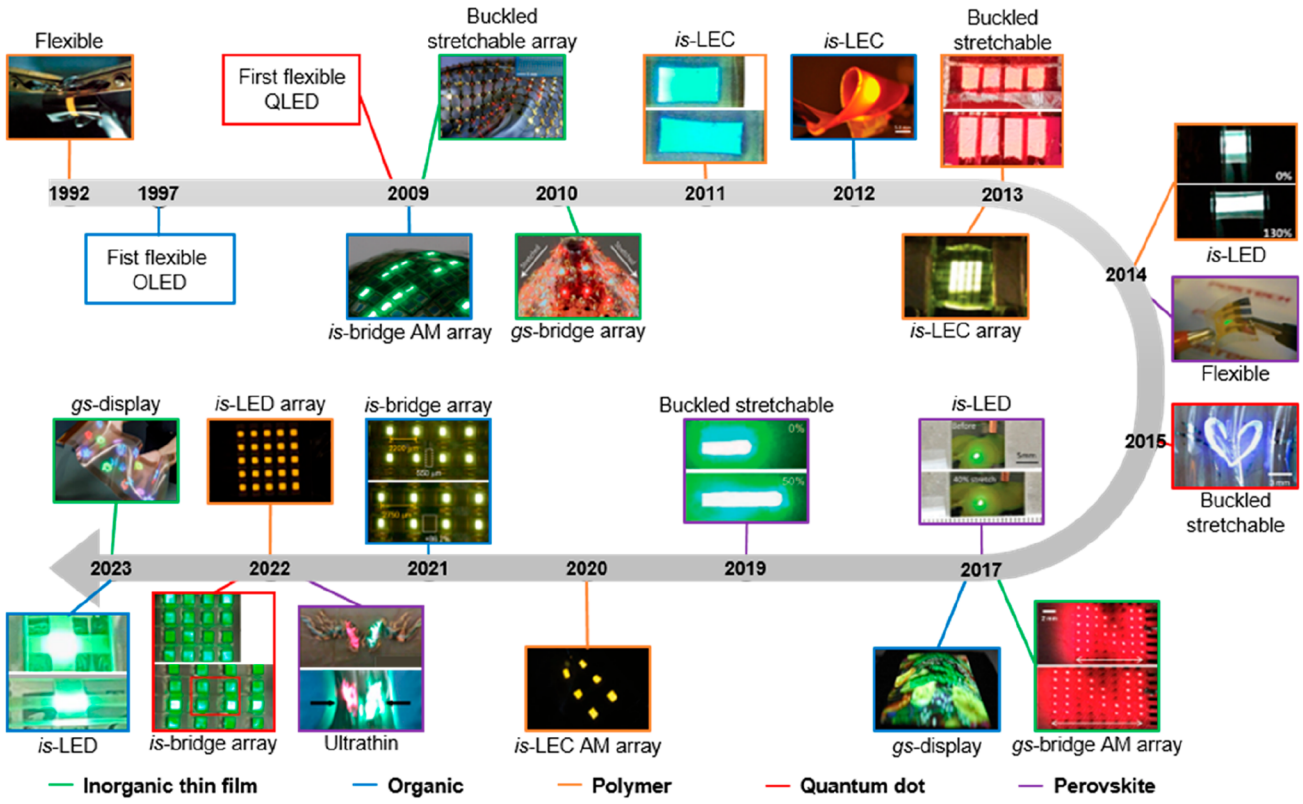

Figure 11. Timeline of the development of flexible/stretchable LEDs. Flexible PLED. Reproduced with permission from ref 335. Copyright 1992 Springer Nature. Intrinsically stretchable (*is*-) bridge active matrix (AM) OLED array. Reproduced with permission from ref 609. Copyright 2009 Springer Nature. Buckled ILED array. Reproduced with permission from ref 347. Copyright 2009 American Association for the Advancement of Science. Geometrically stretchable (*gs*-) bridge ILED array. Reproduced with permission from ref 374. Copyright 2010 Springer Nature. *is*-polymer light emitting electrochemical cell (LEC). Reproduced with permission from ref 431. Copyright 2011 John Wiley & Sons, Inc. *is*-OLEC. Reproduced with permission from ref 434. Copyright 2012 John Wiley & Sons, Inc. Buckled PLED. Reproduced with permission from ref 170. Copyright 2013 Springer Nature. *is*-PLEC array. Reproduced with permission from ref 432. Copyright 2013 Springer Nature. *is*-PLED. Reproduced with permission from ref 184. Copyright 2014 American Chemical Society. Flexible PeLED. Reproduced with permission from ref 338. Copyright 2014 John Wiley & Sons, Inc. Buckled QLED. Reproduced with permission from ref 490. Copyright 2015 Springer Nature. *gs*-bridge AM ILED array. Reproduced with permission from ref 177. Copyright 2017 John Wiley & Sons, Inc. *is*-PeLED. Reproduced with permission from ref 523. Copyright 2017 John Wiley & Sons, Inc. *gs*-OLED display. Reproduced with permission from ref 612. Copyright John Wiley & Sons, Inc. Buckled PeLED. Reproduced with permission from ref 553. Copyright 2019 John Wiley & Sons, Inc. *is*-PLEC AM array. Reproduced with permission from ref 433. Copyright 2020 Springer Nature. *is*-bridge OLED array. Reproduced with permission from ref 121. Copyright 2021 American Association for the Advancement of Science. *is*-bridge QLED array. Reproduced with permission from ref 610. Copyright 2022 Elsevier. *is*-PLED array. Reproduced with permission from ref 447. Copyright 2022 Springer Nature. Ultrathin PeLED. Reproduced with permission from ref 522. Copyright 2022 American Association for the Advancement of Science. *gs*-ILED display. Reproduced with permission from ref 375. Copyright 2023 John Wiley & Sons, Inc. *is*-OLED. Reproduced with permission from ref 448. Copyright 2023 Springer Nature.

TE performance, higher optical transmittance can also be achieved along with improved mechanical performance, since the high connectivity of the nanomaterials lowers the percolation threshold without sacrificing the electrical conductivity. Lee et al. demonstrated the fabrication of intrinsically stretchable TEs based on CNT-enhanced Ag NW networks embedded in a silicone rubber (Figure 10C).[309] The hybrid structure was obtained via sequential filtrations of CNTs ($d \sim 1.2$ nm, $L \sim 2-10$ μm) and Ag NWs ($d \sim 150$ nm, $L \sim 50-100$ μm) through a microporous filter membrane. Sandwiching the nanostructure hybrids between silicon rubbers finalized the TE fabrication process (Figure 10 C (i) and (ii)). The stretchable hybrid TEs exhibited a sheet resistance of ~25 Ω $\square^{-1}$ at high transmittance of over 90%, and stretchability of ~460% (Figure 10 C (iii)).

Wang et al. systematically investigated the effect of Ag NW length and diameter and CNT diameter on the performance of TEs fabricated based on their hybrids.[310] In specific, three types of Ag NWs with variable length-to-diameter ratios were paired with three kinds of CNTs with different diameters. The authors reported that both high electrical conductivity and stretchability of TEs could be achieved by using Ag NWs and CNTs with minimal diameter differences, which was a direct result of efficient capillary-force-induced welding. Use of Ag NWs and CNTs with smaller diameters resulted in the fabrication of TEs with high transmittance and low haze (Figure 10D (i)). When Ag NWs with high aspect ratio were used to fabricate TEs, a low sheet resistance could be achieved when suitable amount of CNTs were added (Figure 10D (ii)). After systematic investigation, an optimized stretchable TE based on Ag NW/CNT hybrid composite exhibited a sheet resistance of 8.7 Ω $\square^{-1}$, with transmittance of 66.4% and high stretchability of 490%. After a cyclic stretching test of 50% tensile strain for 1,000 cycles, the fabricated TE displayed near

https://doi.org/10.1021/acs.chemrev.3c00548
Chem. Rev. XXXX, XXX, XXX−XXX

Table 4. Characteristics of Geometrically Stretchable LEDs, According to Light Emitting Materials (Organic, Polymer, QD, and Perovskite)

Device category	Form factor	Emissive material	Electroluminescent peak (nm)	Full width at half-maximum (nm)	Turn-on voltage (V)	Maximum luminance (cd/m^2)	Peak EQE (%)	Peak current efficiency (cd/A)	Stretchability (%)	Stretching cycle (times)	Ref.
PLED	Ultrathin	–	R: 609, G: 517, B: 460	R: ~40, G: ~70, B: ~50	R: 2.4, G: 2.7, B: 2.8	R,G,B > 10,000	R: 12.6, G: 14.5, B: 6.3	R: 21, G: 53.7, B: 10.4	20	1,000 (stretching at 60%)	585
		SuperYellow	~555	~85	2.4	>8,000	–	7.76	30	1,000 (biaxial stretching at 10%)	426
		AnE-PV stat	630	~75	~3.3	113	~0.44	~3.4	100	–	170
OLED	Ultrathin	CBP:Ir(BT)2(acac)	~562	~58	~3.4	~20,000	–	73	100	20,000 (stretching at 20%)	115
		mCP:Ir(ppy)3	~541	~50	~3	15,110	–	66	112	35,000 (stretching at 20%)	606
		SBSPy-n	408	–	9.3	3,274	2.08	~5	54	–	607
		mCP:Ir(ppy)3	~541	~45	3	20,000	–	72.5	100	6,000 (stretching at 40%)	428
		mCP:Ir(ppy)3	~541	~50	3	8,080	–	62.9	50	1,000 (stretching at 30%)	429
		CBP:Ir(ppy)2	~510	~75	–	~8,500	22.3	82.4	100	1,000 (stretching at 30%)	277
	Island-bridge (geometric)	Alq_3	~530	~30	~4	~2,000	–	3	35	1,000 (stretching at 20%)	116
		Alq_3	–	–	~2.5	~2,500	~2.1	–	140	1,000 (stretching at 140%)	608
		TCTA:TTPA	–	–	5.5	5,000	–	–	50	–	609
		–	525	~65	~2.5	8,510	~26	102	30	1,000 (stretching at 25%)	121
QLED	Ultrathin	R: CdSe/CdS/ZnS QD, G,B: CdSe/ZnS QD	R: 618, G: 520, B: 453	R: 38, G: 35, B: 35	R: 2.8, G: 4.2, B: 6	R: 1,310, G: 1,200, B: 936	–	R: 2.25, G: 1.75, B: 1.42	70	100 (stretching at 70%)	586
		CdSe/ZnS QD	~520	~32	3	43,000	~6	17.52	50	200[b] (1 mm[a])	148
		CdSe/ZnS QD	–	–	~2	14,000	2.35	–	20	1,000 (stretching at 20%)	490
		CdSe/ZnS QD	~525	~40	3.3	50,513	7.94	–	0.047 mm[a]	500[b]	109
		CdSe/ZnS QD	R: ~625, G: ~525, B: ~475	R: ~50, G: ~45, B: ~40	R: ~2, G: ~2.8, B: ~3	R: ~8,000, G: 44,719, B: ~ 1,000	R: ~1.6, G: ~2.25, B: ~0.245	–	0.74 mm[a]	1,000[b]	575
	Island-bridge (geometric)	CdSe/ZnS QD	530	~50	–	~12,500	–	–	50	10,000 (stretching at 40%)	610
		CdSe/CdZnS QD	622	38	5.4	18,641	14.7	–	25	–	611
PeLED	Ultrathin	$MAPbI_3$-FPMAI	~749	~42	~2.1	–	13	–	0.25 mm[a]	10,000[b] (1 mm[a])	531
		$MAPbBr_3$ NC	532	24	3.2	~1,000	–	9.08	50	1,000 (stretching at 20%)	553
		$CsPbBr_3$ NC	516	18	~3	~1,500	~6.2	–	0.25 mm[a]	–	522

[a]Bending radius. [b]Bending cycle.

https://doi.org/10.1021/acs.chemrev.3c00548
Chem. Rev. XXXX, XXX, XXX−XXX

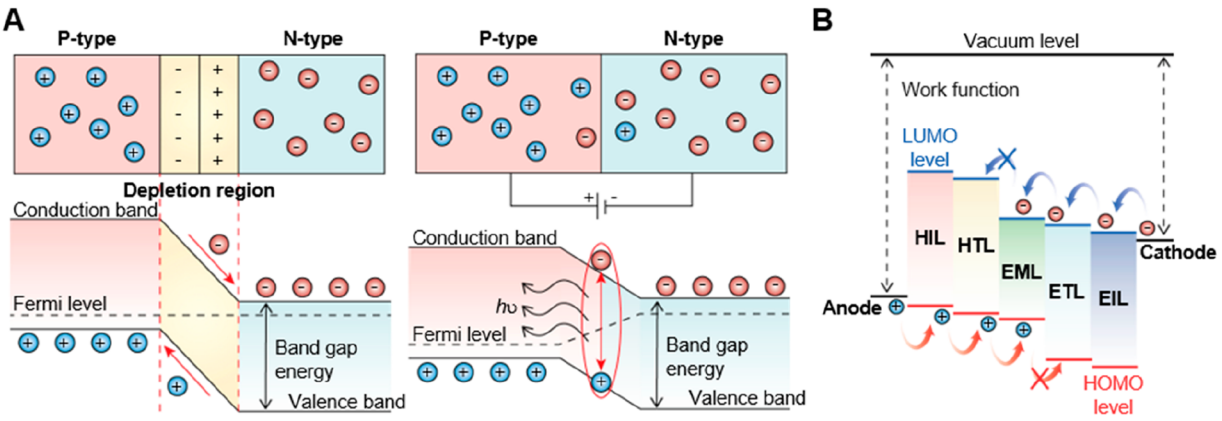

Figure 12. Working principles of a LED. (A) Basic principle of a LED before (left) and after (right) giving forward bias. (B) Structure of a multilayer LED.

50% increase in its resistance, which was still suitable for use in TE applications (Figure 10 D (iii)).

Conducting polymers simultaneously display many advantages and disadvantages for stretchable device fabrication, such as cost-effective solution-based process and smooth surface for subsequent film deposition, but poor chemical stability and conductivity. In this regard, conducting nanomaterials have been strategically combined with them to obtain desired performances, while eliminating their drawbacks. For instance, Yang et al. reported on the fabrication of flexible TEs based on Ag NW/PEDOT:PSS composites via Mayer rod coating of Ag NW/PEDOT:PSS composite ink on PET substrates.[312] Hydroxypropyl methylcellulose and Triton X-100 were used as chemical and mechanical stability enhancers. Flexible Ag NW/PEDOT:PSS-based TEs exhibited a low sheet resistance of 12 $\Omega\,\square^{-1}$ and transmittance of 96% at 550 nm, whereby the introduced PEDOT:PSS lead to nanowelding of Ag NW contacts to enhance both electrical conductivity and mechanical durability. As such, the flexible TEs were highly durable and maintained their performance after wiping for 100 times and bending for 5,000 times. In another report by Cui et al., photopatternable stretchable TEs based on hybrid of spin-coated PEDOT:PSS and spray-coated CNT networks were demonstrated.[311] The presence of a PEDOT:PSS layer resulted in formation of ultrathin, uniform, and continuous CNT conductive film by spray-coating, as compared to irregularly shaped and nonuniform CNT film directly spray-coated on a hydrophobic surface of Si. The uniform CNT network film could be readily patterned using standard photolithography and dry etching, resulting in high-precision versatile electrode patterns. The resulting stretchable TE exhibited a sheet resistance of 90 $\Omega\,\square^{-1}$ and transmittance of 84% at 550 nm, with excellent durability during cyclic stretching test at 50% strain.

3. MATERIALS FOR FLEXIBLE AND STRETCHABLE LEDS

Starting with the invention of the cathode ray tube in 1897, significant advancements have been achieved in display technologies to improve the quality of visual representation by expanding the color range and definition of displays, while also focusing on form factors including larger screen sizes and thinner displays. Along with these advancements, user experience has emerged as a crucial consideration in the display industry. Curved televisions (Samsung Electronics, 2013) and monitors (Samsung Electronics, 2014) were launched for an immersive viewing experience and reduced visual stress for the humans by accommodating natural human eyesight. More recently, foldable smartphones (Samsung Electronics, 2019) and rollable displays (LG Electronics. 2020) have been commercialized, enabling better portability and efficient utilization of space. With the increasing integration between humans and electronic devices, the ability to deform displays according to user requirements has become an important research area. Consequently, the development of flexible and stretchable LEDs, supporting a wide range of deformations, has received significant attentions in recent years. In Figure 11, the evolution of deformable LEDs and displays is depicted, encompassing different emissive materials such as inorganic thin films, organics, polymers, quantum dots (QDs), and perovskites. Following the initial development of flexible LEDs,[335−338] researchers have directed their efforts toward enhancing the degree of deformation freedom, transitioning from flexible to stretchable form factors. Table 4 provides a comprehensive overview of the electrical and mechanical performances of representative examples of flexible and stretchable LEDs, categorized by their light-emitting materials and form factors. In this section, a comprehensive review of the latest key technologies in deformable display applications that utilize various light-emitting materials will be presented, starting with a brief explanation of the operational principles of LEDs.

3.1. Working Principle of LEDs

The LED is a semiconductor device that converts electrical energy into light through a sequence of processes taking place within its constituent materials. The fundamental building block of an LED is a p−n junction, which is created by joining two distinct types of semiconductors: p-type and n-type, characterized by their majority carriers as holes and electrons, respectively. At the p−n junction, a depletion region arises spontaneously due to carrier diffusion, resulting from the potential difference between the two regions (Figure 12A). When a forward bias voltage is applied across the p−n junction, electrons from the n-region and holes from the p-region migrate toward the junction. As these charge carriers traverse the junction, they recombine and emit energy in the

https://doi.org/10.1021/acs.chemrev.3c00548
Chem. Rev. XXXX, XXX, XXX−XXX

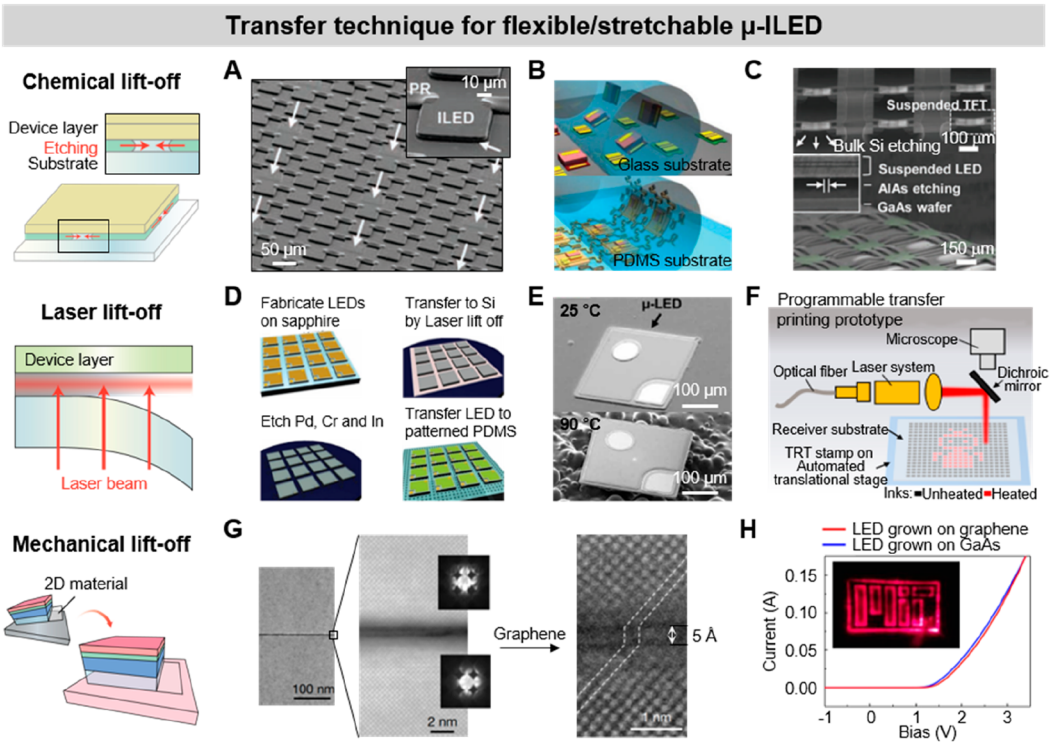

Figure 13. Transfer techniques for flexible/stretchable μ-ILEDs. (A) SEM images of the GaAs wafer after etching the sacrificial layer and an angled-view of an individual ILED (inset). White arrows indicate the removed LEDs with the stamp. Reproduced with permission from ref 347. Copyright 2009 American Association for the Advancement of Science. (B) Schematics of the roll-to-roll transfer printing method during the LED pick-up and the display release. (C) Angled SEM images of a Si thin film transistor (TFT) (top) and LED (bottom) arrays. Reproduced with permission from ref 177. Copyright 2017 John Wiley & Sons, Inc. (D) Schematic illustrations of LED processing steps. Reproduced with permission from ref 355. Copyright 2012 John Wiley & Sons, Inc. (E) SEM images of an LED on thermal release tape before and after heating. (F) Schematic of a laser-assisted programmable transfer printing system. Reproduced with permission from ref 359. Copyright 2020 American Association for the Advancement of Science. (G) STEM images showing excellent remote alignment of the GaAs lattices through the graphene. Insets are convergent beam electron diffraction patterns showing identical zinc-blende (001) orientations. (H) $I-V$ curves of LEDs grown on a graphene/GaAs substrate and directly on a GaAs substrate. Inset image is a lighting LED grown on the graphene/GaAs substrate. Reproduced with permission from ref 365. Copyright 2017 Springer Nature.

form of photons, a phenomenon known as electroluminescence.

In modern LED technology, multiple semiconductor layers, each with specific roles, are incorporated to enhance the efficiency of radiative recombination and exciton formation. The basic process involves the injection of electrons from the cathode and holes from the anode, which subsequently encounter each other inside the emission layer (EML) to form excitons. The annihilation of an electron and a hole within the exciton, known as exciton recombination, releases energy corresponding to the energy difference between the two states. If this recombination leads to the emission of photons, it is termed radiative recombination; otherwise, it results in nonradiative recombination, where the excess energy is dissipated as heat. To achieve high efficiency, brightness, and extended device lifetime, several additional layers, such as the hole injection layer (HIL), hole transport layer (HTL), electron transport layer (ETL), and electron injection layer (EIL), are introduced alongside the EML between the two electrodes (Figure 12B). During the design and selection of materials for these layers, factors including the work functions of the electrodes, carrier mobility, the highest occupied molecular orbital (HOMO) and the lowest unoccupied molecular orbital (LUMO) energy levels of each layer should be considered. This ensures efficient carrier movement, counter-carrier blocking, and balanced charge injection into the EML. Depending on specific requirements, the type of LED can be classified according to the light-emitting material.

3.2. Inorganic Ultrathin Materials

Inorganic semiconductor emitting materials, specifically III–V semiconductors, have been well-established for decades.[339−343] They form a crystal lattice consisting of covalent bonding and exhibit a distinct and continuous energy band structure, leading to high charge mobility through band transport. Due to their material characteristics, inorganic LEDs (ILEDs) are desirable candidates for a deformable device, offering superior device performances in terms of energy consumption, brightness, lifetime, and stability. However, they inherently exhibit a hard and brittle nature, originating from the tight bonding between the periodically arranged atoms. To overcome the mechanical limitations, recently, micro-ILEDs (μ-ILEDs) have garnered attention in both academia and industry after its first introduction by Jin et al. in 2000.[344,345] Ultrathin (approximately 50 μm) and ultrasmall (approximately 100 μm) features of the μ-ILED arrays can provide remarkable degrees of deformability by engineering the device architecture in ways that minimize strain applied to the fragile materials.[367,909,910]

For deformable device applications, epitaxially grown ultrathin inorganic emitters on rigid and flat substrates need

https://doi.org/10.1021/acs.chemrev.3c00548
Chem. Rev. XXXX, XXX, XXX−XXX

to be lifted off and transferred to flexible and stretchable target substrates in a desired arrangement. However, conventional pick-and-place transfer methods,[346] where a robot arm picks up the layers and places them onto the target substrates, are not suitable due to the microscale size and thickness of the μ-LEDs. Hence, fabrication strategies for releasing the desired layers from their growth wafer and transferring them to flexible/stretchable substrates without altering their original configuration have been extensively investigated. In the following section, general transfer techniques for the fabrication of μ-ILEDs will be briefly discussed, with a focus on the pick-up and transfer methods suitable for the deformable substrates.

3.2.1. Transfer Technique of Inorganic Thin Film Semiconductors for Deformable ILEDs. The first μ-ILEDs transferred to a flexible substrate were red-emitting ILEDs consisting of AlInGaP quantum well structures, cladding films, spreaders, and contacts.[347] These epitaxial stacks were deposited on a GaAs wafer with an AlAs sacrificial layer, which could be selectively etched with HF acid. For the precise delineation of μ-ILED pixels, inductively coupled plasma reactive ion etching was conducted while a photolithographically defined SiO_2 layer protected the underneath layers. Photoresist anchors were formed to hold the corners of the μ-ILEDs, followed by undercut etching of the sacrificial layer, resulting in floating of the μ-ILEDs but still tethered to the wafer (Figure 13A). To transfer the μ-ILEDs, a PDMS stamp was adopted, enabling the pick-up of the μ-ILED layers with designed interconnects from the donor substrate using the van der Waals force between the stamp and the layers. Here, the amount of van der Waals force can be precisely controlled by adjusting the peeling velocity of the stamp. Elastomeric stamps with unique geometries like micropyramidal structure,[348] or other kinds of stamp[349] (e.g., tape) can be applied as the pick-up stamp to modulate the adhesive forces, thereby increasing the reliability and repeatability. The completed device using the elastomeric stamp transfer strategy showed optical and electrical performance comparable to that of devices fabricated on a rigid wafer.

Since the elastomeric stamps have shape-tunable properties, they can be adjusted into various forms to support various transfer printing techniques.[350,351] For instance, a cost- and time-efficient sequential roll-to-roll (roll-to-plate) transfer printing technology with extreme transfer accuracy was developed to fabricate AM-display (Figure 13B).[177] In specific, a suspended Si-TFT array was fabricated on a silicon-on-insulator wafer and initially transferred to a carrying substrate after etching the buried oxide (Figure 13C, top). Similarly, a μ-ILED array composed of epitaxially grown AlInGaP active layers on an AlAs sacrificial layer could be lifted off through selectively etching the AlAs (Figure 13C, bottom). The automated roll-to-plate transfer machine exhibited misalignment controllability within 3 μm and a 99.9% transfer yield. After transferring to a glass substrate, several interlayers, via holes, and interconnections were formed to integrate the TFTs and LEDs. The fully integrated device was then printed onto the final elastomeric substrate via a third roll transfer process to complete the AM-display fabrication. The display operated stably at a low-voltage range (below 4 V) and clearly emitted a red light (635 nm), which implied that there was no notable degradation due to the three-step transfer process.

A directional light source, such as a laser, can be utilized in μ-ILED transfer technique, by inducing localized heating, material decomposition, and delamination with its highly concentrated energy. As such, laser lift-off (LLO) technology is a well-established technique to release the μ-ILEDs from the original substrate with high transfer speed and yield.[352−354] As an example, blue μ-ILEDs composed of epitaxially grown GaN, current-spreading layers, metal pads, and a passivation layer were fabricated on a sapphire substrate.[355] The schematic illustration of the LLO transfer steps is described in Figure 13D. Then, a Cr (adhesion layer)/Pd bilayer was coated to bond with the Si carrying substrate by forming an In−Pd bonding. During the LLO process, light passing through the sapphire induced thermal decomposition of GaN into Ga metal and nitrogen gas at the interface of GaN and sapphire, consequently releasing the individual μ-ILEDs. Diluted HCl was used to etch away the residual Ga on the top and unalloyed In at the bottom of the μ-ILEDs, while leaving the alloyed $InPd_x$ to form a suspended configuration tethered to the Si substrate. A PDMS stamp was used to pick-up and transfer the μ-ILEDs to the final substrate, completing the flexible display fabrication, which exhibited nearly identical device performance compared to the as-fabricated μ-ILEDs on the sapphire substrate. For improved production yield, the temporary carrier substrate can be replaced with flexible substrates[356] such as PET and tape, or alternative bonding methods like adhesive bonding can be adopted for deformable devices instead of using a rigid carrying substrate.

Laser can also be used to assist the conventional stamp transfer method by controlling the adhesion of the stamp. For instance, laser heating can modulate the pressure induced by an air cavity,[357] enabling regulated pick-up and release. Also, the pick up and release can be programmed in a stamp made from shape memory polymer, controlled through laser heating.[358] Based on this localized heating approach, a commercial thermal release tape containing thermally expandable microspheres in the adhesive layer was used as a transfer stamp.[359] At a given temperature, a significant volumetric expansion (10 to 45 μm in diameter) occurred due to a liquid−vapor transition of the inner hydrocarbon and softening of the outer polymer shell, resulting in an increase in surface roughness. Such roughness in the surface modulated the adhesion strength (Figure 13E), facilitating programmable transfer printing by enabling the pick-up of devices exclusively from the laser-irradiated region of the tape (Figure 13F). The μ-ILEDs showed consistent current−voltage ($I-V$) characteristics before and after the transfer process, allowing the fabrication of an ultrathin, flexible μ-ILED display. This display incorporated PI supporting, insulating, and encapsulating layers, along with metal interconnects.

Another widely used transfer method is mechanically lifting off epilayers grown using an intermediate layer that facilitates mechanical exfoliation, such as 2D materials with atomic-layered structures.[360−362] For example, GaN layers grown on graphene layers using van der Waals epitaxy could be easily released from the growing substrate.[363] In addition, it has been found that high-quality thin films could be epitaxially grown even in the presence of 2D materials, because epitaxial orientation of the substrate could penetrate the 2D materials (known as remote epitaxy).[364] For instance, a GaAs(001) epilayer was grown on a GaAs(001) wafer coated with monolayer graphene, as confirmed through identical convergent beam electron diffraction patterns in the scanning transmission electron microscopy images of Figure 13G.[365] Based on the high-quality GaAs layer, AlGaInP-GaInP double

https://doi.org/10.1021/acs.chemrev.3c00548
Chem. Rev. XXXX, XXX, XXX−XXX

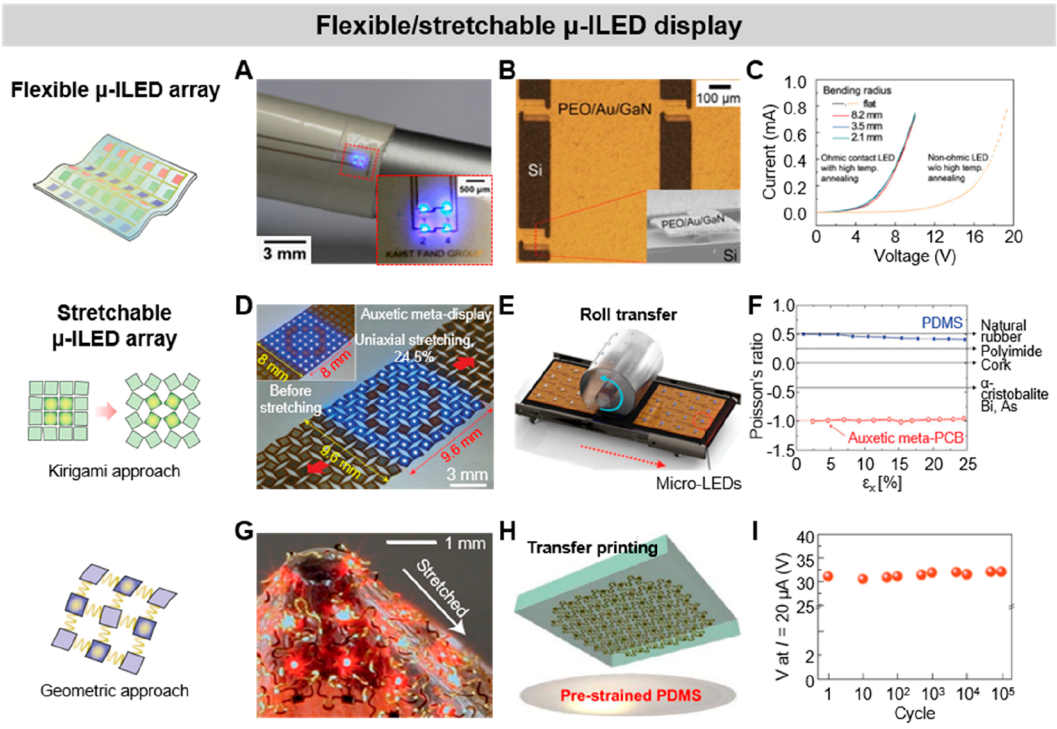

Figure 14. Representative examples of flexible/stretchable μ-ILED displays. (A) Photograph and magnified image of 2 × 2 ultrathin GaN μ-ILED display. (B) Micropatterned GaN followed by the anisotropic etching of the underlying Si layer. (C) $I-V$ curves in various bending radii. Reproduced with permission from ref 372. Copyright 2011 Elsevier. (D) Photographs of stretchable μ-ILED meta display using the kirigami method before (inset) and after stretching. (E) Schematic of roll transfer of μ-ILEDs for meta-display fabrication. (F) Poisson's ratio of PDMS and auxetic metal-PCB with respect to strain. Reproduced with permission from ref 373. Copyright 2022 John Wiley & Sons, Inc. (G) Image of μ-ILED arrays tightly stretched on the sharp tip of a pencil. (H) Schematic illustration of transfer printing to a prestrained PDMS substrate. (I) Voltage at 20 mA current during the 75% horizontal stretching cycles. Reproduced with permission from ref 374. Copyright 2010 Springer Nature.

heterojunction ILEDs were fabricated on the graphene-GaAs substrate (Figure 13H). The ultrathin ILED layers could be easily lifted off from the host substrate by simple mechanical peeling, because the applied external stress exceeded the van der Waals forces at the thin film/graphene or graphene/substrate interfaces. Recently, full-color vertically stacked μ-ILEDs were fabricated through remote epitaxy and van der Waals epitaxy.[366] An AlGaAs-based red LED was grown on a graphene-coated GaAs wafer, and InGaN-based green and blue LEDs were grown on hBN-coated sapphire substrates, then transferred through dry transfer, resulting in single-crystalline RGB layers with 1−2 μm thickness. To prevent downward emissions from the blue and green LEDs to green and red LEDs, PI-based blue and green optical absorbers were inserted, concurrently serving as adhesive interlayers. As a result, full-color vertical μ-ILEDs arrays were fabricated, achieving various EL colors of mixed RGB and the highest resolution of 5,100 pixels per inch (PPI), which is the highest PPI reported for self-emitting RGB μ-ILED displays.

3.2.2. Flexible and Stretchable μ-ILED Displays. Despite the brittle nature of thin film III−V semiconductors, μ-ILEDs can be assembled and integrated into flexible and stretchable displays after their transfer to the deformable substrates, owing to their ultrathin device thickness of several tens of micrometers.[367−371] The device stability and reliability can be improved by locating the fragile active materials near the neutral mechanical plane, where tensile and compressive stresses are neutralized. For example, GaN μ-ILED layers were transferred to a liquid crystal polymer substrate and encapsulated with polytetrafluoroethylene (PTFE), which resulted in a highly flexible device (Figure 14A).[372] On the GaN ILED grown on a Si substrate with ohmic contact pads, plasma-enhanced chemical vapor deposited-SiO_2 (PEO)/Au/Cr were deposited and patterned using photolithography and etching processes to mask the μ-ILEDs. After etching the exposed GaN ILED, anisotropic wet etching of the Si substrate with KOH was conducted to separate μ-ILEDs from the mother substrate (Figure 14B), followed by transfer using a PDMS stamp. At various bending radii (8.2 mm, 3.5 mm, and 2.1 mm), no degradation in optical and electrical properties was observed compared to the flat condition (Figure 14C). The μ-ILEDs endured 2,000 cycles of bending fatigue test at a bending radius of 3.5 mm. Moreover, the μ-ILEDs exhibited high water-resistance owing to the PTFE coating, and their electrical properties remained unchanged even after immersion in a phosphate buffer saline solution for 2 days.

μ-ILED displays can be made stretchable by adopting different geometrical approaches, as mentioned in Chapter 2. One effective approach is the kirigami method, which renders the existing device stretchable using strategically placed cutting and folding lines, without affecting the active devices fabricated on the deformable substrates. The stress exerted on the device is alleviated via shape transformation induced by the cutting/folding lines, thereby granting stretchability to the μ-ILED displays. A challenge in this approach is to maintain the original image during stretching, and to solve this issue, an auxetic meta-display was proposed (Figure 14D).[373] The μ-ILED display, containing a meta-printed circuit board and μ-

https://doi.org/10.1021/acs.chemrev.3c00548
Chem. Rev. XXXX, XXX, XXX−XXX

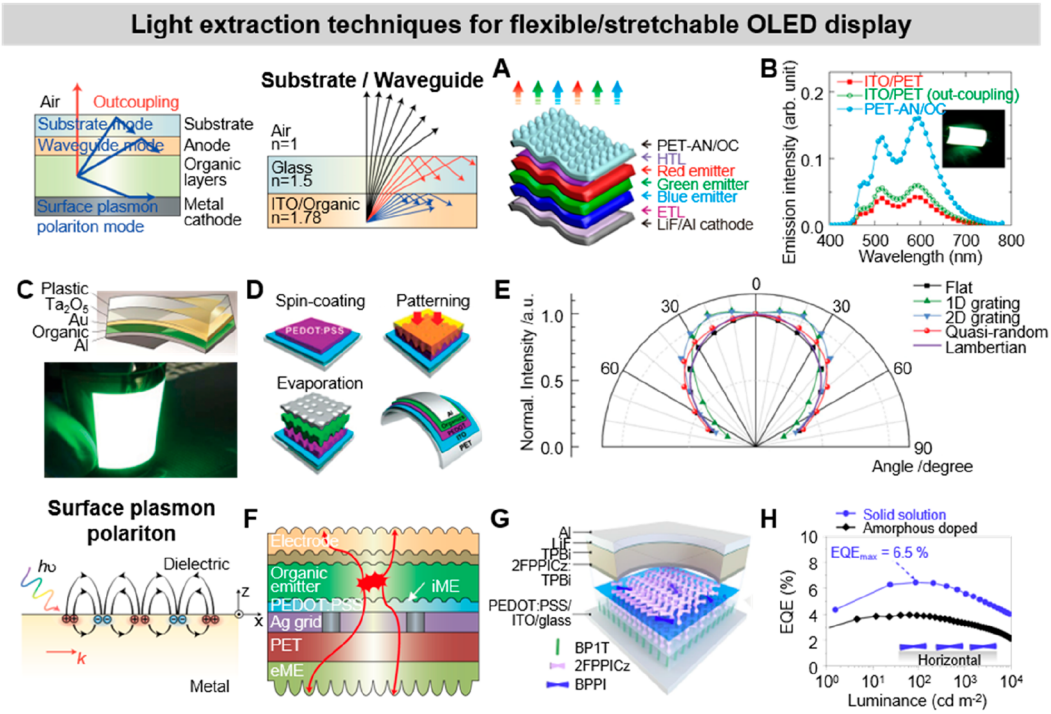

Figure 15. Light extraction techniques for flexible/stretchable OLED displays. (A) Schematic illustration of flexible OLED increasing outcoupling by introducing a nanostructure. (B) EL spectra of various flexible white OLED (inset) in the normal direction. Reproduced with permission from ref 393. Copyright 2015 American Chemical Society. (C) Schematic and photograph of flexible OLED, top and bottom, respectively. Reproduced with permission from ref 397. Copyright 2011 Springer Nature. (D) Schematic of the fabrication process of flexible OLEDs with quasi-random nanostructure. (E) Angle dependence of EL intensities for various flexible OLEDs. Reproduced with permission from ref 401. Copyright 2014 John Wiley & Sons, Inc. (F) Schematic of a transparent flexible OLED with internal outcoupling structure. Reproduced with permission from ref 404. Copyright 2018 John Wiley & Sons, Inc. (G) Schematic illustration of the device with crystalline organic solid-solution thin film. (H) EQE-luminance of solid-solution and amorphous-doped devices. Reproduced with permission from ref 408. Copyright 2023 Springer Nature.

ILEDs, was fabricated through a roll transfer method on a PI film (Figure 14E). Laser cutting was then executed in a specific manner that makes the Poisson's ratio of the substrate to a value of −1 (Figure 14 F). The display consisted of rotational squares and hinges, wherein adjacent rigid pixel squares rotated at the same angles but in opposite directions, and the hinges connecting square pixels expanded uniformly in the direction of stretching. In this manner, the final display could be isotropically stretched until ∼24.5% without distortion.

The island-bridge approach is another widely adopted strategy to render stretchability to devices constructed from nonstretchable materials. For instance, wave-shaped metal interconnects on rubber substrates were used to connect GaN μ-ILED arrays, making them stretchable.[347] In another example, serpentine-shaped metal ribbons were utilized as both a structural bridge and electrical interconnects of each pixel, enabling biaxial stretching (Figure 14G).[374] In detail, μ-ILED arrays connected with serpentine-shaped ribbons were transferred through PDMS stamp onto a prestrained (∼20%) PDMS substrate to further enhance device stretchability (Figure 14H). This design allowed for the dissipation of higher strain levels, enabling the μ-ILED arrays to endure harsh mechanical deformations, including ∼46% diagonal stretching, 100,000 cycles of 75% stretching (Figure 14I), 720° of twisting, pocking, inflation, and other complex distortions. Recently, LG Display unveiled a 12-in. high-resolution full-color stretchable display with 100 PPI resolution and 20% stretchability.[375] An S-form stretchable interconnection system was employed to change the form of display without damage, bringing stretchable display closer to commercialization.

3.3. Organic Materials

Organic emitters have significantly progressed as self-emissive materials for full-color displays since the first high-efficiency small molecule LED was introduced in 1987.[376] Depending on the molecular weight of the organic materials, light-emitting devices can be divided into either OLEDs or PLEDs. Regardless of their molecular weights, organic emitters generally have amorphous structures, with van der Waals interactions between the molecules. Therefore, organic emitters exhibit low carrier mobility due to intermolecular carrier transfer, but they offer high mechanical flexibility compared to inorganic materials. Owing to their flexible nature, organic emitters have attracted considerable attention from both industry and academia as light-emitting materials for deformable displays.[377,378] The breakthrough in OLED was achieved through advancements in the materials engineering of both fluorescent and phosphorescent materials. Generally, fluorescent materials could only use singlet excitons (25%) for light emission, limiting the maximum internal quantum efficiency (IQE) to 25%. However, phosphorescent materials containing heavy metals can use triplet excitons (75%) for light emission,[379,380] allowing for a theoretical IQE of 100%. Also, various strategies for the up-conversion of triple excitons into the singlet excited state have been proposed, based on the high decay rate of fluorescence. These include hybridized local charge-transfer state,[381−383] triple−triplet annihilation,[384−386] and thermally activated delayed fluorescence (TADF),[387−389]

https://doi.org/10.1021/acs.chemrev.3c00548
Chem. Rev. XXXX, XXX, XXX−XXX

to realize highly efficient and low-cost OLEDs. Alongside the advancements in organic light emitters, various technologies have recently been developed to improve the device performance of OLEDs. This section will introduce light extraction strategies to improve the performance of flexible and stretchable OLEDs.

3.3.1. Light Extraction Techniques for Deformable OLEDs. Although a 100% IQE can be achieved for OLEDs, the EQE is still limited because the majority of the generated photons are trapped within the device. This is due to a large difference in the refractive indices of the organic layers ($n \sim 1.6-1.8$), TEs ($n \sim 1.8-2.1$), substrates ($n \leq 1.6$), and air ($n = 1.0$). Light confinement can be divided into substrate mode (between the substrates and air, ~23%), waveguide mode (between the TEs and organic layers, ~15%), and surface plasmon polariton (SPP) mode (between the metal electrodes and organic layers, ~40%), resulting in only about 18% of outcoupling efficiency.[390] Accordingly, light extraction techniques have been adjusted to extract the trapped light inside the devices, which can further improve the efficiency of deformable OLEDs. To reduce light confinement in the substrate mode, light extraction can be increased by decreasing the incident angles at the surface to avoid total internal reflection of the light. Therefore, additional micro/nanostructures on the substrate surface can reduce light confinement in the substrate mode by varying the incident angles.[391,392] Xiang et al. fabricated a PET substrate consisting of built-in TE and optical coupling nanostructures (Figure 15A).[393] On one side of the PET substrate, a flexible electrode was formed by filling Ag ink in a nanoimprinted UV-curable resin with a hexagonal network structure. The other side of the PET substrate was then imprinted with a moth-eye nanostructure using the same resin. The red, green, blue, and white flexible OLEDs using this substrate showed increased device performance (Figure 15B) in terms of EQE, power efficiency, current efficiency, and luminance. Optical modeling demonstrated that field intensity was stronger with the nanostructured PET substrate compared to a bare PET substrate, indicating better light extraction in the nanostructured PET substrate.

Unlike light extraction in substrate mode, addressing the waveguide mode requires a different approach because the device requires internal engineering. Fundamentally, light extraction in the waveguide mode can be enhanced in flexible OLEDs by replacing ITO electrodes with alternative TEs. Moreover, according to Snell's law, the refractive indices between the TEs and the plastic substrates can be matched to avoid total internal reflection, thereby increasing outcoupling in the waveguide mode.[394] As an example, an industrial-grade PEN substrate with a high refractive index ($n = 1.7$) was used to enhance the efficiency of flexible OLEDs by matching the high refractive index of the TE.[395] In different approach, the OMO electrode was suggested to enhance substrate mode extraction and to solve the limitations of metal-dielectric composite electrodes, which exhibited a strong dependence on viewing angle[396] due to the microcavity effect. Wang et al. stacked Ta_2O_5/Au/MoO_3 on a PET substrate (Figure 15C), where semitransparent Au was used as a conductive channel with weak optical microcavity, high refractive index Ta_2O_5 functioned as an outcoupling layer, and MoO_3 was employed as a HTL.[397] The fabricated flexible OLEDs with the stacked electrode demonstrated a maximum EQE of 63% and maintained a high EQE of 60% even at a high luminance of over 10,000 cd m^{-2}.

Micro/nanostructures can be integrated into the internal structure of an OLED device, creating an additional wave vector that matches the momentum required to couple out the waveguide mode.[398,399,245] Periodic nanostructures have been used to exploit Bragg scattering of light, but these structures resulted in EL spectra that are dependent on an angular and viewing angles.[400] To overcome this limitation, quasi-random nanostructures were incorporated into the HIL through the nanoimprint lithography technique.[401] The morphological effect on light outcoupling was confirmed by comparing flexible OLEDs incorporating flat, 1D grating, 2D grating, and quasi-random structures (Figure 15D). The devices with quasi-random structures demonstrated significant improvement in efficiency, with increases of 51.2% and 42.5% in EQE and current efficiency, respectively, compared to those with periodic structures. In optical simulation, nanostructures affect the optical field distribution within the device compared to a localized power flux in a flat device, which increased the outcoupling probability of light. In particular, the quasi-random nanostructures, with their broadened periodicity and random orientation, resulted in enhanced light outcoupling and uniform intensity across a wide range of emission angles (Figure 15E).

Surface plasmons, which are collective oscillations of electrons at the interface between a metal and an organic layer, can absorb and scatter light generated in an OLED, inducing SPP mode light dissipation. One way to release this trapped light is through the resonance between excited surface plasmon and emission energy, resulting in a significant increase in the outcoupling value. The introduction of metallic nanoparticles can facilitate the escape of light by stimulating localized surface plasmon resonance, which can be adjusted by changing the size, shape, type, and spacing of the nanoparticles.[402,403] Additionally, the aforementioned strategies of introducing micro/nanostructures can also decrease surface plasmonic losses. For example, a nanostructured organic layer was used to excite localized surface plasmon resonance.[404] Xiang et al. introduced several strategies to improve light outcoupling efficiency, such as using a nanopatterned metal-dielectric composite electrode (Ag grid), incorporating quasi-periodic nanostructures into the internal device layer (iME), and introducing additional outcoupling structure into external device layer (eME) (Figure 15F). Consequently, replacing ITO with an Ag grid contributed to mitigating light loss within the waveguide mode by removing losses at the interface between ITO and the organic layer. Additionally, both the iME and eME varied the wave vector of light at the internal and the substrate of the device, respectively, effectively reducing light losses in both the waveguide and substrate modes. Simulation results for flexible OLEDs demonstrated that the iME pattern excited certain resonant optical modes, such as localized surface plasmon resonance, which were absent in the devices without iME. This indicated that the use of internal nanostructures could simultaneously extract light in waveguide modes and reduce SPP losses. Consequently, flexible OLEDs on PET substrate with Ag grid, iME, and eME recorded a maximum EQE of 72.4% and a power efficiency of 168.5 lm/W, while maintaining good angular color stability.

In a planar design without any outcoupling structures or layers, outcoupling efficiency can still be increased. Since the SPP wavevector, k_{SPP}, can be calculated as $k_{SPP} = \frac{\omega}{c} / \left(\frac{1}{\varepsilon_m} + \frac{1}{\varepsilon_d}\right)^{0.5}$, where ω, c, ε_m, and ε_d are the angular

https://doi.org/10.1021/acs.chemrev.3c00548
Chem. Rev. XXXX, XXX, XXX−XXX

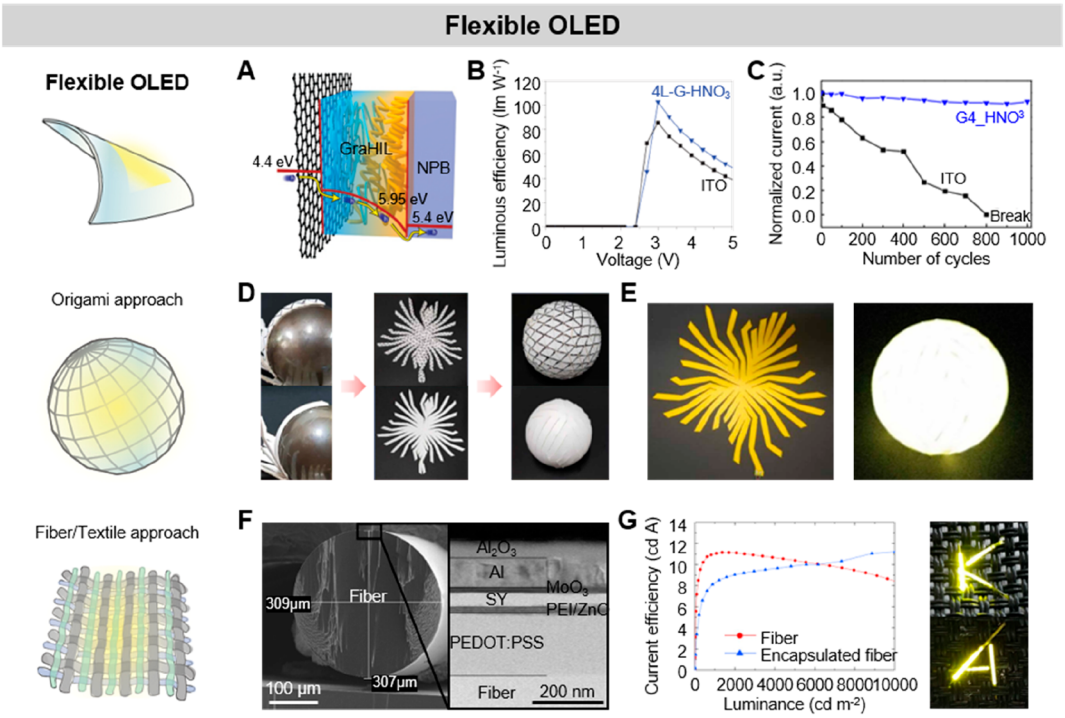

Figure 16. Representative examples of flexible OLEDs. (A) Schematic illustration of a hole-injection process via HTL with a gradient work function. (B) Luminance efficiencies of phosphorescent OLED devices with different anodes. (C) Bending stability of flexible OLED with different anodes. Reproduced with permission from ref 416. Copyright 2012 Springer Nature. (D) Demonstration of computational origami (top) and wrapping (bottom). The crease lines can be ignored when the sum of the folding angles of a net is minimized. (E) Images of flexible OLED panels before (left) and after (right) wrapping and lighting. Reproduced with permission from ref 418. Copyright 2020 American Association for the Advancement of Science. (F) Cross-sectional SEM (left) and HR-STEM (right) image of flexible OLED fiber. (G) Current efficiency-luminance of flexible fiber OLED (left) and photograph of woven fiber (right). Reproduced with permission from ref 424. Copyright 2017 American Chemical Society.

frequency, the speed of light, the relative permittivity of metal, and the relative permittivity of dielectric in a simple configuration, another effective approach to reduce loss in the SPP mode is by replacing one of the transport layers with a low-index layer.[405,406] The horizontally oriented transition dipole moments (TDMs) in the emissive layer naturally emit more light toward the normal direction to the substrate.[407] However, vertically oriented TDMs exhibit the opposite trend and have a transverse magnetic which is prone to the SPP excitation. Therefore, a preferential horizontal orientation of TDMs can be beneficial for enhancing the EQE. Recently, a crystalline organic semiconductor-based OLED with deep blue emission was reported using organic solid solution thin film formation.[408] On a 2,5-di([1,1′-biphenyl]-4-yl)thiophene (BP1T) inducing layer, 2-(4-(9H-carbazol-9-yl)phenyl)-1-(3,5-difluorophenyl)-1H-phenanthro[9,10-d]imidazole (2FPPICz) was deposited by weak epitaxial growth as a crystalline host matrix. Subsequently, 4,4′-bis(1-phenyl-phenanthro[9,10-d]imidazol-2-yl)biphenyl (BPPI) was used as the guest in the EML, following the orientation of the host matrix, and forming a crystalline organic solid solution (Figure 15G). This crystalline thin film, arranged in a horizontal orientation, formed horizontally oriented TDMs up to a 10% concentration of BPPI, showing more than 90% of horizontal dipole ratio from angle-dependent photoluminescence measurements. As a result, compared to doped amorphous EML OLEDs, the 2FPPICz:6% BPPI solid-solution device exhibited a 50% increase in EQE (Figure 15H).

3.3.2. Flexible and Stretchable OLEDs. The first flexible LED was fabricated using an organic emitter in 1992 by Gustafsson et al.,[335] capitalizing on the mechanical flexibility of these materials. Since then, commercial flexible OLED displays have become readily available in forms such as curved displays or foldable/rollable displays. In research, flexible OLEDs have been applied to different types of form factors and deformations, leveraging on the high degree of deformation freedom offered by organic materials.[409−414] To fabricate high-performance flexible OLEDs, the device configuration must be carefully designed with consideration for energy level, balanced charge, as well as optical and mechanical properties, especially when replacing the brittle ITO electrode. For example, graphene exhibits high optical transmittance, flexibility, and smooth surface topology due to its ultrathin characteristics. Despite its fascinating features, graphene needs to be modified to improve carrier injection, due to its relatively low work function (~4.4 eV) compared to the ITO electrodes.[415] For an efficient hole injection to an overlaying organic layer, Han et al. employed a self-organized gradient HIL and perfluorinated ionomer (PFI)-doped PEDOT:PSS as the flexible electrode. This provided a gradient work function through the stacked layers (from 4.4 to 5.95 eV) (Figure 16A).[416] Flexible OLEDs with a four-layer graphene anode p-doped with $AuCl_3$ or HNO_3 showed high maximum current efficiencies of 27.4 and 30.2 cd A^{-1}, respectively, for fluorescent devices, and 98.1 cd A^{-1} for phosphorescent devices (Figure 16B). These efficiencies were significantly higher than those fabricated with an ITO anode. The graphene device endured 1,000

https://doi.org/10.1021/acs.chemrev.3c00548
Chem. Rev. XXXX, XXX, XXX−XXX

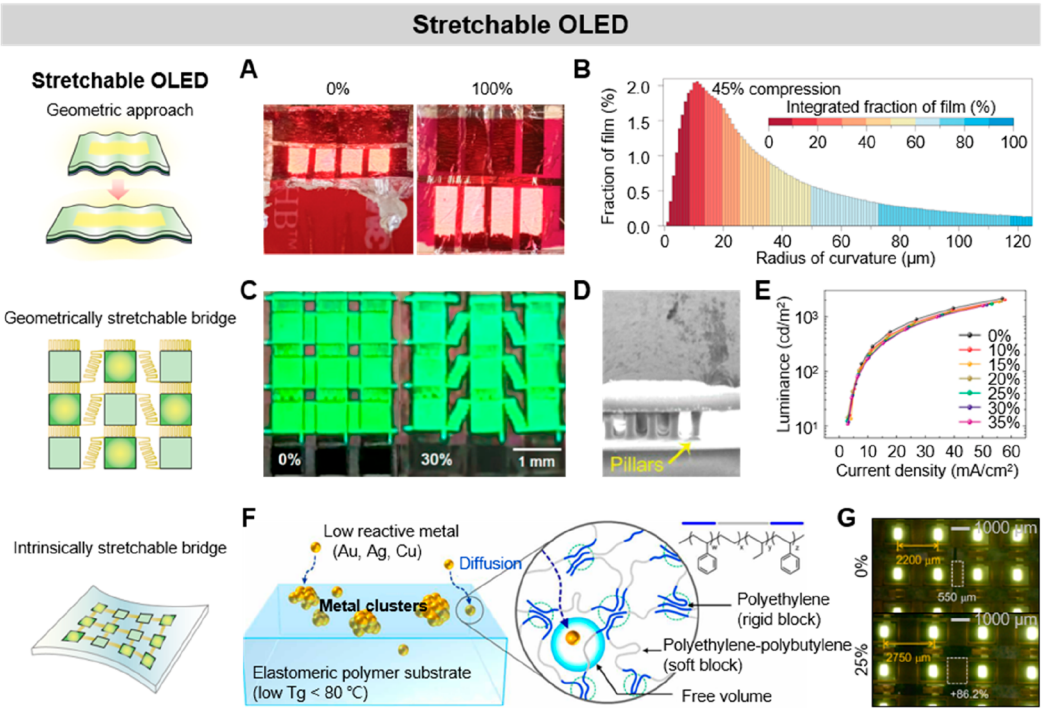

Figure 17. Representative examples of stretchable OLEDs. (A) Images of ultrathin wrinkled PLED before and after 100% stretching. (B) Histograms of the radius of curvature map for 45% compression. Reproduced with permission from ref 170. Copyright 2013 Springer Nature. (C) Microscopic images of stretchable OLEDs with strain values of 0% and 30%. (D) Cross-sectional SEM images of stretchable substrate. (E) Luminance−current density curve of green stretchable OLEDs under different strain values. Reproduced with permission from ref 116. Copyright 2020 American Chemical Society. (F) Schematic of the formation mechanism of stretchable microcracked Au interconnects. (G) Microscopic images of stretchable OLED arrays under different strain values of 0% and 25%. Reproduced with permission from ref 121. Copyright 2021 American Association for the Advancement of Science.

bending cycles, demonstrating an excellent bending stability compared to ITO-based devices, which failed after 800 cycles (Figure 16C).

One of the anticipated features of deformable OLEDs is conformal integration onto arbitrary 3D surfaces without any performance degradation. While developing a stretchable device with high mechanical freedom is one solution, nonstretchable flexible OLEDs with kirigami/origami structures can also achieve conformal integration. The advantage of the kirigami/origami approach lies in the use of well-established organic materials, achieving high device performance. For instance, computational algorithms were introduced to design 2D nonstretchable material platforms to fabricate conformal devices on 3D surfaces with high performance.[417] In another work, a design strategy named "computational wrapping" was developed,[418] which enabled the conformal integration of flexible OLEDs onto highly complex and smooth 3D surfaces without the gaps which were inevitable in the conventional computational origami method (Figure 16D). After obtaining a polyhedral paper net, all crease lines were erased, leaving only the outer cut lines of the net, resulting in a nonpolyhedral developable net. This approach even allowed a brittle Si wafer to cover both concave and convex surfaces without fracturing. Through finite element analysis, it was determined that the Si layer could withstand a thickness of up to 125 μm with 400 facets. Owing to its universality, this method can be applied to flexible OLED panels, enabling them to conformally wrap around various 3D curvilinear surfaces (Figure 16E).

For wearable device applications, breathability is an important factor along with deformability to ensure comfortable use in daily life without causing skin irritations.[419,420] In this sense, many approaches have been reported for directly fabricating displays on textiles or fabrics after applying a planarization layer.[421,422] However, EL fibers can be woven by themselves or together with clothes without an additional layer, offering significant advantages in terms of porosity, flexibility, and durability.[423] Conventional coating processes like thermal deposition are not suitable for cylindrical fibers, so a low-temperature solution process was developed to deposit multiple thin layers of OLEDs evenly for stable fiber OLEDs.[424] Sequentially, conductive PEDOT:PSS, ZnO NPs, polyethylenimine ethoxylated (PEIE), and poly(*p*-phenylenevinylene) (Super Yellow) were dip-coated onto a PET fiber as the cathode, EIL, and EML, respectively (Figure 16F). The thickness of the dip-coated layer was controlled by factors such as the radius of the fiber, the viscosity, surface tension of the solution, and the withdrawal velocity of the dip coating. Subsequently, MoO_3 and Al were thermally evaporated as the HIL and anode, respectively, followed by Al_2O_3 encapsulation to prevent degradation in the materials. The fiber OLED showed a current efficiency of 11.6 cd A^{-1} and a highest luminance of 13,937 cd m^{-2}, with sufficient flexibility to be woven into textiles (Figure 16G). In addition, the feasibility of manufacturing a textile display was demonstrated by incorporating conductive fibers and fiber OLEDs directly into clothing or weaving them together as scan lines and data lines.[425]

https://doi.org/10.1021/acs.chemrev.3c00548
Chem. Rev. XXXX, XXX, XXX−XXX

Table 5. Characteristics of *is*-LEDs

Device category	Emissive material	Turn-on voltage (V)	Maximum luminance (cd/m^2)	Peak EQE (%)	Peak current efficiency (cd/A)	Stretchability (%)	Stretching cycle (times)	Ref.
PLEC	(PF-B)−(PEO−DMA)−LiTf	4.8	200	–	1.16	45	–	431
	SuperYellow−ETPTA−PEO−LiTf	6.8	2200	–	11.4	120	1,000 (stretching at 30%)	432
	SuperYellow−ion-conducting polymer−ETT-15−LiTf	15	–	–	–	30	20 (stretching at 30%)	433
OLEC	Ru(dtb-bpy)3(PF6)2−PDMS	–	–	–	–	27	50 (stretching at 15%)	434
PLED	white emissive polymer−OXD-7	∼7	1,100	–	4	130	100 (stretching at 20%)	439
	SuperYellow−Triton X	8.3	4,400	–	1.6	80	200 (stretching at 40%)	141
	SuperYellow−Triton X	5.3	2,185	–	20.3	20.3	–	306
	(L-SY-PPB)−PAN	6.5	3,780	0.69	2.35	30	50 (stretching at 15%)	440
	SuperYellow−PU	5 (R: ∼ 5, G: ∼ 7, B: ∼ 7.7)	7,450 (R: ∼2,200, G: ∼1,100, B: ∼6,000)	–	∼5.3 (R: ∼0.85, G: ∼2.55, B: ∼1.7)	100	100 (stretching at 40%)	447
	SuperYellow−PEO	3.7	1,754	–	3.14	30	50 (stretching at 10%)	441
OLED	PDKCD (TADF organic polymer)	4.75	2,175	1.7	5.3	60	–	448
PeLED	$MAPbBr_3$ NC−PEO−PVP	2	1,653	∼0.27	–	100	100 (stretching at 20%)	560
	$MAPbBr_3$ NC−PEO	2.4	15,960	–	2.7	40	100 (stretching at 40%)	523

As described in section 3.2.2, an ultrathin form factor can withstand more tensile and compressive stress under deformation. This feature can be adopted for organic emitters, which inherently possess high mechanical endurance, allowing for a significant reduction in the radius of curvature and enhanced ability to tolerate stretching and compression. By attaching an ultrathin OLED device to a prestretched elastomer and subsequently releasing the strain, wrinkles can be formed in the OLEDs, making them structurally stretchable.[426,427] The first demonstration of this approach was presented in 2013,[170] where a PLED was fabricated on a 1.4 μm PET foil substrate using conductive PEDOT:PSS, a semiconducting red light-emitting polymer, and LiF/Al as TE, active layer, and metal electrode, respectively. The ultrathin PLED operated stably even under extreme deformation such as crumpling, and by transferring the PLED onto a prestrained adhesive elastomer, a highly stretchable PLED with up to 100% tensile strain stretchability was developed (Figure 17A). The radius of curvature map, calculated through the height profile of the PLED under 45% compression, revealed bending radii of 10 μm or smaller (Figure 17B). This approach to obtaining stretchable OLEDs through a wrinkled structure has since been further applied in periodic[428] and 2D manners,[429] as well as in random and 1D methods.

The approach of connecting rigid islands with geometrically stretchable interconnects can also be utilized to fabricate stretchable OLEDs. Lim et al. incorporated a stress-relief stretchable substrate into a zigzag-bridged OLED (Figure 17C),[116] where the bridges enabled stretchability and the pillars decentralized the applied stress. Patterned SU-8 was bonded to a PDMS substrate with PDMS pillars (Figure 17D), which served as the stress-relief substrate, and OLED layers were thermally evaporated after depositing a planarization layer. The resulting stretchable OLEDs exhibited a stretchability of 35% and maintained similar electroluminescence performance at different strain levels, with only a slight reduction after 20% strain (Figure 17E). The stress-relief effect of the PDMS pillar substrate was confirmed by simulating four scenarios: island-bridge SU-8 without a substrate, and with flat, island, and pillar PDMS substrates. In the two cases involving SU-8 with flat and island PDMS substrates, significant stress was induced in the SU-8 from the bonded PDMS region. However, the SU-8 with pillar PDMS exhibited less stress than SU-8 without substrate, as the strain transferred to the island was reduced.

Instead of using structurally stretchable interconnects, conductors with intrinsic stretchability can be utilized to connect island-type active OLEDs as stretchable bridges. Conductors with low resistivity and minimal resistance change under strain, such as liquid metal, metal NWs, CNTs, and their composites, can be employed as stretchable interconnects. Furthermore, for high-yield manufacturing and mass production, a method using vacuum-evaporated metal thin films was developed to fabricate stretchable OLED arrays.[121] In this process, metals with low reactivity were diffused into a polymer network at the temperatures near the glass transition temperature of the polymer. In specific, Au was diffused into an SEBS block copolymer and anchored as clusters, forming a microcracked structure that maintained its conduction path under deformation (Figure 17F). The depth of Au diffusion, which controlled crack formation, increased as the deposition rate decreased. After depositing Au as the interconnect, the anode, pixel define layer, organic layers, and cathode were sequentially deposited to fabricate a stretchable OLED array. The resulting stretchable OLED display exhibited no noticeable degradation in device performance up to a strain of 30% (Figure 17G) and demonstrated stable operation during various mechanical deformations, including crumpling, folding, and twisting.

3.3.3. Intrinsically Stretchable LEDs. Stretchable displays are gaining prominence as the next generation displays due to their ability to withstand various deformations. These

https://doi.org/10.1021/acs.chemrev.3c00548
Chem. Rev. XXXX, XXX, XXX−XXX

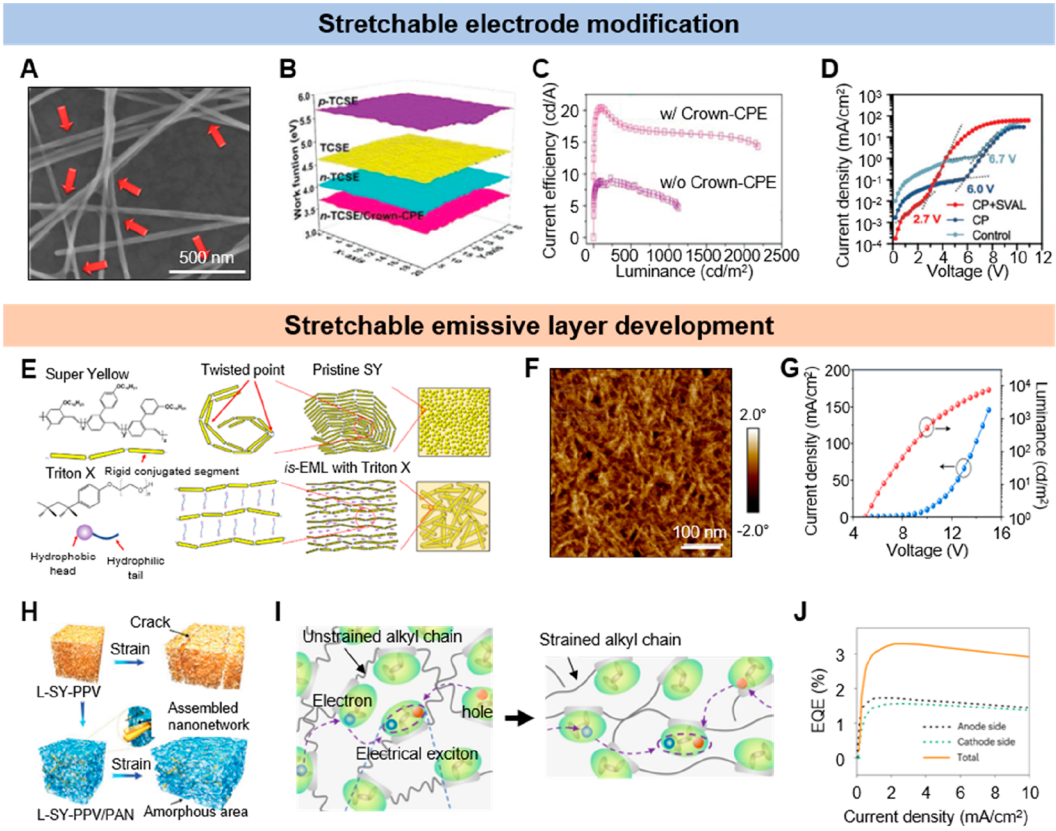

Figure 18. Intrinsically stretchable PLEDs. (A) SEM image of GO-Ag NWs electrode. Red arrows indicate GO-soldered Ag NW junctions. Reproduced with permission from ref 184. Copyright 2014 American Chemical Society. (B) Kelvin probe mapping of work function of TCSE, p-type TCSE, n-type TCSE, and n-type TCSE/interlayer. (C) Current efficiency-luminance characteristic of intrinsically stretchable PLED with and without interlayer. Reproduced with permission from ref 306. Copyright 2022 John Wiley & Sons, Inc. (D) Current density−voltage curve of intrinsically stretchable PLED with different electrode treatments. Reproduced with permission from ref 441. Copyright 2023 John Wiley & Sons, Inc. (E) Schematics showing the microstructures of pristine SY and stretchable emissive polymer mixing triton X. Reproduced with permission from ref 141. Copyright 2021 American Association for the Advancement of Science. (F) An AFM image for a SY/PU film with 50 wt % PU. (G) Current density and luminance characteristics of stretchable PLED. Reproduced with permission from ref 447. Copyright 2022 Springer Nature. (H) 3D schematic of morphology of amorphous L-SY-PPV and L-SY-PPV with 3D penetrating network. Reproduced with permission from ref 440. Copyright 2022 John Wiley & Sons, Inc. (I) Design principle for realizing stretchable TADF polymer via incorporating the soft alkyl chains into the polymer backbone. The soft alkyl chains can effectively dissipate the strain energy during the stretching while excitons are generated at TADF units without affection. (J) EQE measured from both anode and cathode sides of the stretchable OLED and their combination. Reproduced with permission from ref 448. Copyright 2023 Springer Nature.

displays can conform to nonplanar surfaces, accommodate dynamic movements, and adapt to the user's body shape, offering new opportunities to create innovative devices and interfaces that can improve human-machine interactions. As such, in the quest for developing stretchable displays, two approaches to make LEDs stretchable have been actively investigated: one is the geometric engineering of LEDs, and the other is fabricating *is*-LEDs using stretchable materials.[430] Although *gs*-LEDs are more established compared to the latter, they have clear limitations. The *gs*-interconnects in island-bridge stretchable LEDs often lead to a low fill factor of the active area, and the wrinkled stretchable LEDs can cause image distortion and limited viewing angles. Furthermore, sophisticated manufacturing techniques required for these strategies may limit their scalability and commercial viability. In order to address these constraints, researchers are endeavoring to devise *is*-LEDs. Table 5 provides the electrical and mechanical characteristics of reported *is*-LEDs.

In 2011, the first *is*-LED was introduced in the form of polymer LECs,[431] consisting of electrodes made from a composite of single-walled CNTs and poly(*tert*-butyl acrylate), and an emissive layer containing a light-emitting polymer. Initially, *is*-LECs[432−434] were actively studied owing to their simple structure, which comprises an emissive layer made of a light-emitting polymer, ionic conductors and/or electrolyte, sandwiched between two stretchable electrodes. Following a similar structure, *is*-alternating current electroluminescent (ACEL) devices, consisting of two stretchable electrodes enclosing an emissive layer made of inorganic phosphor and elastomer, have been actively reported since their first introduction in 2015.[435−439,110,313] However, both types of devices have limitations compared to conventional LEDs. LECs have a slow turn-on speed as their emissive mechanism is based on ion mobility, and ACEL devices require high operation voltage to excite the electrically isolated light-emitting phosphor. Moreover, both types of devices exhibit relatively inferior electrical and optical performances. Thus, developing *is*-LEDs has become an important research topic despite the challenges involved in developing electrodes and multiple semiconducting layers, in addition to the EML, that possess both high stretchability and high electrical property.

https://doi.org/10.1021/acs.chemrev.3c00548
Chem. Rev. XXXX, XXX, XXX−XXX

To date, most reported *is*-LEDs are PLEDs, owing to the advantages offered by the long molecular chains of light-emitting polymers that help maintain electrical characteristics while being stretched. The development of *is*-PLED has focused on two main aspects: optimizing stretchable electrodes and designing the *is*-semiconducting layer. The bottom electrodes used in the *is*-LEDs need to have an ultrasmooth surface morphology to prevent device breakdown. In this regard, a stretchable composite electrode with conductive nanomaterials embedded in the surface of an elastomer matrix is advantageous. To develop highly stretchable electrodes with high surface conductivity, GO was introduced as a soldering material for Ag NW-based stretchable composite conductors (Figure 18A).[184] GO, with its various oxygen-containing functional groups, could form strong bonds with the Ag NWs, and its high flexibility and toughness contributed to a low sheet resistance of the electrode and stable performance during stretching. Using this electrode as both cathode and anode, a white *is*-PLED, composed of PEDOT:PSS, emissive polymer, and PEIE, was successfully fabricated, exhibiting a brightness of 1,100 cd m^{-2} and a stretchability of 130%.

Metallic NWs, especially Ag NWs, have been widely employed as stretchable electrodes, but their limited contact area with the adjacent layer often results in poor charge injection properties. To address this issue, an interlayer can be inserted between the electrode and the adjacent layer. For instance, a graphene cover layer can be utilized as a charge-spreading promoter on the surface of the embedded Ag NWs electrode.[306] The surface carrier density of the graphene-covered electrode was almost doubled compared to pristine Ag NW networks, owing to the redistribution of charges from the Ag NWs to graphene. The graphene layers were doped with perfluorosulfonic acid (p-type) and PEIE (n-type) to adjust the work function of the electrodes and enhance charge injection. The work function of the cathode was further reduced to 3.57 eV by introducing an anionic crown conjugated polyelectrolyte interlayer, which induces a strong interfacial dipole, to facilitate electron injection (Figure 18B). The fabricated *is*-PLED based on modified graphene/Ag NWs electrodes, stretchable PEDOT:PSS, and stretchable emissive polymer displayed a current efficiency of 20.3 cd A^{-1}, which was the highest reported current efficiency among *is*-PLEDs (Figure 18C). A PM *is*-PLED was also developed, demonstrating a convex stretching capability of 20.3%. Other interlayer examples, such as conductive PEDOT:PSS[432] or ultrathin metal,[440] have also been reported.

In order to avoid solvent attack during the direct coating of the top electrode, the lamination of a free-standing electrode is often exercised, but poor adhesion has been a challenging issue. Recently, a method was developed to improve the interface of the laminated cathode.[441] A uniform contact could be achieved by reducing the roughness of the Ag NW percolation network through cold pressing and welding with controlled pressure and temperature before embedding in polymer. Additionally, solvent-vapor treatment of cyclohexane, which partially solvated the light-emitting polymers, increased the interchain diffusion of the polymer chains, enabling a firmly laminated interface. Earlier electron injection was observed for devices treated with both cold pressing and solvent-vapor compared to those treated with cold pressing alone (Figure 18D). This method effectively reduced the turn-on voltage of *is*-PLED to 3.7 V, with a maximum luminance of 1,754 cd m^{-2} and 30% stretchability.

The design of the *is*-semiconducting layers, particularly the *is*-EML, is another crucial aspect of *is*-PLED construction which must take into account charge transportability, energy-level alignment, and stretchability. Most emissive polymers are conjugated polymers where the conjugated π-electron backbone allows for the delocalization of charge along the polymer backbone, resulting in semiconducting properties.[442,443] Conjugated polymers can be brittle; therefore, additives such as secondary elastomers or surfactants are typically incorporated to increase the free volume within the polymer network and enhance stretchability.[444−446] However, thorough design is required as the insulating properties of these additives may significantly decrease carrier mobility. In this regard, an ionic surfactant (Triton X) was employed as a plasticizer to optimize the mechanical and charge transport properties of an *is*-emissive polymer and an *is*-hole transport polymer (PEDOT:PSS).[141] Specifically, Triton X was found to reduce the interchain interaction within the conjugated polymer and the electrostatic interactions between PEDOT and PSS. By precisely controlling the mixing weight ratio of Triton X to the EML as 1:2, faster carrier mobility was obtained compared to the pristine EML due to a conformational change from a coiled to a linear structure (Figure 18E). For *is*-PEDOT:PSS, 5 weight% of Triton X, which exhibited the highest hole transport property, was utilized. To fabricate the *is*-PLED, Ag NWs and silica aerogel composite embedded in PDMS were used, along with an optimized HTL and emissive layer, ZnO doped with PEIE, and ZnO overcoated Ag NWs, resulting in a maximum luminance of 2,500 cd m^{-2} and stretchability of 80%.

To enhance the stretchability of the emissive polymer in PLEDs while maintaining its charge transportability, a method to introduce regulated nanostructures has been proposed, instead of merely increasing the spacing between interchain distances. In a recent study, nanoconfined emissive polymer structures were introduced by spontaneous phase separation from a soft elastomer.[447] The interaction between the polar groups of the emissive polymer and PU facilitated their homogeneous mixing and percolated nanofiber structures were formed within the emissive polymer, resulting in a uniform distribution of nanofibers in both vertically and horizontally (Figure 18F). This blending method effectively reduced nonradiative trap-assisted recombination by diluting the trap density, achieving the highest luminance and current efficiency in the PLED at a PU weight percentage of 30%. Additionally, an additive consisting of a polyethylene glycol (PEG) backbone and sliding cyclodextrin functionalized with PEG methacrylate side chains was introduced to the conductive PEDOT:PSS to serve as the anode and cathode. This additive induced the formation of PEDOT nanofibers, enhancing electrical conductivity without PEG crystallization for high stretchability. Between the two stretchable electrodes, layers of PEDOT:PSS, TFB, the emissive polymer blend, and PFN-BR with PEIE were used to fabricate the *is*-PLED. A maximum brightness of 7,450 cd m^{-2}, the highest compared to all previously reported *is*-PLEDs, was achieved with a stretchability of 100% (Figure 18G). This method proved versatile and could be adapted to create red, green, and blue *is*-PLED arrays by adjusting the red PPV copolymer, green spiro-copolymer, and blue polyfluorene copolymer.

In PLED devices, which feature a multilayer stacked structure, vertical channel formation inside the emissive polymer is necessary, unlike other semiconductor devices

https://doi.org/10.1021/acs.chemrev.3c00548
Chem. Rev. XXXX, XXX, XXX−XXX

such as FETs, which require horizontal channel formation. To achieve this, a 3D penetrating nanonetwork of emissive polymer was developed by forming low scale nanofibrils within the polymer matrix.[440] The interchain conjugation reinforced charge transport capability, while the amorphous regions promoted polymer chain dynamics. A long phenylenevinylene polymer (L-SY-PPV) with high interchain stacking interaction was used to form a penetrating nanonetwork morphology inside a highly polar polyacrylonitrile (PAN) matrix through aggregation and chain conjugation (Figure 18H). A 5:5 mixing ratio of L-SY-PPV to PAN resulted in a lower Young's modulus and higher charge transport property compared to a pristine L-SY-PPV film. Additionally, an EIL with high electron transport property and stretchability was developed by introducing chelating interactions of PEIE and pBphen with Zn and morphology regulation by reduced Triton X100. As a result, the *is*-PLED fabricated with a serpentine Au, a Au interlayer (3 nm), PEDOT:PSS, the 3D penetrating emissive polymer, PMMA (1 nm), the developed EIL, a Ag interlayer (2 nm), and Ag NWs embedded PDMS exhibited a maximum luminance of 3,780 cd m^{-2} with a stretchability of 30%.

The most widely used polymer emitter for the *is*-PLEDs is Super Yellow, a fluorescent material with inherently low efficiency due to singlet exciton (25%) recombination. TADF emitters, however, have a small energy-level split between singlet and triplet excitons, enabling a reverse intersystem crossing process from triplet to singlet and nearly 100% IQE. To create stretchable TADF polymers, Liu et al. inserted soft alkyl chains between the TADF units within a polymeric backbone (Figure 18I).[448] The TADF unit consisted of an acridine-benzophenone electron donor−acceptor pair linked to an alkyl chain via a benzo-ether capping on a carbazole group. After introducing the alkyl chain, a dihedral angle was observed through density functional theory, ensuring efficient TADF processes. The length of the alkyl chain affected the mechanical properties of the polymer, such as a decrease in glass transition temperature and crack-onset strain, but did not impact the photophysical characteristics when compared to a small-molecule TADF emitter. The TADF polymer with alkyl chains of one carbon, which did not exhibit any cracks under 100% strain in film state, was used for *is*-OLED fabrication along with Ag NWs, PFI-doped PEDOT:PSS, PFN-Br-doped PEIE, and Ag NWs. The device exhibited a stretchability of 60%, an EQE of 3.3%, and a current density of 10.2 cd A^{-1} in total, including both the anode and cathode sides (Figure 18J).

3.4. Inorganic Nanomaterials

In spite of significant advancements in deformable OLED technology, these devices still face limitations stemming from the inherent properties of the organic emissive materials. These materials are highly susceptible to damage from oxygen and humidity and exhibit strong electron−phonon coupling, which in turn results in challenges of durability and color purity (full width at half-maximum (FWHM) of 40−60 nm).[449−451] In addressing these challenges and enabling the development of deformable displays with enhanced performance, a new class of inorganic nanomaterials has recently garnered considerable attention. Unlike the conventional ultrathin inorganic semiconductors covered in section 3.2, these materials can be directly deposited onto deformable substrates with low thermal resistance, offering high spectral purity and wide spectrum coverage. Among the inorganic nanomaterials, this section will cover QDs and perovskites and their application in deformable LEDs.

3.4.1. QD Patterning Strategies for Deformable QLEDs. Colloidal inorganic QDs have emerged as a highly promising class of emissive materials for flexible and stretchable displays, due to their broad spectral tunability from UV to NIR and narrow emission peaks, with a FWHM of less than 30 nm.[452−457] These distinct features of QDs arise from their electronic state structure. At the size of a typical QD (within the range of 2−20 nm), the continuous energy level of a bulk semiconductor transforms into discrete electronic states with a size-dependent energy gap due to the quantum confinement effect. Thus, the emission wavelength of QDs is influenced by both their composition and size, allowing for high color coverage. Additionally, their discrete energy levels give a sharp emission peak with little broadening, enabling high color purity through achieving a narrow size distribution. Currently, core/shell QDs with type-I heterostructures, in which the core comprises a narrower gap material and the shell with a wide band gap material, are widely employed in QLEDs due to the spatial localization of carriers.[134,458,459] The passivation of the shell acts as a barrier to suppress the interaction of excited carriers with the surface trap sites, thereby increasing quantum yield by suppressing the non-radiative carrier recombination. Furthermore, optimizing the core/shell structure, such as controlling the outer shell thickness or introducing an intermediate shell,[460−462] can enhance device efficiency by suppressing interparticle energy transfer between QDs and Auger recombination of charged QDs or by reducing the lattice strain. Since the first demonstration of a QLED based on CdSe QDs and poly(*p*-phenylenevinylene) polymer,[463] QLED structures for balanced charge recombination have been extensively investigated.[464−469] Typically, organic HTLs (e.g., TFB,[470,471] PVK,[472] p-TPD[473]) and inorganic ETLs (e.g., ZnO,[474] ZnMgO[475]) are adopted, with record maximum EQE values of 30.9%,[476,477] 28.7%,[478] and 21.9%,[478] and record maximum brightness of 963,433 cd m^{-2},[477] 614,000 cd m^{-2},[478] and 62,600 cd m^{-2}[478] achieved for red, green, and blue QLEDs, respectively. These numbers surpass the requirements for practical display use. As the resemblance between the display and human eye increases, high-resolution pixels become crucial for realistic image expression,[479,480] motivating efforts to develop high-resolution patterning for wearable, virtual-reality, and augmented-reality displays, all of which are potential applications of deformable displays.

In contrast to vapor-deposited organic emitters, colloidal QDs can only be deposited using solution processes (e.g., spin coating, spray coating, and dip coating). Although these solution processes are simple and cost-effective, they necessitate novel approaches for patterning the resulting film into pixels. Transfer printing (i.e., contact printing)[481−485] is one method to pattern the red-green-blue (RGB) QD layers without cross-contamination. The adhesion between the QD layers and the stamp can be kinetically controlled and increases with the peeling rate, due to the viscoelastic behavior of the elastomeric stamp.[486] This process enables the QD layer to be picked up from the donor substrate (inked) and then released onto a receiver substrate (printed), allowing for solvent-free patterning.

In detail, a QD solution was spin-coated onto a Si donor substrate with self-assembled octadecyltrichlorosilane (ODTS) monolayers. A structured PDMS stamp was then used to pick

https://doi.org/10.1021/acs.chemrev.3c00548
Chem. Rev. XXXX, XXX, XXX−XXX

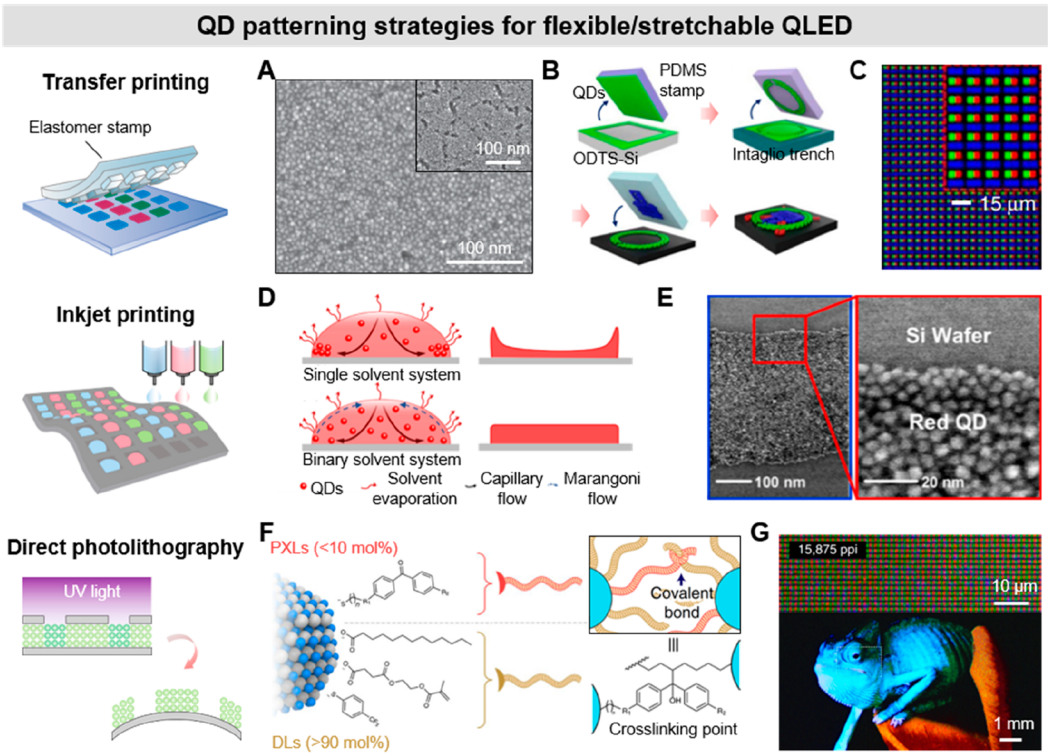

Figure 19. QD patterning strategies for flexible/stretchable QLEDs. (A) SEM images of spin-coated QD film (inset) and transfer-printed QD. Reproduced with permission from ref 481. Copyright 2011 Springer Nature. (B) Schematic illustration of intaglio transfer printing process. (C) The photoluminescent image of the aligned RGB pixels (6 μm) with 2,460 PPI. Reproduced with permission from ref 490. Copyright 2015 Springer Nature. (D) Schematic of inkjet droplet evaporation in single solvent and binary solvent system. Reproduced with permission from ref 499. Copyright 2021 Springer Nature. (E) SEM images of a ~ 400 nm line pattern printed using a nozzle with 1 μm internal diameter. Reproduced with permission from ref 500. Copyright 2015 American Chemical Society. (F) Schematic of dual-ligand QDs. The PXLs (<10 mol %) make QD film UV cross-linkable and DLs (>90 mol %) determine the solubility of QDs. (G) Fluorescent images of aligned RGB pixels (0.8 μm) with 15,875 PPI (top) and vertically stacked RGB patterns (bottom). Reproduced with permission from ref 508. Copyright 2022 Springer Nature.

up the film with the desired pattern, and it was contacted with the receiver substrate to release the QD film to the desired positions, resulting in an RGB pattern. Pressure applied to the stamp compacted the QDs to fill the voids and cracks, resulting in a uniform film morphology that in turn led to low leakage current (Figure 19A).[481] The fabricated QLEDs exhibited ~25−52% higher power efficiencies and brightness compared to those using spin coated QD layers. A 4-in. full-color AM QD display and a flexible RGB QLED could be successfully fabricated using the transfer printing patterning method, owing to its substrate-independent processability. Numerous contact printing methods have also been documented, including transfer printing using a sacrificial layer,[487] nanoimprinting technique,[488] and direct coating.[489] To achieve extremely high-resolution patterning, an intaglio transfer printing technique was proposed that overcame the discrepancy between the structured stamp and the printed pattern.[490] This technique used a fully inked flat elastomeric stamp with a Si intaglio trench to transfer the remaining pattern on the stamp to a receiver substrate (Figure 19B). The large surface energy differences between the PDMS stamp and the target substrate enabled tight binding of the QD layer at the Si trench, allowing for the creation of small pattern sizes of 5 μm. Multiple printing processes resulted in the creation of full-color 2,460 PPI resolution pixels (Figure 19C) and a flexible true white LED.

The inkjet process[491−494] is a promising patterning method for mass production of QLEDs due to its cost-effectiveness, scalability, and reproducibility, as this technique allows direct material deposition on selected locations with minimal waste. To achieve high resolution, good surface morphology, and coverage without clogging the nozzle, several factors such as surface tension, viscosity, and density of the QD inks, should be considered. This involves controlling the concentration, surface ligand, size, distribution of the QDs, and the nature of the solvent.[495−497] Especially, extensive research has been conducted to solve the coffee-ring effect, where QDs concentrate at the perimeter of a droplet due to differential evaporation of the solvent.[498] As one solution, a binary solvent system for QD ink was designed, containing 7:3 of decalin and n-tridecane. The high surface tension of decalin induced a Marangoni flow (Figure 19D), resulting in stable inkjet flow without TFB dissolving and free from the coffee-ring effect.[499] A red QLED fabricated using the developed ink exhibited an EQE of 18.3% and a lifetime comparable to that fabricated from spin-coat QD solutions. The printing method can also be tailored for fine patterning of QDs. For example, electro-hydrodynamic jet printing of QDs in dichlorobenzene was demonstrated, where pattern sizes and the thickness of the QD layer could be optimized by controlling the nozzle diameter, bias voltage, ink composition, and stage speed.[500] A line pattern with a width of almost 400 nm was obtained using this method (Figure 19E), and the fabricated green QLED

https://doi.org/10.1021/acs.chemrev.3c00548
Chem. Rev. XXXX, XXX, XXX−XXX

exhibited a maximum luminance and EQE of 36,000 cd m^{-2} and 2.5%, respectively.

Photolithography[501−503] is another promising approach for patterning the QDs with high industrial applicability. It is a well-established fabrication process that is capable of creating submicrometer scale patterns over large areas, regardless of the substrate using existing manufacturing processes. However, directly contacting QDs with the photoresist is not desirable for QLED applications, as the photoresist interferes with charge transport. The photoresist can first be patterned prior to coating the QD layer and then lifted off, but this method can cause cross-contamination and degradation of the QD layer during the successive RGB patterning process.[504,505] To overcome these challenges, direct photolithography methods that form QD patterns through light exposure have been actively investigated. In one approach, photosensitive inorganic ligands were designed for direct optical lithography of QDs.[506] These ligand molecules were designed with Cat^+X^- ion pairs that bound to the electron-deficient surface sites of the nanocrystals. They are soluble in polar solvents due to the stabilization by the ionic cloud of the dissociated cation, which is tightly bound in nonpolar solvents. By using Cat^+ with photoacid generator (e.g., diphenyliodonium, triphenylsulfonium, *etc.*) and X^- with surface-binding inorganic anions (e.g., $Sn_2S_6^{4-}$, $CdCl_4^{2-}$, MoO_4^{2-}, *etc.*), the cation parts decomposed and generated protons which react with the anion parts under light, altering solubility in solvents. Alternatively, by using the photosensitive X^- groups, such as ammonium 1,2,3,4-thiatriazole-5-thiolate ($NH_4CS_2N_3$), CS_2N_3- groups decomposed into N_2, sulfur, and SCN^- ions after the light exposure, stabilizing the colloidal solution in polar solvents and enabling positive tone pattering. This method could be used to pattern a variety of QDs, including CdSe and InP, as well as other semiconducting, oxide, and metal nanocrystals (NCs).

A photoactive cross-linking process can also be employed to directly bind ligands between adjacent QDs. One approach is incorporating a light-driven ligand cross-linker that reacts with surface ligands, leading to cross-linking between neighboring QDs.[507] However, the addition of a cross-linker can cause electrical insulation, adversely impacting the electrical performance of the QLEDs. To address this concern, Hahm et al. recently introduced photo-cross-linkable ligands (PXLs) which enable cross-linking between QDs without the need for additives.[508] They investigated a dual ligand system consisting of PXLs and dispersing ligands (DLs) for scaffold formation under UV irradiation and solvent versatility, respectively. The PXLs were designed with a benzophenone moiety, featuring $-N(CH_2)_4$ and $-S-$ substituents at both *para* positions to enhance the photosensitivity under 365 nm UV, an alkyl group, and an anchor group (Figure 19F). The solubility of QDs could be controlled by adjusting the DLs since the PXLs portion was less than 10 mol %. Using conventional photolithography equipment, an extremely high-resolution pattern of 15,875 PPI with 0.8 × 0.8 μm^2 RGB subpixels, surpassing the requirements for near-eye hyper-realistic displays, and vertically stacked well-defined full-color image were achieved (Figure 19G). The photopatterned RGB QD films could be successfully developed into a 10 × 10 PM RGB display.

3.4.2. Defect Passivation of Perovskite Nanocrystal for PeLEDs. In recent years, metal halide perovskites (MHP) have gained significant research attention as promising emissive materials for LEDs,[509−513] owing to their narrow emission spectra (FWHM of less than 20 nm), outstanding charge transport properties, and wide color gamut.[514,515] The general molecular formula for MHP is ABX_3, where the A-site represents monovalent cations, the B-site denotes divalent metal cations, and the X-site represents halide anions. The electronic structure of MHP can be tailored by adjusting their atomic composition and lattice structure.[516,517] The exciton binding energy of a 3D MHP is lower than the thermal energy at room-temperature, enabling excitons to easily dissociate into free carriers.[518] Therefore, confined MHPs such as quasi-2D, 2D, and nanocrystals (NCs), have been primarily used as emissive materials in LEDs for the radiative recombination of excitons.[519−521] From a mechanical standpoint, low-dimensional MHPs are more advantageous for developing deformable LEDs due to their superior strain accommodation capabilities. Notably, PeNCs stand out as an ideal candidate for creating deformable perovskite LEDs (PeLEDs),[522,523] owing to their tunable optical properties through size-dependent quantum confinement effect and mechanical robustness, which facilitates their integration as stretchable emissive layers.

Apart from the typical factors that affect the performance of LEDs, such as carrier injection imbalance and auger recombination, MHPs present another significant issue from a materials perspective. The formation of defects in MHPs is inevitable due to both thermodynamic intrinsic defects and kinetic defects during the nucleation and growth. These defects include intrinsic point defects (e.g., vacancies, interstitial defects, and antisite defects), defect pairs (e.g., Frenkel and Schottky defects), and high-dimensional defects (e.g., dislocations and grain boundaries).[524−526] The presence of deep-level defects can lead to nonradiative recombination, reducing photoluminescence quantum yield (PLQY) and significantly decreasing LED efficiency. Furthermore, these defects can cause ion migration and phase segregation, leading to unstable PeLEDs and reduced operational lifetime.[527] Therefore, developing efficient and stable PeLEDs is crucial for creating a deformable PeLED display. In PeNCs, more complex defects are formed caused by capping ligands on the surface, which can easily dissociate during the purification, aging, and dilution processes, as they dynamically bind to the surface.[528−530] Owing to their high surface-to-volume ratio, surface defects are dominant in PeNCs. This section will provide a brief overview of surface passivation strategies for PeNCs, with the aim of improving the efficiency and stability of PeLEDs.

The ionic nature of PeNCs facilitates successful passivation of defects through the formation of ionic interactions. Also, by replacing long alkyl ligands, such as oleic acid (OA) and oleylamine (OAm), with short ligands, both surface passivation and reduction of the insulating effect can be achieved.[531,532] For example, in one study, weakly bound long-chain surface ligands were replaced with 1-hydroxy-3-phenyl-propan-2-aminium iodide (HPAI) and tributylsulfonium iodide (TBSI), which bound to I^- of the $CsPbI_3$ NCs.[533] After synthesizing $CsPbI_3$ NCs with OA and OAm ligands, HPAI and TBSI were sequentially treated, such that HPA^+ cations altered the polarity to enable TBSI ligand treatment. The PeLEDs fabricated using HPAI and TBSI-treated NCs exhibited increased luminance and EQE compared to those using pristine and HPAI-treated NCs, achieving a peak EQE of 6.4%.

The detachment of ligands from the surface of the PeNCs leads to the formation of vacancies at both the A and X sites.

https://doi.org/10.1021/acs.chemrev.3c00548
Chem. Rev. XXXX, XXX, XXX−XXX

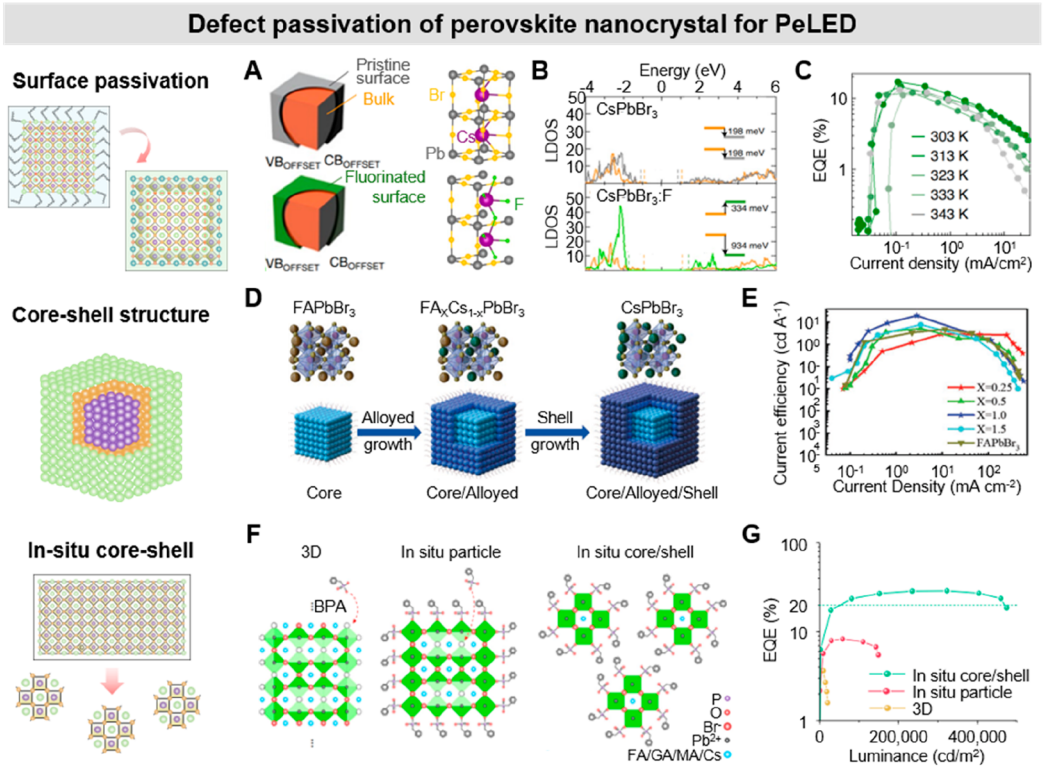

Figure 20. Defect passivation of PeNCs for flexible/stretchable PeLEDs. (A) Schematic of $CsPbBr_3$ and fluoride-treated $CsPbBr_3$ NCs (left) and their atomic structure (right). (B) Local density of states of bulk and surface layers of $CsPbBr_3$ (top) and same system having fluoride ions occupying all bromide-ion positions (bottom). (C) EQE-current density curves of PeLED at different working temperature. Reproduced with permission from ref 536. Copyright 2021 Springer Nature. (D) Schematic illustration of the lattice structure and the synthesis of core $FAPbBr_3$ NCs, core/alloyed-shell $FAPbBr_3/FA_xCs_{1-x}PbBr$, and core/alloyed-shell/shell $FAPbBr_3/FA_xCs_{1-x}PbBr_3$/ $FAPbBr_3/CsPbBr_3$ perovskite NCs. (E) Current efficiency-current density curves of PeLEDs with different molar ratio of Cs/FA. Reproduced with permission from ref 542. Copyright 2020 John Wiley & Sons, Inc. (F) Schematic illustration of the transformation process of 3D perovskite into *in situ* particle and *in situ* core/shell structures by BPA treatment. (G) EQE-luminance curve of PeLED with different perovskite. Reproduced with permission from ref 543. Copyright 2022 Springer Nature.

Inorganic cations, such as Au, Ag, Zn, Na, and Cd, can effectively work as passivators of A-site vacancies.[534] For instance, Ag^+ ions could substitute for Cs^+ ions in $CsPbI_3$ NCs or trap bromide ions in $CsPbBr_3$ NCs, leading to an increased EQE of the PeLEDs.[535] On the other hand, halide vacancies can be passivated using halide anions as passivators. Liu et al. employed a fluoride-based post synthesis treatment on $CsPbBr_3$ NCs to occupy the Br vacancies and partially replace the Br^- anions (Figure 20A).[536] As the proportion of F^- ions increased, the valence band maximum decreased, while the conduction band minimum energies increased, resulting in the formation of a type-I-like junction on the surface of the PeNCs (Figure 20B). Consequently, $CsPbBr_3$:F exhibited higher thermal resistance and stability, maintaining a stable PLQY of 90% up to 370 K without thermal degradation. The fabricated LEDs using $CsPbBr_3$:F NCs showed a maximum EQE of 19.3%, with only a 23% decrease in EQE observed at 343 K (Figure 20C), compared to an 80% drop in conventional PeLEDs at the same temperature.

Adopting a core/shell structure is an effective strategy to passivate the surface defects of the PeNCs, while simultaneously protecting the core perovskite from external environments. When considering core/shell heterojunctions, band alignment that promotes exciton confinement, type-1 and reversed type-1 configurations, are preferred, and minimized lattice mismatch should all be considered to achieve optimal PeLED properties.[537,538] Inorganic semiconductors, such as CdS, ZnS, and PbS, are commonly used as shells for PeNCs.[539,540] In one study, PbS, which has a minimal lattice mismatch with perovskite (<5%), was epitaxially grown on $CsPbI_3$ NCs by growing $CsPbI_3$ NCs in a solution containing ultrasmall PbS clusters.[541] The introduction of PbS passivated the surface defects, resulting in a narrowed PL peak and increased PLQY, leading to an increased EQE of up to 11.8% with improved device storage and operation stability. Additionally, a core/shell structure can be formed using two different MHPs to minimize lattice mismatch. For example, a $CsPbBr_3$ shell was epitaxially grown on the surface of monodispersed $FAPbBr_3$ NCs, where a layer of alloyed $FA_xCs_{1-x}PbBr_3$ was grown between the core and shell to address the lattice mismatch (Figure 20D).[542] The resulting $FAPbBr_3/CsPbBr_3$ NCs exhibited a stable PLQY of up to 93% due to the passivation of surface defects, and better environmental stability, retaining ~80% of PLQY after 70 days storage in ambient conditions, achieving an EQE of 8.1% and a current efficiency of 19.75 cd A^{-1}, which were 4-fold and 8-fold higher, respectively, than bare $FAPbBr_3$-based PeLEDs (Figure 20E). Furthermore, other materials, such as organic semiconductors, inorganic salt, and organic salts, can also be used as shells.

A recent study reported the fabrication of *in situ*-formed core/shell PeNCs by dividing a 3D perovskite film into NCs

https://doi.org/10.1021/acs.chemrev.3c00548
Chem. Rev. XXXX, XXX, XXX−XXX

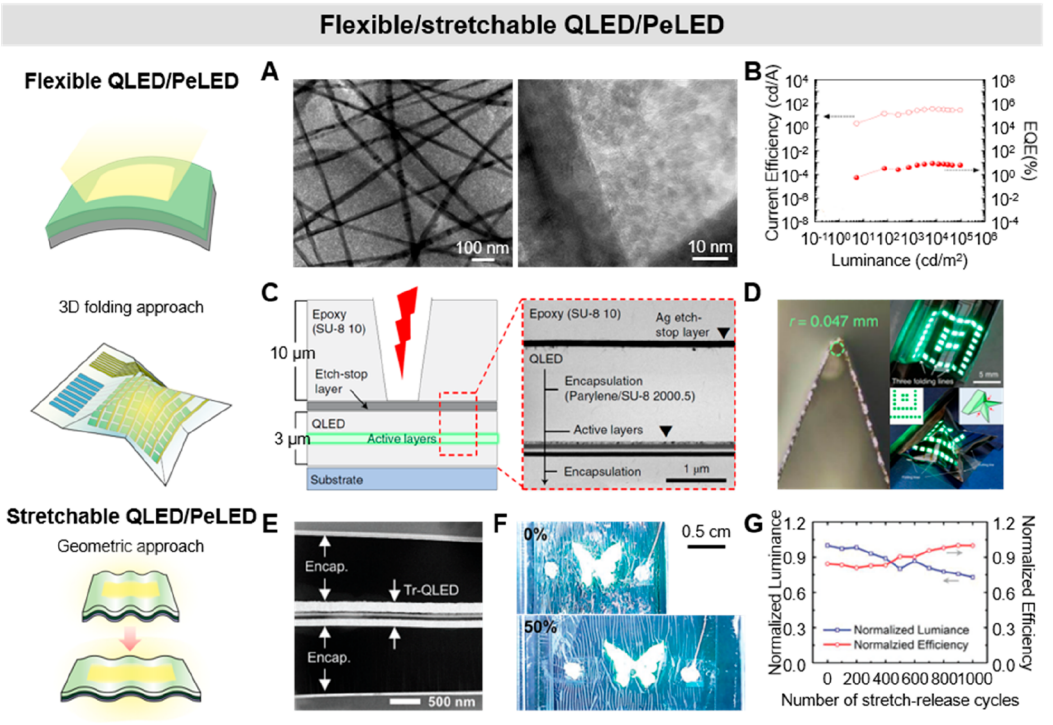

Figure 21. Representative examples of flexible/stretchable QLEDs. (A) Low (left) and high (right) magnified TEM images of ZnO NPs-AgNWs composite electrode. (B) Current density-Luminance-EQE characteristics of a flexible inverted QLED. Reproduced with permission from ref 551. Copyright 2017 American Chemical Society. (C) Cross-sectional schematic and TEM image of the device structure. (D) Bending radius of the device under compressive strain of 70% (left). Right images are pictures of 3D foldable QLED array. Reproduced with permission from ref 109. Copyright 2021 Springer Nature. (E) Cross sectional TEM image of the ultrathin transparent QLED. (F) Ultrathin transparent QLEDs stretched up to 50% without luminance change. Reproduced with permission from ref 148. Copyright 2017 John Wiley & Sons, Inc. (G) Normalized luminance and current efficiency versus stretching cycles between 0% and 20% strains. Reproduced with permission from ref 553. Copyright 2019 John Wiley & Sons, Inc.

surrounded by an organic shell material (Figure 20F).[543] To achieve this, benzylphosphonic acid (BPA) was added to the precursor solution, forming an *in situ* particle structure of $(FA_{0.7}MA_{0.1}GA_{0.2})_{0.87}Cs_{0.13}PbBr_3$. The BPA acted as a ligand and covered the uncoordinated Pb. The perovskite thin film was then exposed to a BPA solution in tetrahydrofuran, creating *in situ* core/shell PeNCs. In this structure, the small BPA molecule with strong acidity penetrated and split the large crystal domain into a nanosized core/shell structure (10 ± 2 nm). The *in situ* core/shell PeNCs exhibited superior carrier confinement and decreased trap density, leading to increased PL intensity and lifetime compared to the 3D perovskite film and *in situ* particles. Green PeLEDs fabricated using these *in situ* core/shell PeNCs showed a remarkably high maximum EQE of 28.9%, a maximum brightness of ~470,000 cd m^{-2}, which was the highest brightness reported among PeLEDs, a low efficiency roll-off of ~5% at 400,000 cd m^{-2} (Figure 20G), and a half-life time of 520 h at an initial brightness of 1,000 cd m^{-2}.

3.4.3. Flexible and Stretchable QLED/PeLEDs. The remarkable optoelectronic properties of QLED/PeLED have led researchers to adapt flexible and stretchable techniques to develop deformable devices.[7,544−549] During the course of deformable device fabrication, flexible electrodes and substrates were employed. For example, to withstand the thermal and solvent treatment during the QLED fabrication process, highly flexible PI films were utilized as the flexible substrate, which can endure high temperatures (~260 °C) and many organic solvents.[550] A flexible TE with an 18 nm thickness of Ag thin film was employed in the top-emitting QLEDs with an Al/ZnO/QDs/2,20,200-tris(N-carbazolyl)triphenylamine/MoO_3/Ag structure. Ag NWs can serve as flexible electrodes themselves or as composites. Kim et al. utilized Ag NWs with ZnO nanoparticles (NPs) as a flexible electrode to fabricate QLEDs, wherein the ZnO NPs served as fillers that interconnect the neighboring Ag NWs electrically (Figure 21A).[551] The fabrication of the flexible electrode started by first coating PMMA overlayer onto a PU-coated PET substrate, then forming the Ag NWs overcoated with ZnO NPs composite electrode, followed by heat-assisted flate-plate pressing to reduce the roughness. An inverted QLED structure of ZnO/QDs/PEIE/p-TPD/MoO_x/Al was developed, which displayed high luminance, current efficiency, and EQE of 50,560 cd m^{-2}, 35.1 cd A^{-1}, and 8.4%, respectively (Figure 21B). Recently, MXene flakes were used to enhance the wire-to-wire adhesion of Ag NWs and interfacial strength with the substrate.[307]

Graphene has also been a promising candidate for flexible TEs. For instance, four-layer methacrylate-doped p-type graphene films (4LGs) were used as an anode to develop flexible PeLEDs.[552] The buffer HIL, consisting of PEDOT:PSS and PFI, was used to regulate the energy level of the device, with the work function of the buffer HIL gradually increasing from the bottom to the top surface (from ~5.2 eV to ~5.95 eV). The flexible PeLED fabricated with a 4LG/buffer HTL/$MAPbBr_3$/1,3,5-Tris(1-phenyl-1H-benzimidazol-2-yl) (TPBi)/LiF/Al structure exhibited a maximum current

https://doi.org/10.1021/acs.chemrev.3c00548
Chem. Rev. XXXX, XXX, XXX−XXX

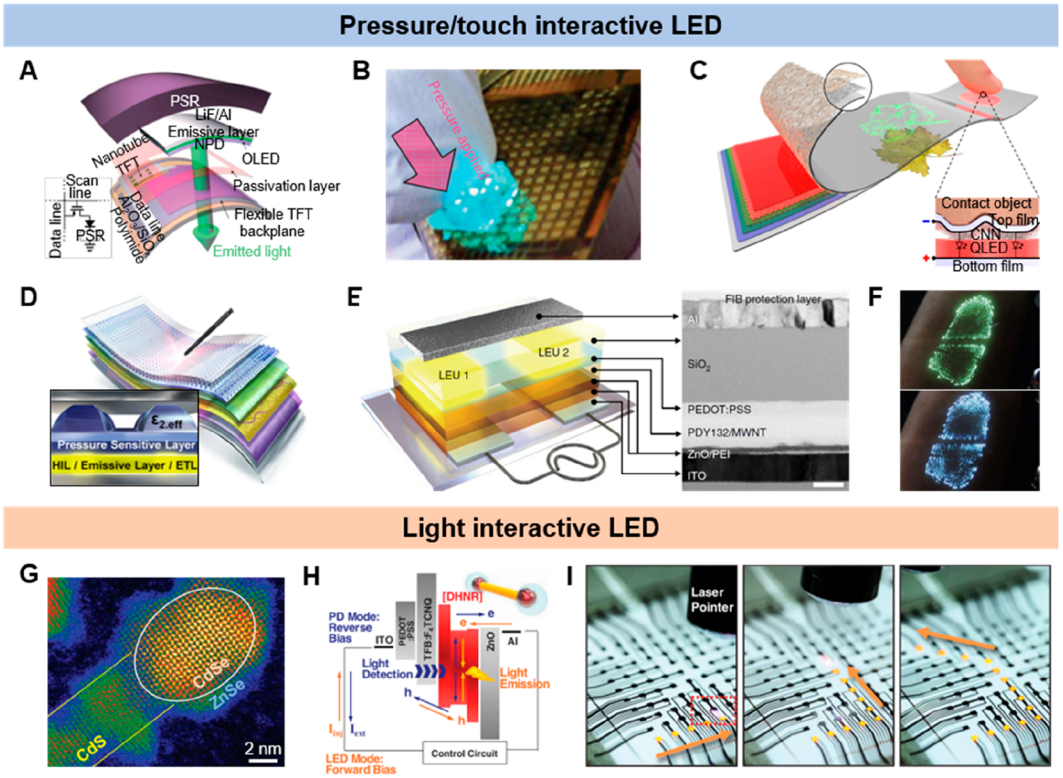

Figure 22. Interactive displays. (A) Schematic layout of a pixel of user-interactive AMOLED. (B) Photograph of a 16 × 16 interactive display visualizing the pressure through lighting pixels. Reproduced with permission from ref 559. Copyright 2013 Springer Nature. (C) Schematic illustration of ultraflexible and transparent interactive QLED using piezoresistive layer. Reproduced with permission from ref 562. Copyright 2020 Springer Nature. (D) Device architecture of field-driven interactive light-emitting device. Reproduced with permission from ref 563. Copyright 2018 American Chemical Society. (E) Schematic of a field-driven light-emitting device with parallel electrodes. Right is cross-sectional TEM image of the device. (F) Photographs of EL images of fingerprint under gentle finger contact. Scale bar in inset indicates 100 nm. Reproduced with permission from ref 565. Copyright 2017 Springer Nature. (G) STEM image of DHNR. (H) Energy band diagram of DHNR-LED along with directions of charge flow for light emission (orange arrows) and detection (blue arrows). (I) Photographs of a light interactive LED array illuminating along the path of laser point. Reproduced with permission from ref 939. Copyright 2018 John Wiley and Sons, Inc.

efficiency and EQE of 18.0 cd A^{-1} and 3.8%, respectively, which was higher than that achieved using an ITO electrode.

Kirigami/origami architecture approaches can be employed to convert 2D devices into 3D structures. In 2021, an ultrathin QLED display was developed into a 3D foldable device using folding and cutting lines formed via laser patterning.[109] An Ag−Al alloy etch-stop layer was coated on top of the QLED encapsulation layer to protect the active layers from over-etching, followed by a thick epoxy overcoating layer (Figure 21C). A microsecond-pulsed CO_2 laser with controlled energy was then used to etch the overcoating epoxy where folding was desired, making it easier to fold since the etched part of the device was thinner than the surrounding parts. With this technology, the 13 μm ultrathin QLED, capable of forming a bending radius of 1.421 mm without etching, could be sharply folded to a radius of 0.047 mm at 70% compressive strain (Figure 21D, left). Based on this technique, preprogrammed ultrathin QLEDs and 8 × 8 PM arrays could be folded into various 3D architectures (Figure 21D, right).

The prestrained approach using the ultrathin device technique can also be applied to fabricate stretchable QLEDs and PeLEDs. In 2015, an ultrathin QLED with a total thickness of ∼2.6 μm was demonstrated to exhibit stretchable features and was used as a wearable electronic tattoo.[490] The device was constructed using a parylene and epoxy bilayer substrate and encapsulation, enabling the active layers (ITO/PEDOT:PSS/TFB/QD/ZnO/LiAl) to be located near the neutral mechanical plane and protected from oxygen and water. The ultrathin device could be affixed to various curved surfaces such as human skin, round glass, and slide glass, and it could withstand deformations such as bending, folding, and crumpling without suffering mechanical fractures. Additionally, an ultrathin transparent QLED was also fabricated,[148] featuring an Al_2O_3 layer on the ETL to protect the active layers during top ITO sputtering and balance the charge-injection. The device had a total thickness of 2.7 μm, including a 1.2 μm thick parylene/epoxy double layer encapsulation (Figure 21E), which was thin enough to form wavy structures. The wrinkled ultrathin device could tolerate 50% of prestretching without breaking (Figure 21F), as the active layer located near the neutral mechanical plane received a peak strain less than the fracture strain of ITO (∼2.2%). A similar technique was used to create a wrinkled ultrathin PeLED,[553] which was adhered to a wrinkled surface of an elastomer by releasing the prestretching. The bottom electrode was composed of an Ag NWs network embedded in a PI film with a thickness of 1−2 μm. The electrode exhibited a low surface roughness of 0.765 nm and exceptional mechanical stability, maintaining a continuous sheet resistance between 18 and 26 Ω $\square^{-1}$ after 10,000 cycles of 0−50% strain. An ultrathin PeLED was then fabricated on top of the ultrathin electrode, with the structure of PEDOT:PSS/4,4′-cyclohexylidenebis[N,N-bis(4-

https://doi.org/10.1021/acs.chemrev.3c00548
Chem. Rev. XXXX, XXX, XXX−XXX

methylphenyl)benzenamine]-doped poly(N-vinyl carbazole)/perovskite QDs/TPBi/cesium fluoride/Al. The resulting wrinkled ultrathin device, which was fabricated by adhesion on a prestreched elastomer substrate with the desired strain, showed stretchability of 50% and endured 1,000 continuous stretch-release cycles with 0−20% strain (Figure 21G).

Despite the superior electrical and optical properties of the inorganic nanomaterials, the desirable device-level characteristics, particularly in the context of deformable device applications, have been mainly achieved by using materials containing toxic chemical substances, such as cadmium-based QDs and lead halide perovskites. Extensive efforts have been devoted to obtaining heavy-metal free LEDs to keep up with the highest device performance, through the utilization of InP QDs,[460] Zinc chalcogenide QDs,[462] Sn-based perovskite,[911] and Cu-based perovskite.[912] Indeed, the incorporation of heavy-metal free nanomaterials in deformable displays can be of paramount significance for human-friendly and user-interactive electronics applications.

4. REPRESENTATIVE HUMAN-CENTRIC APPLICATIONS OF FLEXIBLE AND STRETCHABLE LEDS

As electronic devices become more involved in our daily lives, there is a growing demand for flexible and stretchable devices with user-interactive capabilities. LEDs, serving as lighting elements, can function as a light source in optoelectronic sensors and emissive pixels in displays. Consequently, by incorporating additional components such as transistor arrays, circuitry components, and sensor units, flexible and stretchable LEDs can be effectively utilized in the development of user-interactive applications.[554−558] The deformable feature of these devices contributes to improved wearability and conformability, thereby enhancing user comfort and adaptability to various functions. This section will present notable examples of user-interactive applications utilizing flexible and stretchable LEDs, focusing on display and biomedical applications.

4.1. Display Applications

4.1.1. Interactive Displays. The flexible and stretchable displays, due to their deformable properties, can be incorporated onto various surfaces, including the human body, allowing for numerous functions that were previously unattainable with traditional rigid displays. To create a wearable and patchable HMI, performing multifunctional tasks rapidly and precisely in compact and lightweight design has become crucial for displays. Hence, the idea of an interactive display that can instantly visualize external stimuli from the user has increasingly received attention. In 2013, the development of the first user-interactive AM-OLED display was reported, which could spatially map applied pressure and visualize the response.[559] This was achieved by laminating a pressure sensitive rubber (PSR) on top of a flexible AM array built from CNT TFT AM backplanes and OLED pixels with a PI substrate (Figure 22A). Conductive silver ink was applied as the ground electrode on top of the PSR layer. When pressure was applied to the PSR, conductive carbon NPs inside the rubber contacted each other, reducing the resistance between the cathode of the OLED and the ground electrode, resulting in a current flow that turned on the OLEDs. User-interactive 16 × 16 flexible pixel arrays with different colors of red, green, blue, and yellow were successfully demonstrated, where the pressure profile was visualized by the pressure-responsive lighting of the individual pixels (Figure 22B).

Interactive displays that can respond to mechanical stimuli, such as pressure and strain, have been continuously investigated.[560] For the vertical-type device (vertically stacked active layer between two electrodes), an intermediate layer can be inserted within the device. This can help control the physical contact between the electrical layers and hence modulate the electrical contact. For example, a spacer was integrated to separate the top Ag NWs electrode and the $MAPbBr_3$:PEO active layer to fabricate a touch responsive PeLED that utilized a pressure-induced local Schottky contact to emit light.[561] In another study, a piezoresistive layer was inserted as a pressure-sensing film into a flexible QLED to achieve pressure-responsive electrical contact.[562] A cellulose/NW nanohybrid nanonetwork (CNN) where the cellulose nanofibers encircled each tellurium-poly(3,4-ethylenedioxythiophene):poly(styrenesulfonate) NW, was developed, enabling uniform and ultrathin random networks that could vary the contact resistance depending on the applied pressure (Figure 22C). Accordingly, the QLED incorporating such a CNN showed a fast response (<1 ms) to pressure and super-resolution (>1,000 dots per inch) pressure distribution. In the case of field-driven light-emitting devices, a capacitive pressure sensing layer could be inserted between the electrode and the EML.[563] Subsequent to the sequential deposition of ITO, ZnO, PEI, EML, and PEDOT:PSS layers onto the PET substrate, an ionic gel layer with micropyramids was transferred onto the assembly to function as a pressure-sensitive layer, and top ITO/PET electrodes were positioned on top of it (Figure 22D). An ionic gel with micropatterned pyramidal structures showed increased capacitance under deformation due to the decreased thickness of the pressure-sensing layer from the collapsed pyramidal structure and an increased effective dielectric constant from the increased contact area (Figure 22D). As a result, an AC field-driven EL pressure-sensing display could visualize both static and dynamic pressure information.

Parallel-type field-driven light-emitting devices (active layers on two parallel electrodes) have also been demonstrated as interactive displays.[564] When a conductive object is placed on top of the active layer, the in-plane electric field between the parallel electrodes is transformed into a vertical field, resulting in light emission under an AC field. This principle was applied to create an interactive organic light-emitting board that directly translates the touch of a conductive object into light.[565] Inverted OLED layers were coated on the two parallel electrodes, and a SiO_2 layer was deposited to enable field-driven hole injection by separating the PEDOT:PSS layer from the top electrode (Figure 22E). Any conductive material such as PEDOT:PSS ink, Ag paste, metal-coated structural stamps, and liquid metal could be used as the top electrode to induce light emission. The natural conductivity of the human finger could even be utilized, displaying fingerprints (Figure 22F). Based on this principle, various sensing layers can be incorporated into the device to induce a vertical electric field and obtain interactivity with different stimuli such as liquid, temperature, and magnetic fields.[566−568]

To achieve interactive properties in LEDs, new materials with multiple functionalities can be utilized as EMLs. In general, heterostructure QDs have been used in EL and photovoltaic applications, with type I and II band compositions being advantageous for charge recombination and

https://doi.org/10.1021/acs.chemrev.3c00548
Chem. Rev. XXXX, XXX, XXX−XXX

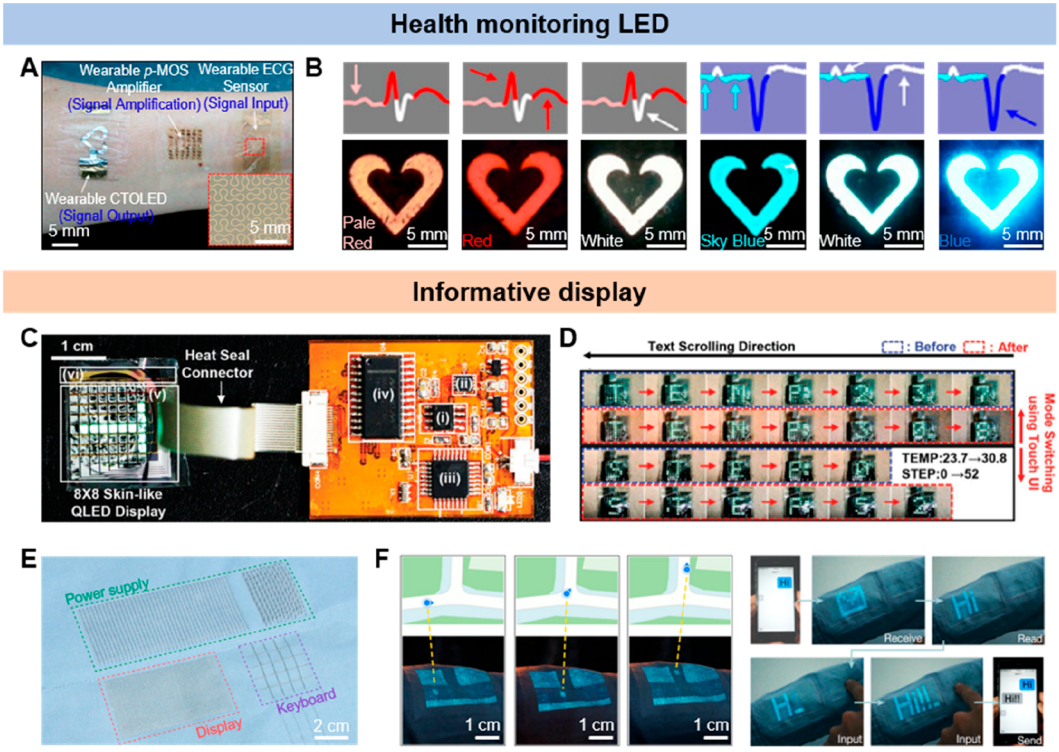

Figure 23. Display integrated systems. (A) Photograph of the wearable system for real-time visual monitoring of the ECG signals through color-tunable ultrathin OLEDs. (B) Color changes of the OLED synchronized with the shape of the measured normal ECG signals (red region) and abnormal ECG signal (blue region). Reproduced with permission from ref 119. Copyright 2017 American Chemical Society. (C) Ultrathin QLED display integrated with the wearable electronics. (D) Photographs of wearable QLED display visualizing the measured temperature and pedometer information. Reproduced with permission from ref 575. Copyright 2017 John Wiley & Sons, Inc. (E) Photograph of an integrated textile system consisting of display, keyboard, and power supply modules. (F) Device operation photographs showing real-time location (left) and receiving and sending messages between the integrated textile system and a smartphone (right). Reproduced with permission from ref 576. Copyright 2021 Nature.

separation, respectively. Double-heterojunction nanorods (DHNRs) possess both type I and II band structures and can serve as both charge-separation and recombination centers (Figure 22G).[569] By simply reversing the bias direction, an LED fabricated with DHNRs can function as both a light-emitting and light-detecting device (Figure 22H). This characteristic was utilized to create a light-responsive interactive display with a 10 × 10 pixel array by connecting it to a circuit board programmed to supply a forward bias when detecting incident light at zero bias (Figure 22I). Additionally, an energy-harvesting display that can charge and light itself was demonstrated, with the LED being driven by a charged supercapacitor during the photovoltaic mode.

4.1.2. Integrated Systems. The display shows various types of information from electrical devices as optical outputs. Flexible and stretchable displays can be integrated with sensors, PDs, power sources, or antennas to serve as an HMI that displays biosignals detected from the sensors.[19,570−573] Koo et al. demonstrated wearable health monitoring OLEDs that visualized the electrocardiogram (ECG) signals obtained from a skin-mounted electrode and signal amplifiers (Figure 23A).[119] The ultrathin OLEDs contained an electron blocking layer, bis[2- (diphenylphosphino)phenyl]ether oxide, between two phosphorescent layers, one blue and the other red, to allow for color tuning based on the working voltage. The electron blocking layer prevented electron flow in the low-voltage regime (5−7 V) but allowed it in the high-voltage regime (11−13 V), resulting in red and blue recombination, respectively. The collected cardiac signals from skin-mounted ECG sensors were amplified through CNT signal amplifiers. Then, signals were processed through a data acquisition unit and computer to deliver the adjusted voltage to the OLEDs. For the real-time ECG monitoring system, software was designed to deliver a voltage that corresponded to pale red, red, and white (5−9 V) for normal signals and white, sky blue, and deep blue (10−13 V) for abnormal signals (Figure 23B). Son et al. reported the fabrication of a fully self-healable and stretchable ACEL display that monitored signals from strain and ECG sensors.[574] The sensors and electrodes for the display were fabricated using stretchable conductors made of Ag NWs and self-healable polymer. An emissive layer was created using a composite of self-healable polymer and EL phosphors. The integrated electronic skin system wirelessly transmitted data collected from the sensors to the display. Each peak of the ECG signals was depicted as the blinking of a heart-shaped pixel, while the heart rate and strain were divided into five regions, which were mapped by lighting each pixel of the five bars on the display. In 2022, intrinsically stretchable PLEDs were integrated with an energy-harvesting system for wireless operation and showed real-time pulse signals by repeatedly blinking.[447]

To enrich the information being delivered, matrix array displays can be used to deliver signals in the form of detailed information, such as text or images, rather than just simple lighting. Kim et al. reported the fabrication of an ultrathin QLED display (~5.5 μm) which could withstand an extreme

https://doi.org/10.1021/acs.chemrev.3c00548
Chem. Rev. XXXX, XXX, XXX−XXX

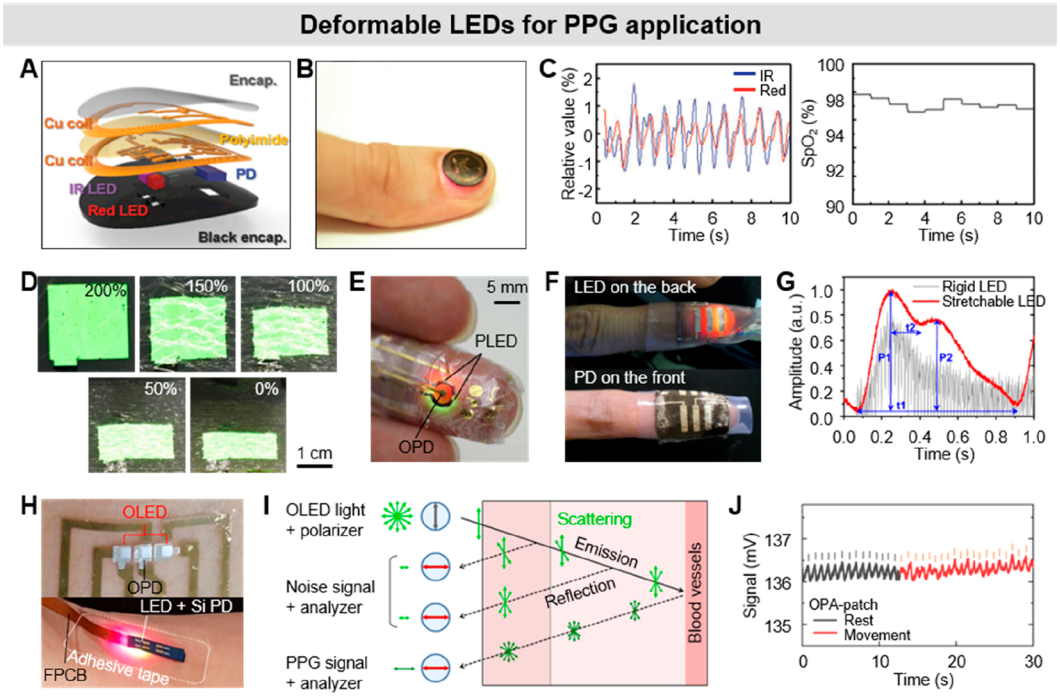

Figure 24. Flexible LEDs in PPG sensors. (A) Schematic illustration of millimeter-scale, NFC enabled pulse oximeter device. (B) Image of an operating device mounted on a thumbnail. (C) Relative values of red and IR signal (left) and calculated SpO_2 (right) from the fingernail. Reproduced with permission from ref 584. Copyright 2016 John Wiley & Sons, Inc. (D) Images of ultrathin PLED during the stretching adhered to a prestretched elastomer. (E) Photograph of an ultraflexible ppg sensor attached on a finger. Reproduced with permission from ref 585. Copyright 2016 American Association for the Advancement of Science. (F) Skin-mounted ppg sensor composed of ultrathin QLED and PD wrapped around the finger. (G) Real-time PPG signal pulse wave. Reproduced with permission from ref 586. Copyright 2017 American Chemical Society. (H) Photograph of stretchable patch-type organic PPG sensor. Reproduced with permission from ref 121. Copyright 2021 American Association for the Advancement of Science. (I) Reflected light in a sensor with an orthogonal polarizer-analyzer (OPA). (J) PPG signal from a patch-type OPA ppg sensor at rest and during the wrist movement. Reproduced with permission from ref 174. Copyright 2022 American Association for the Advancement of Science.

bending radius of 68 μm and 1,000 cycles of repeated bending.[575] As shown in Figure 23C, the display (v) with a capacitive touch sensor (vi) was incorporated into a skin-attachable wearable system equipped with a microcontroller unit (MCU) (iii), an LED driver (iv), a temperature sensor (i), and an accelerometer (ii) on a flexible printed circuit board. The MCU processed the data collected by sensors, calculated the step counts, and monitored the resistive-capacitive delay of the pressure sensor. As a result, an 8 × 8 PM display transmitted the real-time temperature and step count information from the sensors through scrolling text, with the touch sensor serving as the user interface to change the sensing modes (Figure 23D). In 2021, a standalone real-time health monitoring patch was reported, combining a battery, processing module, and health monitoring sensor to display the heart rate information through a stretchable OLED display.[121] Recently, Shi et al. developed a textile display by weaving luminescent warps of silver-plated conductive yarn coated with ZnS phosphor and transparent conductive wefts of ionic liquid-doped PU gel fiber.[576] This display was integrated with a woven keyboard, solar-cell energy harvesting, and energy storage modules, which served as the user interface and power supply, respectively (Figure 23E). The display driver, MCU, and Bluetooth module were used in the system to process electrical signals (Figure 23F). Through a connection with an MCU and a Bluetooth module, the textile display was capable of providing real-time location information, serving as a communication tool, and expressing detected electroencephalogram signals (Figure 23G). Choi et al. fabricated a textile display by weaving LED fibers mounted with 84 × 76 × RGB LEDs onto copper and cotton fibers.[577] Six input devices, including a radio frequency antenna, PD, touch sensor, temperature sensor, biosensor, and energy storage module, were fully fabricated and assembled into the textile platform to demonstrate a smart textile display system.

4.2. Biomedical Applications

4.2.1. Photoplethysmogram Sensors. A PPG sensor[578−580,173] is a prevalent noninvasive health monitoring tool that uses LEDs and PDs to measure the changes in blood volume during cardiac activities. The PD detects the transmitted or reflected light irradiated from the LED, with changes in light intensity occurring due to absorption by the blood vessels. The PPG sensor can continuously monitor vital signals such as heart rate, respiratory rate, oxygen saturation, blood pressure, and cardiac cycle. However, conventional rigid light sources and sensors can cause discontinuities or distortions due to motion artifacts from changes in contact between the PPG sensor and skin.[581−583] To address this issue, flexible and stretchable LEDs and PDs have been developed to achieve conformal contact with the body. To enable mounting on any location of the body, including fingernails, a flexible miniaturized battery-free wireless wearable device was developed.[584] To minimize its size, red and infrared (IR) mini-LED chips with narrowband spectral output were selected. The electronic components, including LEDs, PD,

https://doi.org/10.1021/acs.chemrev.3c00548
Chem. Rev. XXXX, XXX, XXX−XXX

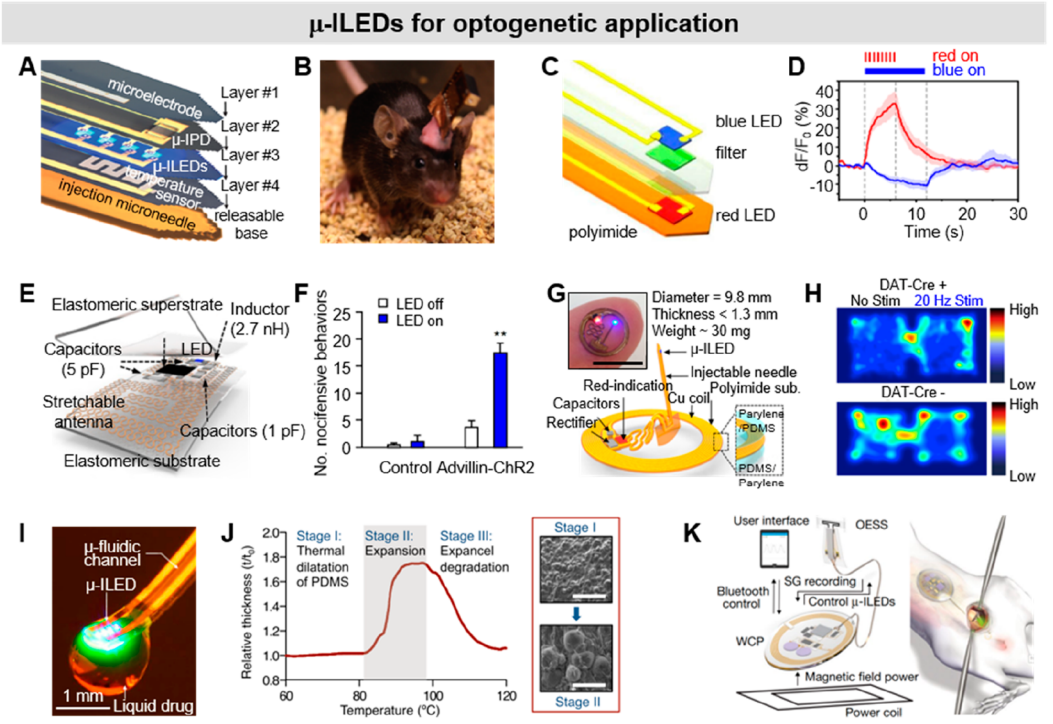

Figure 25. Optogenetics based on flexible/stretchable LEDs. (A) Layout of a multifunctional, implantable optoelectronic device. The system includes a layer for electrophysiological measurement, optical measurement, optical stimulation, and temperature sensing, all bonded to structural support layer. (B) Image of mouse with lightweight, flexible wireless systems. Reproduced with permission from ref 601. Copyright 2013 American Association for the Advancement of Science. (C) Schematic of the dual-color LED probe consisting of vertically stacked blue and red thin film μ-ILEDs with a thin film filter assembled on a flexible PI substrate. (D) Traces of dopamine signals responding to stimulations by red LED (n = 4 mice) and blue LED (n = 4 mice). Reproduced with permission from ref 602. Copyright 2022 Springer Nature. (E) Schematic illustration of the component of miniaturized, fully implantable, soft optoelectronic systems for wireless optogenetics. (F) Number of nocifensive behaviors (flinching, hind paw licking, jumping) when activating the sciatic LED stimulator in Advillin-ChR2 mice but not in controls. Reproduced with permission from ref 603. Copyright 2015 Springer Nature. (G) Schematic illustration of the overall construction of thin, flexible wireless optoelectronic implants. Inset image shows a picture of a completed device on top of fingertip. Scale bar in inset indicates 10 mm. (H) Heatmap showing real-time mouse behavior following 20 Hz photostimulation. There is a chamber preference during stimulation (top) and no observable difference during no stimulation (bottom). Reproduced with permission from ref 604. Copyright 2017 Elsevier. (I) Picture of optofluidic neural probe during simultaneous drug delivery and photostimulation. (J) Thickness variation of thermally expandable composite material as a function of temperature. Right SEM images show the expansion of microspheres at 110 °C. Scale bars in inset indicate 100 μm. Reproduced with permission from ref 605. Copyright 2015 Elsevier. (K) Schematic illustrations of a fully implantable, soft optoelectronic system for wireless, closed-loop optogenetic modulation of bladder function. Right illustration shows the placement of the strain gauge around the bladder and wireless control and power module anterior to the bladder. Reproduced with permission from ref 126. Copyright 2019 Springer Nature.

NFC, MCU, and amplifier, were built in the middle of the millimeter-scale bilayer loop antenna and located near the mechanical neutral plane to tolerate applied mechanical stress (Figure 24A). The complete system had a diameter of ~10 mm, a thickness of ~0.9 mm, and a bending radius of 3 mm, making it suitable for detection at the fingernail and earlobe (Figure 24B). As a result, extracted red and IR PD signals could successfully show physiological changes, including heart rate and SpO_2 level (Figure 24C).

The human skin has much more complex surface topologies than a simple curvilinear structure, and thus achieving high conformability is important. To maximize the biotic-abiotic interface quality, ultrathin PLEDs with a total thickness of 3 μm and a bending radius of less than 100 μm were employed as the light source for PPG sensors (Figure 24D).[585] An ultrathin passivation layer, composed of alternating layers of SiON and parylene, was developed to protect the organic optoelectronic devices from oxygen and water and to position the active layer in a neutral strain position. As a result, an ultraflexible PPG sensor equipped with green and red PLEDs and organic PDs (Figure 24E) was developed, demonstrating a distinct signal detection with amplitudes of 100 to 200 mV and exhibiting little noise, good repeatability, and durability in air for 4 days. Similarly, an ultrathin stretchable QLED was utilized as the light source for a PPG sensor (Figure 24F).[586] For comparison, a stretchable LED and an ITO-based rigid LED were employed to record the pulse wave under the same conditions, with a luminous intensity of 520 cd m^{-2}. In contrast to the rigid LED, the combination of wrinkled QLEDs and PDs detected distinguishable peaks: the incoming blood wave ejected by left ventricular contraction and the reflected wave from the venous plexus at the distal end of the body. This represented peak (P_2/P_1) and time ratios (t_2/t_1) of 75% and 19%, respectively (Figure 24G).

A conformal fit of a patch-type PPG sensor can effectively reduce the motion artifacts and improve measurement accuracy. Lee et al. reported on the development of a standalone health monitoring patch based on organic optoelectronic devices (Figure 24H).[121] The optoelectronic device layers were deposited on a photopatterned stretchable interconnector layer, which was placed above the sacrificial layer, stress relief layer, and stretchable substrate. The thin

https://doi.org/10.1021/acs.chemrev.3c00548
Chem. Rev. XXXX, XXX, XXX−XXX

encapsulation layer consisted of 1.5 μm of poly-(tetrafluoroethylene-*co*-2,2,4-trifluoro-5- trifluoromethoxy-1,3-dioxole) and 100 nm of Al_2O_3, resulting a total thickness of 15 μm. The inclusion of a stress relief layer and stretchable interconnects helped relieve the stress near the device, enabling the stretchable PPG sensor to detect cardiac cycle waveforms with systolic pressure (SP) and diastolic pressure (DP) peaks.

Though the skin-attachable sensor can enhance the contact between the sensor and skin, motion artifacts caused by the temporal change in light scattering from skin tissues can still distort the PPG signals. To overcome this issue, researchers have developed a skin-attachable PPG sensor with an orthogonal polarizer-analyzer (OPA) pair, which reduces motion artifacts by suppressing the amount of light scattered from the skin epidermis.[174] Most light reflected from the skin is scattered at shallow depths from the skin surface, leading to time-dependent variations in the signal with movement. By using polarized light, the reflected light from the small depths of the skin surface is biased in the initial direction, while light reflected from blood vessels has sufficiently dispersed polarization, enabling the selection of the signal by the orthogonal polarizer located at the PD (Figure 24I). To achieve this, a stretchable patch-type PPG sensor was fabricated using two OLEDs and an organic PD with stretchable cracked Au interconnectors on a polarizer-embedded substrate. Even after attaching the sensor to the inner wrist, where the skin movement is relatively large, the OPA-containing device was able to reduce the motion artifacts by over 90% (Figure 24J).

4.2.2. Optogenetics. The optical methods for diagnosis and treatment offer superior spatial controllability and target selectivity compared to alternative methods like electrical stimulation and chemotherapy.[587] However, effective delivery of light in deep regions within the body poses challenges due to the strong scattering and absorption of light by biological tissues. Consequently, the direct internal injection of light sources to the targeted location has proven to be an effective and reliable approach. Traditionally, *in vivo* light delivery involved the use of optical fibers inserted into tissues.[588−590] However, recently, wireless optoelectronic devices, including LEDs, antenna coils, and other electronic components fabricated with biocompatible materials, have been directly implanted to circumvent issues such as soft-tissue damage and motion artifacts.[146,591−593] Among the light sources, thin film μ-ILEDs are particularly advantageous as implantable light delivery systems compared to conventional LEDs. They possess several key attributes, including low bending stiffness (13−18 N m^{-1}), small size (<100 μm), high brightness, long lifetime, high stability, low power consumption, and easy integration with other electrical components. These characteristics enable spatially precise delivery of photons, minimized tissue damage and inflammation, minimal heat generation, and long-term operation, making them highly efficient for implantable light-delivery systems.[913,914]

The μ-ILEDs for implantable optogenetic applications[594−596] have an ultrathin and flexible form, allowing them to conform to the soft surfaces of organs without causing damage. These devices are operated through a wireless powering unit.[597,598] Wireless activation is typically achieved using radiofrequency (RF) energy,[599] where the energy harvested by an antenna is converted into a current through rectifiers or inductive coupling[600] via receiver-transmitter coil alignment. Additional electrical components can be incorporated for multifunctional operation. In 2013, an optogenetic device including arrays of GaN μ-ILEDs, platinum μ-electrodes, platinum resistors, and silicon photodiodes, each serving as optical stimulation, electrophysiological change measurement, temperature sensing, and photodetection, respectively, was reported (Figure 25A).[601] The cellular-scale μ-ILED (6.45 μm thick, 50 × 50 $μm^2$) was epitaxially grown on sapphire and integrated to the strips through transfer printing. A wireless power module based on RF scavenging was mounted on the head of mouse (Figure 25B). The device was implanted into the dopaminergic neurons of the ventral tegmental area in freely moving mice to target ChR2(H134)-eYFP. As a result of target intervention, the mice exhibited behavior indicative of self-stimulation of dopamine. In another research, a dual-color optoelectronic probe was developed to enable bidirectional manipulation of neural activity, consisting of stacked blue GaN and red InGaP μ-ILEDs with a thin film filter interface (Figure 25C).[602] The μ-ILEDs were grown through epitaxial lift-off and assembled through transfer printing. The devices had dimensions of 125 × 180 $μm^2$ and a thickness of ∼5−7 μm, which were designed to target a large nucleus while avoiding tissue heating that can occur due to reduced efficiency of smaller devices. The emission peaks of μ-ILEDs at 630 and 480 nm were in good accordance with the excitation spectra of ChrimsonR and stGtACR2, respectively. When implanted in the ventral tegmental area of a mice, the μ-ILED interfered with dopaminergic neurons, inducing either increased (red) or decreased (blue) dopamine signals (Figure 25D). This effect was clearly demonstrated through mice behavior experiments, which included assessments of rewarding and aversive behaviors and the analysis of social interactions among multiple mice.

To address the challenges posed by bulky external wireless power systems, researchers have developed fully implantable, miniaturized devices with lightweight characteristics. Park et al. reported a thin, soft, and lightweight (16 mg) optoelectronic device with a stretchable wireless RF power and control system.[603] The stretchable antenna and μ-ILEDs were connected through serpentine Ti/Au electrical interconnects that enabled the capture of RF power through capacitive coupling. Subsequently, rectification and voltage multiplication were employed using miniaturized diodes to drive the μ-ILED (Figure 25E). The low elastic modulus of the devices allowed for their implantation both as a stretchable film, facilitating direct interfacing with peripheral nerves, and as a flexible filament, enabling insertion into the narrow spaces of the spinal epidural region. In both cases, when these devices were implanted in mice, they successfully activated the peripheral and spinal pain circuit in freely moving mice through wireless activation of ChR2 expressed in nociceptive pathways. This resulted in spontaneous pain behaviors (Figure 25F) and place aversion. In other research, an optogenetic device with a diameter of 9.8 mm, a thickness of less than 1.3 mm, and a weight of ∼30 mg was developed.[604] The device incorporated a flexible magnetic coil antenna, a rectifier, and indicator μ-ILEDs (red) connected to blue μ-ILEDs. The device was designed to be implanted using an injectable needle (Figure 25G), allowing for targeted deep brain stimulation. The red μ-ILEDs served as an externally visible signal to indicate the system activation, while the blue μ-ILEDs acted as the light source for optogenetic stimulation. A mesolimbic dopaminergic pathway was specifically targeted to evaluate the reliability and effectiveness of wireless stimulation. The results demonstrated that wireless stimulation of dopaminergic

https://doi.org/10.1021/acs.chemrev.3c00548
Chem. Rev. XXXX, XXX, XXX−XXX

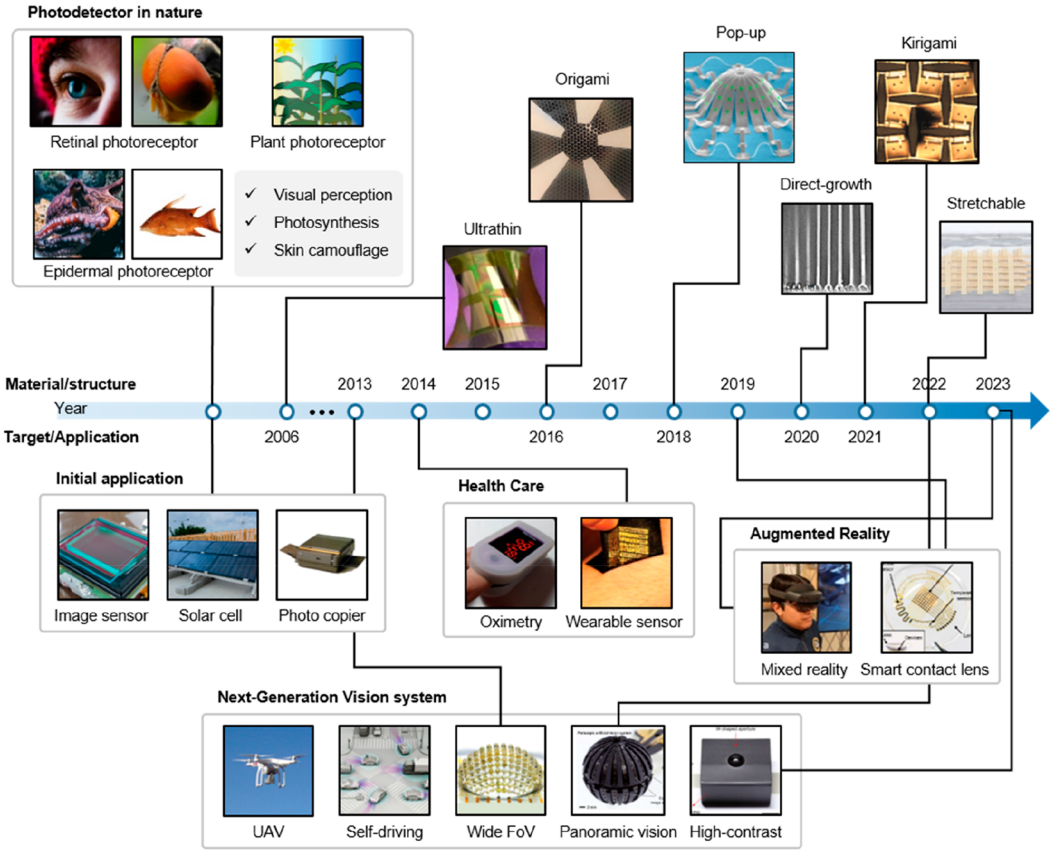

Figure 26. Timeline of the development of flexible/stretchable PDs. Human's photoreceptor. Reproduced with permission from ref 893. Copyright 2015 Springer Nature. Insect's photoreceptor. Reproduced with permission from ref 894. Copyright 2012 Optica Publishing Group. Plant photoreceptor. Reproduced with permission from ref 895. Copyright 2019 Springer Nature. Octopus's epidermal photoreceptor. Reproduced with permission from ref 896. Copyright 2022 American Association for the Advancement of Science. Hogfish's epidermal photoreceptor. Reproduced with permission from ref 897. Copyright 2018 Springer Nature. Vision system for self-driving. Reproduced with permission from ref 898. Copyright 2023 John Wiley & Sons, Inc. Vision system for Unmanned Aerial Vehicle (UAV). Reproduced with permission from ref 899. Copyright 2018 John Wiley & Sons, Inc. Photocopier. Reproduced with permission from ref 940. Copyright 2014 Springer Nature. Solar cell. Reproduced with permission from ref 900. Copyright 2022 Springer Nature. Image sensor. Reproduced with permission from ref 901. Copyright 2019 Optica Publishing Group. Oximetry. Reproduced with permission from ref 902. Copyright 2022 John Wiley & Sons, Inc. Mixed reality device. Reproduced with permission from ref 903. Copyright 2023 Springer Nature. Ultrathin PD. Reproduced with permission from ref 904. Copyright 2018 American Chemical Society. Origami image sensor. Reproduced with permission from ref 889. Copyright 2016 Springer Nature. Wide field vision. Reproduced with permission from ref 835. Copyright 2013 Springer Nature. Wearable sensor. Reproduced with permission from ref 647. Copyright 2014 Springer Nature. Krigami image sensor. Reproduced with permission from ref 667. Copyright 2021 Springer Nature. Pop-up image sensor. Reproduced with permission from ref 669. Copyright 2018 Springer Nature. Flexible perovskite image sensor. Reproduced with permission from ref 905. Copyright 2020 Springer Nature. Stretchable image sensor. Reproduced with permission from ref 208. Copyright 2022 Springer Nature. Smart contact lens. Reproduced with permission from ref 750. Copyright 2019 Springer Nature. H/W HDR vision. Reproduced with permission from ref 840. Copyright 2020 Springer Nature. Panoramic vision. Reproduced with permission from ref 12. Copyright 2022 Springer Nature.

neurons in the ventral tegmental area or nucleus accumbens led to a promotion of rewarding and reinforcing behaviors. This was confirmed through experiments such as stimulation-paired chamber preference (Figure 25H) and self-stimulation via nose poke responses.

The lightweight and miniaturized wireless optogenetic device can also be incorporated into biohybrid robots, which are comprised of artificial materials serving as the mechanical framework and living cellular components for actuation. Leveraging its capability for high spatiotemporal resolution and cell-type specificity, optogenetic-based control has been applied in various contexts, including cardiomyocytes,[915] skeletal muscle tissue,[916,917] and neuromuscular tissue.[918] Kim et al. presented a wirelessly controlled biohybrid robot propelled by a battery-free optoelectronic device with wireless communication capabilities.[919] In this system, 3D-engineered skeletal muscle tissue was formed around an asymmetric hydrogel scaffold. Under illumination by μ-ILEDs, the muscles underwent cyclic contractions, deforming the scaffold, and locomoting the robot through asymmetric friction. Through computational design and the independent stimulation of multiple skeletal muscles, centimeter-scale walking robots successfully attained the capability to execute commands for functions including walking, turning, plowing, and transportation.

The integration of wireless optogenetics with pharmacology has been achieved through the development of a wireless optofluidic probe.[605] The probe was integrated with ultrathin and soft microfluidic drug delivery modules and μ-ILED arrays (Figure 25I). The GaN μ-ILEDs featured lateral dimensions of 100 × 100 μm^2 with a thickness of 6.54 μm, chosen to enable spatially and temporally precise light transmission to the exits

https://doi.org/10.1021/acs.chemrev.3c00548
Chem. Rev. XXXX, XXX, XXX−XXX

Table 6. Characteristics of Flexible and Stretchable Photoresponsive Devices with Classification on the Materials Type and Device Fabrication Methods

Classification		Active material	Device type	Spectra region	On/off ratio (bias)	Detectivity (jones)	# of pixels	Ref.
Nanomaterials	0D	CdSe QD	PC	vis	6×10^3 (0 V)	–	–	705
		PbS QD/Ag NC	PC	UV–vis	16.3 (40 V)	7.1×10^{10}	–	879
		Bilayer PbS QD	PC	vis	152.35 (10 V)	1.71×10^{12}	–	701
		Ag_2Se NP	PC	NIR	6.00×10^2 (5 V)	7.14×10^9	–	706
	1D	Sb_2Se_3	PC	UV–vis	16	–	–	734
		Si/CdS NW	PD	UV–vis–NIR	–	1.3×10^{12}	–	728
		$MAPbI_3$ NW	PD	UV–vis	2.8×10^4 (5 V)	4.16×10^{12}	–	880
		$CsPbI_3$–$CsPbBr_3$ NW	PD	UV–vis	10^3 (5 V)	–	–	881
		Ag-catalyzed GaSb NW	PT	1550 nm	10^4 (0.1 V)	6.7×10^{10}	–	733
		$MAPbI_3$ Nanofibers	PC	UV–vis	207.8 (1 V)	2.23×10^{11}	5 × 5	748
		ZnO NW	PT	UV	3.25×10^5 (1 V)	3.3×10^{17}	–	720
		Si NW	PC	UV–vis	–	9×10^{11}	–	718
		ZrS_3 NB	PC	vis	1.71 (5 V)	–	–	735
	2D	GaS NS	PT	UV	2.94×10^4 (2 V)	10^{12}–10^{13}	–	882
		2D Bi_2O_2Se	PT	vis–NIR	$>10^6$ (0.6 V)	3.0×10^9	3 × 5	883
		Graphdiyne NSs	PEC	UV–vis	–	7.31×10^{10}	–	884
		Ge NM	PD	NIR	1.3×10^3 (−1 V)	–	–	885
		MoS_2/Graphene	PC	vis–NIR	–	–	7 × 8	804
		MoS_2 NS	PC	vis	–	1.8×10^7	–	886
		2DOMCs	PC	UV–vis	100 (10 V)	2.9×10^{11}	–	887
		WSe_2	PT	385–520 nm	2×10^6 (130 mV/dec)	2.63×10^{12} - 1.6×10^{13}	–	888
		$CsPbBr_3$	PC	350–500 nm	–	3.94×10^{12}	10 × 10	764
		$MoSe_2$	PT	vis–NIR	–	1.96×10^{11}	–	765
Structural engineering	Interconnection	Pyronin B/Graphene	PT	∼550 nm	–	–	48	782
		Si	PD	vis	–	–	16 × 16	668
		Si	PD	vis–NIR	>103	–	23 × 23	178
	Krigami/Origami	Si	PD	vis	∼100 (−3 V)	–	32 × 32	667
		Si	PD	vis–NIR	10^3	–	–	889
		Ga_2O_3	PC	UV	$>10^4$ (15 V)	3.3×10^{13}	24	890
		Si	PD	vis	$\sim 10^4$ (−3 V)	–	281	666
		ZnO	PD	UV	13.4 (10 V)	8.14×10^8	–	891
	Pop-up	Si	PD	vis	$>2 \times 10^2$ (4 V)	$>2 \times 10^2$	16 × 16	164
		MoS_2/Graphene	PC	vis	∼427 (3 V)	–	48	669
Organic	–	4HCB	PD	X-ray	–	–	–	892
		PTCDI-C8/TIPS-PEN	PD	UV–vis	10^4–10^5 (0 V)	–	–	790
		TFT-CN	PT	NIR	2.6×10^8 (2.9 V)	3.92×10^{14}	–	791
Hybrid	Inorganic–Organic	CdSe/ZnS QD	PT	vis	–	$\sim 3.8 \times 10^6$	5 × 5 × 3	208
		$MAPbI_3$	PD	vis	–	10^{10}	32 × 32	749
		MoS_2/g-C_3N_4	PC	UV–vis	$\sim 10^4$ (10 V)	4×10^{11}	–	809
		$CH_3NH_3PbI_3$	PD	vis	10^2 (V)	1.35×10^{12}	10 × 10	810
	Mixed-dimensional	ZnO/Graphene	PT	UV	–	–	–	811
		Graphene/GNS/Perovskite	PD	460 - 670 nm	–	$\sim 1.31 \times 10^{13}$	10 × 10	812
		ZnO NW/PbS QD	PT	UV–vis–NIR	–	3.4×10^8	–	747

of the individual microfluidic channels. Each channel of the probe was connected to a distinct reservoir containing an active layer capable of initiating pumping through joule heating induced expansion (Figure 25J). To enable independent control of fluid delivery and optical activation, a battery-powered IR wireless module was developed. The system employed serial communication between a separate IR transmitter and receiver, facilitating programmable activation of individual heaters in the array as well as the μ-ILEDs. In practice, the MCU activated a selected heater for drug delivery and optogenetics upon wireless triggering. In another research, a wireless closed-loop system was implemented in an optogenetic setup by integrating physiological signal monitoring and photostimulation through real-time signal processing to control bladder dysfunction (Figure 25K).[126] The device consisted of various components, including a stretchable strain gauge for measuring bladder activity, a pair of μ-ILEDs for direct optogenetic neuromodulation of the bladder, a base

https://doi.org/10.1021/acs.chemrev.3c00548
Chem. Rev. XXXX, XXX, XXX−XXX

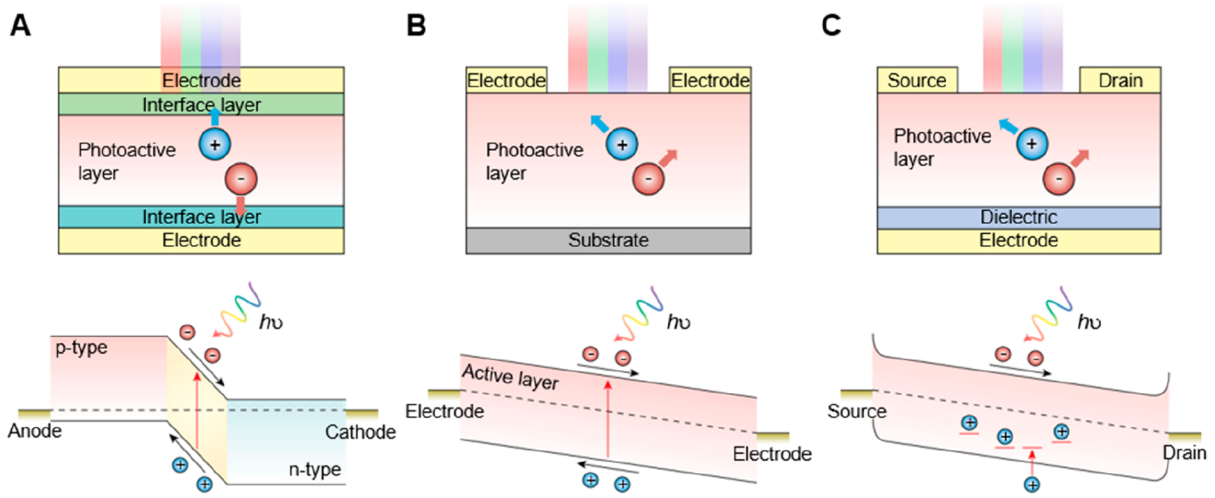

Figure 27. Primary structures of PDs and their working principles. (A) Photodiodes. (B) Photoresistors. (C) PTrs.

station for bidirectional communication and wireless control of the μ-ILED actuators, and a wireless harvesting unit, controlled via customized software. The μ-ILED, emitting 44 ± 11 μW of 540 nm wavelength, were employed to penetrate the entire thickness of bladder wall. The small dimensions of the μ-ILEDs enabled continuous illumination for 1 h with a temperature increase of less than 1 °C in the contacting tissue. The complete closed-loop optogenetic control system could effectively monitor bladder activity by accurately detecting significant decreases in resistance.

5. MATERIALS FOR FLEXIBLE AND STRETCHABLE PDS

The PD is one of the essential components for converting light signals into electronic signals in modern optoelectronic applications, such as biomedical imaging,[613] artificial vision systems,[11,19,614−616] and optical communications.[615−623] Inspired by the photoreceptors in nature, earlier PDs were utilized in various applications (e.g., image sensors, solar cells, and photocopiers). With the rapid growth in wearable devices for healthcare,[624−631] artificial vision systems,[13,632−636] Internet of Things,[577,637,638] and augmented reality,[639,640] the demand for flexible/stretchable PDs has accelerated the development of various fabrication technologies that adopts nanomaterials, hybrids, and structural engineering (Figure 26). To implement flexible/stretchable PDs, the material selection of active materials, electrodes, and substrates is particularly important to ensure sufficient flexibility and optical/electrical performance of the device. For example, soft polymer substrates, such as PET, PDMS, and PI, have been adopted as alternatives to conventional rigid and bulk substrates, providing an elastic platform. Similarly, the nanoscale thinning process and structural design, including serpentine,[641−649] fractals,[650−652] buckling,[653−659] and liquid metals,[660−663] have been explored for developing flexible and stretchable electrodes. For active materials, several approaches, including nanodimensional materials,[664,665] structural engineering,[179,666−670] organic materials[298,671−676] and hybrid composites,[677−685] are introduced to implement the PDs with great flexibility/stretchability and high performance simultaneously. Representative flexible/stretchable PDs with performance parameters are summarized in Table 6.

In this section, recently developed flexible/stretchable PDs are covered in terms of inorganic, organic, hybrid composite active materials, and structural designs. First, three representative PD structures: photodiode, photoresistor, and pTr will be briefly elaborated with their working principles. Then, the flexible/stretchable PDs based on inorganic active materials are covered with regard to two types of fabrication approaches: nanodimensional materials (e.g., 0D, 1D, and 2D) and structural engineering (e.g., kirigami/origami, island-bridge, and pop-up). Next, organic PDs that exhibits intrinsic flexibility and stretchability will be introduced in various photoresponse wavelength range. Lastly, hybrid PDs: inorganic−organic hybrids and mixed-dimensional hybrids (e.g., 0D-1D, 1D-2D, and 0D-2D) will be presented along with representative studies conducted to date.

5.1. Working Principle of PDs

The PDs convert optical signals from incident light into electrical signals, generally based on the photoconductive or photovoltaic effect. The photoconductive effect occurs when absorbed photons induce the generation of extra free carriers, thereby reducing the electrical resistance of the semiconductor.[686,687] Under dim conditions, small dark currents flow between the source and the drain. However, when the semiconductor absorbs photons under illumination, the greater photon energy than the bandgap generates electron−hole pairs, and the free electrons and holes drift. As a result, the net photocurrent increases, leading to a reduction in device resistance. The photogating effect is a particular case of the photoconductive process, which is evoked by photogenerated carriers trapped in localized states on defects or material surfaces.[688,689] Since the photogenerated carriers can recirculate multiple times inside the channel before undergoing recombination, the device that produces the photogating effect typically yields high gain but slower response speeds. Meanwhile, the photovoltaic effect is a prevalent working mechanism in optoelectronic devices, including photodiodes. The photocurrents are generated by the separation of electron−hole pairs, which occurs due to an internal electric field within PN junctions or Schottky junctions. Alternatively, they can be produced by an external electric field when an applied bias voltage is present. The PDs (e.g., photodiodes), operating with the photovoltaic effect, exhibit low dark

https://doi.org/10.1021/acs.chemrev.3c00548
Chem. Rev. XXXX, XXX, XXX−XXX

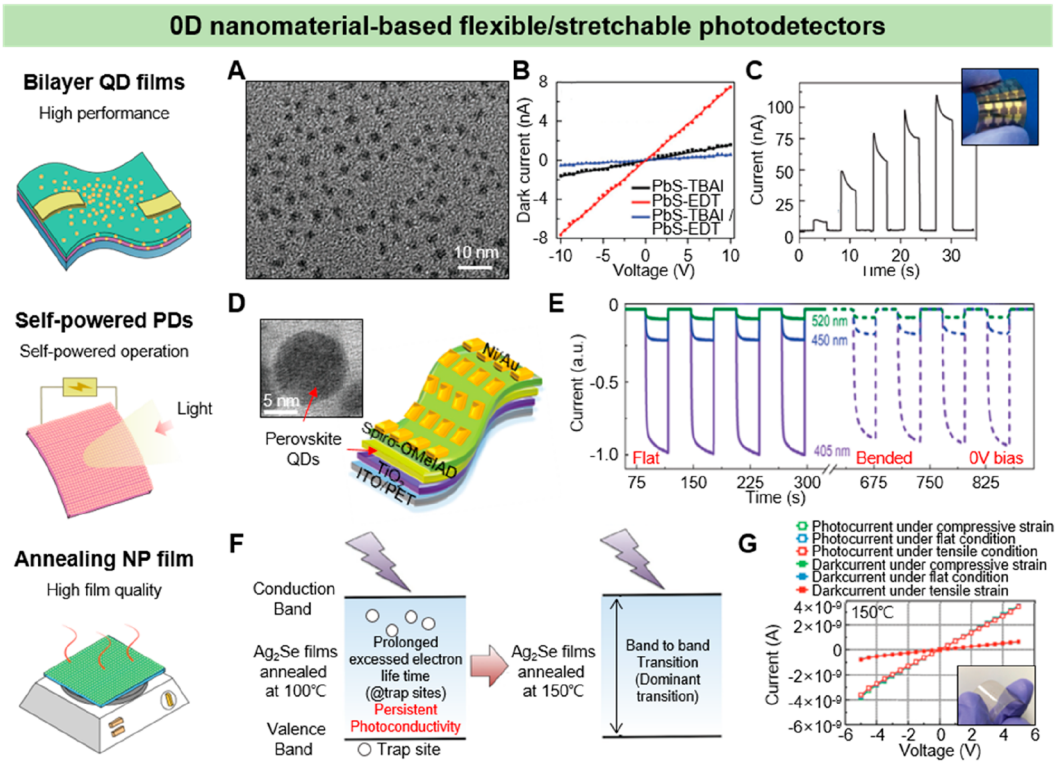

Figure 28. 0D flexible/stretchable PDs. (A) TEM image of an oleic-acid (OA)-capped PbS QDs. (B) *I*−*V* curves of PbS-TBAI (black), PbS-EDT (red), and PbS-TBAI/PbS-EDT (blue) devices in dark condition. (C) On/Off switching characteristics of a flexible bilayer device on PI substrate under increasing light intensities at a bias of 10 V. The inset is a photograph of the bent state device. Reproduced with permission from ref 701. Copyright 2017 John Wiley & Sons, Inc. (D) Schematic illustration of the PD array structure and a TEM image of 0.025 CsBr/KBr-doped $CsPbBr_3$ QDs (inset). (E) Transient photocurrents of device in flat and bending states. The bending angles are 0° (solid lines) and 60° (dashed lines) under illumination. Reproduced with permission from ref 709. Copyright 2020 John Wiley & Sons, Inc. (F) Schematic illustration of photosensing process of the Ag_2Se films annealed at two different temperatures. (G) *I*−*V* curves of the flexible devices based on the Ag_2Se film annealed at 150 °C with different strain conditions. The inset is an image of bent device. Reproduced with permission from ref 706. Copyright 2019 John Wiley & Sons, Inc.

currents, enhancing detectivity. However, their comparatively lower internal gain results in a relatively smaller responsivity compared to devices employing the photoconductive effect.

The PDs can be classified into three structures: photodiodes, photoresistors, and pTrs. Photodiodes with a photovoltaic effect are widely used as flexible and stretchable PD. The photodiode consists of two-terminal electrodes and an active layer for the photoresponse (Figure 27A). In a vertically stacked structure typically adopted for photodiodes, transparent metal materials are selected as top electrodes, such as ITO, so that incident light can reach the active layer underneath the top electrode, producing the electron−hole pairs.[69] The vertical structure also exhibits fast response speeds due to the relatively short distance from the photocarriers in the active layer to the electrodes. Photoresistors have a simple configuration consisting of source and drain electrodes and the active layer that forms two Ohmic contacts (Figure 27B). Unlike the photodiode, the photoresistor generates photocurrents working with the photoconductive effect. They show great dynamic range despite a long response time. The pTrs have been demonstrated by integrating the properties of transistors that amplify the signals and photodiodes that generate photocurrents. The pTr consists of three terminals: source, drain, gate electrodes, and the active layer (Figure 27C). The structure is similar to conventional TFTs, but the photoconductive material substitutes the semiconducting layer. Under illumination, the pTr generates the separation of electron−hole pairs analogous to photodiodes, and then a gate voltage modulates induced photocurrents to amplify the output signals, achieving higher sensitivity than the photodiodes.[69] However, the lateral channel length is difficult to minimize, so the pTr suffers from several disadvantages of long transport length and slow response time.[690,691]

5.2. Inorganic Flexible and Stretchable PDs

Inorganic material-based PDs show good optoelectronic performance, including high carrier mobility owing to the highly advanced fabrication techniques. However, the bulk, brittle, and rigid nature of inorganic semiconducting materials is unfavorable for implementing flexible/stretchable optoelectronic devices.[692] To improve the device's bendability while exploiting high performance of inorganic materials, nanoscale size reduction is adopted. The inorganic nanomaterials such as NPs, NWs, and nanosheets not only reduce flexural rigidity and but also exhibit unique optical and electrical properties compared to their bulk state.[693] As another strategy, various structural engineering techniques using folding, cutting and electrode designs have been developed to reduce stresses and strains during the shape transformation of the device. The following subsections will cover recent advances in inorganic flexible/stretchable PDs based on the nanomaterials and structural engineering.

https://doi.org/10.1021/acs.chemrev.3c00548
Chem. Rev. XXXX, XXX, XXX−XXX

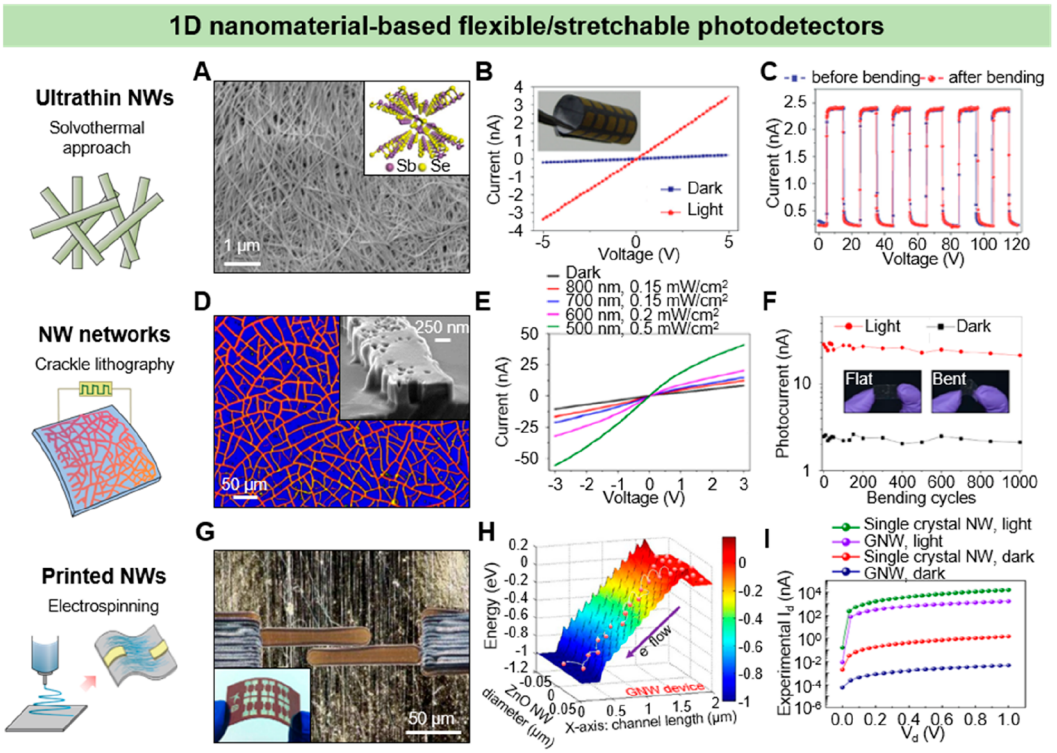

Figure 29. 1D materials for flexible/stretchable PDs. (A) SEM image of a synthesized Sb_2Se_3 nanostructures and schematic diagram of its crystal structure (inset). (B) *I*−*V* curves of a flexible Sb_2Se3 PD on paper substrate in the dark and bright conditions and its photograph (inset). (C) On/Off photoresponse of the devices before bending (blue) and after 100 cycles of bending (red) at a voltage of 5.0 V. Reproduced with permission from ref 734. Copyright 2015 John Wiley & Sons, Inc. (D) Optical image of a silicon NW network on PET substrate and SEM image in cross sectional view of a single silicon NW (inset). (E) *I*−*V* curves of the device under dark and various wavelengths light conditions. (F) Photocurrent measurements of the silicon NW network at different bending cycles up to 1,000 times. The inset are photographs of the flat and bent device. Reproduced with permission from ref 718. Copyright 2014 Springer Nature. (G) Photograph of a printed ZnO granular NW(GNW) PD and the flexible all-printed GNW PD array in bending state (inset). (H) Modeling results of a conduction band energy profiles of a GNW (right) PDs in dark condition. (I) *I*−*V* curves of the single-crystal NW and the GNW-based PDs. Reproduced with permission from ref 720. Copyright 2018 American Chemical Society.

5.2.1. 0D Nanomaterials. 0D nanomaterial-based PDs exhibit distinctive optical, electrical, and mechanical features in relation to the size and shape of semiconducting NPs and QDs.[694] For example, the bandgap of NPs can be tuned by modulating the size.[695] The facile fabrication methods from soluble, low-temperature processable properties of the NPs also improve the device's flexibility and stretchability. Thus, the NPs integrated with flexible substrates enable the implementation of the flexible/stretchable PDs based on ZnO NPs,[696−699] Ag NPs,[700] PbS QDs,[701−704] CdSe QDs,[705] Ag_2Se NPs,[706] and PbSe QDs,[707] HgTe QDs.[708] This section will present 0D nanomaterial-based inorganic, flexible/stretchable PDs.

Ren et al. developed high-performance flexible PDs by using a bilayer PbS QD.[701] Conventional single PbS QD layer devices have limitations such as large dark currents, low on−off ratios, and slow light responses. Although hybrid forms of PbS QD PDs have been demonstrated to improving photoresponsivity, this hybridization induces additional issues that degrade device performance. In this regard, the bilayer structure of tetrabutylammonium iodide (TBAI) and 1,2-ethanedithiol (EDT)-modified PbS QD films successfully improved overall device performance in terms of response speed, sensitivity, dynamic range, and SNR. To implement the bilayer, first, the uniform OA-capped PbS QDs were synthesized with an average diameter of ∼3.1 nm (Figure 28A). Subsequently, the PbS-TBAI film via the TBAI methanol solution and the PbS-EDT film via the EDT acetonitrile solution were formed and assembled to attain the PdS QD bilayer. In the *I*−*V* curves, the fabricated bilayer PbS device showed the lowest dark current compared to the single-layer devices of PbS-TBAI or PbS-EDT (Figure 28B). This is because the depletion region formed around the interface between layers narrows the conducting regions. Due to the compatibility of the QD film with flexible substrate, the flexible bilayer PbS device was fabricated on a PI substrate, presenting good on/off switching performance (Figure 28C).

Shen et al. demonstrated flexible and self-powered PDs based on inorganic perovskite QDs. The introduction of CsBr/KBr precursor in the $CsPbBr_3$ QDs synthesis improved the surface morphology and crystallinity of a perovskite film (Figure 28D, inset), boosting carrier transport and lowering leakage currents of the device.[709] The CsBr/KBr assisted $CsPbBr_3$ QD device was fabricated on the flexible PET substrate (Figure 28D). In the *I*−*V* measurement, the fabricated $CsPbBr_3$ QD PD showed an apparent response under dark conditions and 405, 450, and 520 nm laser lights under self-powered mode. The device exhibited high robustness to bending, maintaining stable on/off switching behavior even after 1600 bending cycles. The repetitive photoresponse test under different light illumination for both flat and bent devices also indicates that the fabricated device is fairly robust to be bent (Figure 28E). Moreover, the consistent electrical

https://doi.org/10.1021/acs.chemrev.3c00548
Chem. Rev. XXXX, XXX, XXX−XXX

stability observed across all 8 × 11 pixels in the flexible PD array suggests that the $CsPbBr_3$ QD-based PD array can be effectively utilized in imaging systems.

Lee et al. developed a flexible near-infrared (NIR) PD based on chalcogenide Ag_2Se NPs.[706] Due to the relatively low melting temperature of bulk Ag_2Se, the Ag_2Se NPs can be formed into high crystalline films on a plastic substrate. Two Ag_2Se-based photoreceptors were fabricated under different annealing temperatures of 100 and 150 °C. When illuminating the 808 nm laser light, the device annealed at 100 °C showed more persistent photoconductivity and high bias voltage dependence than the 150 °C annealed device. This can be explained through the increased drift velocity and reduced carrier transit time at high bias voltage (Figure 28F). Also, the trap sites from defects in 100 °C annealed Ag_2Se film induce prolonged excess electron lifetime, eventually resulting in notable persistent photoconductivity, while the improved film quality in the annealing process at 150 °C effectively reduces the defect-induced trap sites. In the bending test under compressive and tensile strains, the Ag_2Se PD annealed at 150 °C exhibits stable photoresponsivity (Figure 28G).

5.2.2. 1D Nanomaterials. Optoelectronic devices based on 1D nanomaterials, including NWs, nanobelts (NBs), NRs, and nanotubes (NTs), have been developed to improve device performance by exploiting the optical and electrical properties of the 1D nanomaterials.[85,710−713] Their physical advantages, such as a large surface area-to-volume ratio and their wire geometry, are desirable for developing high-quality PDs by extending the photocarrier lifetime, reducing transit time, and enhancing mechanical flexibility.[714−717] The number of flexible/stretchable PDs has been demonstrated by using the 1D nanomaterials, including Si NWs,[718] Ge NWs,[719] ZnO NWs,[720−724] GaN NWs,[725−727] CdS NWs,[728−731] InGaSb NWs,[732] GaSb NWs,[733] Sb_2Se_3 NWs,[734] ZrS_3 NBs,[735] and heterostructured NWs.[736−738] This section will discuss the flexible and stretchable PDs using 1D nanomaterials.

The flexible PD was developed by depositing ultrathin Sb_2Se_3 NWs on the PET and printing paper substrates via the solvothermal approach.[734] The Sb_2Se_3 NWs were synthesized in a controllable manner from the reaction between triphenylantimony and dibenzyldiselenide in ethanol at 200 °C with surfactants (Figure 29A). During the synthesis, the surfactants of both OAm and polyvinylpyrrolidon (PVP) affect the diameter of Sb_2Se_3 NWs. Ultrathin NWs with diameters ranging from 10 to 20 nm and length up to 30 μm were grown by tuning the temperature with surfactants. The Sb_2Se_3 NW-based PDs were fabricated on flexible printing paper substrates (Figure 29B, inset). Due to the 1D geometry of Sb_2Se_3 NWs with the flexible substrate, the device can be bent or rolled, exhibiting high mechanical flexibility. Under dark and bright conditions, the PD on the printing paper showed typical $I-V$ characteristics (Figure 29B). The device stability test with external strains showed no significant degradation before and after 100 cycles of repetitive bending (Figure 29C).

The synthesis of 1D nanostructures can be categorized into top-down and bottom-up fabrication approaches. The top-down approach breaks down bulk materials into 1D nanostructures,[739−741] while the 1D nanostructures grow from the seed precursor in the bottom-up approach.[711,742−744] Besides, various fabrication methods, including crackle lithography,[718,745,746] electrospinning,[290,736,747,748] and template-based growth,[749−753] have been developed to form 1D nanostructures for a simple, cost-effective, and scalable process. Recently, these fabrication methods have been actively used for producing flexible and stretchable 1D PDs. For example, Hossain et al. utilized crackle lithography to produce the percolated Si NW networks for transparent and flexible PDs.[718] Based on the cracked template from spin-coated acrylic resin and following the dry etching process, the highly interconnected Si NW networks can be fabricated via the relatively simple process but in a large area (Figure 29D). In addition, the Si NW networks transferred onto the PET substrate exhibit high transparency in the visible region, which is advantageous for developing transparent electronics. The flexible Si NW network PD array was fabricated with the Au electrodes. The $I-V$ characteristics under the light of various wavelengths (500, 600, 700, and 800 nm) showed that the fabricated device clearly responds to visible light, compared to the dark condition (Figure 29E). The photocurrent variation was measured according to bending cycles up to 1,000 (Figure 29F). There was a slight decrease in the photocurrent, but not that significant, which validated the device's robustness and high flexibility.

Meanwhile, the polycrystalline ZnO granular NW (GNW) PD was demonstrated through an all-printing fabrication process by combining near-field electrospinning and inkjet printing (Figure 29G).[720] In order to fabricate electrospun semiconducting NWs, a mixed solution of zinc acetate (ZnAc) and poly(vinyl alcohol) (PVA) was prepared in a 10 mL syringe with a 50 μm diameter needle. Proper modulation of x- and y-axis syringe motions can print out straight nanofibers. During the electrospinning process, a shadow mask on the substrate enables the patterning of ZnAc/PVA nanofibers. Then, the ZnO GNWs can be achieved through thermal calcination at 420 °C, which is sufficient for using a PI substrate and the mass loss rate of PVA. The flexible ZnO GNW PD array was fabricated by inkjet printing the metal electrodes on the ZnO GNWs. Compared to the ZnO NWs, the GNW device showed a lower dark current and higher photoresponsivity derived from the modulated energy band edge along the GNW axis (Figure 29H). The Schottky barriers originated from grain boundaries hinder the electron transports in the channel, which effectively reduces the dark current flow. Although the GNW PD has lower light currents under illumination than the single-crystalline NW PD due to the barriers, the highly suppressed dark current allows high responsivity to low light levels (Figure 29I). Also, the fabricated device stably responded to the input light even under various bending curvatures from −30 to 30 cm^{-1}.

5.2.3. 2D Nanomaterials. The thin film shape of 2D nanomaterials has been broadly exploited in optoelectronic devices, owing to their advantages derived from the morphology. Conventionally, PDs based on bulk and thick semiconducting materials, including Si, Ge, GaAs, InGaAs, and ZnO, suffer from its rigidness and brittleness, which hinders device flexibility/stretchability. However, when the initial bulk materials become nanomembranes (NMs) or ultrathin layers at the atomic level through thinning, including cleaving, etching, and exfoliation, the withstand range of external strain can be expanded. Thus, the flexible/stretchable 2D PDs have been demonstrated by utilizing a thin film format of active materials such as Si,[770,928] Ge,[885,929,930] GaS,[882] Ag_2S,[931] CdTe,[932] $MoSe_2$,[765] SnS_2,[933] WSe_2,[758] and $CsPbBr_3$.[764]

Besides, the high transparency of 2D thin-layered materials is appealing for soft electronics. To date, there have been a great number of studies on 2D nanomaterial-based PDs with

https://doi.org/10.1021/acs.chemrev.3c00548
Chem. Rev. XXXX, XXX, XXX−XXX

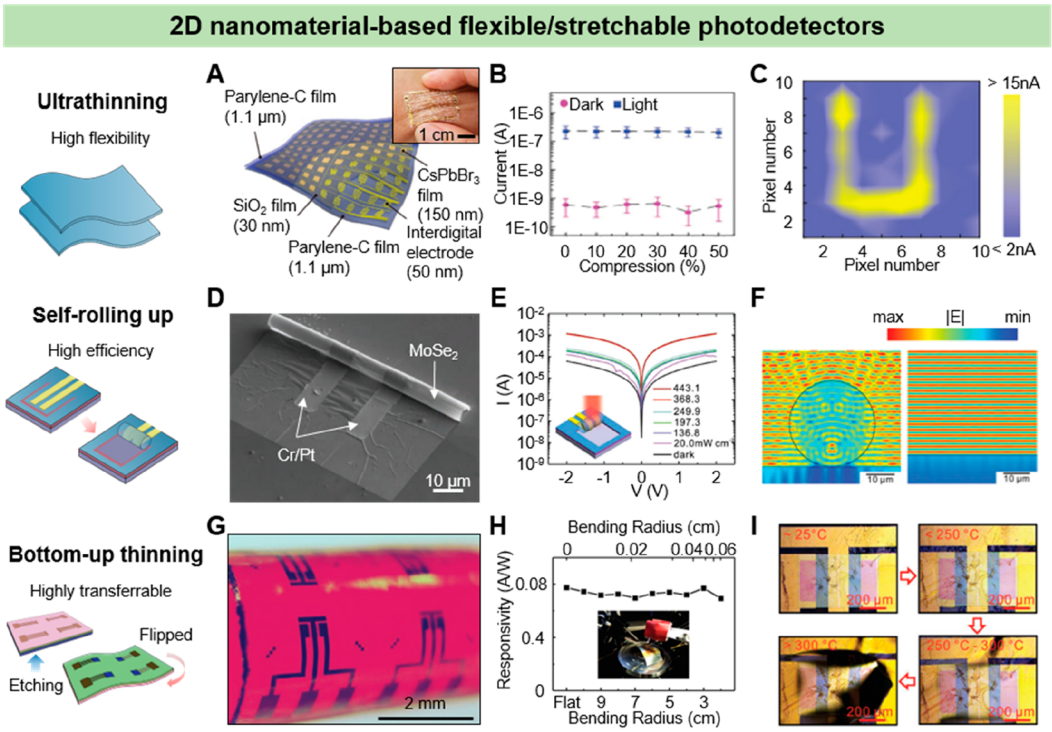

Figure 30. 2D materials for flexible/stretchable PDs. (A) Schematic illustration of an ultrathin lead halide perovskite PD array. The inset shows high flexibility and the conformal lamination on the skin surface of the fabricated device. (B) Photocurrent measurements of the device at different compressive strains. (C) Imaging results of the letter "U" acquired from the PD array. Reproduced with permission from ref 764. Copyright 2021 John Wiley & Sons, Inc. (D) SEM image of rolled-up $MoSe_2$ microtubular PD. (E) $I-V$ curves of tubular PDs under dark and bright state. (F) Simulated results of electromagnetic field distribution in the $MoSe_2$ microtube (left) and the flat $MoSe_2$ film (right). The black line represents $MoSe_2$ membrane. Reproduced with permission from ref 765. Copyright 2019 John Wiley & Sons, Inc. (G) Photograph of a bending state of a silicon NM pTr array. (H) Responsivity of the pTr array at different bending radii and photograph of the experimental setup (inset). (I) Destruction process of the device as the temperature increases. Reproduced with permission from ref 770. Copyright 2018 John Wiley & Sons, Inc.

high performance in terms of flexibility and stretchability, responsivity, and transparency.[754−757] For instance, Zheng et al. demonstrated a flexible and transparent PD using a WSe_2 film operating in a broadband wavelength region.[758] The WSe_2 film via pulsed-laser deposition (PLD) showed great average transparency of 72% in the visible region, achieving high photoresponsivity. The fabricated device can achieve high flexibility and transparency with the flexible PI substrate and ITO electrodes. Likewise, recent studies in 2D nanomaterial PDs have focused on improving flexibility and stretchability, optical/electrical performance, and other functional features such as transparency[759−762] and transient functionality.[763]

Lead halide perovskites are emerging materials for flexible optoelectronic devices because of the simple fabrication techniques of solution processing.[764] However, the vulnerability to polar liquids hinders the practical use of perovskite-based flexible PDs. Wu et al. demonstrated an ultrathin lead halide perovskite ($CsPbBr_3$) 2D NM-based conformable PD array through a vacuum-assisted drop-casting patterning (VADP) process for retina-like vision systems (Figure 30A). Two layers of parylene-C film enhance the mechanical flexibility as a substrate and encapsulate the device from water as a protecting layer, enabling the device to withstand the ambient environment for 6 weeks. The $CsPbBr_3$ PD array showed typical $I-V$ characteristics under dark and 450 nm illumination. The PD array also exhibits no significant degradation of photoelectric performance even under increasing compressive strains up to 50% (Figure 30B). In addition, the imaging demonstration indicates the perovskite device can be utilized as a retina-like imager of the 10 × 10 pixels PD array (Figure 30C).

For the high responsivity, 3D tubular-structured $MoSe_2$ PDs have been demonstrated by incorporating the flexibility of 2D NMs (Figure 30D).[765] Compared to the 2D NMs that show relatively low absorption originated from the small thickness, rolled-up 3D structures can enhance light absorption because of their circular geometry, thus increasing the device photoresponsivity. The device self-rolled from a planar shape to 3D tubular structures via a strained Cr/Pt layer on the $MoSe_2$ film, which acts as both the strained layer and the electrodes. In the $I-V$ characteristics, the tubular-structured PD presented a higher photoresponse to 808 nm light than the planar one (Figure 30E). Inside the microtube, incident light undergoes multiple reflections caused by the local enhancement of the electromagnetic field (Figure 30F). Once the light reflects on the inside surface of the tube, a certain amount of light is absorbed, which in turn increases the total light absorption during the multiple reflections.

Recently, transient electronics have drawn great attention due to the growing demands of technical security.[766−769] Flexible transient PDs on a wafer-compatible transferred Si NM have been developed by Li et al. (Figure 30G).[770] The device was fabricated on a silicon-on-insulator (SOI) substrate and transferred in a wafer scale via a bottom-up thinning process. With the transient layer (PAMS) and polymer substrate (Kapton film), the Si-NM PD presented great

https://doi.org/10.1021/acs.chemrev.3c00548
Chem. Rev. XXXX, XXX, XXX−XXX

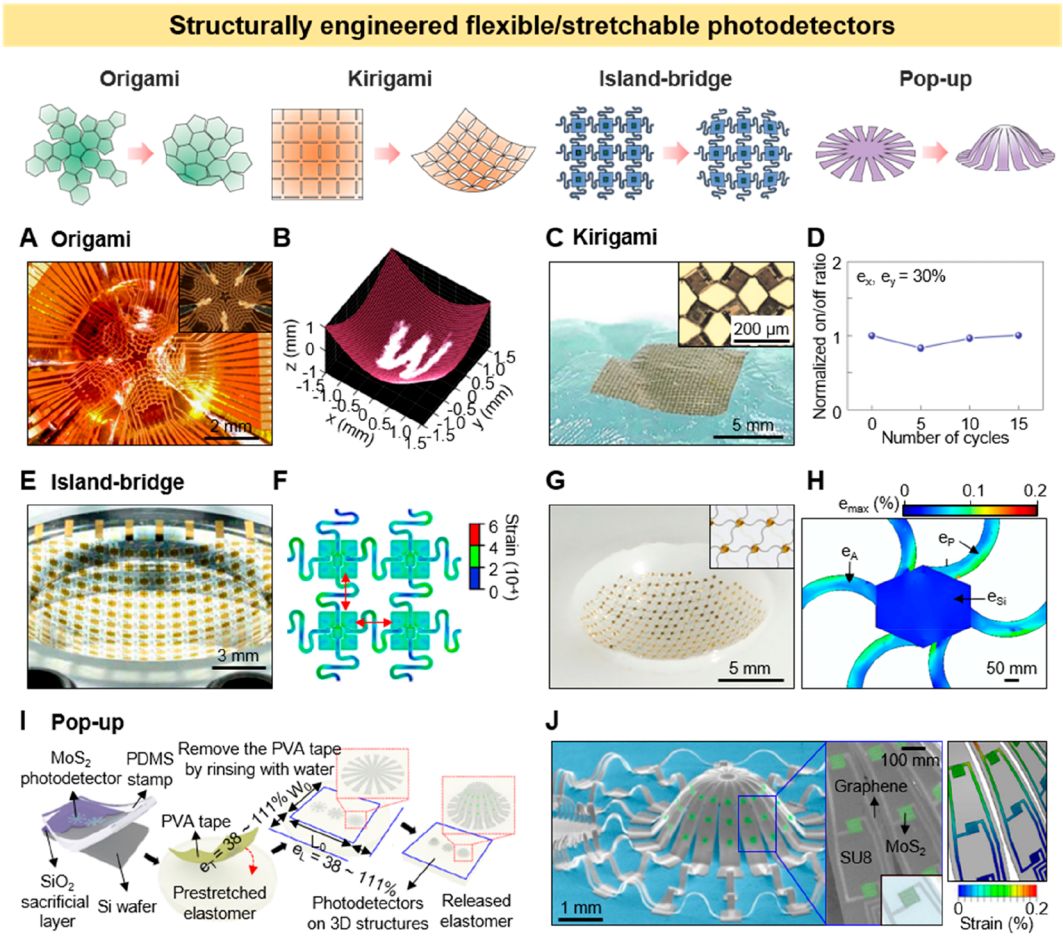

Figure 31. Structurally engineered flexible/stretchable PDs. (A) Photograph of a hemispherically concave silicon PD via an origami and their flat device before bending (inset). (B) Image result of the letter "W" from the artificial electronic eye camera with concave imager. Reproduced with permission from ref 666. Copyright 2017 Springer Nature. (C) Photographs of stretchable kirigami device transferred on an arbitrarily shaped curvy surface. (D) Normalized on/off ratio of photocurrents on a single pixel under different cycles of 30% biaxial stretch. Reproduced with permission from ref 667. Copyright 2021 Springer Nature. (E) Tilted view image of a curved PD array on flexible PDMS membrane. Reproduced with permission from ref 668. Copyright 2011 National Academy of Sciences. (F) Finite element analysis (FEA) of a 2 × 2 pixels' array on the center of the deformed device. The overall biaxial strain is 12% that is below the expected fracture range of the materials. (G) Photograph of a curved PD array with serpentine interconnects with its enlarged view (inset). (H) FEA for the strain distribution analysis in a single pixel of the device. Reproduced with permission from ref 178. Copyright 2020 Springer Nature. (I) Schematic illustration of the fabrication process of a 3D MoS_2 PD array based on pop-up techniques. (J) SEM images of the PD array with color highlights of MoS_2 (green), graphene (light gray), and SU-8 (gray) (left). The inset is its magnified view (left, inset). FEA results represent the strain distribution in the device (right). Reproduced with permission from ref 669. Copyright 2018 Springer Nature.

bending stability under external strains (Figure 30H). The transient feature of the device was also investigated by increasing the temperature. Up to 250 °C, the surface morphology maintained its flat state and the dark current increased due to the high intrinsic carrier density at high temperatures. Although the behavior of PDs gradually degrades ~250 °C, this degradation can be reversed by decreasing the temperature. However, the PAMS starts to deform the device as the temperature increases (>250 °C), and when it approaches the critical temperature of PAMS (e.g., 300 °C), the device is physically destroyed from the high pressure induced by PAMS, resulting in irreversible destruction (Figure 30I).

5.2.4. Structural Engineering. Beyond the fundamental strategies that exploit the properties of nanomaterials or intrinsic flexible/stretchable materials (e.g., organic materials), structural engineering provides another facile route to enhance the flexibility and stretchability of the devices. By cutting/folding materials or doing both, the 2D membrane device can be transformed into a 3D structure while maintaining its optical and electrical performance. To build flexible/stretchable PDs, various structural engineering techniques such as kirigami,[667] origami,[666] interconnection designs,[178,668] and pop-up structures[669] have been introduced.

Origami and kirigami, inspired by traditional paper artworks, are simple and effective ways to convert the device structure via folding and cutting processes.[771,772] Due to their broad degree of freedom in shape deformation, origami/kirigami techniques have been applied in various optoelectronic devices, such as transformable LEDs,[109,773] stretchable robotic arms,[774−776] and foldable solar panels.[777,778] In the field of PDs, the spherical PD arrays were demonstrated using origami methods, both in convex and concave (Figure 31A) forms.[666] The single-crystalline Si-based PD array was transformed into a hemispherical geometry by folding patterned membranes composed of pentagon and hexagon blocks, building the

https://doi.org/10.1021/acs.chemrev.3c00548
Chem. Rev. XXXX, XXX, XXX−XXX

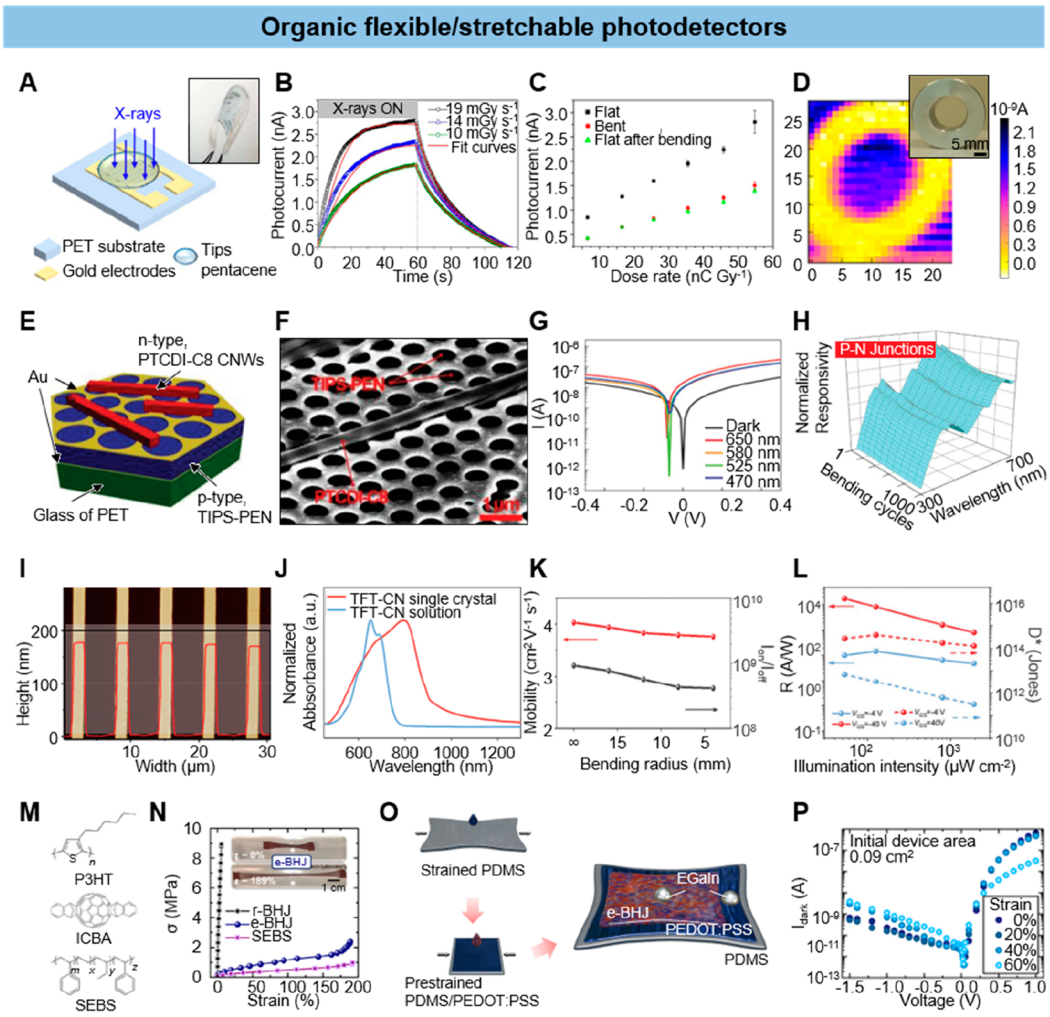

Figure 32. Organic flexible/stretchable PDs. (A) Schematic illustration of a flexible organic X-ray PD and a photograph of bent device (inset). (B) Photoresponse of simulated and experimental results of the PD under different X-ray dose rates. (C) Photocurrents according to the dose rates on before bending (black), during bending (red), and after bending (green) of the device. (D) X-ray image of an aluminum annular ring (inset) by using a single pixel device. Reproduced with permission from ref 670. Copyright 2016 Springer Nature. (E) Schematic illustration of the self-suspended gold nanomesh scaffold with multiple PTCDI-C8 NWs and large TIPS-pentacene crystalline domains. (F) SEM image of the fabricated organic p−n heterojunction on the gold nanomesh scaffold in a tilted view. (G) $I-V$ curves of the flexible organic PD under dark and light illumination with various wavelengths. (H) Photoresponsivity measurement at multiple cycles of bending up to 1,000 times for testing the bending fatigue of the device. Reproduced with permission from ref 790. Copyright 2018 John Wiley & Sons, Inc. (I) AFM image and height measurements of the 1D single-crystal TFT-CN arrays. (J) Normalized absorbance of TFT-CN solution and single-crystal arrays. (K) The mobility and on/off ratio of the device with different bending radii. (L) Photoresponsivity and detectivity at various illumination intensities. Reproduced with permission from ref 791. Copyright 2022 John Wiley & Sons, Inc. (M) Chemical structure of a donor polymer P3HT, an acceptor ICBA, and an elastomer SEBS. (N) Stress (σ) and strain (ε) characteristics of a r-BHJ, e-BHJ, and SEBS film from the uniaxial tensile test. (O) Schematic illustration of the fabrication process for stretchable e-BHJ PDs. (P) $I_{dark}-V$ measurement of stretchable devices at various strain states. Reproduced with permission from ref 792. Copyright 2021 American Association for the Advancement of Science.

half-truncated icosahedron structure. The origami-based device not only can transform its shape but also can minimize pixel resolution and performance. For example, the fabricated concave device successfully collected the letter "W" image, inspired by the artificial eye with a curved retina (Figure 31B). Also, the convex hemispherical device with a microlens array, inspired by the insect compound eye, captured the spot images from a wide field of view. The fabricated concave and convex PD array shows the potential of the origami methods for shape variations in high-resolution and high-quality PDs.

Unlike the origami methods that convert the structure by folding prepatterned membranes, kirigami is based on cutting techniques. For example, by cutting the 2D device with repetitive orthogonal lines, the mechanical flexibility of the PD array was greatly improved, enabling a conformal contact of the device onto an arbitrary surface (Figure 31C).[667] The kirigami imager exhibited high stretchability, withstanding up to 30% of biaxial strains. Pixel performance tests were validated by measuring the on/off photocurrent ratio under biaxially stretched conditions. The results showed that the device maintains its performance after several stretching cycles (Figure 31D).

The metal line interconnections with proper designs can provide the mechanical flexibility of the device by supporting external strains during the deformation process.[163,779−781] In the island-bridge designs, the relatively rigid pixel unit is

https://doi.org/10.1021/acs.chemrev.3c00548
Chem. Rev. XXXX, XXX, XXX−XXX

connected to its neighboring pixels via designed interconnects such as serpentine,[178,668] and fractal.[782] Therefore, the entire structure exhibits a resemblance to a network of islands (pixel units) and bridges (interconnects). Those interconnects alleviate strains forced onto the pixel units, enhancing the overall device flexibility and stretchability. The flexible PD array with designed metal interconnects was demonstrated to develop a tunable imager with zoom capabilities (Figure 31E).[668] The serpentine-shaped designs in the interconnecting electrodes can expand the stretching range of the entire device structure. The result of the finite element analysis (FEA) conducted on a 2 × 2 pixel unit array indicates that the device exhibits low levels of strain, even under a biaxial strain of approximately 12% (Figure 31F). This level of strain is far below the fracture strain of Si photodiodes. Variable zoom imaging was conducted via a combined system of a tunable fluidic lens and various curvatures of the PD array tuned by hydraulics. Similarly, Kim et al. demonstrated a curved imager of 23 × 23 hexagonal PD array in the concave mold with a radius of 7.5 mm (Figure 31G).[178] The serpentine metal lines of the curved imager relieved externally induced strains on the device, as demonstrated by the FEA results (Figure 31H).

The pop-up structure has been utilized for the flexible and stretchable PDs by controlling the adhesion between material interfaces and reducing the mechanical strain via delaminated regions.[669] The device membrane was transferred onto the prestrained elastomeric surface. With the release of the prestrain, the active pixel area remains stuck to the substrate, while the controlled regions (i.e., interconnects) that have weak adhesion with the elastomeric surface pop up, resulting in a significant reduction of the strain on the bonded device area (Figure 31I). The MoS_2-based PDs in a full 3D geometry were demonstrated by utilizing the pop-up structure (Figure 31J, left). The complete MoS_2 device was transferred onto the prestretched elastomer using PVA tape. UV ozone treatment and photoresist patterning were conducted during the process to create the selective delamination areas. Each arm of the hemispherical device structure includes three PDs, which showed minimized strains across the device in the FEA results (Figure 31J, right).

5.3. Organic Flexible and Stretchable PDs

Organic semiconductors have garnered considerable attention for flexible and stretchable PDs due to their unique physical, optical, and electrical properties, such as intrinsic flexiblibity and stretchability, a broadband response range, low fabrication cost, lightweight, and high compatibility with other electronics. These characteristics allow them more accessible to a wide range of applications where conventional inorganic devices are impractical. The tunable features of organic semiconductors via chemical design are also advantageous for the development of functionalized devices, particularly by optimizing the optical bandgap for broadband response or narrowband response to specific wavelengths.[17] Accordingly, flexible/stretchable organic PDs have been deployed in various applications, such as wearable devices, imaging systems, and biosensors.[173,783]

Flexible PDs for detecting ionizing radiation are of interest to address the limitations of traditional flat X-ray imagers, such as X-ray overdose and low imaging quality. Organic materials are attractive for developing soft X-ray detectors due to their advantages of cost-effective/large-scale fabrication via a solution process, high flexibility, and low power supply. X-ray detectors can be categorized into two types: direct and indirect conversions. Direct X-ray detectors convert ionizing radiation into electrical signals, while scintillators that operate with the indirect conversion initially absorb the X-rays, and then, the PD produces photocurrents in response to the emitted visible light from the scintillator. Recently, flexible X-ray detectors were proposed using organic semiconducting materials.[784−788] For example, quasi-direct hybrid organic PDs have been developed for high-resolution X-ray imaging.[789] The detector is composed of terbium-doped gadolinium oxysulfide (GOS:Tb) scintillator particles in the organic PD matrix (P3HT:PCBM). Since the emitted photons from the scintillator particles responding to incident X-rays are rapidly absorbed by the neighboring organic matrix, the conventional limitations of optical crosstalks and low resolution in indirect detectors can be resolved.

Meanwhile, Basiricò et al. demonstrated direct X-ray photoconversion based on flexible organic thin film devices.[670] The device was fabricated by drop casting the bis-(triisopropylsilylethynyl) pentacene (TIPS-pentacene) organic thin film onto a flexible PET substrate with gold electrodes (Figure 32A). Despite the use of low-Z organic material, high sensitivity to ionizing radiation is possible due to the accumulation of holes in the organic thin film. The X-ray photocurrent was measured under different dose rates (Figure 32B). The mechanical flexibility of X-ray detectors is essential for biomedical applications (e.g., bone or/and organ imaging). Conformal contact of the X-ray detector with the curved surfaces of the body can enhance imaging quality by minimizing aberrations and reducing the number of exposures, decreasing the total radiation dose. The flexible X-ray detector on the PET substrate presented high flexibility, withstanding a bending radius of up to 0.3 cm. Although the photoresponsivity showed an inevitable decrease during initial bending, the device exhibited no significant differences in successive bending cycles up to 100 cycles, once after the initial decline observed during the first bend (Figure 32C). The fabricated detector demonstrated X-ray imaging via a single-pixel scan of an aluminum annulus, exhibiting its potential for practical applications (Figure 32D).

In the ultraviolet−visible region, Zhang et al. demonstrated a hollow nanomesh scaffold for fast response, low leakage current and large-scale manufacturability (Figure 32E and 32F).[790] The hollow nanomesh scaffold can be formed onto glass and plastic substrates by using self-assembled polystyrene (PS) nanospheres in a hexagonally close-packed monolayer. Through the nanospheres lithography (NSL), the hollow nanomesh scaffold consisting of cross-linked poly(4-vinylphenol) (CL-PVP) layer and top/bottom gold electrodes was fabricated on the substrates. Then, the N,N′-dioctyl-3,4,9,10-perylenedicarboximide (PTCDI-C8, n-type) NW crystals can be grown on the nanomesh structures by phase-exchange precipitation in a solution. The grown NWs were connected to the top electrodes without passing through the nanomesh. On the other hand, 6,13-bis(triisopropylsilylethinyl)pentacene (TIPS-PEN, p-type) can fill out the cavity in the nanomesh via the molecularly dispersed solution state, contacting the top/bottom electrodes and the n-type NWs, forming p-n heterojunctions. The device showed sufficient photoresponsivity in the $I-V$ characteristics under various wavelengths from UV to visible region (Figure 32G). After 1,000 bending cycles with a bending radius of ∼2 cm, the flexible detector based on the hollow nanomesh scaffold had only slightly

https://doi.org/10.1021/acs.chemrev.3c00548
Chem. Rev. XXXX, XXX, XXX−XXX

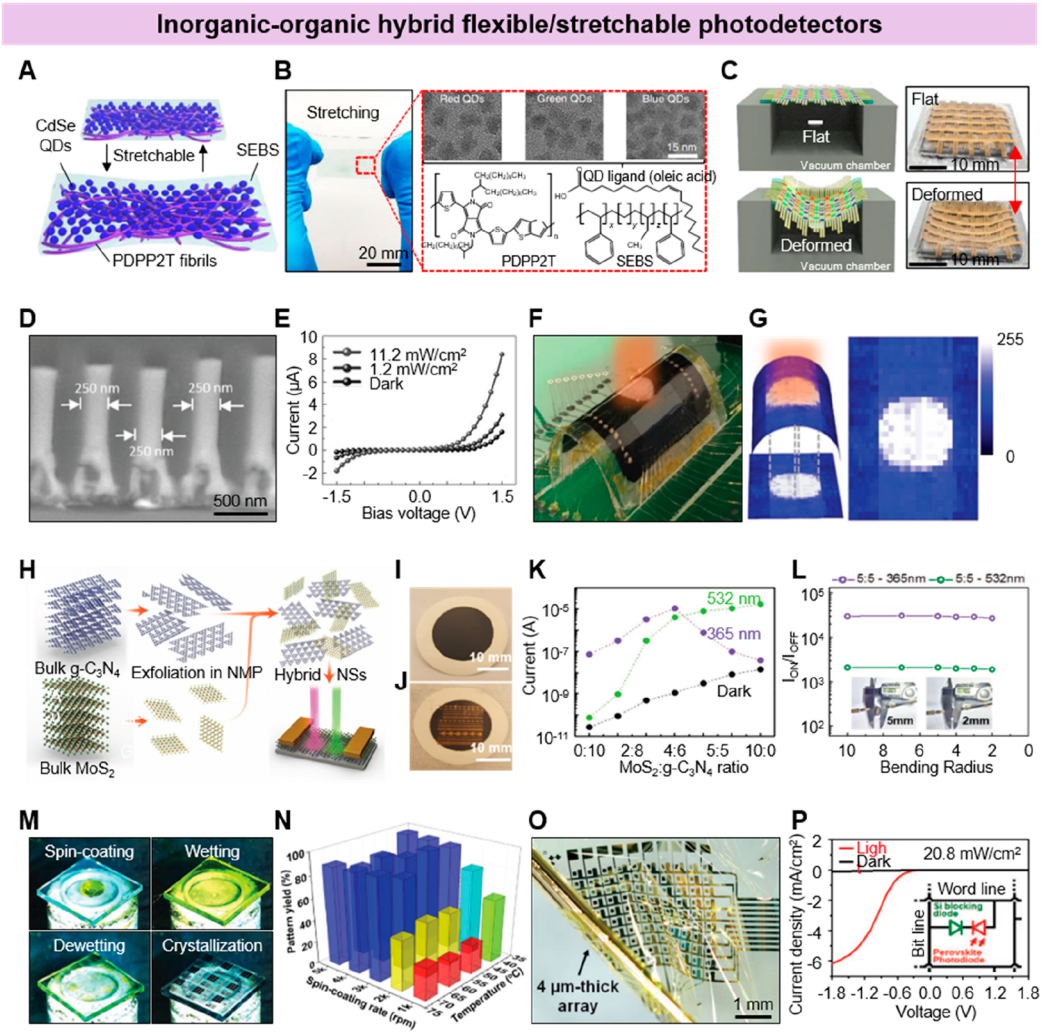

Figure 33. Inorganic−organic hybrid flexible/stretchable PDs. (A) Schematic illustration of the stretchable *is*-QDSN consisting of QDs and semiconducting polymer fibrils (PDPP2T) in the SEBS substrate. (B) Photograph of the 50% stretched *is*-QDSN film on the SEBS substrate (left). The inset is the TEM images of red, green and blue QDs (tow row) and molecular structures of PDPP2T and SEBS (bottom row). (C) Schematic illustrations and photographs of the flat (top) and deformed (bottom) pTr arrays. Reproduced with permission from ref 208. Copyright 2022 Springer Nature. (D) Backscattered-electron (BSE)-mode SEM image of grown $MAPBI_3$ NW in PAM in cross-section view. (E) *I*−*V* characteristics of the PD under various white light intensities. (F) Photograph of the flexible PD with circular light pattern. (G) 3D Image results of circular light pattern from the bent PD in (F) (left). The acquired image is converted in 2D image after correction (right). Reproduced with permission from ref 749. Copyright 2016 John Wiley & Sons, Inc. (H) Schematic illustration of crystal structures of MoS_2 and g-C_3N_4, the preparation process for hybrid NSs, and hybrid NS-based PD. Photographs of (I) the 5:5 hybrid NS film on nylon membrane filter paper via a vacuum filtration and (J) the fabricated PDs. (K) Photocurrent measurements under dark (black), 532 nm (green), and 365 nm (purple) illumination according to the composition ratio of the MoS_2 and g-C_3N_4 hybrid film. (L) On/Off ratios of the photocurrent to the dark current of the 5:5 hybrid NS PD at various bending radius. Reproduced with permission from ref 809. Copyright 2017 John Wiley & Sons, Inc. (M) Photographs of spin-on-patterning (SoP) process for inorganic−organic hybrid perovskite film. (N) Pattern yields during SoP process according to various spin-coating rates and solution temperatures on a SAM-patterned ITO substrate. (O) Photograph of perovskite multiplexed image sensor on flexible thin polymer substrate. (P) Current density−voltage curve of the perovskite multiplexed image sensor under dark and bright conditions. The inset is a circuit diagram of the device. Reproduced with permission from ref 810. Copyright 2017 John Wiley & Sons, Inc.

decreased from the initial photoresponsivity, indicating high mechanical stability to applied external strains (Figure 32H).

High-throughput organic single-crystalline microarrays are promising candidates as active materials for high-performance NIR PDs. However, challenges in the patterning process for rigorously aligned single-crystalline arrays hinder the development of high-performance devices. Recently, Zhang et al. demonstrated a capillary-bridge lithography strategy for constructing high-quality and precisely aligned single-crystalline microarrays (Figure 32I).[791] The micropillar Si template was employed with asymmetric wettability for utilizing dewetting dynamics to synthesize large-area organic microarrays. Along with the asymmetric wettability of micropillars, other parameters of the solvent, temperature, and concentration of semiconductors were also optimized to obtain high-quality furan-thiophene quinoidal compound (TFT-CN) 1D arrays. The fabricated single TFT-CN crystals have maximum absorption in the NIR region due to the redshift during aggregation (Figure 32J). The organic FET (OFET) using the TFT-CN single-crystal microarrays was demonstrated on the flexible PEN substrate. In bending tests, the device performance showed high stability even in the device with a bending

https://doi.org/10.1021/acs.chemrev.3c00548
Chem. Rev. XXXX, XXX, XXX−XXX

radius of 4 mm with high mobility of ~93.3%, compared to its original value at planar state (Figure 32K). Based on the mobility and flexibility of OFET, the photodetecting performance of the 1D TFT-CN PD was also validated under NIR illumination (Figure 32L), indicating that the 1D TFT-CN device can be utilized in various NIR applications including optical communications, biomedical imaging, and environmental monitoring.

The soft and flexible nature of organic materials imparts deformability to the device by releasing stresses. When the flexibility allows the device to withstand external strains from bending or folding states, a stretchable device can endure tensile strains and adhere closely onto curvy surfaces (e.g., skin). Park et al. demonstrated a skin-like organic PDs by utilizing an elastomeric bulk heterojunction (e-BHJ), which exhibits not only high stretchability, but also low optical noise current and high photoresponse.[792] They optimized the blending ratio of a SEBS, a poly(3-hexylthiophene-2,5-diyl) (P3HT), and Indene-C60 bisadduct (ICBA) to attain the e-BHJ with best performance (Figure 32M). In the uniaxial tensile test, the e-BHJ with a 2:1:1 weight ratio of SEBS:P3HT:ICBA shows far lower Young's modulus than a reference BHJ (r-BHJ) that consists of P3HT and ICBA (1:1 by weight) and similar values to pristine SEBS (Figure 32N). Note that the strain at break of e-BHJ is 189%, which is comparable to human tissues. For fully elastomeric organic PDs, first, a PEDOT:PSS film was spin-coated onto a prestrained PDMS substrate. Next, the e-BHJ was spin-coated on the buckled substrate of PDMS/PEDOT:PSS, and a eutectic gallium−indium (EGaIn) was dropped on top for the top electrode (Figure 32O). The PD characteristics of stretchable device up to 60% showed compatible performance compared to those of 0% strain in the dark current measurement (Figure 32P). Although the device failed when above strain percentiles of 60%, the failure can be resolved by modulating prestrain values of buckled PDMS/PEDOT:PSS substrate owing to high stretchability of the e-BHJ.

5.4. Hybrid Flexible and Stretchable PDs

The attempts to enhance optical and electrical properties in single material-based PDs have been expanded by hybridizing different materials, such as inorganic−organic hybrid composites[677,678,793,794] and multidimensional hybrids.[795−801] For instance, organic materials exhibit mechanical flexibility, a simple and low-cost fabrication process, and tunable properties, while inorganic materials possesses high carrier mobility, stability, and a wide bandgap. The favorable optoelectronic characteristics of both materials can be achieved through inorganic−organic hybrid composites. Furthermore, the interface between inorganic−organic hybrids can provide an additional charge-trapping effect, enhancing photoresponsivity.[664] Another approach in material hybridization is the integration of two different dimensional nanomaterials to complement the limitations of a single material. The combination of 0D-1D, 1D-2D, and 0D-2D materials can improve device performances by expanding the spectral response range, enhancing the contact to electrodes, and improving mechanical stability. This section will introduce recent studies in hybrid flexible and stretchable PDs.

5.4.1. Inorganic−Organic Hybrids. High responsivity and mechanical stretchability are essential for developing high-performance PD arrays for wearable electronics and high-quality imaging devices. Although inorganic or organic PDs show good photodetecting ability or excellent flexibility, achieving a device with both properties remains challenging. Hybrid composites of inorganic and organic semiconducting materials have been implemented to exploit optical and electrical properties of both materials, such as increasing photoresponsivity, flexibility and/or stretchability, spectral range, and so forth.[677,802,803] Recently, stretchable, multispectral, and shape-tunable pTr arrays have been demonstrated by utilizing an *is*-QD-based semiconducting composite (*is*-QDSN) (Figure 33A).[208] The *is*-QDSN consists of inorganic QDs (i.e., CdSe core and ZnS shell) with different sizes for multispectral photodetection (e.g., red, green, and blue) and organic semiconducting polymer fibril (poly[2,5-(2-octyldodecyl)-3,6-diketopyrrolopyrrole-*alt*-5,5-(2,5-di(thien-2-yl)-thieno [3,2-*b*]thiophene)] (PDPP2T-TT-OD)) forming percolated network in the SEBS elastomer matrix (Figure 33B). The *is*-QDSN was fabricated with an optimized mixing ratio of QDs, PDPP2T-TT-OD, and SEBS for high optical and electrical properties and as well as stretchability. With the *is*-QDSN film and Au electrodes, an intrinsically stretchable multispectral PD array was implemented. The curvilinear shape of the device can be tuned by modulating the pressure of the vacuum chamber, which deforms the RGB PD array from a flat to a concave shape (Figure 33C). Additionally, the stretchable, color-sensitive, and shape-tunable photodetecting device successfully captured aberration-corrected color patterns with minimized noises through the aid of a deep neural network algorithm.

The 1D NWs are attracting materials for optoelectronic devices due to their optical and electrical properties derived from their geometric features, which are suitable for carrier transportation, acting as a channel. Gu et al. demonstrated high-resolution image sensors based on inorganic−organic hybrid perovskite ($MAPBI_3$) NWs through a vapor−solid−solid reaction (VSSR) process.[749] The nanoengineered templates of porous alumina membrane (PAM) facilitate the geometry-controlled growth of $MAPBI_3$ NWs in the vertical direction (Figure 33D). Based on the $MAPBI_3$ NW array on the PAM substrate, the PD array was fabricated by connecting the ITO top finger electrodes and Au bottom finger electrodes. The device exhibited the typical asymmetric $I-V$ curves of the Schottky photodiode originated from the asymmetric top/bottom contact electrodes (Figure 33E). The flexible $MAPBI_3$ NWs PD was demonstrated on the PET substrate to improve flexibility. Despite the bending state of the device (i.e., convexly bent toward the object), the devices captured a clear image of a circular light pattern (Figure 33F and 33G).

The 2D NMs of MoS_2 possesses intriguing characteristics such as high light absorption, flexibility, and short response times, leading to the demonstration of MoS_2 film-based flexible PDs in recent years.[804−807] However, the high dark current and limited spectral detecting range restrict the practical applications of the MoS_2 device, prompting the hybridization of MoS_2 with organic materials.[808] In this context, inorganic MoS_2 and organic g-C_3N_4 thin film-based flexible PDs were developed using a simple solution process for broadband photodetection from the ultraviolet to the visible region (Figure 33H).[809] MoS_2 and g-C_3N_4 nanosheets, exfoliated from bulk materials, were dispersed by blending the solution. The homogeneously mixed solution was then filtered through nylon membrane filter paper under a vacuum process and dried in a vacuum oven, forming a hybrid composite thin film. Metal electrodes were deposited on the hybrid film consisting of a

https://doi.org/10.1021/acs.chemrev.3c00548
Chem. Rev. XXXX, XXX, XXX−XXX

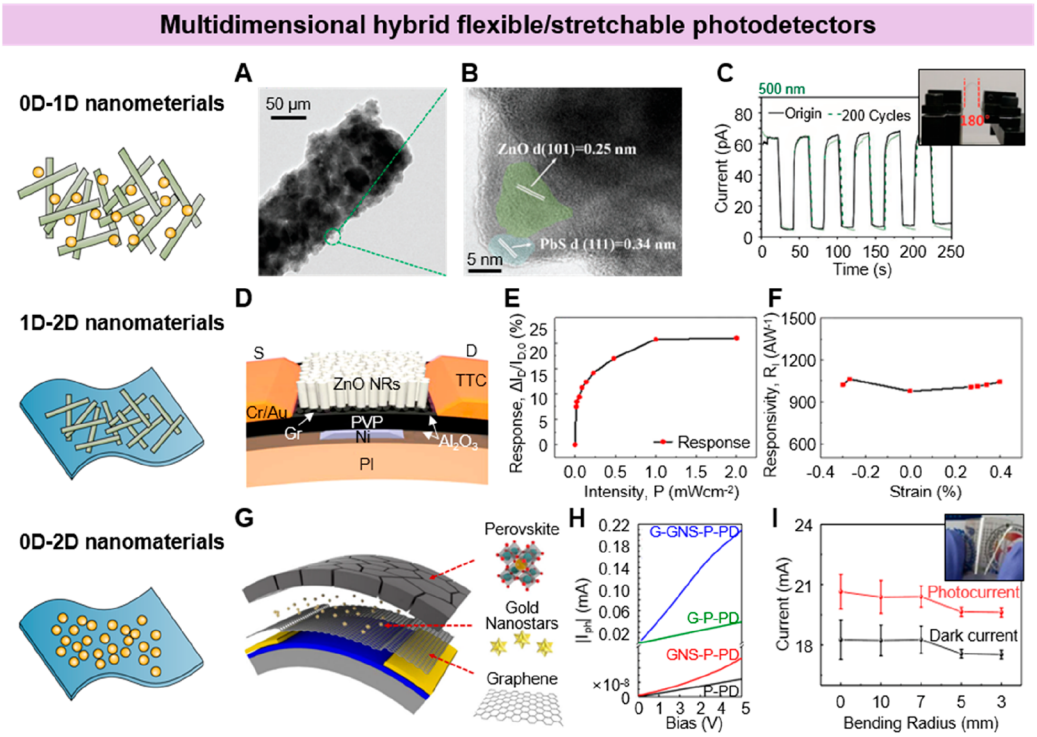

Figure 34. Multidimensional hybrid flexible/stretchable PDs. (A) TEM and (B) HRTEM images of ZnO NW with PbS QDs. (C) $I-T$ curves of the device before and after 200 bending cycles with bending degree of 180°. The inset is a photograph of bended device. Reproduced with permission from ref 747. Copyright 2017 John Wiley & Sons, Inc. (D) Schematic illustration of the hybrid flexible PD of vertical ZnO nanorods and graphene. (E) UV light response of the ZnO nanorods and graphene hybrid PD under various intensities. (F) Responsivity of the device under different strain percentiles. Reproduced with permission from ref 811. Copyright 2015 American Chemical Society. (G) Schematic illustration of flexible hybrid PD with a perovskite layer, gold nanostars (GNSs), and graphene. (H) $I-V$ curves of G-GNS-P-PD, G-P-PD, GNS-P-PD, and P-PD. (I) Photocurrent measurement of flexible hybrid PD with various bending radii and photograph of the bended device (inset). Reproduced with permission from ref 812. Copyright 2020 Springer Nature.

few stacked layers of two materials (Figure 33I and 33J). The dominant photoresponse wavelength changes based on the composition ratio between MoS_2 and g-C_3N_4 in the film (Figure 33K). The dark current decreases as the amount of g-C_3N_4 increases. However, for different wavelengths of 365 and 532 nm, the high responsive wavelength differs according to the composition ratio, indicating that the photoresponse range can be broadened by modulating the composition ratio. The flexible broadband PD was fabricated by depositing the 5:5 hybrid film and metal electrodes on a paper substrate. Under various bending states, the device presented stable photoswitching behaviors, exhibiting its potential for integration into high-performance flexible optoelectronics (Figure 33L).

The high-resolution patterning process of perovskite thin films is essential for practical use as an active layer in optoelectronic devices. Lee et al. reported the high-definition spin-on-patterning (SoP) process of an inorganic−organic perovskite thin film.[810] The prepatterned hydrophobic/hydrophilic surface consisting of a densely packed self-assembled monolayer (SAM) and an oxide substrate, respectively, enables the high-resolution patterning based on the wetting/dewetting behavior of the perovskite precursor solution (Figure 33M). In the SoP process, the spin-coating rate and processing temperature mainly affect the pattern yields (Figure 33N). For the representative material of $CH_3NH_3PbI_{3-x}Cl_x$, as the spin-coating rate increases, the solution thickness rapidly approaches a critical thickness ($H_{critical}$), and a thickness lower than $H_{critical}$ results in higher pattern yields by facilitating dewetting. Consequently, a high pattern yield is available through the modulation of the spin-coating rate and temperature. Based on the SoP process, a flexible multiplexed image sensor was fabricated on the PI substrate (Figure 33O). Each pixel on the imager consists of a perovskite photodiode with a Si NM blocking diode. The On/Off current density of a perovskite-on-silicon pixel showed 2.02 and 2.83 × 10^{-2} mA cm^{-2} at −1 V, respectively. The SoP process enables high-resolution patterning on a flexible perovskite thin film, enhancing compatibility with other electronics (Figure 33P).

5.4.2. Multidimensional Hybrids. The hybrid of different dimensional nanomaterials (e.g., 0D-1D, 1D-2D, 0D-2D) has been introduced to improve device performance beyond that of a single nanomaterial.[795−800] Zheng et al. demonstrated the PbS QDs/ZnO NWs heterostructure-based PD to broaden the photoresponsive wavelength region via electrospinning and exchanging processes (Figure 34A and 34B).[747] Blending ZnO NWs with a narrow bandgap and PbS QDs with a wide bandgap allows for broadening the spectral response range from ultraviolet to NIR. The PbS QD film is spin-coated multiple times on the ZnO electrospun NW array to form the heterostructure composites. The 1,2-ethanedithiol (EDT) solution facilitates the ligand exchange to densify the PbS QDs. The PbS/ZnO heterostructures sufficiently respond under various wavelength light conditions ranging from 300 to 1,000 nm, indicating the broadened photoresponse range compared to pure PbS QDs or ZnO NWs. Besides, the PbS/ZnO-based PD presented a faster response speed than the

https://doi.org/10.1021/acs.chemrev.3c00548
Chem. Rev. XXXX, XXX, XXX−XXX

homogeneous devices. The flexibility and mechanical stability of the device were tested by measuring the photocurrent under an extreme bending state and repeated bending cycles (Figure 34C). Despite the extreme bending angle and repeated bending of 200 cycles, the heterostructure PD maintained the performance of the flat state. Furthermore, the proposed approach can be applied to develop other 0D-1D materials, including ZnO/PbSe and CdO/PbS heterostructures, for similar performance enhancements.

The ZnO nanostructures have been employed to develop UV-sensitive PDs due to their high absorption in UV region. Although the 1-D ZnO nanostructures, including NWs and NRs, show sufficient flexibility and high sensitivity, the weak contact to metal electrodes that easily degrades the performance from bending hinders their practical utilization. For a high-performance flexible UV PD, a hybrid of 1-D ZnO NRs and 2-D graphene has been demonstrated (Figure 34D).[811] Graphene serves as a template for the ZnO NRs growth and a charge transport layer for flexible channel material. Under various UV intensities, the photoresponse of the device rapidly increases with UV increases and saturated at high UV intensities (Figure 34E). To validate the device flexibility, compressive and tensile strains were applied. The photoresponsivity showed that the ZnO NRs/graphene hybrid PD exhibits high mechanical stability to external strains, indicating the high device flexibility (Figure 34F).

The graphene-based PDs show great performances, such as a fast response time and high compatibility with other electronics, owing to their high carrier mobility and mechanical flexibility. However, the low absorption in cross-section and fast recombination rate in pure graphene devices still pose challenges for practical applications. A hybrid material consisting of gold nanostars (GNSs), perovskites, and graphene was introduced to develop flexible, high-performance hybrid graphene PDs (Figure 34G).[812] The sharp tips and spherical core of GNSs enhance the light trapping effect derived from a plasmonic effect, thus inducing strong light amplification. In addition, carrier transfer is improved by combining graphene and perovskites, enabling efficient light harvesting. Four different PDs—perovskite, GNS-perovskite, graphene-perovskite, and graphene-GNS-perovskite—were fabricated to validate the enhanced device performance. In $I-V$ characteristics, graphene-perovskite hybrid devices presented outstanding photoresponse, and notably, the plasmonic effect of GNSs further increased the photocurrents (Figure 34H). The localized surface plasmon resonance effects were investigated through finite-difference time-domain calculation of electric field intensity distribution under blue light of 460 nm in the graphene-perovskite film and graphene-GNS-perovskite film, exhibiting intensified electric field distributions surrounding the GNS at the perovskite layer. Bending tests with various radii and cycles were conducted to validate the performance of the flexible hybrid PD fabricated on the PET substrate. The device showed a sufficient photoresponse and high stability even at a bending radius of 3 mm and after the 1,000 bending cycles (Figure 34I).

6. REPRESENTATIVE HUMAN-CENTRIC APPLICATIONS OF FLEXIBLE AND STRETCHABLE PDS

The PD is one of the primary components for optical sensing in human-robot interactive optoelectronics, including robotic vision systems for autonomous vehicle, drone, surveillance cameras, and health-monitoring wearable devices. While modern Si PD arrays have predominantly been utilized in artificial vision, their rigidity constrains further advancements in terms of system simplification/miniaturization, imaging quality enhancement, and efficient processing. These features that provide key visual information are essential for both human-robot interaction and robotic decision-making. In this regard, flexible/stretchable PD arrays, based on the aforementioned material and structural engineering techniques,[17,173,614,813−815] have been extensively employed to develop artificial vision systems, imitating ocular structures of animal eyes (e.g., curved retina) that is simple but high-performance. Meanwhile, PDs in wearable devices acquire light signals reflected or scattered from the body surface for health monitoring and diagnosis.[613] To collect accurate biosignals and reduce user's discomfort, even during long-term operation, device flexibility and stretchability for achieving conformal contact with the skin are important. This section will cover various applications of artificial vision systems and biosensing systems that incorporate flexible and stretchable PDs in human-robot interactive optoelectronics.

6.1. Artificial Vision Systems

Sensing ability is a crucial factor to most animals for survival that requires tons of external information from visual, auditory, and tactile cues. Visual information, in particular, accounts for a significant portion of the surrounding data, leading to the development of artificial vision systems.[816] The camera, composed of multiple lenses and a planar image sensor, has become a fundamental design of the artificial vision system. With the recent advances of electronics and mechanics, modern machines and robots carry out multiple tasks via diverse sensing systems, including vision.[934,935] Thus, the artificial vision systems have been incorporated as a visual component of machines and robots,[936−938] rather than being a solitary system. This transition necessitates the advanced artificial vision system that has lightweight, small form factor, low energy consumption, and functionalized features (e.g., panoramic vision, object tracking, and high contrast imaging). Regardless of the mature technologies in complementary metal-oxide semiconductor (CMOS) image sensors, conventional cameras suffer from drawbacks in optical and physical properties due to their planar sensor plane.[817,818] Since the lens naturally focuses on the curved image plane, called the Petzval surface, the use of planar image sensors inevitabily results in bulky and complex lens design for compensating a disparity between focal image and sensor plane.[819] Meanwhile, biological eyes have evolved to have a compact and simplified lens configuration attributed by a curved retina or array of individual optical units.[820−824] Therefore, the natural ocular structure implies that a curved form of the PD array can be a way to realize simple but high-quality artificial vision systems, bringing a need of flexible and stretchable image sensors.[817,825−831]

In order to develop curved image sensors, material- and design-based fabrication techniques have been extensively investigated. For example, an ultrathinning technique is adopted to increase the flexibility of the PD array by reducing the total device thickness. However, although the ultrathin device is flexible enough to be bent, it is readily torn or wrinkled when attempting to conformally contact the hemispherical surface, unless it has sufficient stretchability. In this regard, both flexibility and stretchability are vital in the curved

https://doi.org/10.1021/acs.chemrev.3c00548
Chem. Rev. XXXX, XXX, XXX−XXX

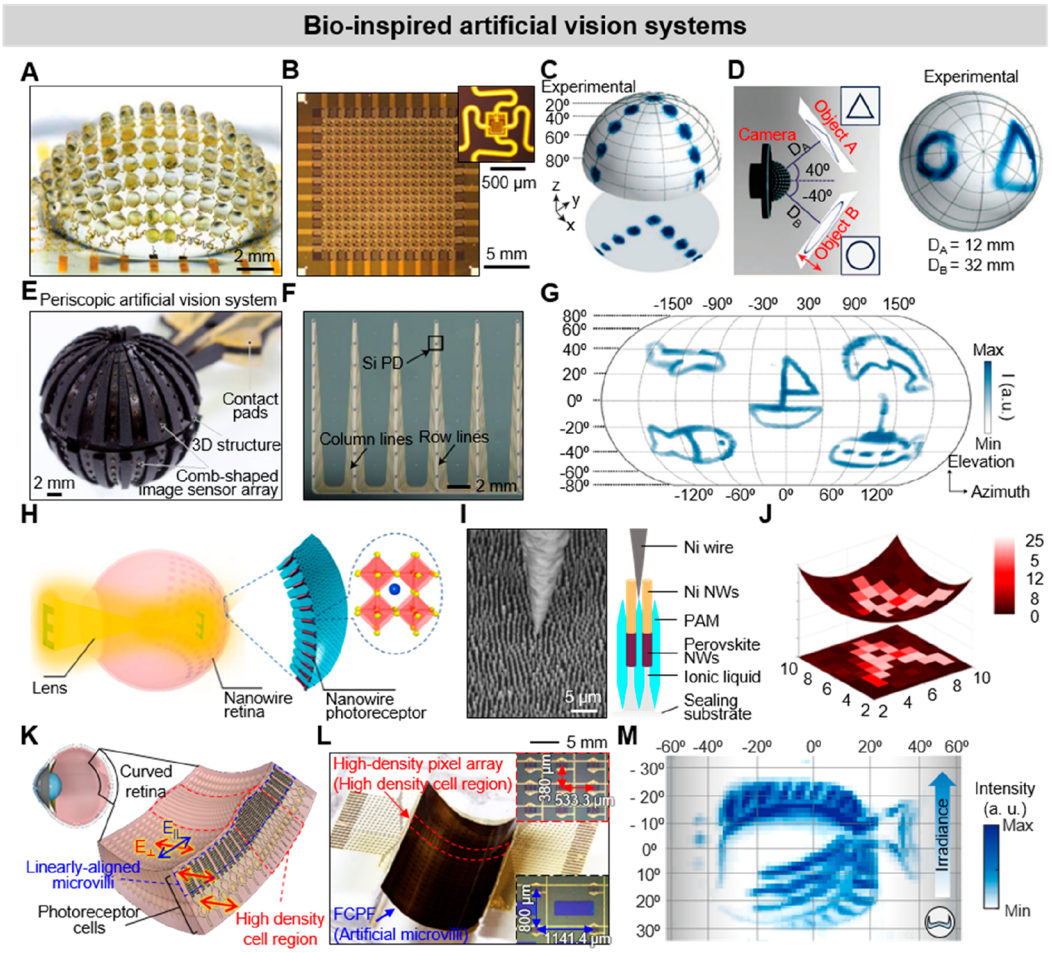

Figure 35. Bioinspired artificial vision systems. (A) Photograph of a curved arthropod-eye-inspired imaging device. (B) Photograph of a 16 × 16 silicon photodiode array with serpentine interconnects. The inset is an enlarged view of a single photodiode. (C) Imaging demonstration of wide field of view from −80° to 80°. (D) Schematic illustration of experimental setup with two objects (left) and resulting image (right). Reproduced with permission from ref 835. Copyright 2013 Springer Nature. (E) Photograph of periscopic artificial vision systems. (F) Photograph of a comb-shaped PD array. (G) Panoramic imaging result from artificial vision in exploded view. Reproduced with permission from ref 12. Copyright 2022 Springer Nature. (H) Schematic illustration of a biomimetic electrochemical eye (EC-EYE) system and perovskite NW photoreceptor on the PAM template. The inset is the crystal structure of perovskite NW photoreceptor. (I) SEM image (left) and schematic illustration (right) of the Ni microwire contact to the NW photoreceptor array. (J) Reconstructed image results of letter "A" acquired from the EC-EYE. Reproduced with permission from ref 750. Copyright 2020 Springer Nature. (K) Schematic illustration of a cuttlefish eye and cross-section of its retina. (L) Photograph of cylindrical silicon photodiode array with surface-integrated flexible CNT polarization film (FCPF). The insets are enlarged view of PDs in two different pixel density regions. (M) Imaging result of a fish-shaped object under uneven illuminating condition. Reproduced with permission from ref 840. Copyright 2023 American Association for the Advancement of Science.

imager development. Recent researches in the curved PD array have utilized various fabrication strategies such as island-bridge structures with designed metal interconnects (e.g., serpentine design) that imparts stretchability between unit PD cells; and direct growth on the curved template. In this subsection, bioinspired artificial eyes with the curved image sensors will be introduced to provide examples of next-generation cameras for robotic vision systems.

The compound eye, mostly found in insects or crustaceans, is based on the convex array of an optical unit composed of a tiny lens and a few or several photoreceptor cells.[614,832−834] The convex array of vision systems exhibits various optical characteristics such as a wide field of view, high motion sensitivity, and infinite depth of field.[14] In order to exploit their optical advantages, an artificial compound eye camera inspired by arthropod vision was developed (Figure 35A).[835] The 16 × 16 elastomeric microlens array was aligned on top of the Si photodiode array, consisting of total 180 artificial ommatidia comparable to those of fire ants. A serpentine interconnection design was adopted in the electrodes of the Si photodiode array for converting the flat device into the convex hemispheric structure, while releasing external strains (Figure 35B). The convex geometry of the system allows a wide field of view imaging of 160 degrees with minimized optical aberrations (Figure 35C). The expanded depth of field was also validated by the focused images of two objects at different distances (Figure 35D), supporting a merit of the compound eye (e.g., infinite depth of field).

Recently, another compound eye camera that can focus images both in water and on land with an extremely wide field of view of nearly 360 deg was demonstrated, mimicking the vision of a fiddler crab (Figure 35E).[12] The comb-shaped artificial ommatidium array, composed of 16 subunits with 8 pixels of each unit (total 128 pixels), was utilized to cover most

https://doi.org/10.1021/acs.chemrev.3c00548
Chem. Rev. XXXX, XXX, XXX−XXX

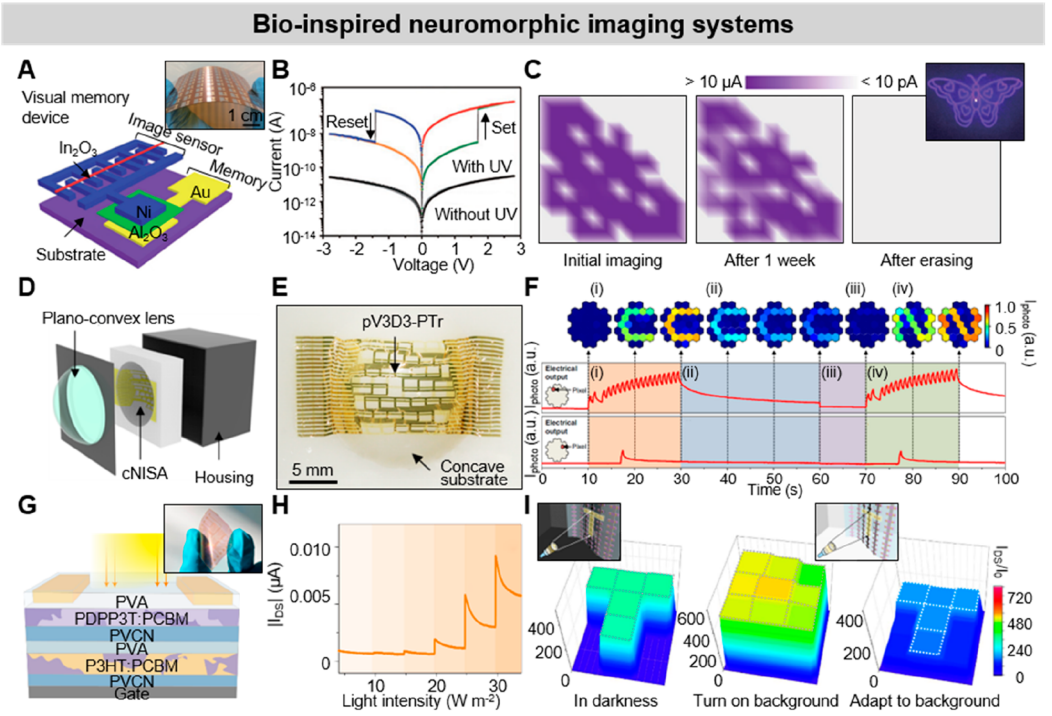

Figure 36. Bioinspired neuromorphic imaging systems. (A) Schematic of the bioinspired visual memory device: image sensor and resistive switching memory. The inset is a photograph of the bended device on the flexible PI substrate. (B) *I*−*V* characteristics of the bioinspired visual memory unit with and without UV light. (C) Imaging data storage and reset features of the bioinspired visual memory device. The inset is a patterned light object image. Reproduced with permission from ref 852. Copyright 2018 John Wiley & Sons, Inc. (D) Schematic illustration of the curved neuromorphic imaging systems in exploded view. (E) Photograph of a curved neuromorphic image sensor array based on the MoS_2-pV3D3 pTr. (F) Image preprocessing demonstrations from noisy optical inputs: (i) preprocessed image acquisition of C-shape object, (ii) decay of the stored C-shape image, (iii) reset of the device, (iv) new image acquisition of N-shape object. Reproduced with permission from ref 20. Copyright 2020 Springer Nature. (G) Schematic of an organic active adaptation transistor (OAAT). The inset is a photograph of the flexible 3 × 3 OAAT array. (H) Current response of the OAAT under various light intensities. (I) Demonstration of human-inspired visual adaptation in the flexible OAAT array. The T-shaped light is projected onto the device under bright (right inset) and dark light conditions (left inset). Reproduced with permission from ref 853. Copyright 2021 Springer Nature.

surfaces of the hemisphere for periscopic vision (Figure 35F). Each pixel data was acquired from the PD array to a customized data acquisition board on a printed circuit board (PCB) that consists of an analogue-to-digital converter (ADC) and field programmable gate array (FPGA) chips. Then, the collected data was transmitted to the computer by USB-based serial communication. The spherical geometry of the device can capture panoramic images vertically 160 degrees by horizontally 300 degrees of field of view (Figure 35G). In addition, the microlens for the artificial ommatidia was fabricated by stacking multiple optical layers with different refractive indices. These stacked layers make incident light experience a gradual change in refractive indices from the flat top surface layer to the bottom layer, endowing the lens that can focus both in water and on land.

Meanwhile, various curved imagers have been investigated to implement the artificial vision of the chambered eye.[20,164,178,666−668,750,836−838] The chambered eye, another type of biological eye mostly found in vertebrates, is composed of a single ball lens and a curved retina that offers low aberration imaging attributed by an optimized retina curvature fitting with the image plane of the lens, and high resolution imaging from highly densified photoreceptor cells.[839] To fully emulate human vision, a photoreceptor array based on vertically grown perovskite NWs was developed (Figure 35H).[750] The perovskite NWs were vertically grown inside a hemispherical PAM template. The growing technique based on the vapor-phase deposition process also allows a high-density NW array to implement high-resolution curved imagers. The acquired data in the photoreceptor array were transferred via liquid-metal wires to a 100 × 1 multiplexer on a PCB controlled by a computer. Although the device validation was conducted with a limited number of pixels (10 × 10 pixels) due to the lack of electrode connecting techniques, the imaging demonstration based on the manual electrode alignment has shown a potential of high-resolution imaging devices (Figure 35I and 35J).

Another flexible image sensor based on island-bridge structures has been demonstrated for high-quality imaging under variant light environments, inspired by the cuttlefish vision.[840] The cuttlefish has evolved to acquire clear vision under vertically uneven light illumination owing to its irregular W-shaped pupil, polarization vision via stacked microvilli, and high-resolvability of target visual fields in high-density photoreceptor cell region of the retina (Figure 35K). To implement artificial cuttlefish vision systems, a cylindrical Si photodiode array (c-Si-PDA) was fabricated with uneven pixel distributions (e.g., low density region of 15 × 15 pixels and high density region of 5 × 31 pixels), which has high pixel density in the specified region for high-resolution imaging in the region of interest (RoI), similar to the cuttlefish retina (Figure 35L). The flexible CNT polarization film (FCPF),

https://doi.org/10.1021/acs.chemrev.3c00548
Chem. Rev. XXXX, XXX, XXX−XXX

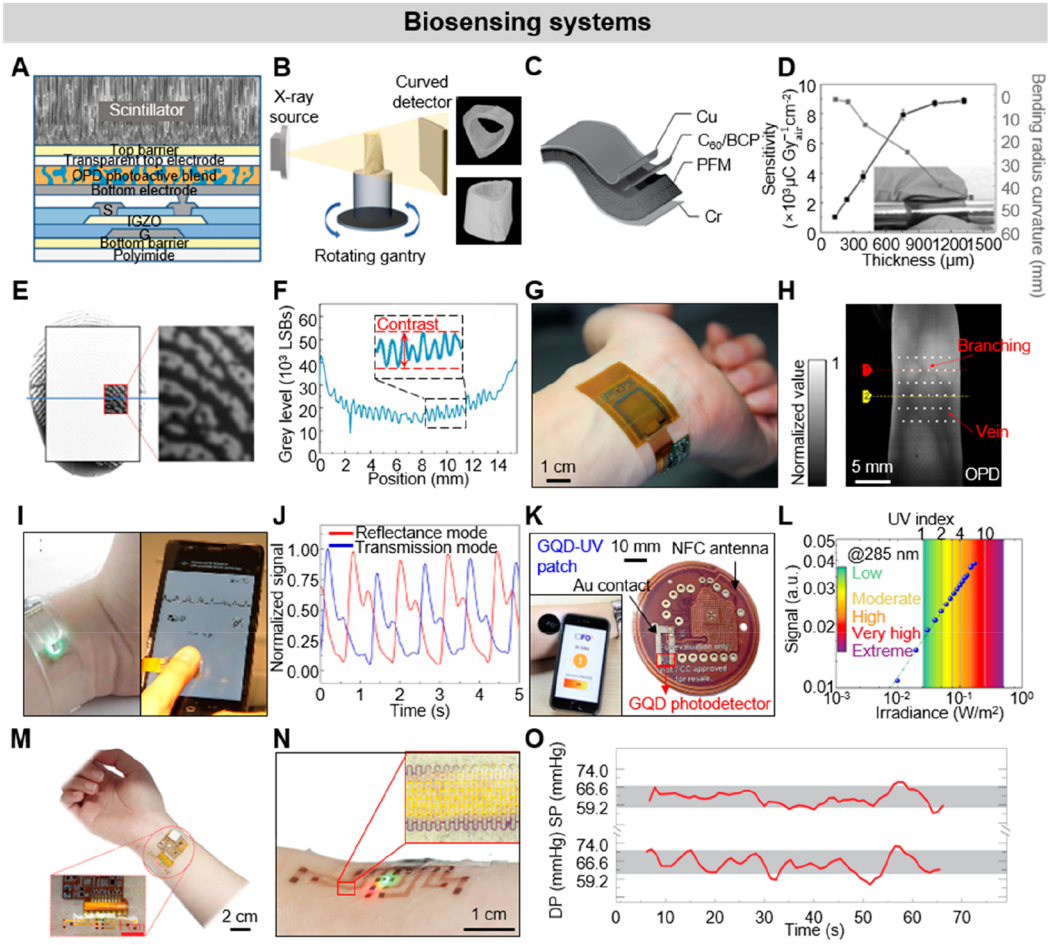

Figure 37. Biosensing systems. (A) Cross-sectional schematic of curved digital X-ray detector. (B) Schematic of cone beam computed tomography (CBCT) X-ray imaging with curved detector. The right inset shows 3D reconstructed images of bone phantom. Reproduced with permission from ref 858. Copyright 2020 Springer Nature. (C) Schematic of a perovskite-filled membrane (PFM) device structure. (D) Measurements of the device sensitivity and bending radius curvature according to device thickness. The error bars are from sensitivities of three devices at each film thickness. The inset shows a photograph of a bended PFM device. Reproduced with permission from ref 859. Copyright 2020 Springer Nature. (E) Fingerprint image from the flexible scanner. The right inset shows close-up view of partial fingerprint that exhibits level 3 details of pores and minute. (F) Signals extracted from LSBs of the cross-section line (blue) in (D). Reproduced with permission from ref 862. Copyright 2021 Springer Nature. (G) Photograph of a conformable imager attached on a wrist. (H) Vein image on a finger using flexible organic PDs. Reproduced with permission from ref 106. Copyright 2020 Springer Nature. (I) Heart rate sensing bracelet on reflectance mode PPG with GQD PDs (left), and pulse monitoring health patch on a finger (right). (j) Normalized PPG signals from health patches with flexible GQD PDs in both reflectance and transmittance modes. (K) Photograph of the GQD PD-based UV health patch. The inset shows the mobile UV index monitoring platform connecting to health patch on the arm. (L) NFC output signals according to the UV irradiance at 285 nm. Reproduced with permission from ref 877. Copyright 2019 American Association for the Advancement of Science. (M) Photograph of the skin-like wearable systems on the wrist with an enlarged view of the device (inset). (N) Photograph of the skin-like device attached on skin. The insets show the detailed features of watch-chain interconnects. (O) Blood pressure measurements during subject walking via skin-like device on the wrist. The gray blocks are ±10 mmHG error. Reproduced with permission from ref 878. Copyright 2020 Oxford University Press.

which acts as the stacked microvilli, was seamlessly transferred to the c-Si-PDA, enabling the discrimination of the polarization state of incident light. By focusing through the W-shaped pupil, the artificial cuttlefish lens, and the c-Si-PDA, the imaging performance was validated in terms of uneven light balancing and high-resolution in RoI (Figure 35M).

The ultimate goal of biological vision systems includes not only visual data collection but also data processing to extract useful information for survival. For instance, human vision senses light signals and efficiently handles the data via the neural process in the visual cortex of the brain to acquire, memorize, and process visual information, enabling the classification and recognition of object size and distance. In contrast, conventional imaging devices perform visual tasks by integrating the image sensor with complementary backend electronics, including central processing units (CPUs), memory devices, and graphics processing units (GPUs), which results in several drawbacks in terms of computing speed and power consumption.[13,841] To realize efficient vision systems mimicking the human visual process, the imaging device that enables both image acquisition and data processing has attracted great attention in recent years.[633,842−851]

The flexible visual memory device has been demonstrated to implement human visual memory by using resistive switching memristors integrated with UV-sensitive image sensors on the flexible PI substrate (Figure 36A).[852] The Al_2O_3-based memristors act as a two-terminal geometry of synapses, operating in two logic states of On/Off states by switching

https://doi.org/10.1021/acs.chemrev.3c00548
Chem. Rev. XXXX, XXX, XXX−XXX

the resistance between the high resistance state (HRS) and low resistance state (LRS), while the In_2O_3-based PDs are stimulated by the UV light for image acquisition. The $I-V$ characteristic of the fabricated visual memory unit was measured with and without UV illumination, showing the resistance switching behavior of the memristor (Figure 36B). The 10 × 10 pixels of visual memory array demonstrates the ability to store and erase the acquired visual information during the imaging test with the patterned light. The imaging pattern was maintained over a week unless the reset voltage is applied (Figure 36C).

The human vision-inspired neuromorphic imaging device was developed for efficient imaging and visual recognition.[20] The human vision systems consist of a simplified optical format due to the hemispherical retina that minimizes optical aberrations and the efficient visual process framework via the optic nerves connected to the visual cortex in the brain. Inspired by these features, the curved geometry was applied to the neuromorphic PD array (total 31 pixels), and the device was combined with a single plano-convex lens, constructing the artificial visual recognition systems that can collect images and conduct data preprocessing (Figure 36D and 36E). The light-sensitive synaptic plasticity (i.e., short-term plasticity (STP) and long-term plasticity (LTP)) was realized via the pTr based on the heterostructure of MoS_2 and poly(1,3,5-trimethyl-1,3,5-trivinyl cyclotrisiloxane) (pV3D3), owing to quasi-linear time-dependent photocurrent generation and prolonged photocurrent decay of the pV3D3 pTr (pV3D3-pTr). The photocurrents from the pixels in the curved neuromorphic image sensor array are amplified and individually processed by the current amplifiers and ADC on the PCB. The imaging demonstration with noisy optical signals validated the preprocessing capabilities of the pV3D3-pTr without additional memory electronics or complex optical systems (Figure 36F).

The biological vision systems conduct feedforward visual adaptation in response to dim or strong light stimuli. By emulating feedforward visual adaptation, a phototriggered organic active adaptation transistor (OAAT) consisting of two bulk heterostructures was fabricated for active photoadaptation under variant light illumination (Figure 36G).[853] The real-time changes in dynamic light intensities demonstrated that the OAAT system responds to stimuli in a step sequence. Therefore, the device operates effectively in various light levels, similar to biological systems (Figure 36H). The flexible 3 × 3 pixel array based on the OAATs on a PET substrate was fabricated as a prototype. Although the image contrast decreases right after exposure to the bright-light background, the device gradually adapts to the background light condition, and the object pattern reveals a sufficiently recognizable contrast (Figure 36I).

6.2. Biosensing Systems

Biosensors measure biosignals such as static signals (e.g., photographs of bones, organs, vessels) and dynamic signals (e.g., blood oxidation, heart rate, and blood pressure) to extract essential information on health conditions or biometric. Flexible PDs are of interest in biosensing applications because of their softness, enabling uniform contact with the skin, thereby reducing noise and improving detection accuracy. The mechanical properties of flexibility and stretchability, photoresponsivity, detecting speed, and resolution need to be modulated according to the target biosignals. The following sections introduce a variety of flexible sensing devices in biomedical applications.

6.2.1. X-ray Imaging Systems. X-ray imaging is one of the static biosignal sensing systems that can visualize the internal body, including organs and bones. The transmittance differences between tissue types enable the extraction of image contrast from X-ray radiation. Depending on the method used to convert X-rays to electric signals, X-ray detectors can be categorized into two major types: indirect conversion and direct conversion. The indirect-type detector consists of a scintillator that emits visible light via the absorption of the X-rays and a photosensor that converts the emitted visible light to electric signals, while the direct-type detector directly detects and converts the X-rays to electric signals. Flat X-ray detectors in both conversion types have predominantly been developed as diagnostic tools in biomedical applications.[854] However, several drawbacks in terms of X-ray dose reduction and low imaging quality (e.g., vignetting) in the rigid and planar detectors necessitate changes to flexible devices.

To overcome the constraints of planar systems, flexible X-ray detectors have been developed.[789,855−857] For example, Breemen et al. demonstrated a curved X-ray detector that consists of a flexible cesium iodide (Csi) scintillator and organic PDs (480 × 640 pixels) with an indium gallium zinc oxide (IGZO) backplane (Figure 37A).[858] By using curved detectors, 3D X-ray imaging was conducted with a rotating gantry, successfully capturing the 3D volume image of the bone phantom (Figure 37B). On the other hand, a direct conversion type X-ray detector array (7 × 11 pixels) based on the perovskite-filled membranes (PFMs) was developed (Figure 37C).[859] The porous nylon membrane as a template was filled with MHP crystals in a liquid form through the vacuum process to enhance the device flexibility. The minimum bending curvature and device sensitivity were tested according to the different PFM thicknesses (Figure 37D). Although the bending curvature can be minimized by thinning the PFM, the device sensitivity, which decreases with thickness, should be considered to attain sufficient X-ray response of the devices.

6.2.2. Biometric Authentication Systems. Various biometrics have been developed for personal identification with the advancement of optoelectronic devices. At present, fingerprints and vein patterns are of interest as widely used subjects in biometric authentication. In fingerprint biometrics, the unique features of fingerprints, such as singular points (e.g., delta and loop) at the global level, minute details of local ridge characteristics at the local level, and intraridge details (e.g., sweat pores) at the fine level, are the key information that requires high-resolution imaging devices.[860−862] Since fingerprints are acquired by scanning the uneven and curvilinear surfaces of the fingertip, a flexible imager that can seamlessly contact the fingertip is highly desired. Recently, a flexible fingerprint imager was demonstrated by using MHP photodiodes and an amorphous IGZO transistor backplane via solution-processing methods (Figure 37E).[862] The fabricated device achieved a high-resolution of 509 PPI and 1,016 PPI, satisfying the minimum resolution of 500 PPI for fingerprint authentication. The obtained fingerprint image from the device shows the intraridge details of pores at the fine level, and the ridge patterns with sufficient contrasts are presented in the cross-section graph of the fingerprint image (Figure 37F).

Vein imaging has attracted great attention in biomedical applications because it provides dual information on static and dynamic biosignals (e.g., vein patterns and blood flow).

https://doi.org/10.1021/acs.chemrev.3c00548
Chem. Rev. XXXX, XXX, XXX−XXX

Regarding static features for biometric authentication, similar to fingerprints, vein offers distinct characteristics of branch patterns of blood vessels, including branch points and angles. Yokota et al. developed a flexible imager consisting of an organic photodiode array and polycrystalline silicon TFT backplane (Figure 37G).[106] The high-resolution imager (252 × 256 pixels, 508 PPI) allows to obtain images of veins inside the finger, clearly showing branch patterns (Figure 37H). Simultaneously, the high speed of the device (i.e., 41 frames per second (fps) can monitor dynamic PPG signals from the pulse wave intensity in the finger.

6.2.3. Health Monitoring Systems. Optical sensors in wearable devices can assist in personal health maintenance by continuously monitoring vital signs (e.g., heart rate, blood oxidation, and respiratory rate)[584,175,863−870] and UV exposure.[871−876] The characteristics of optical sensing, such as noninvasiveness and long-term data acquisition, are advantageous for enhancing public healthcare. Recently, there is a growing need to develop flexible and stretchable PDs to overcome issues in the conventional rigid structure such as motion artifacts and user discomforts. Nanomaterial-based PDs can be a suitable approach in wearable applications due to their high flexibility/stretchability, biocompatibility, and high performance. This subsection will cover user-interactive health monitoring devices.

Flexible PDs based on graphene and QD film were developed for wearable devices that can monitor heart rate, oxygen saturation, and respiratory rate.[877] The graphene and PdS colloidal QD thin film enhance the device flexibility and transparency by controlling the QD film thickness. Several prototypes of wearable devices using flexible PDs were fabricated, including bracelet-type, health patch on the mobile screen, and wireless UV monitoring patch (Figure 37I). The flexible bracelet and patch support PPG by detecting volumetric changes in blood vessels based on two different modes: reflectance and transmission modes, respectively (Figure 37J). In the reflectance mode, the green LED is coupled with the PDs so that the reflected light from the microvessels in the wrist is detected, allowing the extraction of volume changes according to blood circulation, enabling the user's heart rate monitoring. On the other hand, the transmission mode adopts ambient white light transmitted through the finger, and then it is detected from the PDs of the health patch on the mobile screen (Figure 37K). Owing to the broad wavelength sensitivity (300−2000 nm) of PDs, the UV monitoring patch was also demonstrated by adding a flexible short-pass filter that only transmits desired UV wavelength ranges (<400 nm). The flexible circuit boards in the patch can wirelessly transfer data and power to the smartphone. The output NFC signal exhibits a linear response to increased UV irradiance, which can notify the UV index of the ambient environment to the user (Figure 37L).

Skin-like optoelectronic systems that measure continuous noninvasive arterial pressure (CNAP) were demonstrated (Figure 37M).[878] The device consists of three ILEDs, including GaAs-based IR (850 nm) and red (515 nm) light, Al_2O_3-based green light, and four Si-based PDs (400−1100 nm). The metal interconnects of Cu/Cr with 160 nm thickness were patterned with a watch-chained shape, presenting low resistance and high stretchability (Figure 37N). The nanodiamond grinding process was adopted to fabricate thin LEDs and PDs for implementing skin-like devices. The optoelectronics are thinned through mixed solutions of nanodiamond and deionized water. For CNAP measurements, the pulse transit time (PTT) was acquired by detecting PPG signals. In the blood pressure measurements, while walking, the SP and DP showed fluctuating values near 143 and 66 mmHg, respectively, with the maximum absolute error of less than ±14 mmHG (Figure 37O). These errors are acceptable in blood pressure monitoring under the noisy condition of the arm swing during walking.

7. CONCLUSIONS AND PERSPECTIVES

As discussed in this review, technological advancements for flexible and stretchable LEDs and PDs are creating new opportunities for future human-centric electronic devices, especially in the healthcare field. Accompanied by the progress in AI technology, the high-quality physiological data collected from these soft optoelectronic devices can be used to diagnose several diseases including fatal ones. As such, the possibility of high-precision diagnosis using AI models has been readily reported in various scientific and medical journals.[906,907] The users will be able to access the information through wearable displays and take instant measures through the wearable and implanted devices equipped with proper actuating modules if necessary, thus enabling remote diagnosis and therapy. However, the practical realization of such a remote biomedical system seems premature, requiring tremendous efforts from interdisciplinary fields of materials science, electronic device engineering, AI, and medicine. Also, numerous challenges still remain in the materials and device technologies, especially in terms of electrical performance, device and system integration, power management, and safety.

7.1. Challenges for High-Performance, Reproducible Device Fabrication and Their Integration

Despite the significant technological developments for high-performance soft optoelectronic materials and devices, the performance metrics are still incomparable to those made from inorganic, well-established rigid materials, especially after experiencing repetitive deformations. For instance, the percolation of conductive/emissive/photosensitive nanomaterials inside of the soft composites is subject to damage, disconnection, and disentanglement due to fatigue accumulation, which in turn may result in irrecoverable electrical/optoelectronic performance.[25] Correction of the loss in performance by machine-learning techniques may be a viable solution,[208] but further study is required on how the degradation in separate functional layers affects the overall device performance, the range of performance variance in the layers, and how to distinguish the degradation source and identify the modification factor. These areas remain largely unexplored, and fundamental solutions are required to compensate for the degradation in the materials performance. While the device design approaches that utilize the well-established inorganic materials may be adopted, novel device designs and layouts that allow higher device density and circuit design is crucial for practical applications.

Developments in the strategies for reproducible and reliable device fabrication are also required. Since the layers of soft devices are mostly solution-based processes, carefully considering the base solution of different functional materials is crucial to avoid unwanted chemical attacks when sequentially depositing one on top of the other. Transfer processes are required for the layers incompatible for direction deposition, which often results in poor interface qualities between the

https://doi.org/10.1021/acs.chemrev.3c00548
Chem. Rev. XXXX, XXX, XXX−XXX

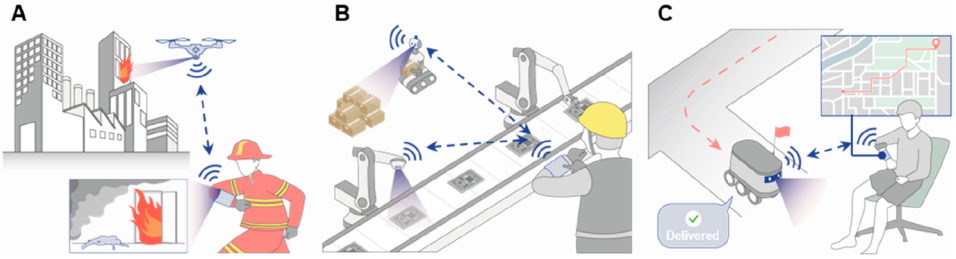

Figure 38. (A–C) Convergence of flexible and stretchable optoelectronic devices with robotics for futuristic applications.

contacted layers. Commonly used methods to improve the interface quality, such as rapid thermal annealing, cannot be applied due to the low thermal budget of the soft materials, so additional methods need to be developed to address the interface issues. Poor interface may be detrimental to the device performance, especially when the devices are subject to mechanical deformation.[55,77] In addition, since many conventional vacuum-based microfabrication tools are not applicable to soft device fabrication, achieving large-area uniformity and reproducibility remains a major challenge. In this regard, scalable processing techniques must be developed to mass produce these soft devices with minimized performance variances.

In addition to the device fabrication techniques, in-depth research needs to be conducted on integrating different soft electronic and optoelectronic functional devices. To achieve multifunctionality, different functional devices must be integrated as a system in a single platform, but this may be extremely difficult as the requirements of material performance may vary between the devices. This means that different materials processes for different functional device fabrication are required to be performed on a single platform, which is highly unlikely to be doable. Even if possible, the assessment of their operation remains, as the functional devices may interfere with one another and exhibit undesirable effects. Investigations on these areas must be accompanied by efforts to downscale the sizes of the soft devices for enhanced performance. To this date, no or extremely few studies report on practical solutions to the described challenges.

7.2. Challenges for Device Management and Safety Issues

Technological advancements are required for flexible and stretchable power modules.[644,908] Batteries are inadequate, especially for implantable devices, since replacing them with new ones requires unwanted surgical procedures that burden the patients or users. In addition, the bulky nature of the battery is unsuitable for biointegration. Developing flexible and stretchable batteries and charging them remotely using RF technology may seem a practical solution, but it may not be applicable for devices that require a consistent power supply for continuous monitoring of physiological activities. Possible heat generation during charging must be checked with utmost priority, as it can be detrimental to the implanted tissues and surrounding microenvironments. In this regard, self-harvesting power from the dynamic micromotions of the implanted tissues and the human body is most desirable in terms of sustaining the device functionality, but significant advancements are required to garner enough energy to empower the soft functional devices.

Finally, the safety issues regarding wearable and implantable devices need to be cleared for actual clinical translation of these soft devices. Since the research on flexible and stretchable electronic and optoelectronic devices for biomedical applications is still in its infancy, there have not been enough studies that reveal long-term stability and reliability for human trials. Most optoelectronic devices require adequate encapsulation and passivation layers at the outermost surfaces, but studies on stretchable encapsulation layers with biocompatibility are lacking as well. For complex operations, such as multiplexable sensors and actuators, active matrices, memory storage/data delivery, and medium-scale circuits, the performance of the basic building block of these soft devices (i.e., stretchable transistors) needs to be significantly improved, especially in terms of operation voltages. To the best of our knowledge, there are only a few studies that report on the operation of stretchable transistors at voltages levels comparable to those of silicon transistors due to the lack of technology for the deposition of high-quality, ultrathin, and stretchable dielectrics.[211] The requirement of high operation voltages (generally from −30 to 30 V for those that employ solution-processed dielectrics) for these stretchable devices is unsafe, especially for biomedical applications.

Although numerous challenges remain, advancements in flexible and stretchable optoelectronic devices, in conjunction with AI technology, offer tangible possibilities for precision medicine based on remote diagnosis and therapy, which undoubtedly will benefit our society and improve the quality of our daily lives. These smart and soft devices are also expected to create synergetic effects when combined with robotic, prosthetic, and/or artificial electronic skin devices, making machines more human friendly and blending into our lives. Possible applications include a wearable display system that shares the vision of a machine (i.e., cameras mounted on a drone), a wearable management system that allows precise control of intelligent robots to replace human labor, and even a delivery system that allows the use of robotic vehicles to carry the deliveries through intimate interaction with the users (Figure 38A–C). We anticipate vigorous endeavors from scientists working in related fields to make this technology come true and for more unexplored but exciting applications.

AUTHOR INFORMATION

Corresponding Authors

Moon Kee Choi − *Department of Materials Science and Engineering, Ulsan National Institute of Science and Technology (UNIST), Ulsan 44919, Republic of Korea; Graduate School of Semiconductor Materials and Devices Engineering, Center for Future Semiconductor Technology (FUST), UNIST, Ulsan 44919, Republic of Korea; Center for Nanoparticle Research, Institute for Basic Science (IBS), Seoul 08826, Republic of Korea;* orcid.org/0000-0003-4536-3393; Email: mkchoi@unist.ac.kr

https://doi.org/10.1021/acs.chemrev.3c00548
Chem. Rev. XXXX, XXX, XXX−XXX

Dae-Hyeong Kim − *Center for Nanoparticle Research, Institute for Basic Science (IBS), Seoul 08826, Republic of Korea; School of Chemical and Biological Engineering, Institute of Chemical Processes, Seoul National University (SNU), Seoul 08826, Republic of Korea; Department of Materials Science and Engineering and Interdisciplinary Program for Bioengineering, SNU, Seoul 08826, Republic of Korea;* orcid.org/0000-0002-4722-1893; Email: dkim98@snu.ac.kr

Young Min Song − *School of Electrical Engineering and Computer Science, Gwangju Institute of Science and Technology (GIST), Gwangju 61005, Republic of Korea; Department of Materials Science and Engineering, Ulsan National Institute of Science and Technology (UNIST), Ulsan 44919, Republic of Korea; Artificial Intelligence (AI) Graduate School, GIST, Gwangju 61005, Republic of Korea;* orcid.org/0000-0002-4473-6883; Email: ymsong@gist.ac.kr

Authors

Sehui Chang − *School of Electrical Engineering and Computer Science, Gwangju Institute of Science and Technology (GIST), Gwangju 61005, Republic of Korea*

Ja Hoon Koo − *Department of Semiconductor Systems Engineering and Institute of Semiconductor and System IC, Sejong University, Seoul 05006, Republic of Korea;* orcid.org/0000-0002-9146-9810

Jisu Yoo − *Department of Materials Science and Engineering, Ulsan National Institute of Science and Technology (UNIST), Ulsan 44919, Republic of Korea*

Min Seok Kim − *School of Electrical Engineering and Computer Science, Gwangju Institute of Science and Technology (GIST), Gwangju 61005, Republic of Korea*

Complete contact information is available at: https://pubs.acs.org/10.1021/acs.chemrev.3c00548

Author Contributions

†S.C., J.H.K., and J.Y. contributed equally.

Notes

The authors declare no competing financial interest.

Biographies

Sehui Chang received her B.S. (2017) from the Department of Physics at University of Suwon. She obtained her M.S. (2020) from the Department of Biomedical Science and Engineering at Gwangju Institute of Science and Technology (GIST). She is a Ph.D. candidate in the School of Electrical Engineering and Computer Science under the guidance of Prof. Young Min Song at GIST. Her current research interest focuses on bioinspired imaging system design/fabrication and the development of advanced optoelectronic devices.

Ja Hoon Koo received his B.S. (2010) and M.S. (2013) in Electrical and Electronics Engineering from Yonsei University. He then worked as a research intern at Prof. Zhenan Bao's group (2013−2014) and earned his Ph.D. (2020) in the Interdisciplinary Program for Bioengineering under the guidance of Prof. Dae-Hyeong Kim at Seoul National University. Since he joined the faculty of the Department of Semiconductor Systems Engineering at Sejong University in 2023, he has focused on intrinsically stretchable electronics and optoelectronics for biomedical applications.

Jisu Yoo received her B.S. (2020) from the Department of Materials Science and Engineering at Ulsan National Institute of Science and Technology (UNIST). Under the supervision of Prof. Moon Kee Choi, she is working on the fabrication and application of intrinsically stretchable optoelectronic devices for her Ph.D. degree at UNIST.

Min Seok Kim received his M.S. (2019) and Ph.D. (2023) in Electrical Engineering and Computer Science from Gwangju Institute of Science and Technology (GIST) under the guidance of Prof. Young Min Song after a B.S. (2017) in Electronic Engineering from Pusan National University. His research focuses on multifunctional imaging systems and advanced optoelectronic devices.

Moon Kee Choi is an associate professor in the Department of Materials Science and Engineering of Ulsan National Institute of Science and Technology (UNIST). She received her B.S. (2009) and Ph.D. (2016) in Chemical and Biological Engineering from Seoul National University under the guidance of Prof. Dae-Hyeong Kim. She conducted her postdoctoral research at UC Berkeley under the supervision of Prof. Seung-Wuk Lee. Now, she is focusing on the development of next-generation optoelectronic-devices, biomedical electronics, and soft robotics with deformable form factors.

Dae-Hyeong Kim is a professor in the School of Chemical and Biological Engineering at Seoul National University, an associate director of Center for Nanoparticle Research of Institute for Basic Science (IBS), and an associate editor of *Science Advances*. He received his B.S. (2000) and M.S. (2002) from the School of Chemical Engineering at Seoul National University. He obtained his Ph.D. (2009) from the Department of Materials Science and Engineering at the University of Illinois at Urbana−Champaign. Since he joined the faculty of the School of Chemical and Biological Engineering at Seoul National University in 2011, he has focused on stretchable and soft electronics for biomedical and energy applications.

Young Min Song is a professor in the School of Electrical Engineering and Computer Science at Gwangju Institute of Science and Technology, an adjunct professor of Artificial Intelligence (AI) Graduate School and Department of Semiconductor Engineering at Gwangju Institute of Science and Technology. He received his B.S. (2004) from the Biomedical Engineering at Yonsei University. He obtained his M.S. (2006) and Ph.D. (2011) in School of Information and Communications at Gwangju Institute of Science and Technology. He worked as a postdoctoral research associate in the Department of Materials Science and Engineering at the University of Illinois at Urbana−Champaign (2011−2013). Since he joined the faculty of the School of Electrical Engineering and Computer Science at Gwangju Institute of Science and Technology in 2016, he has focused on multifunctional nanophotonics, advanced optoelectronic devices/systems, and bioinspired imaging applications.

ACKNOWLEDGMENTS

This work was supported by IBS-R006-D1. This work was supported also by the National Research Foundation of Korea (NRF) grant funded by the Korean government (MSIT) (grant nos. 2023R1A2C3004531, 2021R1I1A1A01060389, 2021R1C1C1007997, 2022R1A5A6000846, and 2021M3H4A3A01062963), and by "Regional innovation mega project" program through the Korea Innovation Foundation funded by Ministry of Science and ICT (grant no. 2023-DD-UP-0015). Lastly, this work was supported by the faculty research fund of Sejong University in 2023.

ABBREVIATIONS

0D = 0-dimensional
1D = 1-dimensional

2D = 2-dimensional
2FPPICz = 2-(4-(9H-carbazol-9-yl)phenyl)-1-(3,5-difluorophenyl)-1H-phenanthro[9,10-d]imidazole
4LG = four-lay methacrylate p-type-doped graphene film
ACEL = alternating current electroluminescent
ADC = analogue-to-digital converter
AI = artificial intelligence
AM = active matrix
AR = aspect-ratio
BP1T = 2,5-di([1,1′-biphenyl]-4-yl)thiophene
BPA = benzylphosphonic acid
BPPI = 4,4′-bis(1-phenyl-phenanthro[9,10-d]imidazol-2-yl)biphenyl
BSE = backscattered-electron
CBCT = cone beam computed tomography
CF = Clear Flex
CL-PVP = cross-linked poly(4-vinylphenol)
CMOS = complementary metal-oxide semiconductor
CNAP = continuous noninvasive arterial pressure
CNN = cellulose/nanowire nanohybrid nanonetwork
CNT = carbon nanotube
CPUs = central processing units
C-PVA = cross-linked poly(vinyl alcohol)
Csi = cesium iodide
c-Si-PDA = cylindrical Si photodiode array
DHNRs = double-heterojunction nanorods
DL = dispersing ligand
DP = diastolic pressure
e-BHJ = elastomeric bulk heterojunction
EC-EYE = electrochemical eye
ECG = electrocardiogram
EDT = 1, 2-ethanedithiol
EDT = 1,2-ethanedithiol
EGaIn = eutectic gallium−indium
EIL = electron injection layer
EL = electroluminescent
EML = emission layer
ENIM-TCB = 1-ethyl-3-methylimidazolium tetracyanoborate
ETL = electron transport layer
FCPF = flexible carbon nanotube polarization film
FEA = finite element analysis
FET = field-effect transistor
FPGA = field programmable gate array
fwhm = full width at half-maximum
GNS = gold nanostar
GNW = granular nanowire
GO = graphene oxide
GOS:Tb = terbium-doped gadolinium oxysulfide scintillator particles
GPUs = graphics processing units
gs- = geometrically stretchable
HIL = hole injection layer
HMI = human-machine interface
HOMO = highest occupied molecular orbital
HPAI = 1-hydroxy-3-phenyl-propan-2-aminium iodide
HRS = high resistance state
HTL = hole transport layer
ICBA = Indene-C60 bisadduct
IGZO = indium gallium zinc oxide
ILED = inorganic light-emitting diode
IQE = internal quantum efficiency
IR = infrared
is- = intrinsically stretchable
is-QDSN = *is*-quantum dot-based semiconducting composite
ITO = indium tin oxide
I−*V* = current−voltage
LEC = light emitting electrochemical cell
LED = light-emitting diode
LLO = laser lift-off
LRS = low resistance state
LS-EFD = liquid substrate electric-field-driven
L-SY-PPV = long phenylenevinylene polymer
LTP = long-term plasticity
LUMO = lowest unoccupied molecular orbital
MCU = microcontroller unit
MHP = metal halide perovskites
NB = nanobelt
NC = nanocrystal
NIR = near-infrared
NM = nanomembrane
NOA63 = Norland Optical Adhesive 63
NP = nanoparticle
NSL = nanospheres lithography
NT = nanotube
NW = nanowire
OA = oleic acid
OAAT = organic active adaptation transistor
OAm = oleylamine
ODA = otadecylamine
ODTS = octadecyltrichlorosilane
OFET = organic field-effect transistor
OLED = organic light-emitting diode
OMO = oxide/metal/oxide
OPA = orthogonal polarizer-analyzer
P3HT = poly(3-hexylthiophene-2,5-diyl)
PAA = poly(acrylic acid)
PAM = porous alumina membrane
PAN = polar polyacrylonitrile
PAni = polyaniline
PATCVD = plasma-assisted thermal chemical vapor deposition
PC = polycarbonate
PCB = printed circuit board
PCG = polycrystalline graphene
PD = Photodetector
PDMS = polydimethylsiloxane
PDPP2T-TT-OD = poly[2,5-(2-octyldodecyl)-3,6-diketopyrrolopyrrole-*alt*-5,5-(2,5-di(thien-2-yl)thieno [3,2-*b*]-thiophene)]
PEDOT:PSS = poly(3,4-ethylenedioxythiophene)-poly(styrenesulfonate)
PEG = polyethylene glycol
PEI = polyethylenimine
PEIE = polyethylenimine ethoxylated
PeLED = perovskite light-emitting diode
PEN = polyethylene naphthalate
PEO = poly(ethylene oxide)
PET = polyethylene terephthalate
PFI = perfluorinated ionomer
PFM = perovskite-filled membrane
PI = polyimide
PLD = pulsed-laser deposition
PLED = polymer light-emitting diode
PLQY = photoluminescence quantum yield

https://doi.org/10.1021/acs.chemrev.3c00548
Chem. Rev. XXXX, XXX, XXX−XXX

PM = passive matrix
PMMA = poly(methyl methacrylate)
PPG = Photoplethysmogram
PPI = pixels per inch
PPy = polypyrrole
PS = polystyrene
PSR = pressure sensitive rubber
PTCDI-C8 = N,N′-dioctyl-3,4,9,10-perylenedicarboximide
PTFE = polytetrafluoroethylene
pTr = phototransistor
PTT = pulse transit time
PU = polyurethane
PUA = polyurethane acrylate
pV3D3 = poly(1,3,5-trimethyl-1,3,5-trivinyl cyclotrisiloxane)
pV3D3-pTr = pV3D3 phototransistor
PVA = poly(vinyl alcohol)
PVD = physical vapor deposition
PVP = polyvinylpyrrolidon
PXL = photo-cross-linkable ligand
QD = quantum dot
QLED = quantum dot light-emitting diode
r-BHJ = reference bulk heterojunction
RF = radiofrequency
RGB = red-green-blue
rGO = reduced graphene oxide
RoI = region of interest
SAM = self-assembled monolayer
SCG = single-crystalline graphene
SEBS = poly(styrene-ehtylene-butylene-styrene)
SNR = signal-to-noise ratio
SOI = silicon-on-insulator
SoP = spin-on-patterning
SP = systolic pressure
SPP = surface plasmon polariton
STP = short-term plasticity
TADF = thermally activated delayed fluorescence
TBAI = tetrabutylammonium iodide
TBSI = tributylsulfonium iodide
TDM = transition dipole moment
TE = transparent electrode
TFT = thin film transistor
TIPS-PEN = 6,13-bis(triisopropylsilylethinyl)pentacene
TIPS-pentacene = bis(triisopropylsilylethynyl) pentacene
TPBi = 1,3,5-Tris(1-phenyl-1H-benzimidazol-2-yl)
UAV = unmanned aerial vehicle
VADP = vacuum-assisted drop-casting patterning
VSSR = vapor−solid−solid reaction
ZnAc = zinc acetate
μ-ILED = microinorganic light-emitting diode

REFERENCES

(1) Ross, I. M. The Invention of the Transistor. *Proc. IEEE* **1998**, *86*, 7−28.
(2) Keum, D. H.; Kim, S.-K.; Koo, J.; Lee, G-HJ.; Jeon, C.; Mok, J. W.; Mun, B. H.; Lee, K. J.; Kamrani, E.; Joo, C.-K.; et al. Wireless Smart Contact Lens for Diabetic Diagnosis and Therapy. *Sci. Adv.* **2020**, *6*, No. eaba35222.
(3) Park, J.; Kim, J.; Kim, S.-Y.; Cheong, W. H.; Park, Y.-G.; Na, K.; Kim, Y.-T.; Heo, J. H.; Lee, C. Y.; et al. Soft, Smart Contact Lenses with Integrations of Wireless Circuits, Glucose Sensors, and Displays. *Sci. Adv.* **2018**, *4*, No. eaap9841.
(4) Ma, X.; Ahadian, S.; Liu, S.; Zhang, J.; Liu, S.; Cao, T.; Lin, W.; Wu, D.; de Barros, N. R.; Zare, M. R.; et al. Smart Contact Lenses for Biosensing Applications. *Adv. Intell. Sys.* **2021**, *3*, 2000263.
(5) Ku, M.; Kim, J.; Won, J.-E.; Kang, W.; Park, Y.-G.; Park, J.; Lee, J.-H.; Cheon, J.; Lee, H. H.; Park, J.-U. Smart, Soft Contact Lens for Wireless Immunosensing of Cortisol. *Sci. Adv.* **2020**, *6*, No. eabb2891.
(6) Quintero, A. V.; Perez-Merino, P.; De Smet, H. Artificial Iris Performance for Smart Contact Lens Vision Correction Applications. *Sci. Rep.* **2020**, *10*, 14641.
(7) Jang, J. H.; Li, S.; Kim, D.-H.; Yang, J.; Choi, M. K. Materials, Device Structures, and Applications of Flexible Perovskite Light-Emitting Diodes. *Adv. Electron. Mater.* **2023**, *9*, 2201271.
(8) Mun, J.; Kim, T. Y.; Myung, D.; Hahn, S. K Smart Contact Lens Containing Hyaluronate-Rose Bengal Conjugate for Biophotonic Myopia Vision Correction. *Biomater. Sci.* **2022**, *10*, 4997−5005.
(9) Xia, Y.; Khamis, M.; Fernandez, F. A.; Heidari, H.; Butt, H.; Ahmed, Z.; Wilkinson, T.; Ghannam, R. State-of-the-Art in Smart Contact Lenses for Human-Machine Interaction. *IEEE Trans. Hum.-Mach. Syst.* **2023**, *53*, 187−200.
(10) Quintero, A. V.; Verplancke, R.; De Smet, H.; Vanfleteren, J. Stretchable Electronic Platform for Soft and Smart Contact Lens Applications. *Adv. Mater. Technol.* **2017**, *2*, 1700073.
(11) Choi, C.; Seung, H.; Kim, D.-H. Bio-Inspired Electronic Eyes and Synaptic Photodetectors for Mobile Artificial Vision. *IEEE Journal on Flexible Electronics* **2022**, *1*, 76−87.
(12) Lee, M.; Lee, G. J.; Jang, H. J.; Joh, E.; Cho, H.; Kim, M. S.; Kim, H. M.; Kang, K. M.; Lee, J. H.; Kim, M.; et al. An Amphibious Artificial Vision System with a Panoramic Visual Field. *Nat. Electron.* **2022**, *5*, 452−459.
(13) Kim, M. S.; Kim, M. S.; Lee, G. J.; Sunwoo, S.-H.; Chang, S.; Song, Y. M.; Kim, D.-H. Bio-Inspired Artificial Vision and Neuromorphic Image Processing Devices. *Adv. Mater. Technol.* **2022**, *7*, 2100144.
(14) Lee, G. J.; Choi, C.; Kim, D.-H.; Song, Y. M. Bioinspired Artificial Eyes: Optic Components, Digital Cameras, and Visual Prostheses. *Adv. Funct. Mater.* **2018**, *28*, 1705202.
(15) Zhang, S.; Wu, Q.; Liu, C.; Wang, T.; Zhang, H.; Wang, J.; Ding, Y.; Chi, J.; Xu, W.; Xiang, Y.; et al. Bio-Inspired Spherical Compound Eye Camera for Simultaneous Wide-Band and Large Field of View Imaging. *Opt. Exp.* **2022**, *30*, 20952−20962.
(16) Dong, T.; Simoes, J.; Yang, Z. Flexible Photodetector Based on 2D Materials: Processing, Architectures, and Applications. *Adv. Mater. Interfaces* **2020**, *7*, 1901657.
(17) Chow, P. C. Y.; Someya, T. Organic Photodetectors for Next-Generation Wearable Electronics. *Adv. Mater.* **2020**, *32*, 19002045.
(18) Xu, H.; Yin, L.; Liu, C.; Sheng, X.; Zhao, N. Recent Advances in Biointegrated Optoelectronic Devices. *Adv. Mater.* **2018**, *30*, 1800156.
(19) Seung, H.; Choi, C.; Kim, D. C.; Kim, J. S.; Kim, J. H.; Kim, J.; Park, S. I.; Lim, J. A.; Yang, J.; Choi, M. K.; et al. Integration of Synaptic Phototransistors and Quantum Dot Light-Emitting Diodes for Visualization and Recognition of UV Patterns. *Sci. Adv.* **2022**, *8*, No. eabq3101.
(20) Choi, C.; Leem, J.; Kim, M.; Taqieddin, A.; Cho, C.; Cho, K. W.; Lee, G. J.; Seung, H.; Bae, H. J.; Song, Y. M.; et al. Curved Neuromorphic Image Sensor Array Using a MoS_2-Organic Heterostructure Inspired by the Human Visual Recognition System. *Nat. Commun.* **2020**, *11*, 5934.
(21) Liao, F.; Zhou, F.; Chai, Y. Neuromorphic Vision Sensors: Principle, Progress, and Perspectives. *J. Semicond.* **2021**, *42*, 013105.
(22) Hong, S.; Cho, H.; Kang, B. H.; Park, K.; Akinwande, D.; Kim, H. J.; Kim, S. Neuromorphic Active Pixel Image Sensor Array for Visual Memory. *ACS Nano* **2021**, *15*, 15362−15370.
(23) Zhu, Q.-B.; Li, B.; Yang, D.-D.; Liu, C.; Feng, S.; Chen, M.-L.; Sun, Y.; Tian, Y.-N.; Su, X.; Wang, X.-M.; et al. A Flexible Ultrasensitive Optoelectronic Sensor Array for Neuromorphic Vision Systems. *Nat. Commun.* **2021**, *12*, 1798.

https://doi.org/10.1021/acs.chemrev.3c00548
Chem. Rev. XXXX, XXX, XXX−XXX

(24) Sunwoo, S.-H.; Ha, K.-H.; Lee, S.; Lu, N.; Kim, D.-H. Wearable and Implantable Soft Bioelectronics: Device Designs and Material Strategies. *Annu. Rev. Chem. Biomol. Eng.* **2021**, *12*, 359−391.
(25) Cho, K. W.; Sunwoo, S.-H.; Hong, Y. J.; Koo, J. H.; Kim, J. H.; Baik, S.; Hyeon, T.; Kim, D.-H. Soft Bioelectronics Based on Nanomaterials. *Chem. Rev.* **2022**, *122*, 5068−5143.
(26) Ryu, H.; Seo, M.-H.; Rogers, J. A. Bioresorbable Metals for Biomedical Applications: from Mechanical Components to Electronic Devices. *Adv. Healthcare Mater.* **2021**, *10*, 2002236.
(27) Vazquez-Guardado, A.; Yang, Y.; Rogers, J. A. Challenges and Opportunities in Flexible, Stretchable, and Morphable Bio-Interfaced Technologies. *Natl. Sci. Rev.* **2022**, *9*, nwac016.
(28) Li, J.; Liu, Y.; Yuan, L.; Zhang, B.; Bishop, E.-S.; Wang, K.; Tang, J.; Zheng, Y.; Xu, W.; Niu, S.; et al. A Tissue-Like Neurotransmitter Sensor for the Brain and Gut. *Nature* **2022**, *606*, 94−101.
(29) Liu, Y.; Feig, V. R.; Bao, Z. Conjugated Polymer for Implantable Electronics Toward Clinical Application. *Adv. Healthcare Mater.* **2021**, *10*, 2001916.
(30) Li, T. L.; Liu, Y.; forro, C.; Yang, X.; Beker, L.; Bao, Z.; Cui, B.; Pasca, S. P. Stretchable Mesh Microelectronics for the Biointegration and Stimulation of Human Neural Organoids. *Biomater.* **2022**, *290*, 121825.
(31) Jiang, Z.; Chen, N.; Yi, Z.; Zhong, J.; Zhang, F.; Ji, S.; Liao, R.; Wang, Y.; Li, H.; Liu, Z.; et al. A 1.3-Micrometer-Thick Elastic Conductor for Seamless On-Skin and Implantable Sensors. *Nat. Electron.* **2022**, *5*, 784−793.
(32) Wang, Y.; Haick, H.; Guo, S.; Wang, C.; Lee, S.; Yokota, T.; Someya, T. Skin Bioelectronics Towards Long-Term, Continuous Health Monitoring. *Chem. Soc. Rev.* **2022**, *51*, 3759−3793.
(33) Song, Y.; Min, J.; Gao, W. Wearable and Implantable Electronics: Moving Toward Precision Therapy. *ACS Nano* **2019**, *13*, 12280−12286.
(34) Koydemir, H. C.; Ozcan, A. Wearable and Implantable Sensors for Biomedical Applications. *Annu. Rev. Anal. Chem.* **2018**, *11*, 127−146.
(35) Han, W. B.; Ko, G.-J.; Jang, T.-M.; Hwang, S.-W. Materials, Devices, and Applications for Wearable and Implantable Electronics. *ACS Appl. Electron. Mater.* **2021**, *3*, 485−503.
(36) Shahriari, D.; Rosenfeld, D.; Anikeeva, P. Emerging Frontier of Peripheral Nerve and Organ Interfaces. *Neuron* **2020**, *108*, 270−285.
(37) Kar, A.; Ahamad, N.; Dewani, M.; Awasthi, L.; Patil, R.; Banerjee, R. Wearable and Implantable Devices for Drug Delivery: Applications and Challenges. *Biomater.* **2022**, *283*, 121435.
(38) Cha, G. D.; Jung, S.; Choi, S. H.; Kim, D.-H. Local Drug Delivery Strategies for Glioblastoma Treatment. *Brain Tummor Res. Treat.* **2022**, *10*, 151−157.
(39) Kang, T.; Cha, G. D.; Park, O. K.; Cho, H. R.; Kim, M.; Lee, J.; Kim, D.; Lee, B.; Chu, J.; Koo, S.; et al. Penetrative and Sustained Drug Delivery Using Injectable Hydrogel Nanocomposites for Postsurgical Brain Tumor Treatment. *ACS Nano* **2023**, *17*, 5435−5447.
(40) Long, Y.; Li, J.; Yang, F.; Wang, J.; Wang, X. Wearable and Implantable Electroceuticals for Therapeutic Electrostimulations. *Adv. Sci.* **2021**, *8*, 2004023.
(41) Joo, H.; Lee, Y.; Kim, J.; Yoo, J.-S.; Yoo, S.; Kim, S.; Arya, A. K.; Kim, S.; Choi, S. H.; Lu, N.; et al. Soft Implantable Drug Delivery Device Integrated Wirelessly with Wearable Devices to Treat Fatal Seizures. *Sci. Adv.* **2021**, *7*, No. eabd4639.
(42) Groth, T.; Stegmayr, B. G.; Ash, S. R.; Kuchinka, J.; Wieringa, F. P.; Fissell, W. H.; Roy, S. Wearable and Implantable Artificial Kidney Devices for End-Stage Kidney Disease Treatment: Current Status and Review. *Artif. Organs* **2023**, *47*, 649−666.
(43) Sun, J.; Wu, X.; Xiao, J.; Zhang, Y.; Ding, J.; Jiang, J.; Chen, Z.; Liu, X.; Wei, D.; Zhou, L.; Fan, H. Hydrogel-Integrated Multimodal Response as a Wearable and Implantable Bidirectional Interface for Biosensor and Therapeutic Electrostimulation. *ACS Appl. Mater. Interfaces* **2023**, *15*, 5897−5909.
(44) Santagati, G. E.; Melodia, T. Experimental Evaluation of Impulsive Ultrasonic Intra-Body Communications for Implantable Biomedical Devices. *IEEE Trans. Mob. Comput.* **2017**, *16*, 367−380.
(45) Chen, P.; Wu, P.; Wan, X.; Wang, Q.; Xu, C.; Yang, M.; Feng, J.; Hu, B.; Luo, Z. Ultrasound-Driven Electrical Stimulation of Peripheral Nerves Based on Implantable Piezoelectric Thin Film Nanogenerators. *Nano Energy* **2021**, *86*, 106123.
(46) Santagati, G. E.; Dave, N.; Melodia, T. Design and Performance Evaluation of an Implantable Ultrasonic Networking Platform for the Internet of Medical Things. *IEEE ACM Trans. Netw.* **2020**, *28*, 29−42.
(47) Seo, H.; Han, S. I.; Song, K.-I.; Seong, D.; Lee, K.; Kim, S. H.; Park, T.; Koo, J. H.; Shin, M.; Baac, H. W.; et al. Durable and Fatigue-Resistant Soft Peripheral Neuroprosthetics for In Vivo Bidirectional Signaling. *Adv. Mater.* **2021**, *33*, 2007346.
(48) Tang, G.; Shi, Q.; Zhang, Z.; He, T.; Sun, Z.; Lee, C. Hybridized Wearable Patch as a Multi-Parameter and Multi-Functional Human-Machine Interface. *Nano Energy* **2021**, *81*, 105582.
(49) Wu, P.; Xiao, A.; Zhao, Y.; Chen, F.; Ke, M.; Zhang, Q.; Zhang, J.; Shi, X.; He, X.; Chen, Y. An Implantable and Versatile Piezoresistive Sensor for the Monitoring of Human-Machine Interface Interactions and the Dynamical Process of Nerve Repair. *Nanoscale* **2019**, *11*, 21103−21118.
(50) Dong, B.; Yang, Y.; Shi, Q.; Xu, S.; Sun, Z.; Zhu, S.; Zhang, Z.; Kwong, D.-L.; Zhou, G.; Ang, K.-W.; et al. Wearable Triboelectric-Human-Machine Interface (THMI) Using Robust Nanophotonic Readout. *ACS Nano* **2020**, *14*, 8915−8930.
(51) Yin, R.; Wang, D.; Zhao, S.; Lou, Z.; Shen, G. Wearable Sensors-Enabled Human-Machine Interaction Systems: from Design to Application. *Adv. Funct. Mater.* **2021**, *31*, 2008936.
(52) Paterno, L.; Lorenzon, L. Soft Robotics in Wearable and Implantable Medical Applications: Translational Challenges and Future Outlooks. *Front. Robot. AI* **2023**, *10*, 1075634.
(53) Zhao, Q.; Li, C.; Shum, H. C.; Du, X. Shape-Adaptable Biodevices for Wearable and Implantable Applications. *Lab Chip* **2020**, *20*, 4321−4341.
(54) Cutrone, A.; Micera, S. Implantable Neural Interfaces and Wearable Tactile Systems for Bidirectional Neuroprosthetics Systems. *Adv. Healthcare Mater.* **2019**, *8*, 1801345.
(55) Koo, J. H.; Song, J.-K.; Yoo, S.; Sunwoo, S.-H.; Son, D.; Kim, D.-H. Unconventional Device and Material Approaches for Monolithic Biointegration of Implantable Sensors and Wearable Electronics. *Adv. Mater. Technol.* **2020**, *5*, 2000407.
(56) Lee, H.; Jiang, Z.; Yokota, T.; Fukuda, K.; Park, S.; Someya, T. Stretchable Organic Optoelectronic Devices: Design of Materials, Structures, and Applications. *Mater. Sci. Eng. R: Rep.* **2021**, *146*, 100631.
(57) Xu, K.; Lu, Y.; Takei, K. Multifunctional Skin-Inspired Flexible Sensor Systems for Wearable Electronics. *Adv. Mater. Technol.* **2019**, *4*, 1800628.
(58) Koo, J. H.; Yun, H.; Lee, W.; Sunwoo, S.-H.; Shim, H. J.; Kim, D.-H. Recent Advances in Soft Electronic Materials for Intrinsically Stretchable Optoelectronic Systems. *Opt. Electron. Adv.* **2022**, *5*, 210131.
(59) Lim, H.-R.; Kim, H. S.; Qazi, R.; Kwon, Y.-T.; Jeong, J.-W.; Yeo, W.-H. Advanced Soft Materials, Sensor Integrations, and Applications of Wearable Flexible Hybrid Electronics in Healthcare, Energy, and Environment. *Adv. Mater.* **2020**, *32*, 1901924.
(60) Sun, Z.; Yang, S.; Zhao, P.; Zhang, J.; Yang, Y.; Ye, X.; Zhao, X.; Cui, N.; Tong, Y.; Liu, Y.; et al. Skin-Like Ultrasensitive Strain Sensor for Full-Range Detection of Human Health Monitoring. *ACS Appl. Mater. Interfaces* **2020**, *12*, 13287−13295.
(61) Song, J.-K.; Kim, M. S.; Yoo, S.; Koo, J. H.; Kim, D.-H. Materials and Devices for Flexible and Stretchable Photodetectors and Light-Emitting Diodes. *Nano Res.* **2021**, *14*, 2919−2937.
(62) Li, H.; Cao, Y.; Wang, Z.; Feng, X. Flexible and Stretchable Inorganic Optoelectronics. *Opt. Mater. Exp.* **2019**, *9*, 4023−4049.

https://doi.org/10.1021/acs.chemrev.3c00548
Chem. Rev. XXXX, XXX, XXX−XXX

(63) Chen, Z.; Obaid, S. N.; Lu, L. Recent Advances in Organic Optoelectronic Devices for Biomedical Applications. *Opt. Mater. Exp.* **2019**, *9*, 3843−3856.
(64) Lee, H. E.; Shin, J. H.; Park, J. H.; Hong, S. K.; Park, S. H.; Lee, S. H.; Lee, J. H.; Kang, I.-S.; Lee, K. J. Micro Light-Emitting Diodes for Display and Flexible Biomedical Applications. *Adv. Funct. Mater.* **2019**, *29*, 1808075.
(65) Murawski, C.; Gather, M. C. Emerging Biomedical Applications of Organic Light-Emitting Diodes. *Adv. Opt. Mater.* **2021**, *9*, 2100269.
(66) Kong, D.; Zhang, K.; Tian, J.; Yin, L.; Sheng, X. Biocompatible and Biodegradable Light-Emitting Materials and Devices. *Adv. Mater. Technol.* **2022**, *7*, 2100006.
(67) Shen, G. Recent Advances of Flexible Sensors for Biomedical Applications. *Prog. Nat. Sci.: Mater.* **2021**, *31*, 872−882.
(68) Liu, S.; Zhang, X.; Gu, X.; Ming, D. Photodetectors Based on Two-Dimensional Materials for Biomedical Application. *Biosens. Bioelectron.* **2019**, *143*, 111617.
(69) Yokota, T.; Fukuda, K.; Someya, T. Recent Progress of Flexible Image Sensors for Biomedical Applications. *Adv. Mater.* **2021**, *33*, 2004416.
(70) Gao, Q.; Zhang, J.; Xie, Z.; Omisore, O.; Zhang, J.; Wang, L.; Li, H. Highly Stretchable Sensors for Wearable Biomedical Applications. *J. Mater. Sci.* **2019**, *54*, 5187−5223.
(71) Choi, C.; Lee, Y.; Cho, K. W.; Koo, J. H.; Kim, D.-H. Wearable and Implantable Soft Bioelectronics Using Two-Dimensional Materials. *Acc. Chem. Res.* **2019**, *52*, 73−81.
(72) Kim, D.-H.; Viventi, J.; Amsden, J. J.; Xiao, J.; Vigeland, L.; Kim, Y.-S.; Blanco, J. A.; Panilaitis, B.; Frechette, E. S.; Contreras, D.; et al. Dissolvable Films of Silk Fibroin for Ultrathin Conformal Bio-Integrated Electronics. *Nat. Mater.* **2010**, *9*, 511−517.
(73) Liu, Y.; Pharr, M.; Salvatore, G. A. Lab-on-Skin: A Review of Flexible and Stretchable Electronics for Wearable Health Monitoring. *ACS Nano* **2017**, *11*, 9614−9635.
(74) Yuk, H.; Lu, B.; Zhao, X. Hydrogel Bioelectronics. *Chem. Soc. Rev.* **2019**, *48*, 1642−1667.
(75) Chen, S.; Sun, L.; Zhou, X.; Guo, Y.; Song, J.; Qian, S.; Liu, Z.; Guan, Q.; Meade Jeffries, E.; Liu, W.; et al. Mechanically and Biologically Skin-Like Elastomers for Bio-Integrated Electronics. *Nat. Commun.* **2020**, *11*, 1107.
(76) Li, H.; Liu, H.; Sun, M.; Huang, Y.; Xu, L. 3D Interfacing Between Soft Electronic Tools and Complex Biological Tissues. *Adv. Mater.* **2021**, *33*, 2004425.
(77) Koo, J. H.; Song, J.-K.; Kim, D.-H.; Son, D. Soft Implantable Bioelectronics. *ACS Mater. Lett.* **2021**, *3*, 1528−1540.
(78) Herbert, R.; Lim, H.-R.; Park, S.; Kim, J.-H.; Yeo, W.-H. Recent Advances in Printing Technologies of Nanomaterials for Implantable Wireless Systems in Health Monitoring and Diagnosis. *Adv. Healthcare Mater.* **2021**, *10*, 2100158.
(79) Wang, L.; Jiang, K.; Shen, G. Wearable, Implantable, and Interventional Medical Devices Based on Smart Electronic Skins. *Adv. Mater. Technol.* **2021**, *6*, 2100107.
(80) Tan, M.; Xu, Y.; Gao, Z.; Yuan, T.; Liu, Q.; Yang, R.; Zhang, B.; Peng, L. Recent Advances in Intelligent Wearable Medical Devices Integrating Biosensing and Drug Delivery. *Adv. Mater.* **2022**, *34*, 2108491.
(81) Yang, Q.; Wei, T.; Yin, R. T.; Wu, M.; Xu, Y.; Koo, J.; Choi, Y. S.; Xie, Z.; Chen, S. W.; Kandela, I.; et al. Photocurable Bioresorbable Adhesives as Functional Interfaces Between Flexible Bioelectronic Devices and Soft Biological Tissues. *Nat. Mater.* **2021**, *20*, 1559−1570.
(82) Hu, L.; Chee, P. L.; Sugiarto, S.; Yu, Y.; Shi, C.; Yan, R.; Yao, Z.; Shi, X.; Zhi, J.; Kai, D.; et al. Hydrogel-Based Flexible Electronics. *Adv. Mater.* **2023**, *35*, 2205326.
(83) Yan, D.; Chang, J.; Zhang, H.; Liu, J.; Song, H.; Xue, Z.; Zhang, F.; Zhang, Y. Soft Three-Dimensional Network Materials with Rational Bio-Mimetic Designs. *Nat. Commun.* **2020**, *11*, 1180.
(84) Bachtiar, E. O.; Erol, O.; Millrod, M.; Tao, R.; Gracias, D. H.; Romer, L. H.; Kang, S. H. 3D Printing and Characterization of a Soft and Biostable Elastomer with High Flexibility and Strength for Biomedical Applications. *J. Mech. Behav. Biomed. Mater.* **2020**, *104*, 103649.
(85) Sunwoo, S.-H.; Han, S. I.; Jung, D.; Kim, M.; Nam, S.; Lee, H.; Choi, S.; Kang, H.; Cho, Y. S.; Yeom, D.-H.; et al. Stretchable Low-Impedance Conductor with Ag-Au-Pt Core-Shell-Shell Nanowires and In Situ formed Pt Nanoparticles for Wearable and Implantable Device. *ACS Nano* **2023**, *17*, 7550−7561.
(86) Lim, C.; Hong, Y. J.; Jung, J.; Shin, Y.; Sunwoo, S.-H.; Baik, S.; Park, O. K.; Choi, S. H.; Hyeon, T.; Kim, J. H.; et al. Tissue-Like Skin-Device Interface for Wearable Bioelectronics by Using Ultra-Soft, Mass-Permeable, and Low-Impedance Hydrogels. *Sci. Adv.* **2021**, *7*, No. eabd3716.
(87) Wang, C.; Yokota, T.; Someya, T. Natural Biopolymer-Based Biocompatible Conductors for Stretchable Bioelectronics. *Chem. Rev.* **2021**, *121*, 2109−2146.
(88) Song, E.; Xie, Z.; Bai, W.; Luan, H.; Ji, B.; Ning, X.; Xia, Y.; Baek, J. M.; Lee, Y.; Avila, R.; et al. Miniaturized Electromechanical Devices for the Characterization of the Biomechanics of Deep Tissue. *Nat. Biomed. Eng.* **2021**, *5*, 759−771.
(89) Wang, X.; Fang, J.; Zhu, W.; Zhong, C.; Ye, D.; Zhu, M.; Lu, X.; Zhao, Y.; Ren, F. Bioinspired Highly Anisotropic, Ultrastrong and Stiff, and Osteoconductive Mineralized Wood Hydrogel Composites for Bone Repair. *Adv. Funct. Mater.* **2021**, *31*, 2010068.
(90) Lee, M.; Shim, H. J.; Choi, C.; Kim, D.-H. Soft High-Resolution Neural Interfacing Probes: Materials and Design Approaches. *Nano Lett.* **2019**, *19*, 2741−2749.
(91) Xie, C.; Wang, X.; He, H.; Ding, Y.; Lu, X. Mussel-Inspired Hydrogels for Self-Adhesive Bioelectronics. *Adv. Funct. Mater.* **2020**, *30*, 1909954.
(92) Dai, Y.; Hu, H.; Wang, M.; Xu, J.; Wang, S. Stretchable Transistors and Functional Circuits for Human-Integrated Electronics. *Nat. Electron.* **2021**, *4*, 17−29.
(93) Li, S.; Cong, Y.; Fu, J. Tissue Adhesive Hydrogel Bioelectronics. *J. Mater. Chem. B* **2021**, *9*, 4423−4443.
(94) Roshanbinfar, K.; Vogt, L.; Ruther, F.; Roether, J. A.; Boccaccini, A. R.; Engel, F. B. Nanofibrous Composite with Tailorable Electrical and Mechanical Properties for Cardiac Tissue Engineering. *Adv. Funct. Mater.* **2020**, *30*, 1908612.
(95) Tringides, C. M.; Vachicouras, N.; de Lazaro, I.; Wang, H.; Trouillet, A.; Seo, B. R.; Elosegui-Artola, A.; Fallegger, F.; Shin, Y.; Casiraghi, C.; et al. Viscoelastic Surface Electrode Arrays to Interface with Viscoelastic Tissues. *Nat. Nanotechnol.* **2021**, *16*, 1019−1029.
(96) Qiu, W.; Huang, Y.; Kong, L.-A.; Chen, Y.; Liu, W.; Wang, Z.; Sun, J.; Wan, Q.; Cho, J. H.; Yang, J.; et al. Optoelectronic In-Ga-Zn-O Memtransistors for Artificial Vision System. *Adv. Funct. Mater.* **2020**, *30*, 2002325.
(97) Jin, C.; Liu, W.; Xu, Y.; Huang, Y.; Nie, Y.; Shi, X.; Zhang, G.; He, P.; Zhang, J.; Cao, H.; et al. Artificial Vision Adaption Mimicked by an Optoelectrical In_2O_3 Transistor Array. *Nano Lett.* **2022**, *22*, 3372−3379.
(98) Xiong, H.; Xu, L.; Gao, C.; Zhang, Q.; Deng, M.; Wang, Q.; Zhang, J.; Fuchs, D.; Li, W.; Cui, A.; et al. Optically Modulated HfS_2-Based Synapses for Artificial Vision Systems. *ACS Appl. Mater. Interfaces* **2021**, *13*, 50132−50140.
(99) Zhou, Z.; Pei, Y.; Zhao, J.; Fu, G.; Yan, X. Visible Light Responsive Optoelectronic Memristor Device Based on CeOx/ZnO Structure for Artificial Vision System. *Appl. Phys. Lett.* **2021**, *118*, 191103.
(100) Sim, K.; Rao, Z.; Ershad, F.; Yu, C. Rubbery Electronics Fully Made of Stretchable Elastomeric Electronic Materials. *Adv. Mater.* **2020**, *32*, 1902417.
(101) Matsuhisa, N.; Chen, X.; Bao, Z.; Someya, T. Materials and Structural Designs of Stretchable Conductors. *Chem. Soc. Rev.* **2019**, *48*, 2946−2966.
(102) Lee, Y.; Oh, J. Y.; Xu, W.; Kim, O.; Kim, T. R.; Kang, J.; Kim, Y.; Son, D.; Tok, J. B.-H.; Park, M. J.; et al. Stretchable Organic Optoelectronic Sensorimotor Synapse. *Sci. Adv.* **2018**, *4*, No. eeat7387.

https://doi.org/10.1021/acs.chemrev.3c00548
Chem. Rev. XXXX, XXX, XXX−XXX

(103) Sharma, N.; Prakash, A.; Sharma, S. An Optoelectronic Muscle Contraction Sensor for Prosthetic Hand Application. *Rev. Sci. Intrum.* **2023**, *94*, 035009.
(104) Liu, Y.-H.; Jing, Y.; Bosse, B.; Damle, S.; Akinin, A.; Bauchner, S.; Thacker, H. D. Assembly Development of a Highly Flexible and Biocompatible Optoelectronic Neural Stimulator for Implantable Retinal Prosthesis. *Proceedings of 2021 IEEE 71st Electronic Components and Technology Conference (ECTC)*; IEEE, 2021; pp 1538−1543.
(105) Khoshmanesh, F.; Thurgood, P.; Pirogova, E.; Nahavandi, S.; Baratchi, S. Wearable Sensors: At the Frontier of Personalised Health Monitoring, Smart Prosthetics, and Assistive Technologies. *Biosens. Bioelectron.* **2021**, *176*, 112946.
(106) Yokota, T.; Nakamura, T.; Kato, H.; Mochizuki, M.; Tada, M.; Uchida, M.; Lee, S.; Koizumi, M.; Yukita, W.; Takimoto, A.; et al. A Conformable Imager for Biometric Authentication and Vital Sign Measurement. *Nat. Electron.* **2020**, *3*, 113−121.
(107) Ku, M.; Hwang, J. C.; Oh, B.; Park, J.-U. Smart Sensing Systems Using Wearable Optoelectronics. *Adv. Intell. Sys.* **2020**, *2*, 1900144.
(108) Koo, J. H.; Kim, D. C.; Shim, H. J.; Kim, T. H.; Kim, D.-H. Flexible and Stretchable Smart Display: Materials, Fabrication, Device Design, and System Integration. *Adv. Funct. Mater.* **2018**, *28*, 1801834.
(109) Kim, D. C.; Yun, H.; Kim, J.; Seung, H.; Yu, W. S.; Koo, J. H.; Yang, J.; Kim, J. H.; Hyeon, T.; Kim, D.-H. Three-Dimensional Foldable Quantum Dot Light-Emitting Diodes. *Nat. Electron.* **2021**, *4*, 671−680.
(110) Tan, Y. J.; Godaba, H.; Chen, G.; Tan, S. T. M.; Wan, G.; Li, G.; Lee, P. M.; Cai, Y.; Li, S.; Shepherd, R. F.; et al. A Transparent, Self-Healing, and High-κ Dielectric for Low-Field-Emission Stretchable Optoelectronics. *Nat. Mater.* **2020**, *19*, 182−188.
(111) Zhao, J.; Chi, Z.; Yang, Z.; Chen, X.; Arnold, M. S.; Zhang, Y.; Xu, J.; Chi, Z.; Aldred, M. P. Recent Developments of Truly Stretchable Thin Film Electronic and Optoelectronic Devices. *Nanoscale* **2018**, *10*, 5764−5792.
(112) Kwon, J.; Suh, Y. D.; Lee, J.; Lee, P.; Han, S.; Hong, S.; Yeo, J.; Lee, H.; Ko, S. H. Recent Progress in Silver Nanowire-Based Flexible/Wearable Optoelectronics. *J. Mater. Chem. C* **2018**, *6*, 7445−7461.
(113) Singh, E.; Singh, P.; Kim, K. S.; Yeom, G. Y.; Nalwa, H. S. Flexible Molybdenum Disulfide (MoS2) Atomic Layers for Wearable Electronics and Optoelectronics. *ACS Appl. Mater. Interfaces* **2019**, *11*, 11061−11105.
(114) Kim, J.; Seong, D.; Kwon, H.; Jin, S.; Kim, H.; Kim, Y.; Jeong, Y.; Lee, K.; Kwon, S. J.; Shin, M.; et al. Lead-Sealed Stretchable Underwater Perovskite-Based Optoelectronics via Self-Recovering Polymeric Nanomaterials. *ACS Nano* **2021**, *15*, 20127−20135.
(115) Yin, D.; Jiang, N.-R.; Liu, Y.-F.; Zhang, X.-L.; Li, A.-W.; Feng, J.; Sun, H.-B. Mechanically Robust Stretchable Organic Optoelectronic Devices Built Using a Simple and Universal Stencil-Pattern Transferring Technology. *Light Sci. Appl.* **2018**, *7*, 35.
(116) Lim, M. S.; Nam, M.; Choi, S.; Jeon, Y.; Son, Y. H.; Lee, S.-M.; Choi, K. C. Two-Dimensionally Stretchable Organic Light-Emitting Diode with Elastic Pillar Arrays for Stress Relief. *Nano Lett.* **2020**, *20*, 1526−1535.
(117) Chen, J.; Wang, J.; Ji, K.; Jiang, B.; Cui, X.; Sha, W.; Wang, B.; Dai, X.; Hua, Q.; Wan, L.; et al. Flexible, Stretchable, and Transparent InGaN/GaN Multiple Quantum Wells/Polyacrylamide Hydrogel-Based Light Emitting Diodes. *Nano Res.* **2022**, *15*, 5492−5499.
(118) Peng, W.; Wu, H. Flexible and Stretchable Photonic Sensors Based on Modulation of Light Transmission. *Adv. Opt. Mater.* **2019**, *7*, 1900329.
(119) Koo, J. H.; Jeong, S.; Shim, H. J.; Son, D.; Kim, J.; Kim, D. C.; Choi, S.; Hong, J.-I.; Kim, D.-H. Wearable Electrocardiogram Monitor Using Carbon Nanotube Electronics and Color-Tunable Organic Light-Emitting Diodes. *ACS Nano* **2017**, *11*, 10032−10041.
(120) Khan, Y.; Han, D.; Ting, J.; Ahmed, M.; Nagisetty, R.; Arias, A. C. Arias Organic Multi-Channel Optoelectronic Sensors for Wearable Health Monitoring. *IEEE Access* **2019**, *7*, 128114−128124.
(121) Lee, Y.; Chung, J. W.; Lee, G. H.; Kang, H.; Kim, J. Y.; Bae, C.; Yoo, H.; Jeong, S.; Cho, H.; Kang, S. G.; et al. Standalone Real-Time Health Monitoring Patch Based on a Stretchable Organic Optoelectronic System. *Sci. Adv.* **2021**, *7*, No. eabg9180.
(122) Biswas, S.; Shao, Y.; Hachisu, T.; Nguyen-Dang, T.; Visell, Y. Integrated Soft Optoelectronics for Wearable Health Monitoring. *Adv. Mater. Technol.* **2020**, *5*, 2000347.
(123) Chen, X.; Luo, F.; Yuan, M.; Xie, D.; Shen, L.; Zheng, K.; Wang, Z.; Li, X.; Tao, L.-Q. A Dual-Functional Graphene-Based Self-Alarm Health-Monitoring E-Skin. *Adv. Funct. Mater.* **2019**, *29*, 1904706.
(124) Gong, Y.; Zhang, Y. Z.; Fang, S.; Liu, C.; Niu, J.; Li, G.; Li, F.; Li, X.; Cheng, T.; Lai, W. Y. Artificial Intelligent Optoelectronic Skin with Anisotropic Electrical and Optical Responses for Multi-Dimensional Sensing. *Applied Physics Reviews.* **2022**, *9*, 021403.
(125) Arumugam, S.; Colburn, D. A.; Sia, S. K. Biosensors for Personal Mobile Health: A System Architecture Perspective. *Adv. Mater. Technol.* **2020**, *5*, 1900720.
(126) Mickle, A. D.; Won, S. M.; Noh, K. N.; Yoon, J.; Meacham, K. W.; Xue, Y.; McIlvried, L. A.; Copits, B. A.; Samineni, V. K.; Crawford, K. E.; et al. A Wireless Closed-Loop System for Optogenetic Peripheral Neuromodulation. *Nature* **2019**, *565*, 361−365.
(127) Kathe, C.; Michoud, F.; Schönle, P.; Rowald, A.; Brun, N.; Ravier, J.; Furfaro, I.; Paggi, V.; Kim, K.; Soloukey, S. Wireless Closed-Loop Optogenetics Across the Entire Dorsoventral Spinal Cord in Mice. *Nat. Biotechnol.* **2022**, *40*, 198−208.
(128) Zhang, X.; Mehvish, D.; Yang, H. Implantable and Biodegradable Closed-Loop Devices for Autonomous Electrotherapy. *SmartMat* **2023**, *4*, No. e1172.
(129) Ouyang, W.; Lu, W.; Zhang, Y.; Liu, Y.; Kim, J. U.; Shen, H.; Wu, Y.; Luan, H.; Kilner, K.; Lee, S. P. A Wireless and Battery-Less Implant for Multimodal Closed-Loop Neuromodulation in Small Animals. *Nat. Biomed. Eng.* **2023**, *7*, 1252−1269.
(130) Song, E.; Li, J.; Won, S. M.; Bai, W.; Rogers, J. A. Materials for Flexible Bioelectronic Systems as Chronic Neural Interfaces. *Nat. Mater.* **2020**, *19*, 590−603.
(131) Liu, K.; Ouyang, B.; Guo, X.; Guo, Y.; Liu, Y. Advances in Flexible Organic Field-Effect Transistors and Their Applications for Flexible Electronics. *npj Flex Electron.* **2022**, *6*, 1.
(132) Gao, W.; Ota, H.; Kiriya, D.; Takei, K.; Javey, A. Flexible Electronics Toward Wearable Sensing. *Acc. Chem. Res.* **2019**, *52* (3), 523−533.
(133) Qinglei, G.; Zengfeng, D. Inorganic Flexible Electronics: Materials, Strategies, and Applications. In *Nanomembranes: Materials, Properties, and Applications*; Mei, Y., Huang, G., Li, X., Eds.; Wiley-VCH GmbH, 2022; pp 85−104.
(134) Choi, M. K.; Yang, J.; Hyeon, T.; Kim, D.-H. Flexible Quantum Dot Light-Emitting Diodes for Next-Generation Displays. *npj Flex. Electron.* **2018**, *2*, 10.
(135) Yin, L.; Lv, J.; Wang, J. Structural Innovations in Printed, Flexible, and Stretchable Electronics. *Adv. Mater. Technol.* **2020**, *5*, 2000694.
(136) Xue, Z.; Song, H.; Rogers, J. A.; Zhang, Y.; Huang, Y. Mechanically-Guided Structural Designs in Stretchable Inorganic Electronics. *Adv. Mater.* **2020**, *32*, 1902254.
(137) Wu, W. Stretchable Electronics: Functional Materials, Fabrication Strategies, and Applications. *Adv. Mater.* **2019**, *20*, 187−224.
(138) Kim, D. C.; Shim, H. J.; Lee, W.; Koo, J. H.; Kim, D. H. Material-Based Approaches for the Fabrication of Stretchable Electronics. *Adv. Mater.* **2020**, *32*, 1902743.
(139) Wu, X.; Fu, W.; Chen, H. Conductive Polymers for Flexible and Stretchable Organic Optoelectronic Applications. *ACS Appl. Polym. Mater.* **2022**, *4* (7), 4609−4623.

https://doi.org/10.1021/acs.chemrev.3c00548
Chem. Rev. XXXX, XXX, XXX−XXX

(140) Liu, K.; Bian, Y.; Kuang, J.; Huang, X.; Li, Y.; Shi, W.; Zhu, Z.; Liu, G.; Qin, M.; Zhao, Z.; et al. Ultrahigh-Performance Optoelectronic Skin Based on Intrinsically Stretchable Perovskite-Polymer Heterojunction Transistors. *Adv. Mater.* **2022**, *34*, 2107304.
(141) Kim, J.-H.; Park, J.-W. Intrinsically Stretchable Organic Light-Emitting Diodes. *Sci. Adv.* **2021**, *7*, No. eabd9715.
(142) Wang, B.; Qin, Y.; Tan, W.; Tao, Y.; Kong, Y. Smartly Designed 3D N-Doped Mesoporous Graphene for High-Performance Supercapacitor Electrodes. *Electrochim. Acta* **2017**, *241*, 1−9.
(143) Lee, C.; Wei, X.; Kysar, J. W.; Hone, J. Measurement of the Elastic Properties and Intrinsic Strength of Monolayer Graphene. *Science* **2008**, *321*, 385−388.
(144) Park, S.; Fukuda, K.; Wang, M.; Lee, C.; Yokota, T.; Jin, H.; Jinno, H.; Kimura, H.; Zalar, P.; Matsuhisa, N.; et al. Ultraflexible Near-Infrared Organic Photodetectors for Conformal Photoplethysmogram Sensors. *Adv. Mater.* **2018**, *30*, 1802359.
(145) Chow, P. C.; Someya, T. Organic Photodetectors for Next-Generation Wearable Electronics. *Adv. Mater.* **2020**, *32*, 1902045.
(146) Yamagishi, K.; Kirino, I.; Takahashi, I.; Amano, H.; Takeoka, S.; Morimoto, Y.; Fujie, T. Tissue-Adhesive Wirelessly Powered Optoelectronic Device for Metronomic Photodynamic Cancer Therapy. *Nat. Biomed. Eng.* **2019**, *3*, 27−36.
(147) Kim, C. Y.; Ku, M. J.; Qazi, R.; Nam, H. J.; Park, J. W.; Nam, K. S.; Oh, S.; Kang, I.; Jang, J.-H.; Kim, W. Y.; et al. Soft Subdermal Implant Capable of Wireless Battery Charging and Programmable Controls for Applications in Optogenetics. *Nat. Commun.* **2021**, *12*, 535.
(148) Choi, M. K.; Yang, J.; Kim, D. C.; Dai, Z.; Kim, J.; Seung, H.; Kale, V. S.; Sung, S. J.; Park, C. R.; Lu, N.; et al. Extremely Vivid, Highly Transparent, and Ultrathin Quantum Dot Light-Emitting Diodes. *Adv. Mater.* **2018**, *30*, 1703279.
(149) Chen, X.; Shehzad, K.; Gao, L.; Long, M.; Guo, H.; Qin, S.; Wang, X.; Wang, F.; Shi, Y.; Hu, W.; et al. Graphene Hybrid Structures for Integrated and Flexible Optoelectronics. *Adv. Mater.* **2020**, *32*, 1902039.
(150) Zhao, R.; Gu, Z.; Li, P.; Zhang, Y.; Song, Y. Flexible and Wearable Optoelectronic Devices Based on Perovskites. *Adv. Mater. Technol.* **2022**, *7*, 2101124.
(151) Bitla, Y.; Chu, Y.-H. Van der Waals Oxide Heteroepitaxy for Soft Transparent Electronics. *Nanoscale* **2020**, *12*, 18523.
(152) Kim, D.-H.; Ahn, J.-H.; Choi, W. M.; Kim, H.-S.; Kim, T.-H.; Song, J.; Huang, Y. Y.; Liu, Z.; Lu, C.; Rogers, J. A. Stretchable and Foldable Silicon Integrated Circuits. *Science* **2008**, *320*, 507−511.
(153) Fukuda, K.; Yu, K.; Someya, T. The Future of Flexible Organic Solar Cells. *Adv. Energy Mater.* **2020**, *10*, 2000765.
(154) Hong, Y. J.; Jeong, H.; Cho, K. W.; Lu, N.; Kim, D. H. Wearable and Implantable Devices for Cardiovascular Healthcare: from Monitoring to Therapy Based on Flexible and Stretchable Electronics. *Adv. Funct. Mater.* **2019**, *29*, 1808247.
(155) Feig, V. R.; Tran, H.; Lee, M.; Bao, Z. Mechanically Tunable Conductive Interpenetrating Network Hydrogels That Mimic the Elastic Moduli of Biological Tissue. *Nat. Commun.* **2018**, *9*, 2740.
(156) Shi, Y.; Liu, R.; He, L.; Feng, H.; Li, Y.; Li, Z. Recent Development of Implantable and Flexible Nerve Electrodes. *Smart Mater.* **2020**, *1*, 131−147.
(157) Renz, A. F.; Reichmuth, A. M.; Stauffer, F.; Thompson-Steckel, G.; Vörös, J. A Guide Towards Long-term Functional Electrodes Interfacing Neuronal Tissue. *J. Neural Eng.* **2018**, *15*, 061001.
(158) Li, S.; Bai, H.; Shepherd, R. F.; Zhao, H. Bio-inspired Design and Additive Manufacturing of Soft Materials, Machines, Robots, and Haptic Interfaces. *Chem. Int. Ed.* **2019**, *58*, 11182.
(159) Mehrali, M.; Bagherifard, S.; Akbari, M.; Thakur, A.; Mirani, B.; Mehrali, M.; Hasany, M.; Orive, G.; Das, P.; Emneus, J.; et al. Blending Electronics with the Human Body: A Pathway Toward a Cybernetic Future. *Adv. Sci.* **2018**, *5*, 1700931.
(160) Lipomi, D. J.; Tee, B. C. K.; Vosgueritchian, M.; Bao, Z. Stretchable Organic Solar Cells. *Adv. Mater.* **2011**, *23*, 1771−1775.
(161) Li, H.; Ma, Y.; Huang, Y. Material Innovation and Mechanics Design for Substrates and Encapsulation of Flexible Electronics: A Review. *Mater. Horiz.* **2021**, *8*, 383−400.
(162) Yan, Z.; Wang, B.; Wang, K. Stretchability and Compressibility of a Novel Layout Design for Flexible Electronics Based on Bended Wrinkle Geometries. *Compos. B. Eng.* **2019**, *166*, 65−73.
(163) Kim, D.-H.; Song, J.; Choi, W. M.; Kim, H.-S.; Kim, R.-H.; Liu, Z.; Huang, Y. Y.; Hwang, K.-C.; Zhang, Y.-W.; Rogers, J. A. Materials and Noncoplanar Mesh Designs for Integrated Circuits with Linear Elastic Responses to Extreme Mechanical Deformations. *Proc. Natl. Acad. Sci. U. S. A.* **2008**, *105*, 18675−18680.
(164) Ko, H. C.; Stoykovich, M. P.; Song, J.; Malyarchuk, V.; Choi, W. M.; Yu, C.-J.; Geddes III, J. B.; Xiao, J.; Wang, S.; Huang, Y.; Rogers, J. A. A Hemispherical Electronic Eye Camera Based on Compressible Silicon Optoelectronics. *Nature* **2008**, *454*, 748−753.
(165) Lee, J.; Wu, J.; Shi, M.; Yoon, J.; Park, S. I.; Li, M.; Liu, Z.; Huang, Y.; Rogers, J. A. Stretchable GaAs Photovoltaics with Designs That Enable High Areal Coverage. *Adv. Mater.* **2011**, *23*, 986−991.
(166) Tang, Y.; Lin, G.; Han, L.; Qiu, S.; Yang, S.; Yin, J. Design of Hierarchically Cut Hinges for Highly Stretchable and Reconfigurable Metamaterials with Enhanced Strength. *Adv. Mater.* **2015**, *27*, 7181−7190.
(167) Morikawa, Y.; Yamagiwa, S.; Sawahata, H.; Numano, R.; Koida, K.; Ishida, M.; Kawano, T. Ultrastretchable Kirigami Bioprobes. *Adv. Healthcare Mater.* **2018**, *7*, 1701100.
(168) Zhang, Y.; Yan, Z.; Nan, K.; Xiao, D.; Liu, Y.; Luan, H.; Fu, H.; Wang, X.; Yang, Q.; Wang, J. A Mechanically Driven form of Kirigami as a Route to 3D Mesostructures in Micro/Nanomembranes. *Proc. Natl. Acad. Sci. U.S.A.* **2015**, *112*, 11757−11764.
(169) He, J.; Zhou, R.; Zhang, Y.; Gao, W.; Chen, T.; Mai, W.; Pan, C. Strain-Insensitive Self-Powered Tactile Sensor Arrays Based on Intrinsically Stretchable and Patternable Ultrathin Conformal Wrinkled Graphene-Elastomer Composite. *Adv. Funct. Mater.* **2022**, *32*, 2107281.
(170) White, M. S.; Kaltenbrunner, M.; Głowacki, E. D.; Gutnichenko, K.; Kettlgruber, G.; Graz, I.; Aazou, S.; Ulbricht, C.; Egbe, D. A. M.; Miron, M. C.; et al. Ultrathin, Highly Flexible and Stretchable PLEDs. *Nat. Photonics* **2013**, *7*, 811−816.
(171) Hashemi, S. A.; Ramakrishna, S.; Aberle, A. G. Recent Progress in Flexible-Wearable Solar Cells for Self-Powered Electronic Devices. *Energy Environ. Sci.* **2020**, *13*, 685.
(172) Zhao, J.; Zha, J.; Zeng, Z.; Tan, C. Recent Advances in Wearable Self-Powered Energy Systems Based on Flexible Energy Storage Devices Integrated with Flexible Solar Cells. *J. Mater. Chem. A* **2021**, *9*, 18887.
(173) Jinno, H.; Yokota, T.; Koizumi, M.; Yukita, W.; Saito, M.; Osaka, I.; Fukuda, K.; Someya, T. Self-Powered Ultraflexible Photonic Skin for Continuous Bio-Signal Detection via Air-Operation-Stable Polymer Light-Emitting Diodes. *Nat. Commun.* **2021**, *12*, 2234.
(174) Lee, G. H.; Kang, H.; Chung, J. W.; Lee, Y.; Yoo, H.; Jeong, H.; Kim, J.-Y.; Kang, S.-G.; Jun, J.-Y.; et al. Stretchable PPG Sensor with Light Polarization for Physical Activity-Permissible Monitoring. *Sci. Adv.* **2022**, *8*, No. eabm3622.
(175) Yan, T.; Li, Z.; Cao, F.; Chen, J.; Wu, L.; Fang, X. An All-Organic Self-Powered Photodetector with Ultraflexible Dual-Polarity Output for Biosignal Detection. *Adv. Mater.* **2022**, *34*, 2201303.
(176) Zhao, G.; Zhang, Y.; Shi, N.; Liu, Z.; Zhang, X.; Wu, M.; Pan, C.; Liu, H.; Li, L.; Wang, Z. L. Transparent and Stretchable Triboelectric Nanogenerator for Self-Powered Tactile Sensing. *Nano Energy* **2019**, *59*, 302−310.
(177) Choi, M.; Jang, B.; Lee, W.; Lee, S.; Kim, T. W.; Lee, H.-J.; Kim, J.-H.; Ahn, J.-H. Stretchable Active Matrix Inorganic Light-Emitting Diode Display Enabled by Overlay-Aligned Roll-Transfer Printing. *Adv. Funct. Mater.* **2017**, *27*, 1606005.
(178) Kim, M. S.; Lee, G. J.; Choi, C.; Kim, M. S.; Lee, M.; Liu, S.; Cho, K. W.; Kim, H. M.; Cho, H.; Choi, M. K.; Lu, N.; Song, Y. M.; Kim, D.-H. An Aquatic-Vision-Inspired Camera Based on a Monocentric Lens and a Silicon Nanorod Photodiode Array. *Nat. Electron.* **2020**, *3*, 546−553.

https://doi.org/10.1021/acs.chemrev.3c00548
Chem. Rev. XXXX, XXX, XXX−XXX

(179) Sempionatto, J. R.; Lin, M.; Yin, L.; De la Paz, E.; Pei, K.; Sonsa-Ard, T.; de Loyola Silva, A. N.; Khorshed, A. A.; Zhang, F.; Tostado, N.; et al. An Epidermal Patch for the Simultaneous Monitoring of Haemodynamic and Metabolic Biomarkers. *Nat. Biomed. Eng.* **2021**, *5*, 737−748.
(180) Yang, J. C.; Lee, S.; Ma, B. S.; Kim, J.; Song, M.; Kim, S. Y.; Kim, D. W.; Kim, T.-S.; Park, S. Geometrically Engineered Rigid Island Array for Stretchable Electronics Capable of withstanding Various Deformation Modes. *Sci. Adv.* **2022**, *8*, No. eabn3863.
(181) Kim, J.; Son, D.; Lee, M.; Song, C.; Song, J.-K.; Koo, J. H.; Lee, D. J.; Shim, H. J.; Kim, J. H.; Lee, M.; et al. A Wearable Multiplexed Silicon Nonvolatile Memory Array Using Nanocrystal Charge Confinement. *Sci. Adv.* **2016**, *2*, No. e1501101.
(182) Son, D.; Koo, J. H.; Song, J.-K.; Kim, J.; Lee, M.; Shim, H. J.; Park, M.; Lee, M.; Kim, J. H.; Kim, D.-H. Stretchable Carbon Nanotube Charge-Trap Floating-Gate Memory and Logic Devices for Wearable Electronics. *ACS Nano* **2015**, *9*, 5585−5593.
(183) Xu, R.; Zverev, A.; Hung, A.; Shen, C.; Irie, L.; Ding, G.; Whitmeyer, M.; Ren, L.; Griffin, B.; Melcher, J.; et al. Kirigami-Inspired, Highly Stretchable Microsupercapacitor Patches Fabricated by Laser Conversion and Cutting. *Microsyst Nanoeng.* **2018**, *4*, 36.
(184) Liang, J.; Li, L.; Tong, K.; Ren, Z.; Hu, W.; Niu, X.; Chen, Y.; Pei, Q. Silver Nanowire Percolation Network Soldered with Graphene Oxide at Room Temperature and Its Application for Fully Stretchable Polymer Light-Emitting Diodes. *ACS Nano* **2014**, *8*, 1590−1600.
(185) Kim, S.-J.; Kim, T.; Kim, D.; Ju, B.-K. Layer-by-Layer Assembled Nano-Composite Multilayer Gas Barrier Film Manufactured with Stretchable Substrate. *Appl. Sci.* **2021**, *11*, 5794.
(186) Zhou, J.; Long, X.; Huang, J.; Jiang, C.; Zhuo, F.; Guo, C.; Li, H.; Fu, Y.; Duan, H. Multiscale and Hierarchical Wrinkle Enhanced Graphene/Ecoflex Sensors Integrated with Human-Machine Interfaces and Cloud-Platform. *npj Flex. Electron.* **2022**, *6*, 55.
(187) Kocs, L.; Albert, E.; Tegze, B.; Kabai-Faix, M.; Major, C.; Szalai, A.; Basa, P.; Horvolgyi, Z. Silica Sol-Gel Coatings with Improved Light Transmittance and Stability. *Period. Polytech. Chem. Eng.* **2017**, *62*, 21−31.
(188) Erdogan, N.; Erden, F.; Astarlioglu, A. T.; Ozdemir, M.; Ozbay, S.; Aygun, G.; Ozyuzer, L. ITO/Au/ITO Multilayer Thin Films on Transparent Polycarbonate with Enhanced EMI Shielding Properties. *Curr. Appl. Phys.* **2020**, *20*, 489−497.
(189) Qi, D.; Zhang, K.; Tian, G.; Jiang, B.; Huang, Y. Stretchable Electronics Based on PDMS Substrates. *Adv. Mater.* **2021**, *33*, 2003155.
(190) Ouyang, W.; Chen, J.; He, J. H.; Fang, X. Improved Photoelectric Performance of UV Photodetector Based on ZnO Nanoparticle-Decorated BiOCl Nanosheet Arrays onto PDMS Substrate: The Heterojunction and Ti_3C_2Tx MXene Conduction Layer. *Adv. Electron. Mater.* **2020**, *6*, 2000168.
(191) Yu, H.; Azhar, E. A.; Belagodu, T.; Lim, S.; Dey, S. ZnO Nanowire-Based Visible-Transparent Ultraviolet Detectors on Polymer Substrates. *J. Appl. Phys.* **2012**, *111*, 102806.
(192) Jeon, Y. P.; Park, J. H.; Kim, T. W. Highly Flexible Triboelectric Nanogenerators Fabricated Utilizing Active Layers with a ZnO Nanostructure on Polyethylene Naphthalate Substrates. *Appl. Surf. Sci.* **2019**, *466*, 210−214.
(193) Kinner, L.; Bauch, M.; Wibowo, R. A.; Ligorio, G.; List-Kratochvil, E. J. W.; Dimopoulos, T. Polymer Interlayers on Flexible PET Substrates Enabling Ultra-High Performance, ITO-Free Dielectric/Metal/Dielectric Transparent Electrode. *Mater. Design* **2019**, *168*, 107663.
(194) Pandey, A.; Yadav, R.; Kaur, M.; Singh, P.; Gupta, A.; Husale, S. High Performing Flexible Optoelectronic Devices Using Thin Films of Topological Insulator. *Sci. Rep.* **2021**, *11*, 832.
(195) Yin, J.; Hui, H.; Fan, B.; Bian, J.; Du, J.; Yang, H. Preparation and Properties of Polyimide Composite Membrane with High Transmittance and Surface Hydrophobicity for Lightweight Optical System. *Membranes* **2022**, *12*, 592.
(196) Zhang, G.; Chen, Q.; Xie, C.; Wang, Y.; Zhao, C.; Xiao, C.; Wei, Y.; Li, W. Mechanical-Robust and Recyclable Polyimide Substrates Coordinated with Cyclic Ti-oxo Cluster for Flexible Organic Solar Cells. *npj Flex. Electron.* **2022**, *6*, 37.
(197) Lien, D.-H.; Wang, H.-P.; Chen, S.-B.; Chi, Y.-C.; Wu, C.-L.; Lin, G.-R.; Liao, Y.-C.; He, J.-H. 360 Omnidirectional, Printable and Transparent Photodetectors for Flexible Optoelectronics. *npj Flex. Electron.* **2018**, *2*, 19.
(198) Zhang, H.; An, L.; Wang, X.; Niu, C.; Hou, X. A Colorless, Transparent, and Mechanically Robust Polyurethane Elastomer: Synthesis, Chemical Resistance, and Adhesive Properties. *New J. Chem.* **2022**, *46*, 4762−4771.
(199) Zhang, W.; Liu, Y.; Pei, X.; Yuan, Z.; Zhang, Y.; Zhao, Z.; Hao, H.; Long, R.; Liu, N. Stretchable MoS_2 Artificial Photoreceptors for E-Skin. *Adv. Funct. Mater.* **2022**, *32*, 2107524.
(200) Cho, E.; Kim, K. N.; Yong, H.; Choi, W. J.; Park, J.-S.; Lee, S.-J. Highly Transparent and Water-Repellent Hierarchical-Wrinkled-Architecture Triboelectric Nanogenerator with Ultrathin Plasma-Polymer-Fluorocarbon Film for Artificial Triboelectric Skin. *Nano Energy* **2022**, *103*, 107785.
(201) Hassan, M.; Abbas, G.; Li, N.; Afzal, A.; Haider, Z.; Ahmed, S.; Xu, X.; Pan, C.; Peng, Z. Significance of Flexible Substrates for Wearable and Implantable Devices. *Adv. Mater. Technol.* **2022**, *7*, 2100773.
(202) Yu, C.; Gong, W.; Zhang, J.; Lv, W.; Tian, W.; Fan, X.; Yao, Y. Hot Pressing-Induced Alignment of Hexagonal Boron Nitride in SEBS Elastomer for Superior Thermally Conductive Composites. *RSC Adv.* **2018**, *8*, 25835−25845.
(203) Fryń, P.; Lalik, S.; Górska, N.; Iwan, A.; Marzec, M. Comparison of the Dielectric Properties of Ecoflex® with L,D-Poly(lactic acid) or Polycaprolactone in the Presence of SWCN or 5CB. *Materials* **2021**, *14*, 1719.
(204) Jiao, H.; Zhang, M.; Du, C.; Zhang, Z.; Huang, W.; Huang, Q. Intrinsically Stretchable All-Carbon-Nanotube Transistors with Styrene-Ethylene-Butylene-Styrene as Gate Dielectrics Integrated by Photolithography-Based Process. *RSC Adv.* **2020**, *10*, 8080−8086.
(205) Wang, S.; Xu, J.; Wang, W.; Wang, G.-J. N.; Rastak, R.; Molina-Lopez, F.; Chung, J. W.; Niu, S.; Feig, V. R.; Lopez, J.; et al. Skin Electronics from Scalable Fabrication of an Intrinsically Stretchable Transistor Array. *Nature* **2018**, *555*, 83−88.
(206) Wang, Y.; Huang, X.; Li, T.; Li, L.; Guo, X.; Jiang, P. Polymer-Based Gate Dielectrics for Organic Field-Effect Transistors. *Chem. Mater.* **2019**, *31* (7), 2212−2240.
(207) Raveendran, R.; Nagaraj, M.; Namboothiry, M. A. High-Performance, Transparent Solution-Processed Organic Field-Effect Transistor with Low-k Elastomeric Gate Dielectric and Liquid Crystalline Semiconductor: Promises and Challenges. *ACS Appl. Electron. Mater.* **2020**, *2*, 3336−3345.
(208) Song, J.-K.; Kim, J.; Yoon, J.; Koo, J. H.; Jung, H.; Kang, K.; Sunwoo, S.-H.; Yoo, S.; Chang, H.; Jo, J.; Baek, W.; Lee, S.; Lee, M.; Kim, H. J.; Shin, M.; Yoo, Y. J.; Song, Y. M.; Hyeon, T.; Kim, D.-H.; Son, D. Stretchable Colour-Sensitive Quantum Dot Nanocomposites for Shape-Tunable Multiplexed Phototransistor Arrays. *Nat. Nanotechnol.* **2022**, *17*, 849−856.
(209) Lee, M. Y.; Oh, Y.; Hong, J.; Lee, S. J.; Seong, D. G.; Um, M. K.; Oh, J. H. Fabrication of Stretchable and Transparent Core-Shell Polymeric Nanofibers Using Coaxial Electrospinning and Their Application to Phototransistors. *Adv. Electron. Mater.* **2021**, *7*, 2001000.
(210) Mahato, A. K.; Bharti, D.; Saxena, P.; Raghuwanshi, V.; Varun, I.; Tiwari, S. P. Influence of Molecular Weight of Polymer Dielectric on the Photo-Response of Solution-Processed OFETs. *Polymer* **2021**, *224*, 123724.
(211) Koo, J. H.; Kang, J.; Lee, S.; Song, J.-K.; Choi, J.; Yoon, J.; Park, H. J.; Sunwoo, S.-H.; Kim, D. C.; Nam, W.; et al. A Vacuum-Deposited Polymer Dielectric for Wafer-Scale Stretchable Electronics. *Nat. Electron.* **2023**, *6*, 137−145.
(212) Lu, X.; Zhang, Y.; Zheng, Z. Metal-Based Flexible Transparent Electrodes: Challenges and Recent Advances. *Adv. Electron. Mater.* **2021**, *7*, 2001121.

https://doi.org/10.1021/acs.chemrev.3c00548
Chem. Rev. XXXX, XXX, XXX−XXX

(213) Bi, Y. G.; Liu, Y. F.; Zhang, X. L.; Yin, D.; Wang, W. Q.; Feng, J.; Sun, H. B. Ultrathin Metal Films as the Transparent Electrode in ITO-Free Organic Optoelectronic Devices. *Adv. Opt. Mater.* **2019**, *7*, 1800778.
(214) Zhao, G.; Shen, W.; Jeong, E.; Lee, S.-G.; Yu, S. M.; Bae, T.-S.; Lee, G.-H.; Han, S. Z.; Tang, J.; Choi, E.-A.; et al. Ultrathin Silver Film Electrodes with Ultralow Optical and Electrical Losses for Flexible Organic Photovoltaics. *ACS Appl. Mater. Interfaces* **2018**, *10*, 27510−27520.
(215) Shi, L.; Song, J.; Zhang, Y.; Li, G.; Wang, W.; Hao, Y.; Wu, Y.; Cui, Y. High-Performance Flexible Organic Photomultiplication Photodetector Based on an Ultra-Thin Silver Film Transparent Electrode. *Nanotechnology* **2020**, *31*, 314001.
(216) Huang, J.; Liu, X.; Lu, Y.; Zhou, Y.; Xu, J.; Li, J.; Wang, H.; Fang, J.; Yang, Y.; Wang, W.; et al. Seed-Layer-Free Growth of Ultra-Thin Ag Transparent Conductive Films Imparts Flexibility to Polymer Solar Cells. *Sol. Energy Mater. Sol. Cells* **2018**, *184*, 73−81.
(217) Li, Y.; Feng, J.; Wang, Y.; He, B.; Zhao, Y.; Xu, C.; Wang, J. Highly Conductive and Flexible Electrodes Based on Ultrathin Aluminum-Doped Zinc Oxide Epitaxial Films. *Appl. Surf. Sci.* **2021**, *568*, 150925.
(218) Kossoy, A.; Merk, V.; Simakov, D.; Leosson, K.; Kéna-Cohen, S.; Maier, S. A. Optical and Structural Properties of Ultra-Thin Gold Films. *Adv. Opt. Mater.* **2015**, *3*, 71−77.
(219) Yin, D.; Chen, Z.-Y.; Jiang, N.-R.; Liu, Y.-F.; Bi, Y.-G.; Zhang, X.-L.; Han, W.; Feng, J.; Sun, H.-B. Highly Transparent and Flexible Fabric-Based Organic Light Emitting Devices for Unnoticeable Wearable Displays. *Org. Electron.* **2020**, *76*, 105494.
(220) Bi, Y.-G.; Yi, F.-S.; Ji, J.-H.; Ma, C.; Wang, W.-Q.; Feng, J.; Sun, H.-B. Ultrathin Au Electrodes Based on a Hybrid Nucleation Layer for Flexible Organic Light-Emitting Devices. *IEEE Trans. Nanotechnol.* **2018**, *17*, 1077−1081.
(221) Xiong, P.; Liu, Y.; Ding, T.; Chen, P.; Wang, H.; Duan, Y. Transparent Electrodes Based on Ultrathin/Ultra Smooth Cu Films Produced Through Atomic Layer Deposition as New ITO-Free Organic Light-Emitting Devices. *Org. Electron.* **2018**, *58*, 18−24.
(222) Zhao, G.; Kim, S. M.; Lee, S. G.; Bae, T. S.; Mun, C.; Lee, S.; Yu, H.; Lee, G. H.; Lee, H. S.; Song, M.; et al. Bendable Solar Cells from Stable, Flexible, and Transparent Conducting Electrodes Fabricated Using a Nitrogen-Doped Ultrathin Copper Film. *Adv. Funct. Mater.* **2016**, *26*, 4180−4191.
(223) Zhao, G.; Wang, W.; Bae, T.-S.; Lee, S.-G.; Mun, C.; Lee, S.; Yu, H.; Lee, G.-H.; Song, M.; Yun, J. Stable Ultrathin Partially Oxidized Copper Film Electrode for Highly Efficient Flexible Solar Cells. *Nat. Commun.* **2015**, *6* (1), 8830.
(224) Xiong, W.; Liu, H.; Chen, Y.; Zheng, M.; Zhao, Y.; Kong, X.; Wang, Y.; Zhang, X.; Kong, X.; Wang, P.; et al. Highly Conductive, Air-Stable Silver Nanowire@Ion Gel Composite Films Toward Flexible Transparent Electrodes. *Adv. Mater.* **2016**, *28*, 7167.
(225) Lian, L.; Dong, D.; Feng, D.; He, G. Low Roughness Silver Nanowire Flexible Transparent Electrode by Low-Temperature Solution Processing for Organic Light Emitting Diodes. *Org. Electron.* **2017**, *49*, 9−18.
(226) Wang, Y.; Liu, P.; Wang, H.; Zeng, B.; Wang, J.; Chi, F. Flexible Organic Light-Emitting Devices with Copper Nanowire Composite Transparent Conductive Electrode. *J. Mater. Sci.* **2019**, *54*, 2343−2350.
(227) Sun, W.-J.; Xu, L.; Jia, L.-C.; Zhou, C.-G.; Xiang, Y.; Yin, R.-H.; Yan, D.-X.; Tang, J.-H.; Li, Z.-M. Highly Conductive and Stretchable Carbon Nanotube/Thermoplastic Polyurethane Composite for Wearable Heater. *Compos. Sci. Technol.* **2019**, *181*, 107695.
(228) Che, B.; Zhou, D.; Li, H.; He, C.; Liu, E.; Lu, X. A Highly Bendable Transparent Electrode for Organic Electrochromic Devices. *Org. Electron.* **2019**, *66*, 86−93.
(229) Siwal, S. S.; Saini, A. K.; Rarotra, S.; Zhang, Q.; Thakur, V. K. Recent Advancements in Transparent Carbon Nanotube Films: Chemistry and Imminent Challenges. *J. Nanostructure Chem.* **2021**, *11*, 93−130.
(230) Chen, Y.; Yue, Y. Y.; Wang, S. R.; Zhang, N.; Feng, J.; Sun, H. B. Graphene as a Transparent and Conductive Electrode for Organic Optoelectronic Devices. *Adv. Electron. Mater.* **2019**, *5*, 1900247.
(231) Ma, Y.; Zhi, L. Graphene-Based Transparent Conductive Films: Material Systems, Preparation, and Applications. *Small Methods* **2019**, *3*, 1800199.
(232) Zhang, M.; Yeow, J. T. A Flexible, Scalable, and Self-Powered Mid-Infrared Detector Based on Transparent PEDOT:PSS/Graphene Composite. *Carbon* **2020**, *156*, 339−345.
(233) Kayser, L. V.; Lipomi, D. J. Stretchable Conductive Polymers and Composites Based on PEDOT and PEDOT:PSS. *Adv. Mater.* **2019**, *31*, 1806133.
(234) Huseynova, G.; Hyun Kim, Y.; Lee, J.-H.; Lee, J. Rising Advancements in the Application of PEDOT:PSS as a Prosperous Transparent and Flexible Electrode Material for Solution-Processed Organic Electronics. *J. Inf. Dispersion* **2020**, *21*, 71−91.
(235) Ma, C.; Luo, H.; Liu, M.; Yang, H.; Liu, H.; Zhang, X.; Jiang, L. Preparation of Intrinsic Flexible Conductive PEDOT:PSS@Ionogel Composite Film and Its Application for Touch Panel. *J. Chem. Eng.* **2021**, *425*, 131542.
(236) Hwang, B.-Y.; Choi, S.-H.; Lee, K.-W.; Kim, J.-Y. Highly Stretchable and Transparent Electrode Film Based on SWCNT/Silver Nanowire Hybrid Nanocomposite. *Compos. B. Eng.* **2018**, *151*, 1−7.
(237) Ricciardulli, A. G.; Yang, S.; Wetzelaer, G. J. A.; Feng, X.; Blom, P. W. Hybrid Silver Nanowire and Graphene-Based Solution-Processed Transparent Electrode for Organic Optoelectronics. *Adv. Funct. Mater.* **2018**, *28*, 1706010.
(238) Xu, T.; Kong, D.; Tang, H.; Qin, X.; Li, X.; Gurung, A.; Kou, K.; Chen, L.; Qiao, Q.; Huang, W. Transparent MoS_2/PEDOT Composite Counter Electrodes for Bifacial Dye-Sensitized Solar Cells. *ACS omega* **2020**, *5* (15), 8687−8696.
(239) Fan, X.; Nie, W.; Tsai, H.; Wang, N.; Huang, H.; Cheng, Y.; Wen, R.; Ma, L.; Yan, F.; Xia, Y. PEDOT:PSS for Flexible and Stretchable Electronics: Modifications, Strategies, and Applications. *Adv. Sci.* **2019**, *6*, 1900813.
(240) Dauzon, E.; Mansour, A. E.; Niazi, M. R.; Munir, R.; Smilgies, D.-M.; Sallenave, X.; Plesse, C.; Goubard, F.; Amassian, A. Conducting and Stretchable PEDOT:PSS Electrodes: Role of Additives on Self-Assembly, Morphology, and Transport. *ACS Appl. Mater. Interfaces* **2019**, *11*, 17570−17582.
(241) Lee, H. B.; Jin, W.-Y.; Ovhal, M. M.; Kumar, N.; Kang, J.-W. Flexible Transparent Conducting Electrodes Based on Metal Meshes for Organic Optoelectronic Device Applications: A Review. *J. Mater. Chem. C* **2019**, *7*, 1087−1110.
(242) Nguyen, V. H.; Papanastasiou, D. T.; Resende, J.; Bardet, L.; Sannicolo, T.; Jiménez, C.; Muñoz-Rojas, D.; Nguyen, N. D.; Bellet, D. Advances in Flexible Metallic Transparent Electrodes. *Small* **2022**, *18*, 2106006.
(243) Sennett, R.; Scott, G. The Structure of Evaporated Metal Films and Their Optical Properties. *Josa* **1950**, *40*, 203−211.
(244) Bae, S. K.; Choo, D. C.; Kang, H. S.; Yoo, K. H.; Kim, T. W. Transparent Ultra-Thin Silver Electrodes formed via a Maskless Evaporation Process for Applications in Flexible Organic Light-Emitting Devices. *Nano Energy* **2020**, *71*, 104649.
(245) Xu, L.-H.; Ou, Q.-D.; Li, Y.-Q.; Zhang, Y.-B.; Zhao, X.-D.; Xiang, H.-Y.; Chen, J.-D.; Zhou, L.; Lee, S.-T.; Tang, J.-X. Microcavity-Free Broadband Light Outcoupling Enhancement in Flexible Organic Light-Emitting Diodes with Nanostructured Transparent Metal-Dielectric Composite Electrodes. *ACS Nano* **2016**, *10*, 1625−1632.
(246) Bellchambers, P.; Walker, M.; Huband, S.; Dirvanauskas, A.; Hatton, R. A. Enhanced Oxidation Stability of Transparent Copper Films Using a Hybrid Organic-Inorganic Nucleation Layer. *ChemNanoMat* **2019**, *5*, 619−624.
(247) Hanmandlu, C.; Liu, C.-C.; Chen, C.-Y.; Boopathi, K. M.; Wu, S.-H.; Singh, M.; Mohapatra, A.; Lin, H.-W.; Chang, Y.-C.; Chang, Y.-C.; et al. Top Illuminated Hysteresis-Free Perovskite Solar Cells Incorporating Microcavity Structures on Metal Electrodes: A

https://doi.org/10.1021/acs.chemrev.3c00548
Chem. Rev. XXXX, XXX, XXX−XXX

Combined Experimental and Theoretical Approach. *ACS Appl. Mater. Interfaces* **2018**, *10*, 17973−17984.
(248) Xue, Z.; Liu, X.; Zhang, N.; Chen, H.; Zheng, X.; Wang, H.; Guo, X. High-Performance NiO/Ag/NiO Transparent Electrodes for Flexible Organic Photovoltaic Cells. *ACS Appl. Mater. Interfaces* **2014**, *6*, 16403−16408.
(249) Kim, D. Y.; Han, Y. C.; Kim, H. C.; Jeong, E. G.; Choi, K. C. Highly Transparent and Flexible Organic Light-Emitting Diodes with Structure Optimized for Anode/Cathode Multilayer Electrodes. *Adv. Funct. Mater.* **2015**, *25*, 7145−7153.
(250) Zhao, D.; Zhang, C.; Kim, H.; Guo, L. J. High-Performance Ta_2O_5/Al-Doped Ag Electrode for Resonant Light Harvesting in Efficient Organic Solar Cells. *Adv. Energy Mater.* **2015**, *5*, 1500768.
(251) Jeong, S.; Jung, S.; Kang, H.; Lee, D.; Choi, S. B.; Kim, S.; Park, B.; Yu, K.; Lee, J.; Lee, K. Role of Polymeric Metal Nucleation Inducers in Fabricating Large-Area, Flexible, and Transparent Electrodes for Printable Electronics. *Adv. Funct. Mater.* **2017**, *27*, 1606842.
(252) Bi, Y.-G.; Feng, J.; Ji, J.-H.; Chen, Y.; Liu, Y.-S.; Li, Y.-F.; Liu, Y.-F.; Zhang, X.-L.; Sun, H.-B. Ultrathin and Ultrasmooth Au Films as Transparent Electrodes in ITO-Free Organic Light-Emitting Devices. *Nanoscale* **2016**, *8*, 10010−10015.
(253) Lee, J.; Walker, M.; Varagnolo, S.; Huband, S.; Hatton, R. A. Stabilizing Silver Window Electrodes for Organic Photovoltaics Using a Mercaptosilane Monolayer. *ACS Appl. Energy Mater.* **2019**, *2*, 5198−5205.
(254) Wang, H.; Wang, Z.; Xu, X.; Zhao, W.; Wu, D.; Muhammad, M.; Liu, Y.; Chen, C.; Liu, B.; Duan, Y. A Novel Nucleation Inducer for Ultrathin Au Anodes in High Efficiency and Flexible Organic Optoelectronic Devices. *Adv. Opt. Mater.* **2020**, *8*, 1901320.
(255) Bae, H. W.; Kim, S. K.; Lee, S.; Song, M. G.; Lampande, R.; Kwon, J. H. Thermally Evaporated Organic/Ag/Organic Multilayer Transparent Conducting Electrode for Flexible Organic Light-Emitting Diodes. *Adv. Electron. Mater.* **2019**, *5*, 1900620.
(256) Zhang, C.; Zhao, D.; Gu, D.; Kim, H.; Ling, T.; Wu, Y. K. R.; Guo, L. J. An Ultrathin, Smooth, and Low-Loss Al-Doped Ag Film and Its Application as a Transparent Electrode in Organic Photovoltaics. *Adv. Mater.* **2014**, *26*, 5696−5701.
(257) Zhang, C.; Huang, Q.; Cui, Q.; Ji, C.; Zhang, Z.; Chen, X.; George, T.; Zhao, S.; Guo, L. J. High-Performance Large-Scale Flexible Optoelectronics Using Ultrathin Silver Films with Tunable Properties. *ACS Appl. Mater. Interfaces* **2019**, *11*, 27216−27225.
(258) Ji, C.; Liu, D.; Zhang, C.; Jay Guo, L. Ultrathin-Metal-Film-Based Transparent Electrodes with Relative Transmittance Surpassing 100%. *Nat. Commun.* **2020**, *11*, 3367.
(259) Yun, J.; Wang, W.; Bae, T. S.; Park, Y. H.; Kang, Y.-C.; Kim, D.-H.; Lee, S.; Lee, G.-H.; Song, M.; Kang, J.-W. Preparation of Flexible Organic Solar Cells with Highly Conductive and Transparent Metal-Oxide Multilayer Electrodes Based on Silver Oxide. *ACS Appl. Mater. Interfaces* **2013**, *5*, 9933−9941.
(260) Wang, W.; Song, M.; Bae, T. S.; Park, Y. H.; Kang, Y. C.; Lee, S. G.; Kim, S. Y.; Kim, D. H.; Lee, S.; Min, G.; et al. Transparent Ultrathin Oxygen-Doped Silver Electrodes for Flexible Organic Solar Cells. *Adv. Funct. Mater.* **2014**, *24*, 1551−1561.
(261) Gu, D.; Zhang, C.; Wu, Y.-K.; Guo, L. J. Ultrasmooth and Thermally Stable Silver-Based Thin Films with Subnanometer Roughness by Aluminum Doping. *ACS Nano* **2014**, *8*, 10343−10351.
(262) Khan, A.; Liang, C.; Huang, Y.-T.; Zhang, C.; Cai, J.; Feng, S.-P.; Li, W.-D. Template-Electrodeposited and Imprint-Transferred Microscale Metal-Mesh Transparent Electrodes for Flexible and Stretchable Electronics. *Adv. Eng. Mater.* **2019**, *21*, 1900723.
(263) Yu, J.-S.; Jung, G. H.; Jo, J.; Kim, J. S.; Kim, J. W.; Kwak, S.-W.; Lee, J.-L.; Kim, I.; Kim, D. Transparent Conductive Film with Printable Embedded Patterns for Organic Solar Cells. *Sol. Energy Mater. Sol. Cells* **2013**, *109*, 142−147.
(264) Kim, W.; Kim, S.; Kang, I.; Jung, M. S.; Kim, S. J.; Kim, J. K.; Cho, S. M.; Kim, J. H.; Park, J. H. Hybrid Silver Mesh Electrode for ITO-Free Flexible Polymer Solar Cells with Good Mechanical Stability. *ChemSusChem* **2016**, *9*, 1042−1049.
(265) Li, Z.; Li, H.; Zhu, X.; Peng, Z.; Zhang, G.; Yang, J.; Wang, F.; Zhang, Y. F.; Sun, L.; Wang, R.; et al. Directly Printed Embedded Metal Mesh for Flexible Transparent Electrode via Liquid Substrate Electric-Field-Driven Jet. *Adv. Sci.* **2022**, *9*, 2105331.
(266) Han, B.; Huang, Y.; Li, R.; Peng, Q.; Luo, J.; Pei, K.; Herczynski, A.; Kempa, K.; Ren, Z.; Gao, J. Bio-Inspired Networks for Optoelectronic Applications. *Nat. Commun.* **2014**, *5*, 5674.
(267) Yu, Y.; Zhang, Y.; Li, K.; Yan, C.; Zheng, Z. Bio-Inspired Chemical Fabrication of Stretchable Transparent Electrodes. *Small* **2015**, *11*, 3444−3449.
(268) Li, L.; Fan, Q.; Xue, H.; Zhang, S.; Wu, S.; He, Z.; Wang, J. Recrystallized Ice-Templated Electroless Plating for Fabricating Flexible Transparent Copper Meshes. *RSC Adv.* **2020**, *10*, 9894−9901.
(269) Li, P.; Zhao, Y.; Ma, J.; Yang, Y.; Xu, H.; Liu, Y. Facile Fabrication of Ultraflexible Transparent Electrodes Using Embedded Copper Networks for Wearable Pressure Sensors. *Adv. Mater. Technol.* **2020**, *5*, 1900823.
(270) Zhang, Z.; Zhang, X.; Xin, Z.; Deng, M.; Wen, Y.; Song, Y. Controlled Inkjetting of a Conductive Pattern of Silver Nanoparticles Based on the Coffee-Ring Effect. *Adv. Mater.* **2013**, *25*, 6714−6718.
(271) Tai, Y.-L.; Yang, Z.-G. Flexible, Transparent, Thickness-Controlable SWCNT/PEDOT:PSS Hybrid Films Based on Coffee-Ring Lithography for Functional Noncontact Sensing Device. *Langmuir* **2015**, *31*, 13257−13264.
(272) Guo, C. F.; Sun, T.; Liu, Q.; Suo, Z.; Ren, Z. Highly Stretchable and Transparent Nanomesh Electrodes Made by Grain Boundary Lithography. *Nat. Commun.* **2014**, *5*, 3121.
(273) Schneider, J.; Rohner, P.; Thureja, D.; Schmid, M.; Galliker, P.; Poulikakos, D. Electrohydrodynamic NanoDrip Printing of High Aspect Ratio Metal Grid Transparent Electrodes. *Adv. Funct. Mater.* **2016**, *26*, 833−840.
(274) Zhang, B.; Lee, H.; Byun, D. Electrohydrodynamic Jet Printed 3D Metallic Grid: Toward High-Performance Transparent Electrodes. *Adv. Eng. Mater.* **2020**, *22*, 1901275.
(275) Song, J. K.; Son, D.; Kim, J.; Yoo, Y. J.; Lee, G. J.; Wang, L.; Choi, M. K.; Yang, J.; Lee, M.; Do, K.; et al. Wearable force Touch Sensor Array Using a Flexible and Transparent Electrode. *Adv. Funct. Mater.* **2017**, *27*, 1605286.
(276) Kim, G.; Lim, J. W.; Lee, J.; Heo, S. J. Flexible Multilayered Transparent Electrodes with Less Than 50 nm Thickness Using Nitrogen-Doped Silver Layers for Flexible Heaters. *Mater. Res. Bull.* **2022**, *149*, 111703.
(277) Choi, D. K.; Kim, D. H.; Lee, C. M.; Hafeez, H.; Sarker, S.; Yang, J. S.; Chae, H. J.; Jeong, G.-W.; Choi, D. H.; Kim, T. W.; et al. Highly Efficient, Heat Dissipating, Stretchable Organic Light-Emitting Diodes Based on a MoO_3/Au/MoO_3 Electrode with Encapsulation. *Nat. Commun.* **2021**, *12*, 2864.
(278) Li, H.; Shen, H.; Zhu, X.; Zhang, J.; Li, Y.; Bai, H.; Chen, J.; Zeng, J.; Zheng, J.; Yue, Z.; et al. Investigation on Highly Flexible CZTS Solar Cells Using Transparent Conductive ZnO/Cu/ZnO Films. *Colloids Surf. A Physicochem. Eng. Asp.* **2023**, *663*, 131084.
(279) Choi, S.; Han, S. I.; Kim, D.; Hyeon, T.; Kim, D.-H. High-Performance Stretchable Conductive Nanocomposites: Materials, Processes, and Device Applications. *Chem. Soc. Rev.* **2019**, *48*, 1566−1595.
(280) Nam, S.; Park, C.; Sunwoo, S.-H.; Kim, M.; Lee, H.; Lee, M.; Kim, D.-H. Soft Conductive Nanocomposites for Recording Biosignals on Skin. *Soft Sci.* **2023**, DOI: 10.20517/ss.2023.19.
(281) Park, C.; Kim, M. S.; Kim, H. H.; Sunwoo, S.-H.; Jung, D. J.; Choi, M. K.; Kim, D.-H. Stretchable Conductive Nanocomposites and Their Applications in Wearable Devices. *Appl. Phys. Rev.* **2022**, *9*, 021312.
(282) Shim, H. J.; Sunwoo, S. H.; Kim, Y.; Koo, J. H.; Kim, D. H. Functionalized Elastomers for Intrinsically Soft and Bio-Integrated Electronics. *Adv. Healthc. Mater.* **2021**, *10*, 2002105.
(283) Huang, S.; Liu, Y.; Zhao, Y.; Ren, Z.; Guo, C. F. Flexible Electronics: Stretchable Electrodes and Their Future. *Adv. Funct. Mater.* **2019**, *29*, 1805924.

https://doi.org/10.1021/acs.chemrev.3c00548
Chem. Rev. XXXX, XXX, XXX−XXX

(284) Yun, G.; Tang, S.-Y.; Lu, H.; Zhang, S.; Dickey, M. D.; Li, W. Hybrid-Filler Stretchable Conductive Composites: from Fabrication to Application. *Small Science* **2021**, *1*, 2000080.
(285) Llerena Zambrano, B.; Renz, A. F.; Ruff, T.; Lienemann, S.; Tybrandt, K.; Vörös, J.; Lee, J. Soft Electronics Based on Stretchable and Conductive Nanocomposites for Biomedical Applications. *Adv. Healthc. Mater.* **2021**, *10*, 2001397.
(286) Han, J.; Yang, J.; Gao, W.; Bai, H. Ice-Templated, Large-Area Silver Nanowire Pattern for Flexible Transparent Electrode. *Adv. Funct. Mater.* **2021**, *31*, 2010155.
(287) Park, S. B.; Han, J. W.; Kim, J. H.; Wibowo, A. F.; Prameswati, A.; Park, J.; Lee, J.; Moon, M. W.; Kim, M. S.; Kim, Y. H. Multifunctional Stretchable Organic-Inorganic Hybrid Electronics with Transparent Conductive Silver Nanowire/Biopolymer Hybrid Films. *Adv. Opt. Mater.* **2021**, *9*, 2002041.
(288) Gao, Z.; Yiu, C.; Liu, Y.; Li, D.; Mei, L.; Zeng, Z.; Yu, X. Stretchable Transparent Conductive Elastomers for Skin-Integrated Electronics. *J. Mater. Chem. C* **2020**, *8*, 15105−15111.
(289) Li, D.; Lai, W. Y.; Feng, F.; Huang, W. Post-Treatment of Screen-Printed Silver Nanowire Networks for Highly Conductive Flexible Transparent Films. *Adv. Mater. Interfaces* **2021**, *8*, 2100548.
(290) Wu, H.; Kong, D.; Ruan, Z.; Hsu, P.-C.; Wang, S.; Yu, Z.; Carney, T. J.; Hu, L.; Fan, S.; Cui, Y. A Transparent Electrode Based on a Metal Nanotrough Network. *Nat. Nanotechnol.* **2013**, *8*, 421−425.
(291) Sun, Y.; Chang, M.; Meng, L.; Wan, X.; Gao, H.; Zhang, Y.; Zhao, K.; Sun, Z.; Li, C.; Liu, S.; et al. Flexible Organic Photovoltaics Based on Water-Processed Silver Nanowire Electrodes. *Nat. Electron.* **2019**, *2*, 513−520.
(292) Cui, N.; Song, Y.; Tan, C.-H.; Zhang, K.; Yang, X.; Dong, S.; Xie, B.; Huang, F. Stretchable Transparent Electrodes for Conformable Wearable Organic Photovoltaic Devices. *npj Flex. Electron.* **2021**, *5*, 31.
(293) Hwang, I.; Seong, M.; Yi, H.; Ko, H.; Park, H. H.; Yeo, J.; Bae, W. G.; Park, H. W.; Jeong, H. E. Low-Resistant Electrical and Robust Mechanical Contacts of Self-Attachable Flexible Transparent Electrodes with Patternable Circuits. *Adv. Funct. Mater.* **2020**, *30*, 2000458.
(294) Zhang, H.; Wang, S.; Tian, Y.; Wen, J.; Hang, C.; Zheng, Z.; Huang, Y.; Ding, S.; Wang, C. High-Efficiency Extraction Synthesis for High-Purity Copper Nanowires and Their Applications in Flexible Transparent Electrodes. *Nano Mater. Sci.* **2020**, *2*, 164−171.
(295) Hu, W.; Wang, R.; Lu, Y.; Pei, Q. An Elastomeric Transparent Composite Electrode Based on Copper Nanowires and Polyurethane. *J. Mater. Chem. C* **2014**, *2*, 1298−1305.
(296) Zhou, Y.; Azumi, R.; Shimada, S. A Highly Durable, Stretchable, Transparent and Conductive Carbon Nanotube-Polymeric Acid Hybrid Film. *Nanoscale* **2019**, *11*, 3804−3813.
(297) Chen, J.; Zhu, Y.; Jiang, W. A Stretchable and Transparent Strain Sensor Based on Sandwich-Like PDMS/CNTs/PDMS Composite Containing an Ultrathin Conductive CNT Layer. *Compos. Sci. Technol.* **2020**, *186*, 107938.
(298) Jang, W.; Kim, B. G.; Seo, S.; Shawky, A.; Kim, M. S.; Kim, K.; Mikladal, B.; Kauppinen, E. I.; Maruyama, S.; Jeon, I.; Wang, D. H. Strong Dark Current Suppression in Flexible Organic Photodetectors by Carbon Nanotube Transparent Electrodes. *Nano Today* **2021**, *37*, 101081.
(299) Roh, J. S.; Jang, J. K.; Kwon, N.; Bok, S.; Kim, Y. J.; Jeon, C.; Yoon, H. W.; Kim, H. W.; Lim, B.; Park, H. B. Macroscopic Properties of Single-Crystalline and Polycrystalline Graphene on Soft Substrate for Transparent Electrode Applications. *Carbon* **2021**, *178*, 181−189.
(300) Han, Y.; Park, B. J.; Eom, J. H.; Jella, V.; Ippili, S.; Pammi, S.; Choi, J. S.; Ha, H.; Choi, H.; Jeon, C.; et al. Direct Growth of Highly Conductive Large-Area Stretchable Graphene. *Adv. Sci.* **2021**, *8*, 2003697.
(301) Hong, J.-Y.; Kim, W.; Choi, D.; Kong, J.; Park, H. S. Omnidirectionally Stretchable and Transparent Graphene Electrodes. *ACS Nano* **2016**, *10*, 9446−9455.
(302) Liu, L.; Li, S.; Wu, L.; Chen, D.; Cao, K.; Duan, Y.; Chen, S. Enhanced Flexibility and Stability of PEDOT:PSS Electrodes Through Interfacial Crosslinking for Flexible Organic Light-Emitting Diodes. *Org. Electron.* **2021**, *89*, 106047.
(303) Teo, M. Y.; Kim, N.; Kee, S.; Kim, B. S.; Kim, G.; Hong, S.; Jung, S.; Lee, K. Highly Stretchable and Highly Conductive PEDOT:PSS/Ionic Liquid Composite Transparent Electrodes for Solution-Processed Stretchable Electronics. *ACS Appl. Mater. Interfaces* **2017**, *9*, 819−826.
(304) Dauzon, E.; Lin, Y.; Faber, H.; Yengel, E.; Sallenave, X.; Plesse, C.; Goubard, F.; Amassian, A.; Anthopoulos, T. D. Stretchable and Transparent Conductive PEDOT:PSS-Based Electrodes for Organic Photovoltaics and Strain Sensors Applications. *Adv. Funct. Mater.* **2020**, *30*, 2001251.
(305) Yang, Y.; Chen, S.; Li, W.; Li, P.; Ma, J.; Li, B.; Zhao, X.; Ju, Z.; Chang, H.; Xiao, L.; et al. Reduced Graphene Oxide Conformally Wrapped Silver Nanowire Networks for Flexible Transparent Heating and Electromagnetic Interference Shielding. *ACS Nano* **2020**, *14*, 8754−8765.
(306) Zhou, H.; Han, S. J.; Harit, A. K.; Kim, D. H.; Kim, D. Y.; Choi, Y. S.; Kwon, H.; Kim, K.-N.; Go, G.-T.; Yun, H. J.; et al. Graphene-Based Intrinsically Stretchable 2D-Contact Electrodes for Highly Efficient Organic Light-Emitting Diodes. *Adv. Mater.* **2022**, *34*, 2203040.
(307) Jiang, W.; Lee, S.; Zhao, K.; Lee, K.; Han, H.; Oh, J.; Lee, H.; Kim, H.; Koo, C. M.; Park, C. Flexible and Transparent Electrode of Hybrid $Ti_3C_2T_X$ MXene-Silver Nanowires for High-Performance Quantum Dot Light-Emitting Diodes. *ACS Nano* **2022**, *16*, 9203−9213.
(308) Alshammari, A. S. Improved Electrical Stability of Silver NWs Based Hybrid Transparent Electrode Interconnected with Polymer Functionalized CNTs. *Mater. Res. Bull.* **2019**, *111*, 245−250.
(309) Lee, P.; Ham, J.; Lee, J.; Hong, S.; Han, S.; Suh, Y. D.; Lee, S. E.; Yeo, J.; Lee, S. S.; Lee, D.; et al. Highly Stretchable or Transparent Conductor Fabrication by a Hierarchical Multiscale Hybrid Nanocomposite. *Adv. Funct. Mater.* **2014**, *24*, 5671−5678.
(310) Wang, Y.; Kong, X.; Gao, J.; Gong, M.; Lin, X.; Zhang, L.; Guo, M.; Wang, D. Customizable Stretchable Transparent Electrodes Based on AgNW/CNT Hybrids via Tailoring Sizes of Building Blocks. *ACS Appl. Electron. Mater.* **2022**, *4*, 1186−1195.
(311) Cui, N.; Tang, Q.; Ren, H.; Zhao, X.; Tong, Y.; Liu, Y. A Photolithographic Stretchable Transparent Electrode for an All-Solution-Processed Fully Transparent Conformal Organic Transistor Array. *J. Mater. Chem. C* **2019**, *7*, 5385−5393.
(312) Yang, H.; Bai, S.; Chen, T.; Zhang, Y.; Wang, H.; Guo, X. Facile Fabrication of Large-Scale Silver Nanowire-PEDOT:PSS Composite Flexible Transparent Electrodes for Flexible Touch Panels. *Mater. Res. Express* **2019**, *6*, 086315.
(313) Shin, H.; Sharma, B. K.; Lee, S. W.; Lee, J.-B.; Choi, M.; Hu, L.; Park, C.; Choi, J. H.; Kim, T. W.; Ahn, J.-H. Stretchable Electroluminescent Display Enabled by Graphene-Based Hybrid Electrode. *ACS Appl. Mater. Interfaces* **2019**, *11*, 14222−14228.
(314) Bai, S.; Guo, X.; Chen, T.; Zhang, Y.; Zhang, X.; Yang, H.; Zhao, X. Solution-Processed Fabrication of Silver Nanowire-MXene@PEDOT:PSS Flexible Transparent Electrodes for Flexible Organic Light-Emitting Diodes. *Compos. Part A Appl. Sci. Manuf.* **2020**, *139*, 106088.
(315) Chen, Y.; Carmichael, R. S.; Carmichael, T. B. Patterned, Flexible, and Stretchable Silver Nanowire/Polymer Composite Films as Transparent Conductive Electrodes. *ACS Appl. Mater. Interfaces* **2019**, *11*, 31210−31219.
(316) Hu, L.; Wu, H.; Cui, Y. Metal Nanogrids, Nanowires, and Nanofibers for Transparent Electrodes. *MRS Bull.* **2011**, *36*, 760−765.
(317) Huang, X.; Yin, Z.; Wu, S.; Qi, X.; He, Q.; Zhang, Q.; Yan, Q.; Boey, F.; Zhang, H. Graphene-Based Materials: Synthesis, Characterization, Properties, and Applications. *small* **2011**, *7*, 1876−1902.
(318) Chang, H.; Wu, H. Graphene-Based Nanomaterials: Synthesis, Properties, and Optical and Optoelectronic Applications. *Adv. Funct. Mater.* **2013**, *23*, 1984−1997.

https://doi.org/10.1021/acs.chemrev.3c00548
Chem. Rev. XXXX, XXX, XXX−XXX

(319) He, M.; Jung, J.; Qiu, F.; Lin, Z. Graphene-Based Transparent Flexible Electrodes for Polymer Solar Cells. *J. Mater. Chem.* **2012**, *22*, 24254−24264.
(320) Si, P.; Trinidad, J.; Chen, L.; Lee, B.; Chen, A.; Persic, J.; Lyn, R.; Leonenko, Z.; Zhao, B. PEDOT:PSS Nano-Gels for Highly Electrically Conductive Silver/Epoxy Composite Adhesives. *J. Mater. Sci. Mater. Electron.* **2018**, *29*, 1837−1846.
(321) Fan, Z.; Ouyang, J. Thermoelectric Properties of PEDOT:PSS. *Adv. Electron. Mater.* **2019**, *5*, 1800769.
(322) El Zein, A.; Huppé, C.; Cochrane, C. Development of a Flexible Strain Sensor Based on PEDOT:PSS for Thin Film Structures. *Sensors* **2017**, *17*, 1337.
(323) Molberg, M.; Crespy, D.; Rupper, P.; Nüesch, F.; Månson, J. A. E.; Löwe, C.; Opris, D. M. High Breakdown Field Dielectric Elastomer Actuators Using Encapsulated Polyaniline as High Dielectric Constant Filler. *Adv. Funct. Mater.* **2010**, *20*, 3280−3291.
(324) Sreeja, R.; Sharma, P.; Najidha, S.; Jayan, S. R.; Predeep, P. Semi-Interpenetrating Conducting Elastomer Composite Thin Films from Polyaniline. *Polym. Polym. Compos.* **2006**, *14*, 261−269.
(325) DS, P. D.; Thekkedath, J.; Kutty, S. K. N. Synthesis and Characterization of Conducting Composites of Polypyrrole/Polypyrrole-Coated Short Nylon Fiber and Natural Rubber. *Polym. Plast. Technol. Eng.* **2012**, *51*, 823−831.
(326) Kurian, A. S.; Souri, H.; Mohan, V. B.; Bhattacharyya, D. Highly Stretchable Strain Sensors Based on Polypyrrole-Silicone Rubber Composites for Human Motion Detection. *Sens. Actuator A Phys.* **2020**, *312*, 112131.
(327) Preston, C.; Dobashi, Y.; Nguyen, N. T.; Sarwar, M. S.; Jun, D.; Plesse, C.; Sallenave, X.; Vidal, F.; Aubert, P.-H.; Madden, J. D. Intrinsically Stretchable Integrated Passive Matrix Electrochromic Display Using PEDOT:PSS Ionic Liquid Composite. *ACS Appl. Mater. Interfaces* **2023**, *15* (23), 28288−28299.
(328) Park, J.; Hwang, J. C.; Kim, G. G.; Park, J. U. Flexible Electronics Based on One-Dimensional and Two-Dimensional Hybrid Nanomaterials. *InfoMat* **2020**, *2*, 33−56.
(329) Lim, Y. W.; Jin, J.; Bae, B. S. Optically Transparent Multiscale Composite Films for Flexible and Wearable Electronics. *Adv. Mater.* **2020**, *32*, 1907143.
(330) Li, Y.; Wang, B.; Hu, H.; Zhang, J.; Wei, B.; Yang, L. Pseudo-Biological Highly Performance Transparent Electrodes Based on Capillary Force-Welded Hybrid AgNW Network. *IEEE Access* **2019**, *7*, 177944−177953.
(331) Wang, P.; Jian, M.; Zhang, C.; Wu, M.; Ling, X.; Zhang, J.; Wei, B.; Yang, L. Highly Stretchable Graphene-Based Flexible Hybrid Transparent Conductive Electrodes for Organic Solar Cells. *Adv. Mater. Interfaces* **2022**, *9*, 2101442.
(332) Lian, L.; Xi, X.; Dong, D.; He, G. Highly Conductive Silver Nanowire Transparent Electrode by Selective Welding for Organic Light Emitting Diode. *Org. Electron.* **2018**, *60*, 9−15.
(333) Wang, Y.; Zhang, L.; Wang, D. Ultrastretchable Hybrid Electrodes of Silver Nanowires and Multiwalled Carbon Nanotubes Realized by Capillary-Force-Induced Welding. *Adv. Mater. Technol.* **2019**, *4*, 1900721.
(334) Shajari, S.; Ramakrishnan, S.; Karan, K.; Sudak, L. J.; Sundararaj, U. Ultrasensitive Wearable Sensor with Novel Hybrid Structures of Silver Nanowires and Carbon Nanotubes in Fluoroelastomer: Multi-Directional Sensing for Human Health Monitoring and Stretchable Electronics. *Appl. Mater. Today* **2022**, *26*, 101295.
(335) Gustafsson, G.; Cao, Y.; Treacy, G. M.; Klavetter, F.; Colaneri, N.; Heeger, A. J. Flexible Light-Emitting Diodes Made from Soluble Conducting Polymers. *Nature* **1992**, *357*, 477−479.
(336) Gu, G.; Burrows, P. E.; Venkatesh, S.; forrest, S. R.; Thompson, M. E. Vacuum-Deposited, Nonpolymeric Flexible Organic Light-Emitting Devices. *Optic. Lett.* **1997**, *22*, 172−174.
(337) Tan, Z.; Xu, J.; Zhang, C.; Zhu, T.; Zhang, F.; Hedrick, B.; Pickering, S.; Wu, J.; Su, H.; Gao, S.; et al. Colloidal Nanocrystal-Based Light-Emitting Diodes Fabricated on Plastic Toward Flexible Quantum Dot Optoelectronics. *J. Appl. Phys.* **2009**, *105*, 034312.
(338) Kim, Y.-H.; Cho, H.; Heo, J. H.; Kim, T.-S.; Myoung, S.; Lee, C.-L.; Im, S. H.; Lee, T.-W. Multicolored Organic/Inorganic Hybrid Perovskite Light-Emitting Diodes. *Adv. Mater.* **2015**, *27*, 1248−1254.
(339) Nakamura, S.; Harada, Y.; Seno, M. Novel Metalorganic Chemical Vapor Deposition System for GaN Growth. *Appl. Phys. Lett.* **1991**, *58*, 2021−2023.
(340) Nakamura, S.; Senoh, M.; Iwasa, N.; Nagahama, S. High-Brightness InGaN Blue, Green and Yellow Light-Emitting Diodes with Quantum Well Structures. *Jpn. J. Appl. Phys.* **1995**, *34*, L797−L799.
(341) Parbrook, P. J.; Corbett, B.; Han, J.; Seong, T.; Amano, H. Micro-Light Emitting Diode: from Chips to Applications. *Laser Photon. Rev.* **2021**, *15*, 2000133.
(342) Behrman, K.; Kymissis, I. Micro Light-Emitting Diodes. *Nat. Electron.* **2022**, *5*, 564−573.
(343) Pimputkar, S.; Speck, J. S.; DenBaars, S. P.; Nakamura, S. Prospects for LED Lighting. *Nat. Photonics* **2009**, *3*, 180−182.
(344) Jin, S. X.; Li, J.; Li, J. Z.; Lin, J. Y.; Jiang, H. X. GaN Microdisk Light Emitting Diodes. *Appl. Phys. Lett.* **2000**, *76*, 631−633.
(345) Jin, S. X.; Li, J.; Lin, J. Y.; Jiang, H. X. InGaN/GaN Quantum Well Interconnected Microdisk Light Emitting Diodes. *Appl. Phys. Lett.* **2000**, *77*, 3236−3238.
(346) Virey, E. H.; Baron, N.; Bouhamri, Z. Overlooked Challenges for MicroLED Displays. *SID Symp. Dig. Technol. Pap.* **2019**, *50*, 129−132.
(347) Park, S.-I.; Xiong, Y.; Kim, R.-H.; Elvikis, P.; Meitl, M.; Kim, D.-H.; Wu, J.; Yoon, J.; Yu, C.-J.; Liu, Z.; et al. Printed Assemblies of Inorganic Light-Emitting Diodes for Deformable and Semitransparent Displays. *Science* **2009**, *325*, 977−981.
(348) Kim, S.; Wu, J.; Carlson, A.; Rogers, J. A. Microstructured Elastomeric Surfaces with Reversible Adhesion and Examples of Their Use in Deterministic Assembly by Transfer Printing. *Proc. Natl. Acad. Sci. U. S. A.* **2010**, *107*, 17095−17100.
(349) Kim, J.; Kim, J.-H.; Cho, S.-H.; Whang, K.-H. Selective Lift-Off of GaN Light-Emitting Diode from a Sapphire Substrate Using 266-nm Diode-Pumped Solid-State Laser Irradiation. *Appl. Phys. A: Mater. Sci. Process.* **2016**, *122*, 305.
(350) Cok, R. S.; Meitl, M.; Rotzoll, R.; Melnik, M.; Fecioru, A.; Trindade, A. J.; Raymond, B.; Bonafede, S.; Gomez, D.; Moore, T.; et al. Inorganic Light-Emitting Diode Displays Using Micro-Transfer Printing. *J. Soc. Inf. Dispersion* **2017**, *25*, 589.
(351) Bower, C. A.; Bonafede, S.; Pearson, A.; Raymond, B.; Prevatte, C.; Weeks, T.; Kneeburg, D.; Radauscher, E.; Vick, E.; Verreen, C.; et al. Mass Transfer Throughput and Yield Using Elastomer Stamps. *SID Symp. Dig. Technol. Pap.* **2021**, *52*, 849−852.
(352) Wang, F.; Liu, Q.; Xia, J.; Huang, M.; Wang, X.; Dai, W.; Zhang, G.; Yu, D.; Li, J.; Sun, R. Laser Lift-Off Technologies for Ultra-Thin Emerging Electronics: Mechanisms, Applications, and Progress. *Adv. Mater. Technol.* **2023**, *8*, 2201186.
(353) Delaporte, P.; Alloncle, A.-P. Laser-Induced forward Transfer: A High-Resolution Additive Manufacturing Technology. *Opt. Laser Technol.* **2016**, *78*, 33.
(354) Wong, W. S.; Sands, T.; Cheung, N. W.; Kneissl, M.; Bour, D. P.; Mei, P.; Romano, L. T.; Johnson, N. M. Fabrication of Thin-Film InGaN Light-Emitting Diode Membranes by Laser Lift-Off. *Appl. Phys. Lett.* **1999**, *75*, 1360−1362.
(355) Kim, T.-I.; Jung, Y. H.; Song, J.; Kim, D.; Li, Y.; Kim, H.-S.; Song, I.-S.; Wierer, J. J.; Pao, H. A.; Huang, Y.; et al. High-Efficiency, Microscale GaN Light-Emitting Diodes and Their Thermal Properties on Unusual Substrates. *Small* **2012**, *8*, 1643−1649.
(356) Pan, Z.; Guo, C.; Wang, X.; Liu, J.; Cao, R.; Gong, Y.; Wang, J.; Liu, N.; Chen, Z.; Wang, L.; et al. Wafer-Scale Micro-LEDs Transferred onto an Adhesive Film for Planar and Flexible Displays. *Adv. Mater. Technol.* **2020**, *5*, 2000549.
(357) Luo, H.; Wang, C.; Linghu, C.; Yu, K.; Wang, C.; Song, J. Laser-Driven Programmable Non-Contact Transfer Printing of Objects onto Arbitrary Receivers via an Active Elastomeric Microstructured Stamp. *Nat. Sci. Rev.* **2020**, *7*, 296−304.

https://doi.org/10.1021/acs.chemrev.3c00548
Chem. Rev. XXXX, XXX, XXX−XXX

(358) Huang, Y.; Zheng, N.; Cheng, Z.; Chen, Y.; Lu, B.; Xie, T.; Feng, X. Direct Laser Writing-Based Programmable Transfer Printing via Bioinspired Shape Memory Reversible Adhesive. *ACS Appl. Mater. Interfaces* **2016**, *8*, 35628−35633.
(359) Wang, C.; Linghu, C.; Nie, S.; Li, C.; Lei, Q.; Tao, X.; Zeng, Y.; Du, Y.; Zhang, S.; Yu, K.; et al. Programmable and Scalable Transfer Printing with High Reliability and Efficiency for Flexible Inorganic Electronics. *Sci. Adv.* **2020**, *6*, No. eabb2393.
(360) Kim, H.; Kim, J. C.; Jeong, Y.; Yu, J.; Lu, K.; Lee, D.; Kim, N.; Jeong, H. Y.; Kim, J.; Kim, S. Role of Transferred Graphene on Atomic Interaction of GaAs for Remote Epitaxy. *J. Appl. Phys.* **2021**, *130*, 174901.
(361) Kim, J.; Bayram, C.; Park, H.; Cheng, C.-W.; Dimitrakopoulos, C.; Ott, J. A.; Reuter, K. B.; Bedell, S. W.; Sadana, D. K. Principle of Direct Van der Waals Epitaxy of Single-Crystalline Films on Epitaxial Graphene. *Nat. Commun.* **2014**, *5*, 4836.
(362) Roh, I.; Goh, S. H.; Meng, Y.; Kim, J. S.; Han, S.; Xu, Z.; Lee, H. E.; Kim, Y.; Bae, S.-H. Applications of Remote Epitaxy and Van der Waals Epitaxy. *Nano Converg.* **2023**, *10*, 20.
(363) Chung, K.; Lee, C.-H.; Yi, G.-C. Transferable GaN Layers Grown on ZnO-Coated Graphene Layers for Optoelectronic Devices. *Science* **2010**, *330*, 655−657.
(364) Kim, H.; Chang, C. S.; Lee, S.; Jiang, J.; Jeong, J.; Park, M.; Meng, Y.; Ji, J.; Kwon, Y.; Sun, X.; et al. Remote Epitaxy. *Nat. Rev. Methods Primers* **2022**, *2*, 40.
(365) Kim, Y.; Cruz, S. S.; Lee, K.; Alawode, B. O.; Choi, C.; Song, Y.; Johnson, J. M.; Heidelberger, C.; Kong, W.; Choi, S.; et al. Remote Epitaxy Through Graphene Enables Two-Dimensional Material-Based Layer Transfer. *Nature* **2017**, *544*, 340−343.
(366) Shin, J.; Kim, H.; Sundaram, S.; Jeong, J.; Park, B.-I.; Chang, C. S.; Choi, J.; Kim, T.; Saravanapavanantham, M.; Lu, K.; et al. Vertical Full-Colour Micro-LEDs via 2D Materials-Based Layer Transfer. *Nature* **2023**, *614*, 81−87.
(367) Asad, M.; Li, Q.; Sachdev, M.; Wong, W. S. Thermal and Optical Properties of High-Density GaN Micro-LED Arrays on Flexible Substrates. *Nano Energy* **2020**, *73*, 104724.
(368) Kang, J.; Luo, H.; Tang, W.; Zhao, J.; Wang, Y.-M.; Tsong, T.; Lu, P.; Gupta, A.; Zeng, L.; Zhang, Z.; et al. Enabling Processes and Designs for Tight-Pitch Micro-LED Based Stretchable Display. *SID Symp. Dig. Technol. Pap.* **2021**, *52*, 1056−1059.
(369) Kim, N.; Kim, J.; Seo, J.; Hong, C.; Lee, J. Stretchable Inorganic LED Displays with Double-Layer Modular Design for High Fill Factor. *ACS Appl. Mater. Interfaces* **2022**, *14*, 4344−4351.
(370) Lee, Y.; Kim, B. J.; Hu, L.; Hong, J.; Ahn, J.-H. Morphable 3D Structure for Stretchable Display. *Mater. Today* **2022**, *53*, 51−57.
(371) Lee, S.-L.; Cheng, C.-C.; Liu, C.-J.; Yeh, C.-N.; Lin, Y.-C. 9.4-Inch 228-PPI Flexible Micro-LED Display. *J. SID* **2021**, *29*, 360−369.
(372) Lee, S. Y.; Park, K.-I.; Huh, C.; Koo, M.; Yoo, H. G.; Kim, S.; Ah, C. S.; Sung, G. Y.; Lee, K. J. Water-Resistant Flexible GaN LED on a Liquid Crystal Polymer Substrate for Implantable Biomedical Applications. *Nano Energy* **2012**, *1*, 145−151.
(373) Jang, B.; Won, S.; Kim, J.; Kim, J.; Oh, M.; Lee, H.-J.; Kim, J.-H. Auxetic Meta-Display: Stretchable Display without Image Distortion. *Adv. Funct. Mater.* **2022**, *32*, 2113299.
(374) Kim, R.-H.; Kim, D.-H.; Xiao, J.; Kim, B. H.; Park, S.-I.; Panilaitis, B.; Ghaffari, R.; Yao, J.; Li, M.; Liu, Z.; et al. Waterproof AlInGaP Optoelectronics on Stretchable Substrates with Applications in Biomedicine and Robotics. *Nat. Mater.* **2010**, *9*, 929−937.
(375) Jung, H.; Park, C. I.; Gee, M. B.; Choi, J.; Jeong, Y. R.; Min, S. J.; Song, J. H.; Lim, M. S.; Kim, M.; Kim, T.; et al. High-Resolution Active-Matrix Micro-LED Stretchable Displays. *J. SID* **2023**, *31*, 201−210.
(376) Tang, C. W.; VanSlyke, S. A. Organic Electroluminescent Diodes. *Appl. Phys. Lett.* **1987**, *51*, 913−915.
(377) Song, J.; Lee, H.; Jeong, E. G.; Choi, K. C.; Yoo, S. Organic Light-Emitting Diodes: Pushing Toward the Limits and Beyond. *Adv. Mater.* **2020**, *32*, 1907539.
(378) Zhang, D.; Huang, T.; Duan, L. Emerging Self-Emissive Technologies for Flexible Displays. *Adv. Mater.* **2020**, *32*, 1902391.
(379) Baldo, M. A.; O'Brien, D. F.; You, Y.; Shoustikov, A.; Sibley, S.; Thompson, M. E.; forrest, S. R. Highly Efficient Phosphorescent Emission from Organic Electroluminescent Devices. *Nature* **1998**, *395*, 151−154.
(380) Yang, X.; Zhou, G.; Wong, W.-Y. Functionalization of Phosphorescent Emitters and Their Host Materials by Main-Group Elements for Phosphorescent Organic Light-Emitting Devices. *Chem. Soc. Rev.* **2015**, *44*, 8484−8575.
(381) Li, W.; Pan, Y.; Xiao, R.; Peng, Q.; Zhang, S.; Ma, D.; Li, F.; Shen, F.; Wang, Y.; Yang, B.; et al. Employing ∼ 100% Excitons in OLEDs by Utilizing a Fluorescent Molecule with Hybridized Local and Charge-Transfer Excited State. *Adv. Funct. Mater.* **2014**, *24*, 1609−1614.
(382) Zhang, H.; Zeng, J.; Luo, W.; Wu, H.; Zeng, C.; Zhang, K.; Feng, W.; Wang, Z.; Zhao, Z.; Tang, Z. Synergistic Tuning of the Optical and Electrical Performance of AIEgens with a Hybridized Local and Charge-Transfer Excited State. *J. Mater. Chem. C* **2019**, *7*, 6359−6368.
(383) Yao, L.; Zhang, S.; Wang, R.; Li, W.; Shen, F.; Yang, B.; Ma, Y. Highly Efficient Near-Infrared Organic Light-Emitting Diode Based on a Butterfly-Shaped Donor-Acceptor Chromophore with Strong Solid-State Fluorescence and a Large Proportion of Radiative Excitons. *Angew. Chem.* **2014**, *53*, 2119.
(384) Chiang, C.-J.; Kimyonok, A.; Etherington, M. K.; Griffiths, G. C.; Jankus, V.; Turksoy, F.; Monkman, A. P. Ultrahigh Efficiency Fluorescent Single and Bi-Layer Organic Light Emitting Diodes: The Key Role of Triplet Fusion. *Adv. Funct. Mater.* **2013**, *23*, 739−746.
(385) Lin, B.-Y.; Easley, C. J.; Chen, C.-H.; Tseng, P.-C.; Lee, M.-Z.; Sher, P.-H.; Wang, J.-K.; Chiu, T.-L.; Lin, C.-F.; Bardeen, C. J.; et al. Exciplex-Sensitized Triplet-Triplet Annihilation in Heterojunction Organic Thin-Film. *ACS Appl. Mater. Interfaces* **2017**, *9*, 10963−10970.
(386) Tang, X.; Bai, Q.; Shan, T.; Li, J.; Gao, Y.; Liu, F.; Liu, H.; Peng, Q.; Yang, B.; Li, F.; et al. Efficient Nondoped Blue Fluorescent Organic Light-Emitting Diodes (OLEDs) with a High External Quantum Efficiency of 9.4% @ 1000 cd m^{-2} Based on Phenanthroimidazole-Anthracene derivative. *Adv. Funct. Mater.* **2018**, *28*, 1705813.
(387) Endo, A.; Sato, K.; Yoshimura, K.; Kai, T.; Kawada, A.; Miyazaki, H.; Adachi, C. Efficient Up-Conversion of Triplet Excitons into a Singlet State and Its Application for Organic Light Emitting Diodes. *Appl. Phys. Lett.* **2011**, *98*, 083302.
(388) Uoyama, H.; Goushi, K.; Shizu, K.; Nomura, H.; Adachi, C. Highly Efficient Organic Light-Emitting Diodes from Delayed Fluorescence. *Nature* **2012**, *492*, 234−238.
(389) Ahn, D. H.; Kim, S. W.; Lee, H.; Ko, I. J.; Karthik, D.; Lee, J. Y.; Kwon, J. H. Highly Efficient Blue Thermally Activated Delayed Fluorescence Emitters Based on Symmetrical and Rigid Oxygen-Bridged Boron Acceptors. *Nat. Photonics* **2019**, *13*, 540−546.
(390) Zou, S.-J.; Shen, Y.; Xie, F.-M.; Chen, J.-D.; Li, Y.-Q.; Tang, J.-X. Recent Advances in Organic Light-Emitting Diodes: Toward Smart Lighting and Displays. *Mater. Chem. Front.* **2020**, *4*, 788−820.
(391) Möller, S.; forrest, S. R. Improved Light Out-Coupling in Organic Light Emitting Diodes Employing Ordered Microlens Arrays. *J. Appl. Phys.* **2002**, *91*, 3324−3327.
(392) Yang, J. P.; Bao, Q. Y.; Xu, Z. Q.; Li, Y. Q.; Tang, J. X.; Shen, S. Light Out-Coupling Enhancement of Organic Light-Emitting Devices with Microlens Array. *J. Appl. Phys.* **2010**, *97*, 223303.
(393) Xiang, H.-Y.; Li, Y.-Q.; Zhou, L.; Xie, H.-J.; Li, C.; Ou, Q.-D.; Chen, L.-S.; Lee, C.-S.; Lee, S.-T.; Tang, J.-X. Outcoupling-Enhanced Flexible Organic Light-Emitting Diodes on Ameliorated Plastic Substrate with Built-In Indium-Tin-Oxide-Free Transparent Electrode. *ACS Nano* **2015**, *9*, 7553−7562.
(394) Gu, G.; Garbuzov, D. Z.; Burrows, P. E.; Venkatesh, S.; forrest, S. R.; Thompson, M. E. High-External-Quantum-Efficiency Organic Light-Emitting Devices. *Optic. Lett.* **1997**, *22*, 396−398.
(395) Kim, E.; Cho, H.; Kim, K.; Koh, T.-W.; Chung, J.; Lee, J.; Park, Y.; Yoo, S. A Facile Route to Efficient, Low-Cost Flexible Organic Light-Emitting Diodes: Utilizing the High Refractive Index

and Built-In Scattering Properties of Industrial-Grade PEN Substrates. *Adv. Mater.* **2015**, *27*, 1624−1631.
(396) Schwab, T.; Schubert, S.; Müller-Meskamp, L.; Leo, K.; Gather, M. C. Eliminating Micro-Cavity Effects in White Top-Emitting OLEDs by Ultra-Thin Metallic Top Electrodes. *Adv. Optic. Mater.* **2013**, *1*, 921−925.
(397) Wang, Z. B.; Helander, M. G.; Qiu, J.; Puzzo, D. P.; Greiner, M. T.; Hudson, Z. M.; Wang, S.; Liu, Z. W.; Lu, Z. H. Unlocking the Full Potential of Organic Light-Emitting Diodes on Flexible Plastic. *Nat. Photonics* **2011**, *5*, 753−757.
(398) Koo, W. H.; Jeong, S. M.; Araoka, F.; Ishikawa, K.; Nishimura, S.; Toyooka, T.; Takezoe, H. Light Extraction from Organic Light-Emitting Diodes Enhanced by Spontaneously formed Buckles. *Nat. Photonics* **2010**, *4*, 222−226.
(399) Zhou, L.; Jiang, X.; Li, Y.; Shi, A.; Chen, J.; Ou, Q.; Liu, H.; Tang, J. Light Extraction of Trapped Optical Modes in Polymer Light-Emitting Diodes with Nanoimprinted Double-Pattern Gratings. *ACS Appl. Mater. Interfaces* **2014**, *6*, 18139−18146.
(400) Jeong, S. M.; Araoka, F.; Machida, Y.; Ishikawa, K.; Takezoe, H.; Nishimura, S.; Suzaki, G. Enhancement of Normally Directed Light Outcoupling from Organic Light-Emitting Diodes Using Nanoimprinted Low-Refractive-Index Layer. *Appl. Phys. Lett.* **2008**, *92*, 083307.
(401) Wang, R.; Xu, L.-H.; Li, Y.-Q.; Zhou, L.; Li, C.; Ou, Q.-D.; Chen, J.-D.; Shen, S.; Tang, J.-X. Broadband Light Outcoupling Enhancement of Flexible Organic Light-Emitting Diodes Using Biomimetic Quasirandom Nanostructures. *Adv. Optic. Mater.* **2015**, *3*, 203−210.
(402) Yang, K. Y.; Choi, K. C.; Ahn, C. W. Surface Plasmon-Enhanced Spontaneous Emission Rate in an Organic Light-Emitting Device Structure: Cathode Structure for Plasmonic Application. *Appl. Phys. Lett.* **2009**, *94*, 173301.
(403) choi, H.; Ko, S.-J.; Choi, Y.; Joo, P.; Kim, T.; Lee, B. R.; Jung, J.-W.; Choi, H. J.; Cha, M.; Jeong, J.-R.; et al. Versatile Surface Plasmon Resonance of Carbon-Dot-Supported Silver Nanoparticles in Polymer Optoelectronic Devices. *Nat. Photonics* **2013**, *7*, 732−738.
(404) Xiang, H.-Y.; Li, Y.-Q.; Meng, S.-S.; Lee, C.-S.; Chen, L.-S.; Tang, J.-X. Extremely Efficient Transparent Flexible Organic Light-Emitting Diodes with Nanostructured Composite Electrodes. *Adv. Optic. Mater.* **2018**, *6*, 1800831.
(405) Lee, J.; Han, T.-H.; Park, M.-H.; Jung, D. Y.; Seo, J.; Seo, H.-K.; Cho, H.; Kim, E.; Chung, J.; Choi, S.-Y.; et al. Synergetic Electrode Architecture for Efficient Graphene-Based Flexible Organic Light-Emitting Diodes. *Nat. Commun.* **2016**, *7*, 11791.
(406) Shin, H.; Lee, J.-H.; Moon, C.-K.; Huh, J.-S.; Sim, B.; Kim, J.-J. Sky-Blue Phosphorescent OLEDs with 34.1% External Quantum Efficiency Using a Low Refractive Index Electron Transporting Layer. *Adv. Mater.* **2016**, *28*, 4920−4925.
(407) Frischeisen, J.; Yokoyama, D.; Endo, A.; Adachi, C.; Brütting, W. Increased Light Outcoupling Efficiency in Dye-Doped Small Molecule Organic Light-Emitting Diodes with Horizontally Oriented Emitters. *Org. Electron.* **2011**, *12*, 809−817.
(408) Sun, P.; Liu, D.; Zhu, F.; Yan, D. An Efficient Solid-Solution Crystalline Organic Light-Emitting Diode with Deep-Blue Emission. *Nat. Photonics* **2023**, *17*, 264−272.
(409) Su, R.; Park, S. H.; Ouyang, X.; Ahn, S. I.; McAlpine, M. V. 3D-Printed Flexible Organic Light-Emitting Diode Displays. *Sci. Adv.* **2022**, *8*, No. eabl8798.
(410) Liu, Y.-F.; Feng, J.; Bi, Y.-G.; Yin, D.; Sun, H.-B. Recent Developments in Flexible Organic Light-Emitting Devices. *Adv. Mater. Technol.* **2019**, *4*, 1800371.
(411) Jeong, S. Y.; Shim, H. R.; Na, Y.; Kang, K. S.; Jeon, Y.; Choi, S.; Jeong, E. G.; Park, Y. C.; Cho, A.-E.; Lee, J.; et al. Foldable and Washable Textile-Based OLEDs with a Multi-Functional Near-Room-Temperature Encapsulation Layer for Smart E-Textiles. *npj Flex. Electron.* **2021**, *5*, 15.
(412) Zhou, L.; Xiang, H.-Y.; Shen, S.; Li, Y.-Q.; Chen, J.-D.; Xie, H.-J.; Goldthorpe, I. A.; Chen, L.-S.; Lee, S.-T.; Tang, J.-X. High-Performance Flexible Organic Light-Emitting Diodes Using Embedded Silver Network Transparent Electrodes. *ACS Nano* **2014**, *8*, 12796−12805.
(413) Yao, L.-Q.; Qin, Y.; Li, X.-C.; Xue, Q.; Liu, F.; Cheng, T.; Li, G.-J.; Zhang, X.; Lai, W.-Y. High-Efficiency Stretchable Organic Light-Emitting Diodes Based on Ultra-Flexible Printed Embedded Metal Composite Electrodes. *InfoMat* **2023**, *5*, No. e12410.
(414) Lian, C.; Piksa, M.; Yoshida, K.; Persheyev, S.; Pawlik, K. J.; Matczyszyn, K.; Samuel, I. D. W. Flexible Organic Light-Emitting Diodes for Antimicrobial Photodynamic Therapy. *npj Flex. Electron.* **2019**, *3*, 18.
(415) Wu, J.; Agrawal, M.; Becerril, H. A.; Bao, Z.; Liu, Z.; Chen, Y.; Peumans, P. Organic Light-Emitting Diodes on Solution-Processed Graphene Transparent Electrodes. *ACS Nano* **2010**, *4*, 43−48.
(416) Han, T.-H.; Lee, Y.; Choi, M.-R.; Woo, S.-H.; Bae, S.-H.; Hong, B. H.; Ahn, J.-H.; Lee, T.-W. Extremely Efficient Flexible Organic Light-Emitting Diodes with Modified Graphene Anode. *Nat. Photonics* **2012**, *6*, 105−110.
(417) Konaković, M.; Crane, K.; Deng, B.; Bouaziz, S.; Piker, D.; Pauly, M. Beyond Developable: Computational Design and Fabrication with Auxetic Materials. *ACM Trans. Graph.* **2016**, *35*, 89.
(418) Lee, Y.-K.; Xi, Z.; Lee, Y.-J.; Kim, Y.-H.; Hao, Y.; Choi, H.; Lee, M.-G.; Joo, Y.-C.; Kim, C.; Lien, J.-M.; et al. Computational Wrapping: A Universal Method to Wrap 3D-Curved Surfaces with Nonstretchable Materials for Conformal Devices. *Sci. Adv.* **2020**, *6*, No. eaax6212.
(419) Shi, J.; Liu, S.; Zhang, L.; Yang, B.; Shu, L.; Yang, Y.; Ren, M.; Wang, Y.; Chen, J.; Chen, W.; et al. Smart Textile-Integrated Microelectronic Systems for Wearable Applications. *Adv. Mater.* **2020**, *32*, 1901958.
(420) Heo, J. S.; Eom, J.; Kim, Y.-H.; Park, S. K. Recent Progress of Textile-Based Wearable Electronics: A Comprehensive Review of Materials, Devices, and Applications. *Small* **2018**, *14*, 1703034.
(421) Yin, D.; Chen, Z.-Y.; Jiang, N.-R.; Liu, Y.-F.; Bi, Y.-G.; Zhang, X.-L.; Han, W.; Feng, J.; Sun, H.-B. Highly Flexible Fabric-Based Organic Light-Emitting Devices for Conformal Wearable Displays. *Adv. Funct. Mater.* **2020**, *5*, 1900942.
(422) Kim, W.; Kwon, S.; Lee, S.-M.; Kim, J. Y.; Han, Y.; Kim, E.; Choi, K. C.; Park, S.; Park, B.-C. Soft Fabric-Based Flexible Organic Light-Emitting Diodes. *Org. Electron.* **2013**, *14*, 3007−3013.
(423) Hwang, Y. H.; Kwon, S.; Shin, J. B.; Kim, H.; Son, Y. H.; Lee, H. S.; Noh, B.; Nam, M.; Choi, K. C. Bright-Multicolor, Highly Efficient, and Addressable Phosphorescent Organic Light-Emitting Fibers: Toward Wearable Textile Information Displays. *Adv. Funct. Mater.* **2021**, *31*, 2009336.
(424) Kwon, S.; Kim, H.; Choi, S.; Jeong, E. G.; Kim, D.; Lee, S.; Lee, H. S.; Seo, Y. C.; Choi, K. C. Weavable and Highly Efficient Organic Light-Emitting Fibers for Wearable Electronics: A Scalable, Low-Temperature Process. *Nano Lett.* **2018**, *18*, 347−356.
(425) Song, Y. J.; Kim, J.-W.; Cho, H.-E.; Son, Y. H.; Lee, M. H.; Lee, J.; Choi, K. C.; Lee, S.-M. Fibertronic Organic Light-Emitting Diodes Toward Fully Addressable, Environmentally Robust, Wearable Displays. *ACS Nano* **2020**, *14*, 1133−1140.
(426) Jeong, S.; Yoon, H.; Lee, B.; Lee, S.; Hong, Y. Distortion-Free Stretchable Light-Emitting Diodes via Imperceptible Microwrinkles. *Adv. Mater. Technol.* **2020**, *5*, 2000231.
(427) Choi, M.; Bae, S.-R.; Hu, L.; Hoang, A. T.; Kim, S. Y.; Ahn, J.-H. Full-Color Active-Matrix Organic Light-Emitting Diode Display on Human Skin Based on a Large-Area MoS_2 Backplane. *Sci. Adv.* **2020**, *6*, No. eabb5898.
(428) Yin, D.; Feng, J.; Ma, R.; Liu, Y.-F.; Zhang, Y.-L.; Zhang, X.-L.; Bi, Y.-G.; Chen, Q.-D.; Sun, H.-B. Efficient and Mechanically Robust Stretchable Organic Light-Emitting Devices by a Laser-Programmable Buckling Process. *Nat. Commun.* **2016**, *7*, 11573.
(429) Yin, D.; Feng, J.; Jiang, N.-R.; Ma, R.; Liu, Y.-F.; Sun, H.-B. Two-Dimensional Stretchable Organic Light-Emitting Devices with High Efficiency. *ACS Appl. Mater. Interfaces* **2016**, *8*, 31166−31171.
(430) Yoo, J.; Li, S.; Kim, D.-H.; Yang, J.; Choi, M. K. Materials and Design Strategies for Stretchable Electroluminescent Devices. *Nanoscale Horiz.* **2022**, *7*, 801−821.

https://doi.org/10.1021/acs.chemrev.3c00548
Chem. Rev. XXXX, XXX, XXX−XXX

(431) Yu, Z.; Niu, X.; Liu, Z.; Pei, Q. Intrinsically Stretchable Polymer Light-Emitting Devices Using Carbon Nanotube-Polymer Composite Electrodes. *Adv. Mater.* **2011**, *23*, 3989−3994.
(432) Liang, J.; Li, L.; Niu, X.; Yu, Z.; Pei, Q. Elastomeric Polymer Light-Emitting Devices and Displays. *Nat. Photonics* **2013**, *7*, 817−824.
(433) Liu, J.; Wang, J.; Zhang, Z.; Molina-Lopez, F.; Wang, G.-J. N.; Schroeder, B. C.; Yan, X.; Zeng, Y.; Zhao, O.; Tran, H.; et al. Fully Stretchable Active-Matrix Organic Light-Emitting Electrochemical Cell Array. *Nat. Commun.* **2020**, *11*, 3362.
(434) Filiatrault, H. L.; Porteous, G. C.; Carmichael, R. S.; Davidson, G. J. E.; Carmichael, T. B. Stretchable Light-Emitting Electrochemical Cells Using an Elastomeric Emissive Material. *Adv. Mater.* **2012**, *24*, 2673−2678.
(435) Wang, J.; Yan, C.; Chee, E. J.; Lee, P. S. Highly Stretchable and Self-Deformable Alternating Current Electroluminescent Devices. *Adv. Mater.* **2015**, *27*, 2876−2882.
(436) Larson, C.; Peele, B.; Li, S.; Robinson, S.; Totaro, M.; Beccai, L.; Mazzolai, B.; Shepherd, R. Highly Stretchable Electroluminescent Skin for Optical Signaling and Tactile Sensing. *Science* **2016**, *351*, 1071−1074.
(437) Zhou, Y.; Zhao, C.; Wang, J.; Li, Y.; Li, C.; Zhu, H.; Feng, S.; Cao, W.; Kong, D. Stretchable High-Permittivity Nanocomposites for Epidermal Alternating-Current Electroluminescent Displays. *ACS Materials Lett.* **2019**, *1*, 511−518.
(438) Li, S.; Peele, B. N.; Larson, C. M.; Zhao, H.; Shepherd, R. F. A Stretchable Multicolor Display and Touch Interface Using Photopatterning and Transfer Printing. *Adv. Mater.* **2016**, *28*, 9770−9775.
(439) Yoo, J.; Ha, S.; Lee, G. H.; Kim, Y.; Choi, M. K. Stretchable High-Resolution User-Interactive Synesthesia Displays for Visual-Acoustic Encryption. *Adv. Funct. Mater.* **2023**, *33*, 2302473.
(440) Liu, Y.; Zhu, M.; Sun, J.; Shi, W.; Zhao, Z.; Wei, X.; Huang, X.; Guo, Y.; Liu, Y. A Self-Assembled 3D Penetrating Nanonetwork for High-Performance Intrinsically Stretchable Polymer Light-Emitting Diodes. *Adv. Mater.* **2022**, *34*, 2201844.
(441) Han, S. J.; Zhou, H.; Kwon, H.; Woo, S.-J.; Lee, T.-W. Achieving Low-Voltage Operation of Intrinsically Stretchable Organic Light-Emitting Diodes. *Adv. Funct. Mater.* **2023**, *33*, 2211150.
(442) Burroughes, J. H.; Bradley, D. D. C.; Brown, A. R.; Marks, R. N.; Mackay, K.; Friend, R. H.; Burns, P. L.; Holmes, A. B. Light-Emitting Diodes Based on Conjugated Polymers. *Nature* **1990**, *347*, 539−541.
(443) Zheng, H.; Zheng, Y.; Liu, N.; Ai, N.; Wang, Q.; Wu, S.; Zhou, J.; Hu, D.; Yu, S.; Han, S.; et al. All-Solution Processed Polymer Light-Emitting Diode Displays. *Nat. Commun.* **2013**, *4*, 1971.
(444) Vosgueritchian, M.; Lipomi, D. J.; Bao, Z. Highly Conductive and Transparent PEDOT:PSS Films with a Fluorosurfactant for Stretchable and Flexible Transparent Electrodes. *Adv. Funct. Mater.* **2012**, *22*, 421−428.
(445) Wang, G.-J. N.; Gasperini, A.; Bao, Z. Stretchable Polymer Semiconductors for Plastic Electronics. *Adv. Electron. Mater.* **2018**, *4*, 1700429.
(446) Kim, D. W.; Kong, M.; Jeong, U. Interface Design for Stretchable Electronic Devices. *Adv. Sci.* **2021**, *8*, 2004170.
(447) Zhang, Z.; Wang, W.; Jiang, Y.; Wang, Y.-X.; Wu, Y.; Lai, J.-C.; Niu, S.; Xu, C.; Shih, C.-C.; Wang, C.; et al. High-Brightness All-Polymer Stretchable LED with Charge-Trapping Dilution. *Nature* **2022**, *603*, 624−630.
(448) Liu, W.; Zhang, C.; Alessandri, R.; Diroll, B. T.; Li, Y.; Liang, H.; Fan, X.; Wang, K.; Cho, H.; Liu, Y.; et al. High-Efficiency Stretchable Light-Emitting Polymers from Thermally Activated Delayed Fluorescence. *Nat. Mater.* **2023**, *22*, 737−745.
(449) Sun, Y.; Jiang, Y.; Sun, X. W.; Zhang, S.; Chen, S. Beyond OLED: Efficient Quantum Dot Light-Emitting Diodes for Display and Lighting Applications. *Chem. Rec.* **2019**, *19*, 1729−1752.
(450) Bussolotti, F.; Yang, J.; Yamaguchi, T.; Yonezawa, K.; Sato, K.; Matsunami, M.; Tanaka, K.; Nakayama, Y.; Ishii, H.; Ueno, N.; et al. Hole-Phonon Coupling Effect on the Band Dispersion of Organic Molecular Semiconductors. *Nat. Commun.* **2017**, *8*, 173.
(451) Aziz, H.; Popovic, Z. D.; Hu, N.-X.; Hor, A.-M.; Xu, G. Degradation Mechanism of Small Molecule-Based Organic Light-Emitting Devices. *Science* **1999**, *283*, 1900−1902.
(452) Pietryga, J. M.; Park, Y.-S.; Lim, J.; Fidler, A. F.; Bae, W. K.; Brovelli, S.; Klimov, V. I. Spectroscopic and Device Aspects of Nanocrystal Quantum Dots. *Chem. Rev.* **2016**, *116*, 10513−10622.
(453) Coe, S.; Woo, W. K.; Bawendi, M.; Bulović, V. Electroluminescence from Single Monolayers of Nanocrystals in Molecular Organic Devices. *Nature* **2002**, *420*, 800−803.
(454) Kagan, C. R.; Lifshitz, E.; Sargent, E. H.; Talapin, D. V. Building Devices from Colloidal Quantum Dots. *Science* **2016**, *353*, aac5523.
(455) Chen, O.; Zhao, J.; Chauhan, V. P.; Cui, J.; Wong, C.; Harris, D. K.; Wei, H.; Han, H.-S.; Fukumura, D.; Jain, R. K.; et al. Compact High-Quality CdSe-CdS Core-Shell Nanocrystals with Narrow Emission Linewidths and Suppressed Blinking. *Nat. Mater.* **2013**, *12*, 445−451.
(456) Park, J.; An, K.; Hwang, Y.; Park, J.-G.; Noh, H.-J.; Kim, J.-Y.; Park, J.-H.; Hwang, N.-M.; Hyeon, T. Ultra-Large-Scale Syntheses of Monodisperse Nanocrystals. *Nat. Mater.* **2004**, *3*, 891−895.
(457) Shirasaki, Y.; Supran, G. J.; Bawendi, M. G.; Bulović, V. Emergence of Colloidal Quantum-Dot Light-Emitting Technologies. *Nat. Photonics* **2013**, *7*, 13−23.
(458) Hines, M. A.; Guyot-Sionnest, P. Synthesis and Characterization of Strongly Luminescing ZnS-Capped CdSe Nanocrystals. *J. Phys. Chem.* **1996**, *100*, 468−471.
(459) Dabbousi, B. O.; Rodriguez-Viejo, J.; Mikulec, F. V.; Heine, J. R.; Mattoussi, H.; Ober, R.; Jensen, K. F.; Bawendi, M. G. (CdSe)ZnS Core-Shell Quantum Dots: Synthesis and Characterization of a Size Series of Highly Luminescent Nanocrystallites. *J. Phys. Chem. B* **1997**, *101* (46), 9463−9475.
(460) Won, Y.-H.; Cho, O.; Kim, T.; Chung, D.-Y.; Kim, T.; Chung, H.; Jang, H.; Lee, J.; Kim, D.; Jang, E. Highly Efficient and Stable InP/ZnSe/ZnS Quantum Dot Light-Emitting Diodes. *Nature* **2019**, *575*, 634−638.
(461) Lee, T.; Kim, B. J.; Lee, H.; Hahm, D.; Bae, W. K.; Lim, J.; Kwak, J. Bright and Stable Quantum Dot Light-Emitting Diodes. *Adv. Mater.* **2022**, *34*, 2106276.
(462) Kim, T.; Kim, K.-H.; Kim, S.; Choi, S.-M.; Jang, H.; Seo, H.-K.; Lee, H.; Chung, D.-Y.; Jang, E. Efficient and Stable Blue Quantum Dot Light-Emitting Diode. *Nature* **2020**, *586*, 385−389.
(463) Colvin, V. L.; Schlamp, M. C.; Alivisatos, A. P. Light-Emitting Diodes Made from Cadmium Selenide Nanocrystals and a Semiconducting Polymer. *Nature* **1994**, *370*, 354−357.
(464) Jang, E.; Jang, H. Review: Quantum Dot Light-Emitting Diodes. *Chem. Rev.* **2023**, *123*, 4663−4692.
(465) Cho, K.-S.; Lee, E. K.; Joo, W.-J.; Jang, E.; Kim, T.-H.; Lee, S. J.; Kwon, S.-J.; Han, J. Y.; Kim, B.-K.; Choi, B. L.; et al. High-Performance Crosslinked Colloidal Quantum-Dot Light-Emitting Diodes. *Nat. Photonics* **2009**, *3*, 341−345.
(466) Lee, K.-H.; Lee, J.-H.; Kang, H.-D.; Park, B.; Kwon, Y.; Ko, H.; Lee, C.; Lee, J.; Yang, H. Over 40 cd/A Efficient Green Quantum Dot Electroluminescent Device Comprising Uniquely Large-Sized Quantum Dots. *ACS Nano* **2014**, *8*, 4893−4901.
(467) Yoon, S. H.; Gwak, D.; Kim, H. H.; Woo, H. J.; Cho, J.; Choi, J. W.; Choi, W. K.; Song, Y. J.; Lee, C.-L.; Park, J.; et al. Insertion of an Inorganic Barrier Layer as a Method of Improving the Performance of Quantum Dot Light-Emitting Diodes. *ACS Photonics* **2019**, *6*, 743−748.
(468) moon, H.; Lee, C.; Lee, W.; Kim, J.; Chae, H. Stability of Quantum Dots, Quantum Dot Films, and Quantum Dot Light-Emitting Diodes for Display Applications. *Adv. Mater.* **2019**, *31*, 1804294.
(469) Caruge, J. M.; Halpert, J. E.; Wood, V.; Bulović, V.; Bawendi, M. G. Colloidal Quantum-Dot Light-Emitting Diodes with Metal-Oxide Charge Transport Layers. *Nat. Photonics* **2008**, *2*, 247−250.
(470) Shen, H.; Gao, Q.; Zhang, Y.; Lin, Y.; Lin, Q.; Li, Z.; Chen, L.; Zeng, Z.; Li, X.; Jia, Y.; et al. Visible Quantum Dot Light-Emitting

https://doi.org/10.1021/acs.chemrev.3c00548
Chem. Rev. XXXX, XXX, XXX−XXX

Diodes with Simultaneous High Brightness and Efficiency. *Nat. Photonics* **2019**, *13*, 192−197.
(471) Cao, W.; Xiang, C.; Yang, Y.; Chen, Q.; Chen, L.; Yan, X.; Qian, L. Highly Stable QLEDs with Improved Hole Injection via Quantum Dot Structure Tailoring. *Nat. Commun.* **2018**, *9*, 2608.
(472) Han, C.-Y.; Lee, S.-H.; Song, S.-W.; Yoon, S.-Y.; Jo, J.-H.; Jo, D.-Y.; Kim, H.-M.; Lee, B.-J.; Kim, H.-S.; Yang, H. More Than 9% Efficient ZnSeTe Quantum Dot-Based Blue Electroluminescent Devices. *ACS Energy Lett.* **2020**, *5*, 1568−1576.
(473) Li, Y.; Hou, X.; Dai, X.; Yao, Z.; Lv, L.; Jin, Y.; Peng, X. Stoichiometry-Controlled InP-Based Quantum Dots: Synthesis, Photoluminescence, and Electroluminescence. *J. Am. Chem. Soc.* **2019**, *141*, 6448−6452.
(474) Stouwdam, J. W.; Janssen, R. A. J. Red, Green, and Blue Quantum Dot LEDs with Solution Processable ZnO Nanocrystal Electron Injection Layers. *J. Mater. Chem.* **2008**, *18*, 1889−1894.
(475) Moon, H.; Lee, W.; Kim, J.; Lee, D.; Cha, S.; Shin, S.; Chae, H. Composition-Tailored ZnMgO Nanoparticles for Electron Transport Layers of Highly Efficient and Bright InP-Based Quantum Dot Light Emitting Diodes. *Chem. Commun.* **2019**, *55*, 13299−13302.
(476) Song, J.; Wang, O.; Shen, H.; Lin, Q.; Li, Z.; Wang, L.; Zhang, X.; Li, L. S. Over 30% External Quantum Efficiency Light-Emitting Diodes by Engineering Quantum Dot-Assisted Energy Level Match for Hole Transport Layer. *Adv. Funct. Mater.* **2019**, *29*, 1808377.
(477) Fang, Y.; Bai, P.; Li, J.; Xiao, B.; Wang, Y.; Wang, Y. Highly Efficient Red Quantum Dot Light-Emitting Diodes by Balancing Charge Injection and Transport. *ACS Appl. Mater. Interfaces* **2022**, *14*, 21263−21269.
(478) Deng, Y.; Peng, F.; Lu, Y.; Zhu, X.; Jin, W.; Qiu, J.; Dong, J.; Hao, Y.; Di, D.; Gao, Y.; et al. Solution-Processed Green and Blue Quantum-Dot Light-Emitting Diodes with Eliminated Charge Leakage. *Nat. Photonics* **2022**, *16*, 505−511.
(479) Yang, J.; Choi, M. K.; Yang, U. J.; Kim, S. Y.; Kim, Y. S.; Kim, J. H.; Kim, D.-H.; Hyeon, T. Toward Full-Color Electroluminescent Quantum Dot Displays. *Nano Lett.* **2021**, *21*, 26−33.
(480) Meng, T.; Zheng, Y.; Zhao, D.; Hu, H.; Zhu, Y.; Xu, Z.; Xu, Z.; Ju, S.; Jing, J.; Chen, X.; et al. Ultrahigh-Resolution Quantum-Dot Light-Emitting Diodes. *Nat. Photonics* **2022**, *16*, 297−303.
(481) Kim, T.-H.; Cho, K.-S.; Lee, E. K.; Lee, S. J.; Chae, J.; Kim, J. W.; Kim, D. H.; Kwon, J.-Y.; Amaratunga, G.; Lee, S. Y.; et al. Full-Colour Quantum Dot Displays Fabricated by Transfer Printing. *Nat. Photonics* **2011**, *5*, 176−182.
(482) Cho, H.; Kwak, J.; Lim, J.; Park, M.; Lee, D.; Bae, W. K.; Kim, Y. S.; Char, K.; Lee, S.; Lee, C. Soft Contact Transplanted Nanocrystal Quantum Dots for Light-Emitting Diodes: Effect of Surface Energy on Device Performance. *ACS Appl. Mater. Interfaces* **2015**, *7*, 10828−10833.
(483) Kim, B. H.; Nam, S.; Oh, N.; Cho, S.-Y.; Yu, K. J.; Lee, C. H.; Zhang, J.; Deshpande, K.; Trefonas, P.; Kim, J.-H.; et al. Multilayer Transfer Printing for Pixelated, Multicolor Quantum-Dot Light-Emitting Diodes. *ACS Nano* **2016**, *10*, 4920−4925.
(484) Li, X.; Hu, B.; Du, Z.; Wu, Y.; Jiang, L. Asymmetric Wettability Interfaces Induced a Large-Area Quantum Dot Microstructure Toward High-Resolution Quantum Dot Light-Emitting Diodes. *ACS Appl. Mater. Interfaces* **2019**, *11*, 28520−28526.
(485) Nam, T. W.; Kim, M.; Wang, Y.; Kim, G. Y.; Choi, W.; Lim, H.; Song, K. M.; Choi, M.-J.; Jeon, D. Y.; Grossman, J. C.; et al. Thermodynamic-Driven Polychromatic Quantum Dot Patterning for Light-Emitting Diodes Beyond Eye-Limiting Resolution. *Nat. Commun.* **2020**, *11*, 3040.
(486) Meitl, M. A.; Zhu, Z.-T.; Kumar, V.; Lee, K. J.; Feng, X.; Huang, Y. Y.; Adesida, I.; Nuzzo, R. G.; Rogers, J. A. Transfer Printing by Kinetic Control of Adhesion to an Elastomeric Stamp. *Nat. Mater.* **2006**, *5*, 33−38.
(487) Kim, T.-H.; Chung, D.-Y.; Ku, J.; Song, I.; Sul, S.; Kim, D.-H.; Cho, K.-S.; Choi, B. L.; Min Kim, J.; Hwang, S.; et al. Heterogeneous Stacking of Nanodot Monolayers by Dry Pick-and-Place Transfer and Its Applications in Quantum-Dot Light-Emitting Diodes. *Nat. Commun.* **2013**, *4*, 2637.
(488) Agrawal, H.; Garnett, E. C. Nanocube Imprint Lithography. *ACS Nano* **2020**, *14*, 11009−11016.
(489) Kim, L.; Anikeeva, P. O.; Coe-Sullivan, S. A.; Steckel, J. S.; Bawendi, M. G.; Bulović, V. Contact Printing of Quantum Dot Light-Emitting Devices. *Nano Lett.* **2008**, *8*, 4513−4517.
(490) Choi, M. K.; Yang, J.; Kang, K.; Kim, D. C.; Choi, C.; Park, C.; Kim, S. J.; Chae, S. I.; Kim, Y.-H.; et al. Wearable Red-Green-Blue Quantum Dot Light-Emitting Diode Array Using High-Resolution Intaglio Transfer Printing. *Nat. Commun.* **2015**, *6*, 7149.
(491) Liu, Y.; Li, F.; Xu, Z.; Zheng, C.; Guo, T.; Xie, X.; Qian, L.; Fu, D.; Yan, X. Efficient All-Solution Processed Quantum Dot Light-Emitting Diodes Based on Inkjet Printing Technique. *ACS Appl. Mater. Interfaces* **2017**, *9*, 25506−25512.
(492) Zhao, J.; Yan, Y.; Gao, Z.; Du, Y.; Dong, H.; Yao, J.; Zhao, Y. S. Full-Color Laser Displays Based on Organic Printed Microlaser Arrays. *Nat. Commun.* **2019**, *10*, 870.
(493) Han, J.; Ko, D.; Park, M.; Roh, J.; Jung, H.; Lee, Y.; Kwon, Y.; Sohn, J.; Bae, W. K.; Chin, B. D.; Lee, C. Toward High-Resolution, Inkjet-Printed, Quantum Dot Light-Emitting Diodes for Next-Generation Displays. *J. SID* **2016**, *24*, 545−551.
(494) Xiong, X.; Wei, C.; Xie, L.; Chen, M.; Tang, P.; Shen, W.; Deng, Z.; Li, X.; Duan, Y.; Su, W.; et al. Realizing 17.0% External Quantum Efficiency in Red Quantum Dot Light-Emitting Diodes by Pursuing the Ideal Inkjet-Printed Film and Interface. *Org. Electron.* **2019**, *73*, 247−254.
(495) Haverinen, H. M.; Myllylä, R. A.; Jabbour, G. E. Inkjet Printing of Light-Emitting Quantum Dots. *Appl. Phys. Lett.* **2009**, *94*, 073108.
(496) Wood, V.; Panzer, M. J.; Chen, J.; Bradley, M. S.; Halpert, J. E.; Bawendi, M. G.; Bulovi ć, V. Inkjet-Printed Quantum Dot-Polymer Composites for Full-Color AC-Driven Displays. *Adv. Mater.* **2009**, *21*, 2151−2155.
(497) Yang, P.; Zhang, L.; Kang, D. J.; Strahl, R.; Kraus, T. High-Resolution Inkjet Printing of Quantum Dot Light-Emitting Microdiode Arrays. *Adv. Optic. Mater.* **2020**, *8*, 1901429.
(498) Li, H.; Duan, Y.; Shao, Z.; Zhang, G.; Li, H.; Huang, Y.; Yin, Z. High-Resolution Pixelated Light-Emitting Diodes Based on Electrohydrodynamic Printing and Coffee-Ring-Free Quantum Dot Film. *Adv. Mater. Technol.* **2020**, *5*, 2000401.
(499) Chen, M.; Xie, L.; Wei, C.; Yi, Y.-Q.-Q.; Chen, X.; Yang, J.; Zhuang, J.; Li, F.; Su, W.; Cui, Z. High-Performance Inkjet-Printed QLEDs with 18.3% EQE: Improving Interfacial Contact by Novel Halogen-Free Binary Solvent System. *Nano Res.* **2021**, *14*, 4125−4131.
(500) Kim, B. H.; Onses, M. S.; Lim, J. B.; Nam, S.; Oh, N.; Kim, H.; Yu, K. J.; Lee, J. W.; Kim, J.-H.; Kang, S.-K.; et al. High-Resolution Patterns of Quantum Dots formed by Electrohydrodynamic Jet Printing for Light-Emitting Diodes. *Nano Lett.* **2015**, *15*, 969−973.
(501) Keum, H.; Jiang, Y.; Park, J. K.; Flanagan, J. C.; Shim, M.; Kim, S. Photoresist Contact Patterning of Quantum Dot Films. *ACS Nano* **2018**, *12*, 10024−10031.
(502) Myeong, S.; Chon, B.; Kumar, S.; Son, H.-J.; Kang, S. O.; Seo, S. Quantum Dot Photolithography Using a Quantum Dot Photoresist Composed of an Organic-Inorganic Hybrid Coating Layer. *Nanoscale Adv.* **2022**, *4*, 1080−1087.
(503) Park, S. Y.; Lee, S.; Yang, J.; Kang, M. S. Patterning Quantum Dots via Photolithography: A Review. *Adv. Mater.* **2023**, *35*, 2300546.
(504) Mei, W.; Zhang, Z.; Zhang, A.; Li, D.; Zhang, X.; Wang, H.; Chen, Z.; Li, Y.; Li, X.; Xu, X. High-Resolution, Full-Color Quantum Dot Light-Emitting Diode Display Fabricated via Photolithography Approach. *Nano Res.* **2020**, *13*, 2485−2491.
(505) Park, J.-S.; Kyhm, J.; Kim, H. H.; Jeong, S.; Kang, J.; Lee, S.; Lee, K.-T.; Park, K.; Barange, N.; Han, J.; et al. Alternative Patterning Process for Realization of Large-Area, Full-Color, Active Quantum Dot Display. *Nano Lett.* **2016**, *16*, 6946−6953.
(506) Wang, Y.; Fedin, I.; Zhang, H.; Talapin, D. V. Direct Optical Lithography of Functional Inorganic Nanomaterials. *Science* **2017**, *357*, 385−388.

https://doi.org/10.1021/acs.chemrev.3c00548
Chem. Rev. XXXX, XXX, XXX−XXX

(507) Yang, J.; Hahm, D.; Kim, K.; Rhee, S.; Lee, M.; Kim, S.; Chang, J. H.; Park, H. W.; Lim, J.; Lee, M.; et al. High-Resolution Patterning of Colloidal Quantum Dots via Non-Destructive, Light-Driven Ligand Crosslinking. *Nat. Commun.* **2020**, *11*, 2874.
(508) Hahm, D.; Lim, J.; Kim, H.; Shin, J.-W.; Hwang, S.; Rhee, S.; Chang, J. H.; Yang, J.; Lim, C. H.; Jo, H.; Choi, B.; Cho, N. S.; Park, Y.-S.; Lee, D. C.; Hwang, E.; Chung, S.; Kang, C.-m.; Kang, M. S.; Bae, W. K. Direct Patterning of Colloidal Quantum Dots with Adaptable Dual-Ligand Surface. *Nat. Nanotechnol.* **2022**, *17*, 952−958.
(509) Jiang, J.; Chu, Z.; Yin, Z.; Li, J.; Yang, Y.; Chen, J.; Wu, J.; You, J.; Zhang, X. Red Perovskite Light-Emitting Diodes with Efficiency Exceeding 25% Realized by Co-Spacer Cations. *Adv. Mater.* **2022**, *34*, 2204460.
(510) Cao, Y.; Wang, N.; Tian, H.; Guo, J.; Wei, Y.; Chen, H.; Miao, Y.; Zou, W.; Pan, K.; He, Y.; et al. Perovskite Light-Emitting Diodes Based on Spontaneously formed Submicrometer-Scale Structures. *Nature* **2018**, *562*, 249−253.
(511) Ma, D.; Lin, K.; Dong, Y.; Choubisa, H.; Proppe, A. H.; Wu, D.; Wang, Y.-K.; Chen, B.; Li, P.; Fan, J. Z.; et al. Distribution Control Enables Efficient Reduced-Dimensional Perovskite LEDs. *Nature* **2021**, *599*, 594−598.
(512) Lin, K.; Xing, J.; Quan, L. N.; de Arquer, F. P. G.; Gong, X.; Lu, J.; Xie, L.; Zhao, W.; Zhang, D.; Yan, C.; et al. Perovskite Light-Emitting Diodes with External Quantum Efficiency Exceeding 20%. *Nature* **2018**, *562*, 245−248.
(513) Zhang, D.; Zhang, Q.; Ren, B.; Zhu, Y.; Abdellah, M.; Fu, Y.; Cao, B.; Wang, C.; Gu, L.; Ding, Y.; et al. Large-Scale Planar and Spherical Light-Emitting Diodes Based on Arrays of Perovskite Quantum Wires. *Nat. Photonics* **2022**, *16*, 284−290.
(514) Stranks, S. D.; Snaith, H. J. Metal-Halide Perovskites for Photovoltaic and Light-Emitting Devices. *Nat. Nanotechnol.* **2015**, *10*, 391−402.
(515) Hassan, Y.; Ashton, O. J.; Park, J. H.; Li, G.; Sakai, N.; Wenger, B.; Haghighirad, A. A.; Noel, N. K.; Song, M. H.; Lee, B. R.; et al. Facile Synthesis of Stable and Highly Luminescent Methylammonium Lead Halide Nanocrystals for Efficient Light Emitting Devices. *J. Am. Chem. Soc.* **2019**, *141*, 1269−1279.
(516) Jang, D. M.; Park, K.; Kim, D. H.; Park, J.; Shojaei, F.; Kang, H. S.; Ahn, J.-P.; Lee, J. W.; Song, J. K. Reversible Halide Exchange Reaction of Organometal Trihalide Perovskite Colloidal Nanocrystals for Full-Range Band Gap Tuning. *Nano Lett.* **2015**, *15*, 5191−5199.
(517) Protesescu, L.; Yakunin, S.; Bodnarchuk, M. I.; Krieg, F.; Caputo, R.; Hendon, C. H.; Yang, R. X.; Walsh, A.; Kovalenko, M. V. Nanocrystals of Cesium Lead Halide Perovskites (CsPbX3, X = Cl, Br, and I): Novel Optoelectronic Materials Showing Bright Emission with Wide Color Gamut. *Nano Lett.* **2015**, *15*, 3692−3696.
(518) Herz, L. M. Charge-Carrier Dynamics in Organic-Inorganic Metal Halide Perovskites. *Annu. Rev. Phys. Chem.* **2016**, *67*, 65−89.
(519) Liu, Y.; Tao, C.; Cao, Y.; Chen, L.; Wang, S.; Li, P.; Wang, C.; Liu, C.; Ye, F.; Hu, S.; et al. Synergistic Passivation and Stepped-Dimensional Perovskite Analogs Enable High-Efficiency Near-Infrared Light-Emitting Diodes. *Nat. Commun.* **2022**, *13*, 7425.
(520) Liu, Z.; Qiu, W.; Peng, X.; Sun, G.; Liu, X.; Liu, D.; Li, Z.; He, F.; Shen, C.; Gu, Q.; et al. Perovskite Light-Emitting Diodes with EQE Exceeding 28% Through a Synergetic Dual-Additive Strategy for Defect Passivation and Nanostructure Regulation. *Adv. Mater.* **2021**, *33*, 2103268.
(521) you, M.; Wang, H.; Cao, F.; Zhang, C.; Zhang, T.; Kong, L.; Wang, L.; Zhao, D.; Zhang, J.; Yang, X. Improving Efficiency and Stability in Quasi-2D Perovskite Light-Emitting Diodes by a Multifunctional LiF Interlayer. *ACS Appl. Mater. Interfaces* **2020**, *12*, 43018−43023.
(522) Kwon, J. I.; Park, G.; Lee, G. H.; Jang, J. H.; Sung, N. J.; Kim, S. Y.; Yoo, J.; Lee, K.; Karl, M.; Shin, T. J.; et al. Ultrahigh-Resolution Full-Color Perovskite Nanocrystal Patterning for Ultrathin Skin-Attachable Displays. *Sci. Adv.* **2022**, *8*, No. eadd0697.
(523) Bade, S. G. R.; Shan, X.; Hoang, P. T.; Li, J.; Geske, T.; Cai, L.; Pei, Q.; Wang, C.; Yu, Z. Stretchable Light-Emitting Diodes with Organometal-Halide-Perovskite-Polymer Composite Emitters. *Adv. Mater.* **2017**, *29*, 1607053.
(524) Xue, J.; Wang, R.; Yang, Y. The Surface of Halide Perovskites from Nano to Bulk. *Nat. Rev. Mater.* **2020**, *5*, 809−827.
(525) Ye, J.; Byranvand, M. M.; Martínez, C. O.; Hoye, R. L. Z.; Saliba, M.; Polavarapu, L. Defect Passivation in Lead-Halide Perovskite Nanocrystals and Thin Films: Toward Efficient LEDs and Solar Cells. *Angew. Chem., Int. Ed.* **2021**, *133*, 21804−21828.
(526) Kang, J.; Wang, L.-W. High Defect Tolerance in Lead Halide Perovskite CsPbBr3. *J. Phys. Chem. Lett.* **2017**, *8*, 489−493.
(527) Yuan, Y.; Huang, J. Ion Migration in Organometal Trihalide Perovskite and Its Impact on Photovoltaic Efficiency and Stability. *Acc. Chem. Res.* **2016**, *49*, 286−293.
(528) Haydous, F.; Gardner, J. M.; Cappel, U. B. The Impact of Ligands on the Synthesis and Application of Metal Halide Perovskite Nanocrystals. *J. Mater. Chem. A* **2021**, *9*, 23419−23443.
(529) Brinck, S. T.; Infante, I. Surface Termination, Morphology, and Bright Photoluminescence of Cesium Lead Halide Perovskite Nanocrystals. *ACS Energy Lett.* **2016**, *1*, 1266−1272.
(530) Cho, H.; Kim, Y.-H.; Wolf, C.; Lee, H.-D.; Lee, T.-W. Improving the Stability of Metal Halide Perovskite Materials and Light-Emitting Diodes. *Adv. Mater.* **2018**, *30*, 1704587.
(531) Zhao, L.; Rolston, N.; Lee, K. M.; Zhao, X.; Reyes-Martinez, M. A.; Tran, N. L.; Yeh, Y.-W.; Yao, N.; Scholes, G. D.; Loo, Y.-L.; et al. Influence of Bulky Organo-Ammonium Halide Additive Choice on the Flexibility and Efficiency of Perovskite Light-Emitting Devices. *Adv. Funct. Mater.* **2018**, *28*, 1802060.
(532) Ren, Z.; Li, L.; Yu, J.; Ma, R.; Xiao, X.; Chen, R.; Wang, K.; Sun, X. W.; Yin, W.-J.; Choy, W. C. H. Simultaneous Low-Order Phase Suppression and Defect Passivation for Efficient and Stable Blue Light-Emitting Diodes. *ACS Energy Lett.* **2020**, *5*, 2569−2579.
(533) Lan, Y.-F.; Yao, J.-S.; Yang, J.-N.; Song, Y.-H.; Ru, X.-C.; Zhang, Q.; Feng, L.-Z.; Chen, T.; Song, K.-H.; Yao, H.-B. Spectrally Stable and Efficient Pure Red $CsPbI_3$ Quantum Dot Light-Emitting Diodes Enabled by Sequential Ligand Post-Treatment Strategy. *Nano Lett.* **2021**, *21*, 8756−8763.
(534) Song, J.; Fang, T.; Li, J.; Xu, L.; Zhang, F.; Han, B.; Shan, Q.; Zeng, H. Organic-Inorganic Hybrid Passivation Enables Perovskite QLEDs with an EQE of 16.48%. *Adv. Mater.* **2018**, *30*, 1805409.
(535) Lu, M.; Zhang, X.; Bai, X.; Wu, H.; Shen, X.; Zhang, Y.; Zhang, W.; Zheng, W.; Song, H.; Yu, W. W.; et al. Spontaneous Silver Doping and Surface Passivation of $CsPbI_3$ Perovskite Active Layer Enable Light-Emitting Devices with an External Quantum Efficiency of 11.2%. *ACS Energy Lett.* **2018**, *3*, 1571−1577.
(536) Liu, M.; Wan, Q.; Wang, H.; Carulli, F.; Sun, X.; Zheng, W.; Kong, L.; Zhang, Q.; Zhang, C.; Zhang, Q.; et al. Suppression of Temperature Quenching in Perovskite Nanocrystals for Efficient and Thermally Stable Light-Emitting Diodes. *Nat. Photonics* **2021**, *15*, 379−385.
(537) Shen, X.; Kang, K.; Yu, Z.; Jeong, W. H.; Choi, H.; Park, S. H.; Stranks, S. D.; Snaith, H. J.; Friend, R. H.; Lee, B. R. Passivation Strategies for Mitigating Defect Challenges in Halide Perovskite Light-Emitting Diodes. *Joule* **2023**, *7*, 272−308.
(538) Ahmed, G. H.; Yin, J.; Bakr, O. M.; Mohammed, O. F. Successes and Challenges of Core/Shell Lead Halide Perovskite Nanocrystals. *ACS Energy Lett.* **2021**, *6*, 1340−1357.
(539) Tang, X.; Yang, J.; Li, S.; Liu, Z.; Hu, Z.; Hao, J.; Du, J.; Leng, Y.; Qin, H.; Lin, X.; et al. Single Halide Perovskite/Semiconductor Core/Shell Quantum Dots with Ultrastability and Nonblinking Properties. *Adv. Sci.* **2019**, *6*, 1900412.
(540) Ravi, V. K.; Saikia, S.; Yadav, S.; Nawale, V. V.; Nag, A. $CsPbBr_3$/ZnS Core/Shell Type Nanocrystals for Enhancing Luminescence Lifetime and Water Stability. *ACS Energy Lett.* **2020**, *5*, 1794−1796.
(541) Zhang, X.; Lu, M.; Zhang, Y.; Wu, H.; Shen, X.; Zhang, W.; Zheng, W.; Colvin, V. L.; Yu, W. W. PbS Capped $CsPbI_3$ Nanocrystals for Efficient and Stable Light-Emitting Devices Using p-i-n Structures. *ACS Cent. Sci.* **2018**, *4*, 1352−1359.

https://doi.org/10.1021/acs.chemrev.3c00548
Chem. Rev. XXXX, XXX, XXX−XXX

(542) Zhang, C.; Wang, S.; Li, X.; Yuan, M.; Turyanska, L.; Yang, X. Core/Shell Perovskite Nanocrystals: Synthesis of Highly Efficient and Environmentally Stable FAPbBr3/CsPbBr3 for LED Applications. *Adv. Funct. Mater.* **2020**, *30*, 1910582.
(543) Kim, J. S.; Heo, J.-M.; Park, G.-S.; Woo, S.-J.; Cho, C.; Yun, H. J.; Kim, D.-H.; Park, J.; Lee, S.-C.; Park, S.-H.; et al. Ultra-Bright, Efficient, and Stable Perovskite Light-Emitting Diodes. *Nature* **2022**, *611*, 688−694.
(544) Lin, Q.; Zhu, Y.; Wang, Y.; Li, D.; Zhao, Y.; Liu, Y.; Li, F.; Huang, W. Flexible Quantum Dot Light-Emitting Device for Emerging Multifunctional and Smart Applications. *Adv. Mater.* **2023**, *35*, 2210385.
(545) Yu, H.; Zhu, H.; Xu, M.; Zhang, J.; Feng, H.; Zhang, L.; Liu, S.; Xie, W. High-Efficiency, Large-Area, Flexible Top-Emitting Quantum-Dot Light-Emitting Diode. *ACS Photonics* **2023**, *10*, 2192−2200.
(546) Zhao, F.; Chen, D.; Chang, S.; Huang, H.; Tong, K.; Xiao, C.; Chou, S.; Zhong, H.; Pei, Q. Highly Flexible Organometal Halide Perovskite Quantum Dot-Based Light-Emitting Diodes on a Silver Nanowire-Polymer Composite Electrode. *J. Mater. Chem. C* **2017**, *5*, 531.
(547) Jung, D. H.; Park, J. H.; Lee, H. E.; Byun, J.; Im, T. H.; Lee, G. Y.; Seok, J. Y.; Yun, T.; Lee, K. J.; Kim, S. O. Flash-Induced Ultrafast Recrystallization of Perovskite for Flexible Light-Emitting Diodes. *Nano Energy* **2019**, *61*, 236−244.
(548) Zhao, X.; Tan, Z.-K. Large-Area Near-Infrared Perovskite Light-Emitting Diodes. *Nat. Photonics* **2020**, *14*, 215−218.
(549) Fang, Y.; Ding, K.; Wu, Z.; Chen, H.; Li, W.; Zhao, S.; Zhang, Y.; Wang, L.; Zhou, J.; Hu, B. Architectural Engineering of Nanowire Network Fine Pattern for 30 μm Wide Flexible Quantum Dot Light-Emitting Diode Application. *ACS Nano* **2016**, *10*, 10023−10030.
(550) Yang, X.; Mutlugun, E.; Dang, C.; Dev, K.; Gao, Y.; Tan, S. T.; Sun, X. W.; Demir, H. V. Highly Flexible, Electrically Driven, Top-Emitting, Quantum Dot Light-Emitting Stickers. *ACS Nano* **2014**, *8*, 8224−8231.
(551) Kim, D.; Fu, Y.; Kim, S.; Lee, W.; Lee, K.-H.; Chung, H. K.; Lee, H.-J.; Yang, H.; Chae, H. Polyethylenimine Ethoxylated-Mediated All-Solution-Processed High-Performance Flexible Inverted Quantum Dot-Light-Emitting Device. *ACS Nano* **2017**, *11*, 1982−1990.
(552) Seo, H.-K.; Kim, H.; Lee, J.; Park, M.-H.; Jeong, S.-H.; Kim, Y.-H.; Kwon, S.-J.; Han, T.-H.; Yoo, S.; Lee, T.-W. Efficient Flexible Organic/Inorganic Hybrid Perovskite Light-Emitting Diodes Based on Graphene Anode. *Adv. Mater.* **2017**, *29*, 1605587.
(553) Li, Y.-F.; Chou, S.-Y.; Huang, P.; Xiao, C.; Liu, X.; Xie, Y.; Zhao, F.; Huang, Y.; Feng, J.; Zhong, H.; et al. Stretchable Organometal-Halide-Perovskite Quantum-Dot Light-Emitting Diodes. *Adv. Mater.* **2019**, *31*, 1807516.
(554) Lee, Y.; Jung, G.; Jin, S. W.; Ha, J. S. Flexible Thin-Film Speaker Integrated with an Array of Quantum-Dot Light-Emitting Diodes for the Interactive Audiovisual Display of Multi-Functional Sensor Signals. *ACS Appl. Mater. Interfaces* **2022**, *14*, 48844−48856.
(555) Mu, G.; Rao, T.; Qi, Y.; Ma, S.; Hao, Q.; Chen, M.; Tang, X. Color-Tunable Organic Light-Emitting Displays for Interactive Multi-Signal Visualization. *Adv. Funct. Mater.* **2023**, *33*, 2301280.
(556) Hu, H.-W.; Shen, T.-L.; Lin, T.-Y.; Chen, Y.-F. Interactive Color-Changing Electronic Skin Based on Flexible and Piezoelectrically Tunable Quantum Dots Light-Emitting Diodes. *Adv. Optic. Mater.* **2020**, *8*, 1901715.
(557) Ju, S.; Zhu, Y.; Hu, H.; Liu, Y.; Xu, Z.; Zheng, J.; Mao, C.; Yu, Y.; Yang, K.; Lin, L.; et al. Dual-Function Perovskite Light-Emitting/Sensing Devices for Optical Interactive Display. *Light Sci. Appl.* **2022**, *11*, 331.
(558) Kwon, D.-K.; Myoung, J.-M. Wearable and Semitransparent Pressure-Sensitive Light-Emitting Sensor Based on Electrochemiluminescence. *ACS Nano* **2020**, *14*, 8716−8723.
(559) Wang, C.; Hwang, D.; Yu, Z.; Takei, K.; Park, J.; Chen, T.; Ma, B.; Javey, A. User-Interactive Electronic Skin for Instantaneous Pressure Visualization. *Nat. Mater.* **2013**, *12*, 899−904.
(560) Jiang, D.-H.; Liao, Y.-C.; Cho, C.-J.; Veeramuthu, L.; Liang, F.-C.; Wang, T.-C.; Chueh, C.-C.; Satoh, T.; Tung, S.-H.; Kuo, C.-C. Facile Fabrication of Stretchable Touch-Responsive Perovskite Light-Emitting Diodes Using Robust Stretchable Composite Electrodes. *ACS Appl. Mater. Interfaces* **2020**, *12*, 14408−14415.
(561) Chou, S.-Y.; Ma, R.; Li, Y.; Zhao, F.; Tong, K.; Yu, Z.; Pei, Q. Transparent Perovskite Light-Emitting Touch-Responsive Device. *ACS Nano* **2017**, *11*, 11368−11375.
(562) Lee, B.; Oh, J.-Y.; Cho, H.; Joo, C. W.; Yoon, H.; Jeong, S.; Oh, E.; Byun, J.; Kim, H.; Lee, S.; et al. Ultraflexible and Transparent Electroluminescent Skin for Real-Time and Super-Resolution Imaging of Pressure Distribution. *Nat. Commun.* **2020**, *11*, 663.
(563) Lee, S. W.; Cho, S. H.; Kang, H. S.; Kim, G.; Kim, J. S.; Jeong, B.; Kim, E. H.; Yu, S.; Hwang, I.; Han, H.; et al. Electroluminescent Pressure-Sensing Displays. *ACS Appl. Mater. Interfaces* **2018**, *10*, 13757−13766.
(564) Xu, X.; Hu, D.; Yan, L.; Fang, S.; Shen, C.; Loo, Y.-L.; Lin, Y.; Haines, C. S.; Li, N.; Zakhidov, A. A.; et al. Polar-Electrode-Bridged Electroluminescence Displays: 2D Sensors Remotely Communicating Optically. *Adv. Mater.* **2017**, *29*, 1703552.
(565) Kim, E. H.; Cho, S. H.; Lee, J. H.; Jeong, B.; Kim, R. H.; Yu, S.; Lee, T.-W.; Shim, W.; Park, C. Organic Light Emitting Board for Dynamic Interactive Display. *Nat. Commun.* **2017**, *8*, 14964.
(566) Lee, S. W.; Baek, S.; Park, S.-W.; Koo, M.; Kim, E. H.; Lee, S.; Jin, W.; Kang, H.; Park, C.; Kim, G.; et al. 3D Motion Tracking Display Enabled by Magneto-Interactive Electroluminescence. *Nat. Commun.* **2020**, *11*, 6072.
(567) Jin, W.; Kim, E. H.; Lee, S.; Yu, S.; Han, H.; Kim, G.; Lee, S. W.; Jang, J.; Lee, C. E.; Shin, W.; et al. Tandem Interactive Sensing Display De-Convoluting Dynamic Pressure and Temperature. *Adv. Funct. Mater.* **2021**, *31*, 2010492.
(568) Yang, B.; Zhao, Y.; Ali, M. U.; Ji, J.; Yan, H.; Zhao, C.; Cai, Y.; Zhang, C.; Meng, H. Asymmetrically Enhanced Coplanar-Electrode Electroluminescence for Information Encryption and Ultrahighly Stretchable Displays. *Adv. Mater.* **2022**, *34*, 2201342.
(569) Oh, N.; Kim, B. H.; Cho, S.-Y.; Nam, S.; Rogers, S. P.; Jiang, Y.; Flanagan, J. C.; Zhai, Y.; Kim, J.-H.; Lee, J.; Yu, Y.; et al. Double-Heterojunction Nanorod Light-Responsive LEDs for Display Applications. *Science* **2017**, *355*, 616−619.
(570) Li, Z.; Waldron, J.; Detchprohm, T.; Wetzel, C.; Karlicek, R. F.; Chow, T. P. Monolithic Integration of Light-Emitting Diodes and Power Metal-Oxide-Semiconductor Channel High-Electron-Mobility Transistors for Light-Emitting Power Integrated Circuits in GaN on Sapphire Substrate. *Appl. Phys. Lett.* **2013**, *102*, 192107.
(571) Wu, T.; Sher, C.-W.; Lin, Y.; Lee, C.-F.; Liang, S.; Lu, Y.; Chen, S.-W. H.; Guo, W.; Kuo, H.-C.; Chen, Z. Mini-LED and Micro-LED: Promising Candidates for the Next Generation Display Technology. *Appl. Sci.* **2018**, *8*, 1557.
(572) Trotta, R.; Atkinson, P.; Plumhof, J. D.; Zallo, E.; Rezaev, R. O.; Kumar, S.; Baunack, S.; Schröter, J. R.; Rastelli, A.; Schmidt, O. G. Nanomembrane Quantum-Light-Emitting Diodes Integrated onto Piezoelectric Actuators. *Adv. Mater.* **2012**, *24*, 2668−2672.
(573) Son, D.; Chae, S. I.; Kim, M.; Choi, M. K.; Yang, J.; Park, K.; Kale, V. S.; Koo, J. H.; Choi, C.; Lee, M.; et al. Colloidal Synthesis of Uniform-Sized Molybdenum Disulfide Nanosheets for Wafer-Scale Flexible Nonvolatile Memory. *Adv. Mater.* **2016**, *28*, 9326.
(574) Son, D.; Kang, J.; Vardoulis, O.; Kim, Y.; Matsuhisa, N.; Oh, J. Y.; To, J. W.; Mun, J.; Katsumata, T.; Liu, Y.; et al. An Integrated Self-Healable Electronic Skin System Fabricated via Dynamic Reconstruction of a Nanostructured Conducting Network. *Nat. Nanotechnol.* **2018**, *13*, 1057−1065.
(575) Kim, J.; Shim, H. J.; Yang, J.; Choi, M. K.; Kim, D. C.; Kim, J.; Hyeon, T.; Kim, D.-H. Ultrathin Quantum Dot Display Integrated with Wearable Electronics. *Adv. Mater.* **2017**, *29*, 1700217.
(576) Shi, X.; Zuo, Y.; Zhai, P.; Shen, J.; Yang, Y.; Gao, Z.; Liao, M.; Wu, J.; Wang, J.; Xu, X.; et al. Large-Area Display Textiles Integrated with Functional Systems. *Nature* **2021**, *591*, 240−245.
(577) Choi, H. W.; Shin, D.-W.; Yang, J.; Lee, S.; Figueiredo, C.; Sinopoli, S.; Ullrich, K.; Jovančić, P.; Marrani, A.; Momentè, R.; et al.

https://doi.org/10.1021/acs.chemrev.3c00548
Chem. Rev. XXXX, XXX, XXX−XXX

Smart Textile Lighting/Display System with Multifunctional Fibre Devices for Large Scale Smart Home and IoT Applications. *Nat. Commun.* **2022**, *13*, 814.
(578) Tamura, T.; Maeda, Y.; Sekine, M.; Yoshida, M. Wearable Photoplethysmographic Sensors—Past and Present. *Electronics* **2014**, *3*, 282−302.
(579) Castaneda, D.; Esparza, A.; Ghamari, M.; Soltanpur, C.; Nazeran, H. A Review on Wearable Photoplethysmography Sensors and Their Potential Future Applications in Health Care. *Int. J. Biosens. Bioelectron.* **2018**, *4*, 195−202.
(580) lee, I.; Park, N.; Lee, H.; Hwang, C.; Kim, J. H.; Park, S. Systematic Review on Human Skin-Compatible Wearable Photoplethysmography Sensors. *Appl. Sci.* **2021**, *11*, 2313.
(581) Zhang, Y.; Liu, B.; Zhang, Z. Combining Ensemble Empirical Mode Decomposition with Spectrum Subtraction Technique for Heart Rate Monitoring Using Wrist-Type Photoplethysmography. *Biomed. Signal Process. Control* **2015**, *21*, 119−125.
(582) Wang, C.-F.; Wang, T.-Y.; Kuo, P.-H.; Wang, H.-L.; Li, S.-Z.; Lin, C.-M.; Chan, S.-C.; Liu, T.-Y.; Lo, Y.-C.; Lin, S.-H.; et al. Upper-Arm Photoplethysmographic Sensor with One-Time Calibration for Long-Term Blood Pressure Monitoring. *Biosensors* **2023**, *13*, 321.
(583) Seok, D.; Lee, S.; Kim, M.; Cho, J.; Kim, C. Motion Artifact Removal Techniques for Wearable EEG and PPG Sensor Systems. *Front.Electron.* **2021**, *2*, 685513.
(584) Kim, J.; Gutruf, P.; Chiarelli, A. M.; Heo, S. Y.; Cho, K.; Xie, Z.; Banks, A.; Han, S.; Jang, K.-I.; Lee, J. W.; et al. Miniaturized Battery-Free Wireless Systems for Wearable Pulse Oximetry. *Adv. Funct. Mater.* **2017**, *27*, 1604373.
(585) Yokota, T.; Zalar, P.; Kaltenbrunner, M.; Jinno, H.; Matsuhisa, N.; Kitanosako, H.; Tachibana, Y.; Yukita, W.; Koizumi, M.; Someya, T. Ultraflexible Organic Photonic Skin. *Sci. Adv.* **2016**, *2*, No. e1501856.
(586) Kim, T.-H.; Lee, C.-S.; Kim, S.; Hur, J.; Lee, S.; Shin, K. W.; Yoon, Y.-Z.; Choi, M. K.; Yang, J.; Kin, D.-H.; et al. Fully Stretchable Optoelectronic Sensors Based on Colloidal Quantum Dots for Sensing Photoplethysmographic Signals. *ACS Nano* **2017**, *11*, 5992−6003.
(587) Fenno, L.; Yizhar, O.; Deisseroth, K. The Development and Application of Optogenetics. *Annu. Rev. Neurosci.* **2011**, *34*, 389−412.
(588) Liu, x.; Ramirez, S.; Pang, P. T.; Puryear, C. B.; Govindarajan, A.; Deisseroth, K.; Tonegawa, S. Optogenetic Stimulation of a Hippocampal Engram Activates Fear Memory Recall. *Nature* **2012**, *484*, 381−385.
(589) Gunaydin, L. A.; Grosenick, L.; Finkelstein, J. C.; Kauvar, I. V.; Fenno, L. E.; Adhikari, A.; Lammel, S.; Mirzabekov, J. J.; Airan, R. D.; Zalocusky, K. A.; et al. Natural Neural Projection Dynamics Underlying Social Behavior. *Cell* **2014**, *157*, 1535−1551.
(590) Pisanello, F.; Sileo, L.; Oldenburg, I. A.; Pisanello, M.; Martiradonna, L.; Assad, J. A.; Sabatini, B. L.; De Vittorio, M. Multipoint-Emitting Optical Fibers for Spatially Addressable In Vivo Optogenetics. *Neuron* **2014**, *82*, 1245−1254.
(591) Bansal, A.; Shikha, S.; Zhang, Y. Towards Translational Optogenetics. *Nat. Biomed. Eng.* **2023**, *7*, 349−369.
(592) Zhang, H.; Gutruf, P.; Meacham, K.; Montana, M. C.; Zhao, X.; Chiarelli, A. M.; Vázquez-Guardado, A.; Norris, A.; Lu, L.; Guo, Q.; et al. Wireless, Battery-Free Optoelectronic Systems as Subdermal Implants for Local Tissue Oximetry. *Sci. Adv.* **2019**, *5*, No. eaaw0873.
(593) Jung, Y. H.; Kim, J. U.; Lee, J. S.; Shin, J. H.; Jung, W.; Ok, J.; Kim, T.-I. Injectable Biomedical Devices for Sensing and Stimulating Internal Body Organs. *Adv. Mater.* **2020**, *32*, 1907478.
(594) Lee, S. H.; Kim, J.; Shin, J. H.; Lee, H. E.; Kang, I. S.; Gwak, K.; Kim, D. S.; Kim, D.; Lee, K. J. Optogenetic Control of Body Movements via Flexible Vertical Light-Emitting Diodes on Brain Surface. *Nano Energy* **2018**, *44*, 447−455.
(595) McAlinden, N.; Massoubre, D.; Richardson, E.; Gu, E.; Sakata, S.; Dawson, M. D.; Mathieson, K. Thermal and Optical Characterization of Micro-LED Probes for In Vivo Optogenetic Neural Stimulation. *Opt. Lett.* **2013**, *38*, 992−994.
(596) Yang, Y.; Wu, M.; Vázquez-Guardado, A.; Wegener, A. J.; Grajales-Reyes, J. G.; Deng, Y.; Wang, T.; Avila, R.; Moreno, J. A.; Minkowicz, S.; et al. Wireless Multilateral Devices for Optogenetic Studies of Individual and Social Behaviors. *Nat. Neurosci.* **2021**, *24*, 1035−1045.
(597) Seo, D.; Neely, R. M.; Shen, K.; Singhal, U.; Alon, E.; Rabaey, J. M.; Carmena, J. M.; Maharbiz, M. M. Wireless Recording in the Peripheral Nervous System with Ultrasonic Neural Dust. *Neuron* **2016**, *91*, 529−539.
(598) Lee, H. E.; Park, J. H.; Jang, D.; Shin, J. H.; Im, T. H.; Lee, J. H.; Hong, S. K.; Wang, H. S.; Kwak, M. S.; Peddigari, M.; et al. Optogenetic Brain Neuromodulation by Stray Magnetic Field via Flash-Enhanced Magneto-Mechano-Triboelectric Nanogenerator. *Nano Energy* **2020**, *75*, 104951.
(599) Noh, K. N.; Park, S. I.; Qazi, R.; Zou, Z.; Mickle, A. D.; Grajales-Reyes, J. G.; Jang, K.-I.; Gereau, I. V.; R, W.; Xiao, J.; et al. Miniaturized, Battery-Free Optofluidic Systems with Potential for Wireless Pharmacology and Optogenetics. *Small* **2018**, *14*, 1702479.
(600) Folcher, M.; Oesterle, S.; Zwicky, K.; Thekkottil, T.; Heymoz, J.; Hohmann, M.; Christen, M.; El-Baba, M. D.; Buchmann, P.; Fussenegger, M. Mind-Controlled Transgene Expression by a Wireless-Powered Optogenetic Designer Cell Implant. *Nat. Commun.* **2014**, *5*, 5392.
(601) Kim, T.-I.; McCall, J. G.; Jung, Y. H.; Huang, X.; Siuda, E. R.; Li, Y.; Song, J.; Song, Y. M.; Pao, H. A.; Kim, R.-H.; et al. Injectable, Cellular-Scale Optoelectronics with Applications for Wireless Optogenetics. *Science* **2013**, *340*, 211−216.
(602) Li, L.; Lu, L.; Ren, Y.; Tang, G.; Zhao, Y.; Cai, X.; Shi, Z.; Ding, H.; Liu, C.; Cheng, D.; et al. Colocalized, Bidirectional Optogenetic Modulations in Freely Behaving Mice with a Wireless Dual-Color Optoelectronic Probe. *Nat. Commun.* **2022**, *13*, 839.
(603) Park, S. I.; Brenner, D. S.; Shin, G.; Morgan, C. D.; Copits, B. A.; Chung, H. U.; Pullen, M. Y.; Noh, K. N.; Davidson, S.; Oh, S. J.; et al. Soft, Stretchable, Fully Implantable Miniaturized Optoelectronic Systems for Wireless Optogenetics. *Nat. Biotechnol.* **2015**, *33*, 1280−1286.
(604) Shin, G.; Gomez, A. M.; Al-Hasani, R.; Jeong, Y. R.; Kim, J.; Xie, Z.; Banks, A.; Lee, S. M.; Han, S. Y.; Yoo, C. J.; et al. Flexible Near-Field Wireless Optoelectronics as Subdermal Implants for Broad Applications in Optogenetics. *Neuron* **2017**, *93*, 509−521.
(605) Jeong, J.-W.; McCall, J. G.; Shin, G.; Zhang, Y.; Al-Hasani, R.; Kim, M.; Li, S.; Sim, J. Y.; Jang, K.-I.; Shi, Y.; et al. Wireless Optofluidic Systems for Programmable In Vivo Pharmacology and Optogenetics. *Cell* **2015**, *162*, 662−674.
(606) Yin, D.; Jiang, N.-R.; Chen, Z.-Y.; Liu, Y.-F.; Bi, Y.-G.; Zhang, X.-L.; Feng, J.; Sun, H.-B. Roller-Assisted Adhesion Imprinting for High-Throughput Manufacturing of Wearable and Stretchable Organic Light-Emitting Devices. *Adv. Optic. Mater.* **2020**, *8*, 1901525.
(607) Li, X.-C.; Yao, L.; Song, W.; Liu, F.; Wang, W.; Chen, J.; Xue, Q.; Lai, W.-Y. Intrinsically Stretchable Electroluminescent Elastomers with Self-Confinement Effect for Highly Efficient Non-Blended Stretchable OLEDs. *Angew. Chem.* **2023**, *135*, No. e202213749.
(608) Kim, T.; Lee, H.; Jo, W.; Kim, T.-S.; Yoo, S. Realizing Stretchable OLEDs: A Hybrid Platform Based on Rigid Island Arrays on a Stress-Relieving Bilayer Structure. *Adv. Mater. Technol.* **2020**, *5*, 2000494.
(609) Sekitani, T.; Nakajima, H.; Maeda, H.; Fukushima, T.; Aida, T.; Hata, K.; Someya, T. Stretchable Active-Matrix Organic Light-Emitting Diode Display Using Printable Elastic Conductors. *Nat. Mater.* **2009**, *8*, 494−499.
(610) Lee, H.; Kim, D. S.; Jin, S. W.; Lee, H.; Jeong, Y. R.; You, I.; Zi, G.; Ha, J. S. Stretchable Array of CdSe/ZnS Quantum-Dot Light Emitting Diodes for Visual Display of Bio-Signals. *Chem. Eng. J.* **2022**, *427*, 130858.
(611) Kim, S. H.; Baek, G. W.; Yoon, J.; Seo, S.; Park, J.; Hahm, D.; Chang, J. H.; Seong, D.; Seo, H.; Oh, S.; et al. A Bioinspired Stretchable Sensory-Neuromorphic System. *Adv. Mater.* **2021**, *33*, 2104690.

https://doi.org/10.1021/acs.chemrev.3c00548
Chem. Rev. XXXX, XXX, XXX−XXX

(612) Hong, J.-H.; Shin, J. M.; Kim, G. M.; Joo, H.; Park, G. S.; Hwang, I. B.; Kim, M. W.; Park, W.-S.; Chu, H. Y.; Kim, S. 9.1-Inch Stretchable AMOLED Display Based on LTPS Technology. *J. SID* **2017**, *25*, 194−199.
(613) Stanciu, S. G.; Konig, K.; Song, Y. M.; Wolf, L.; Charitidis, C. A.; Bianchini, P.; Goetz, M. Toward Next-Generation Endoscopes Integrating Biomimetic Video Systems, Nonlinear Optical Microscopy, and Deep Learning. *Biophysics Rev.* **2023**, *4*, 021307.
(614) Borst, A.; Plett, J. Seeing the World Through an Insect's Eyes. *Nature* **2013**, *497*, 47−48.
(615) Gao, W.; Xu, Z.; Han, X.; Pan, C. Recent Advances in Curved Image Sensor Arrays for Bioinspired Vision System. *Nano Today* **2022**, *42*, 101366.
(616) Tsai, W.-L.; Chen, C.-Y.; Wen, Y.-T.; Yang, L.; Cheng, Y.-L.; Lin, H.-W. Band-Tunable Microcavity Perovskite Artificial Human Photoreceptors. *Adv. Mater.* **2019**, *31*, 1900231.
(617) Chen, F.; Li, C.; Shang, C.; Wang, K.; Huang, Q.; Zhao, Q.; Zhu, H.; Ding, J. Ultrafast Response of Centimeter Scale Thin $CsPbBr_3$ Single Crystal Film Photodetector for Optical Communication. *Small* **2022**, *18*, 2203565.
(618) Wang, T.; Zheng, D.; Zhang, J.; Qiao, J.; Min, C.; Yuan, X.; Somekh, M.; Feng, F. High-Performance and Stable Plasmonic-Functionalized formamidinium-Based Quasi-2D Perovskite Photodetector for Potential Application in Optical Communication. *Adv. Funct. Mater.* **2022**, *32*, 2208694.
(619) Deng, X.; Li, Z.; Cao, F.; Hong, E.; Fang, X. Woven Fibrous Photodetectors for Scalable UV Optical Communication Device. *Adv. Funct. Mater.* **2023**, *33*, 2213334.
(620) Liu, S.; Jiao, S.; Zhao, Y.; Lu, H.; Yang, S.; Wang, D.; Gao, S.; Wang, J.; Zhao, L. Bi_2O_3 Layer-Integrated, Double-Sided Responsive, Waveband-Discriminated Perovskite Photodetector for Encrypted Optical Communication. *Adv. Optical Mater.* **2023**, *11*, 2300831.
(621) Qiao, B.-S.; Wang, S.-Y.; Zhang, Z.-H.; Lian, Z.-D.; Zheng, Z.-Y.; Wei, Z.-P.; Li, L.; Ng, K. W.; Wang, S.-P.; Liu, Z.-B. Photosensitive Dielectric 2D Perovskite-Based Photodetector for Dual Wavelength Demultiplexing. *Adv. Mater.* **2023**, *35*, 2300632.
(622) Li, L.; Wang, D.; Zhang, D.; Ran, W.; Yan, Y.; Li, Z.; Wang, L.; Shen, G. Near-Infrared Light Triggered Self-Powered Mechano-Optical Communication System Using Wearable Photodetector Textile. *Adv. Funct. Mater.* **2021**, *31*, 2104782.
(623) Rein, M.; Favrod, V. D.; Hou, C.; Khudiyev, T.; Stolyarov, A.; Cox, J.; Chung, C.-C.; Chhav, C.; Ellis, M.; Joannopoulos, J.; et al. Diode Fibres for Fabric-Based Optical Communications. *Nature* **2018**, *560*, 214−218.
(624) Zhou, Y.; Qiu, X.; Wan, Z.; Long, Z.; Poddar, S.; Zhang, Q.; Ding, Y.; Chan, C. L. J.; Zhang, D.; Zhou, K.; Lin, Y.; Fan, Z. Halide-Exchanged Perovskite Photodetectors for Wearable Visible-Blind Ultraviolet Monitoring. *Nano Energy* **2022**, *100*, 107516.
(625) Qiu, M.; Sun, P.; Liu, Y.; Huang, Q.; Zhao, C.; Li, Z.; Mai, W. Visualized UV Photodetectors Based on Prussian Blue/TiO_2 for Smart Irradiation Monitoring Application. *Adv. Mater. Technol.* **2018**, *3*, 1700288.
(626) Xu, X.; Chen, J.; Cai, S.; Long, Z.; Zhang, Y.; Su, L.; He, S.; Tang, C.; Liu, P.; Peng, H.; Fang, X. A Real-Time Wearable UV-Radiation Monitor Based on a High-Performance p-CuZnS/n-TiO_2 Photodetector. *Adv. Mater.* **2018**, *30*, 1803165.
(627) An, J.; Le, T.-S. D.; Lim, H. J.; Tran, V. T.; Zhan, Z.; Gao, Y.; Zheng, L.; Sun, G.; Kim, Y.-J. Single-Step Selective Laser Writing of Flexible Photodetectors for Wearable Optoelectronics. *Adv. Sci.* **2018**, *5*, 1800496.
(628) Ju, D.; Liu, X.; Zhu, Z.; Wang, S.; Liu, S.; Gu, Y.; Chang, J.; Liu, Q.; Zou, Y. Solution Processed Membrane-Based Wearable ZnO/Graphene Schottky UV Photodetectors with Imaging Application. *Nanotechnology* **2019**, *30*, 375701.
(629) Liu, K.; Bian, Y.; Kuang, J.; Huang, X.; Li, Y.; Shi, W.; Zhu, Z.; Liu, G.; Qin, M.; Zhao, Z.; et al. Ultrahigh-Performance Optoelectronic Skin Based on Intrinsically Stretchable Perovskite-Polymer Heterojunction Transistors. *Adv. Mater.* **2022**, *34*, 2107304.
(630) Wang, B.; Thukral, A.; Xie, Z.; Liu, L.; Zhang, X.; Huang, W.; Yu, X.; Yu, C.; Marks, T. J.; Facchetti, A. Flexible and Stretchable Metal Oxide Nanofiber Networks for Multimodal and Monolithically Integrated Wearable Electronics. *Nat. Commun.* **2020**, *11*, 2405.
(631) Heo, S.; Ha, J.; Son, S. J.; Choi, I. S.; Lee, H.; Oh, S.; Jekal, J.; Kang, M. H.; Lee, G. J.; Jung, H. H.; Yea, J.; Lee, T.; Lee, Y.; Choi, J.-W.; Xu, S.; Choi, J. H.; Jeong, J.-W.; Song, Y. M.; Rah, J.-C.; Keum, H.; Jang, K.-I. Instant, Multiscale Dry Transfer Printing by Atomic Diffusion Control at Heterogeneous Interfaces. *Sci. Adv.* **2021**, *7*, No. eabh0040.
(632) Zhang, Y.; Tao, T. H. A Bioinspired Wireless Epidermal Photoreceptor for Artificial Skin Vision. *Adv. Funct. Mater.* **2020**, *30*, 200381.
(633) Hu, Y.; Yang, H.; Huang, J.; Zhang, X.; Tan, B.; Shang, H.; Zhang, S.; Feng, W.; Zhu, J.; Zhang, J.; Shuai, Y.; Jia, D.; Zhou, Y.; Hu, P. Flexible Optical Synapses Based on In_2Se_3/MoS_2 Heterojunctions for Artificial Vision Systems in the Near-Infrared Range. *ACS Appl. Mater. Interfaces* **2022**, *14*, 55839−55849.
(634) Bhatnagar, P.; Patel, M.; Lee, K.; Kim, J. Self-Powered Transparent Photodetector for Subretinal Visual Functions of Wide-Field-of-View and Broadband Perception. *InfoMater.* **2023**, *5*, No. e12408.
(635) Wang, Q.; Zhang, G.; Zhang, H.; Duan, Y.; Yin, Z.; Huang, Y. High-Resolution, Flexible, and Full-Color Perovskite Image Photodetector via Electrohydrodynamic Printing of Ionic-Liquid-Based Ink. *Adv. Funct. Mater.* **2021**, *31*, 2100857.
(636) Zhu, Y.; Geng, C.; Hu, L.; Liu, L.; Zhu, Y.; Yao, Y.; Li, C.; Ma, Y.; Li, G.; Chen, Y. Skin-Like Near-Infrared II Photodetector with High Performance for Optical Communication, Imaging, and Proximity Sensing. *Chem. Mater.* **2023**, *35*, 2114−2124.
(637) Zhu, Z.; Gu, Y.; Wang, S.; Zou, Y.; Zeng, H. Improving Wearable Photodetector Textiles via Precise Energy Level Alignment and Plasmonic Effect. *Adv. Electron. Mater.* **2017**, *3*, 1700281.
(638) Zubair, A.; Wang, X.; Mirri, F.; Tsentalovich, D. E.; Fujimura, N.; Suzuki, D.; Soundarapandian, K. P.; Kawano, Y.; Pasquali, M.; Kono, J. Carbon Nanotube Woven Textile Photodetector. *Phys. Rev. Mater.* **2018**, *2*, 015201.
(639) Kim, J. J.; Wang, Y.; Wang, H.; Lee, S.; Yokota, T.; Someya, T. Skin Electronics: Next-Generation Device Platform for Virtual and Augmented Reality. *Adv. Funct. Mater.* **2021**, *31*, 2009602.
(640) Guo, S.; Wu, K.; Li, C.; Wang, H.; Sun, Z.; Xi, D.; Zhang, S.; Ding, W.; Zaghloul, M. E.; et al. Integrated Contact Lens Sensor System Based on Multifunctional Ultrathin MoS_2 Transistors. *Matter* **2021**, *4*, 969−985.
(641) Zhang, Y.; Xu, S.; Fu, H.; Lee, J.; Su, J.; Hwang, K.-C.; Rogers, J. A.; Huang, Y. Buckling in Serpentine Microstructures and Applications in Elastomer-Supported Ultra-Stretchable Electronics with High Areal Coverage. *Soft Matter* **2013**, *9*, 8062.
(642) Zhang, Y.; Fu, H.; Su, Y.; Xu, S.; Cheng, H.; Fan, J. A.; Hwang, K.-C.; Rogers, J. A.; Huang, Y. Mechanics of Ultra-Stretchable Self-Similar Serpentine Interconnects. *Acta Mater.* **2013**, *61*, 7816−7827.
(643) Zhang, Y.; Wang, S.; Li, X.; Fan, J. A.; Xu, S.; Song, Y. M.; Choi, K.-J.; Yeo, W.-H.; Lee, W.; Nazaar, S. N.; Lu, B.; Yin, L.; Hwang, K.-C.; Rogers, J. A.; Huang, Y. Experimental and Theoretical Studies of Serpentine Microstructures Bonded to Prestrained Elastomers for Stretchable Electronics. *Adv. Funct. Mater.* **2014**, *24*, 2028−2037.
(644) Hong, S.; Lee, J.; Do, K.; Lee, M.; Kim, J. H.; Lee, S.; Kim, D.-H. Stretchable Electrode Based on Laterally Combed Carbon Nanotubes for Wearable Energy Harvesting and Storage Devices. *Adv. Funct. Mater.* **2017**, *27*, 1704353.
(645) Nasreldin, M.; Delattre, R.; Marchiori, B.; Ramuz, M.; Maria, S.; de Bougrenet de la Tocnaye, J. L.; Djenizian, T. Microstructured Electrodes Supported on Serpentine Interconnects for Stretchable Electronics. *APL Mater.* **2019**, *7*, 031507.
(646) Jiang, C.; Li, Q.; Fan, S.; Guo, Q.; Bi, S.; Wang, X.; Cao, X.; Liu, Y.; Song, J. Hyaline and Stretchable Haptic Interfaces Based on

https://doi.org/10.1021/acs.chemrev.3c00548
Chem. Rev. XXXX, XXX, XXX−XXX

Serpentine-Shaped Silver Nanofiber Networks. *Nano Energy* **2020**, *73*, 104782.
(647) Jang, K.-I.; Han, S. Y.; Xu, S.; Mathewson, K. E.; Zhang, Y.; Jeong, J.-W.; Kim, G.-T.; Webb, R. C.; Lee, J. W.; Dawidczyk, T. J.; et al. Rugged and Breathable forms of Stretchable Electronics with Adherent Composite Substrates for Transcutaneous Monitoring. *Nat. Commun.* **2014**, *5*, 4779.
(648) Jang, K.-I.; Chung, H. U.; Xu, S.; Lee, C. H.; Luan, H.; Jeong, J.; Cheng, H.; Kim, G.-T.; Han, S. Y.; Lee, J. W.; et al. Soft Network Composite Materials with Deterministic and Bio-Inspired Designs. *Nat. Commun.* **2015**, *6*, 6566.
(649) Jang, K.-I.; Jung, H. N.; Lee, J. W.; Xu, S.; Liu, Y. H.; Ma, Y.; Jeong, J.-W.; Song, Y. M.; Kim, J.; Kim, B. H.; et al. Ferromagnetic, Folded Electrode Composite as a Soft Interface to the Skin for Long-Term Electrophysiological Recording. *Adv. Funct. Mater.* **2016**, *26*, 7281−7290.
(650) Fan, J. A.; Yeo, W.-H.; Su, Y.; Hattori, Y.; Lee, W.; Jung, S.-Y.; Zhang, Y.; Liu, Z.; Cheng, H.; Falgout, L.; et al. Fractal Design Concepts for Stretchable Electronics. *Nat. Commun.* **2014**, *5*, 3266.
(651) Zhang, Y.; Fu, H.; Xu, S.; Fan, J. A.; Hwang, K.-C.; Jiang, J.; Rogers, J. A.; Huang, Y. A Hierarchical Computational Model for Stretchable Interconnects with Fractal-Inspired Designs. *J. Mech. Phys. Solids* **2014**, *72*, 115−130.
(652) Yun, J.; Lee, H.; Song, C.; Jeong, Y. R.; Park, J. W.; Lee, J. H.; Kim, D. S.; Keum, K.; Kim, M. S.; Jin, S. W.; et al. A Fractal-Designed Stretchable and Transparent Microsupercapacitor as a Skin-Attachable Energy Storage Device. *J. Chem. Eng.* **2020**, *387*, 124076.
(653) Jiang, H.; Khang, D.-Y.; Song, J.; Sun, Y.; Huang, Y.; Rogers, J. A. Finite Deformation Mechanics in Buckled Thin Films on Compliant Supports. *Proc. Natl. Acad. Sci. U. S. A.* **2007**, *104*, 15607−15612.
(654) Wang, S.; Song, J.; Kim, D.-H.; Huang, Y.; Rogers, J. A. Local Versus Global Buckling of Thin Films on Elastomeric Substrates. *Appl. Phys. Lett.* **2008**, *93*, 023126.
(655) Lee, J.; Chung, S.; Song, H.; Kim, S.; Hong, Y. Lateral-Crack-Free, Buckled, Inkjet-Printed Silver Electrodes on Highly Pre-Stretched Elastomeric Substrates. *J. Phys. D: Appl. Phys.* **2013**, *46*, 105305.
(656) Hu, X.; Dou, Y.; Li, J.; Liu, Z. Buckled Structures: Fabrication and Applications in Wearable Electronics. *Small* **2019**, *15*, 1804805.
(657) Kim, B. S.; Kwon, H.; Kwon, H. J.; Pyo, J. B.; Oh, J.; Hong, S. Y.; Park, J. H.; Char, K.; Ha, J. S.; Son, J. G.; et al. Buckling Instability Control of 1D Nanowire Networks for a Large-Area Stretchable and Transparent Electrode. *Adv. Funct. Mater.* **2020**, *30*, 1910214.
(658) Jang, K.-I.; Li, K.; Chung, H. U.; Xu, S.; Jung, H. N.; Yang, Y.; Kwak, J. W.; Jung, H. H.; Song, J.; Yang, C.; et al. Self-Assembled Three-Dimensional Network Designs for Soft Electronics. *Nat. Commun.* **2017**, *8*, 15894.
(659) Kim, B. H.; Lee, J.; Won, S. M.; Xie, Z.; Chang, J.-K.; Yu, Y.; Cho, Y. K.; Jang, H.; Jeong, J. Y.; Lee, Y.; et al. Three-Dimensional Silicon Electronic Systems Fabricated by Compressive Buckling Process. *ACS Nano* **2018**, *12*, 4164−4171.
(660) Chu, K.; Song, B. G.; Yang, H.-I.; Kim, D.-M.; Lee, C. S.; Park, M.; Chung, C.-M. Smart Passivation Materials with a Liquid Metal Microcapsule as Self-Healing Conductors for Sustainable and Flexible Perovskite Solar Cells. *Adv. Funct. Mater.* **2018**, *28*, 1800110.
(661) Park, T. H.; Kim, J.-H.; Seo, S. Facile and Rapid Method for Fabricating Liquid Metal Electrodes with Highly Precise Patterns via One-Step Coating. *Adv. Funct. Mater.* **2020**, *30*, 2003694.
(662) Won, P.; Jeong, S.; Majidi, C.; Ko, S. H. Recent Advances in Liquid-Metal-Based Wearable Electronics and Materials. *iScience* **2021**, *24*, 102698.
(663) Chen, X.; Lian, H.; Mo, D.; Ma, X.; Gong, M.; Sun, D. Self-Supporting 3D Printed Flexible Liquid Metal Electrodes for Electrostatically Microfluidic Valves. *J. Micromech. Microeng.* **2021**, *31*, 115005.
(664) Xie, C.; Yan, F. Flexible Photodetectors Based on Novel Functional Materials. *Small* **2017**, *13*, 1701822.
(665) Patel, M.; Pataniya, P. M.; Patel, V.; Sumesh, C. K. Flexible Photodetector Based on Graphite/ZnO-WS2 Nanohybrids on Paper. *J. Mater. Sci.: Mater. Electron.* **2022**, *33*, 13771−13781.
(666) Zhang, K.; Jung, Y. H.; Mikael, S.; Seo, J.-H.; Kim, M.; Mi, H.; Zhou, H.; Xia, Z.; Zhou, W.; Gong, S.; et al. Origami Silicon Optoelectronics for Hemispherical Electronics Eye Systems. *Nat. Commun.* **2017**, *8*, 1782.
(667) Rao, Z.; Lu, Y.; Li, Z.; Sim, K.; Ma, Z.; Xiao, J.; Yu, C. Curvy, Shape-Adaptive Imagers Based on Printed Optoelectronic Pixels with a Kirigami Design. *Nat. Electron.* **2021**, *4*, 513−521.
(668) Jung, I.; Xiao, J.; Malyarchuk, V.; Lu, C.; Li, M.; Liu, Z.; Yoon, J.; Huang, Y.; Rogers, J. A. Dynamically Tunable Hemispherical Electronic Eye Camera System with Adjustable Zoom Capability. *Proc. Natl. Acad. Sci. U. S. A.* **2011**, *108*, 1788−1793.
(669) Lee, W.; Liu, Y.; Lee, Y.; Sharma, B. K.; Shinde, S. M.; Kim, S. D.; Nan, K.; Yan, Z.; Han, M.; Huang, Y.; et al. Two-Dimensional Materials in Functional Three-Dimensional Architectures with Application in Photodetection and Imaging. *Nat. Commun.* **2018**, *9*, 1417.
(670) Basiricò, L.; Ciavatti, A.; Cramer, T.; Cosseddu, P.; Bonfiglio, A.; Fraboni, B. Direct X-Ray Photoconversion in Flexible Organic Thin Film Devices Operated Below 1V. *Nat. Commun.* **2016**, *7*, 13063.
(671) Xu, X.; Davanco, M.; Qi, X.; Forrest, S. R. Direct Transfer Patterning on Three-Dimensionally Deformed Surfaces at Micrometer Resolutions and Its Application to Hemispherical Focal Plane Detector Arrays. *Org. Electron.* **2008**, *9*, 1122−1127.
(672) Kim, Y.; Zhu, C.; Lee, W.-Y.; Smith, A.; Ma, H.; Li, X.; Son, D.; Matsuhisa, N.; Kim, J.; Bae, W.-G.; et al. A Hemispherical Image Sensor Array Fabricated with Organic Photomemory Transistors. *Adv. Mater.* **2023**, *35*, 2203541.
(673) Ge, Z.; Xu, N.; Zhu, Y.; Zhao, K.; Ma, Y.; Li, G.; Chen, Y. Visible to Mid-Infrared Photodetection Based on Flexible 3D Graphene/Organic Hybrid Photodetector with Ultrahigh Responsivity at Ambient Conditions. *ACS Photonics* **2022**, *9*, 59−67.
(674) Wei, Y.; Chen, H.; Liu, T.; Wang, S.; Jiang, Y.; Song, Y.; Zhang, J.; Zhang, X.; Lu, G.; Huang, F.; et al. Self-Powered Organic Photodetectors with High Detectivity for Near Infrared Light Detection Enabled by Dark Current Reduction. *Adv. Funct. Mater.* **2021**, *31*, 2106326.
(675) Simone, G.; Dyson, M. J.; Meskers, S. C. J.; Janssen, R. A. J.; Gelinck, G. H. Organic Photodetectors and Their Application in Large Area and Flexible Image Sensors: The Role of Dark Current. *Adv. Funct. Mater.* **2020**, *30*, 1904205.
(676) Byeon, H.; Kim, B.; Hwang, H.; Kim, M.; Yoo, H.; Song, H.; Lee, S. H.; Lee, B. H. Flexible Organic Photodetectors with Mechanically Robust Zinc Oxide Nanoparticle Thin Films. *ACS Appl. Mater. Interfaces* **2023**, *15*, 10926−10935.
(677) Tian, W.; Zhou, H.; Li, L. Hybrid Organic-Inorganic Perovskite Photodetectors. *Small* **2017**, *13*, 1702107.
(678) Trung, T. Q.; Dang, V. Q.; Lee, H.-B.; Kim, D.-I.; Moon, S.; Lee, N.-E.; Lee, H. An Omnidirectionally Stretchable Photodetector Based on Organic-Inorganic Heterojunctions. *ACS Appl. Mater. Interfaces* **2017**, *9*, 35958−35967.
(679) Zhang, J.; Huang, Y.; Tan, Z.; Li, T.; Zhang, Y.; Jia, K.; Lin, L.; Sun, L.; Chen, X.; Li, Z.; et al. Low-Temperature Heteroepitaxy of 2D PbI_2/Graphene for Large-Area Flexible Photodetectors. *Adv. Mater.* **2018**, *30*, 1803194.
(680) Mukherjee, S.; Jana, S.; Sinha, T. K.; Das, S.; Ray, S. Y. Infrared Tunable, Two Colour-Band Photodetectors on Flexible Platforms Using 0D/2D PbS-MoS_2 Hybrids. *Nanoscale Adv.* **2019**, *1*, 3279.
(681) Du, J.; Liao, Q.; Hong, M.; Liu, B.; Zhang, X.; Yu, H.; Xiao, J.; Gao, L.; Gao, F.; Kang, Z.; et al. Piezotronic Effect on Interfacial Charge Modulation in Mixed-Dimensional Van der Waals Heterostructure for Ultrasensitive Flexible Photodetectors. *Nano Energy* **2019**, *58*, 85−93.
(682) Zhang, Y.; Xu, Y.; Gao, L.; Liu, X.; Fu, Y.; Ma, C.; Ge, Y.; Cao, R.; Zhang, X.; Al-Hartomy, O. A.; et al. Mxene-Based Mixed-

https://doi.org/10.1021/acs.chemrev.3c00548
Chem. Rev. XXXX, XXX, XXX−XXX

Dimensional Schottky Heterojunction towards Self-Powered Flexible High-Performance Photodetector. *Mater. Today Phys.* **2021**, *21*, 100479.
(683) Reddy B, K. S.; Veeralingam, S.; Borse, P. H.; Badhulika, S. 1D NiO-3D Fe_2O_3 Mixed Dimensional Heterostructure for Fast Response Flexible Broadband Photodetector. *Nanotechnology* **2022**, *33*, 235201.
(684) Zhu, J.; Wei, S.; Tang, J.; Hu, Y.; Dai, X.; Zi, Y.; Wang, M.; Xiang, Y.; Huang, W. Mxene V_2CT_X Nanosheet/Bismuth Quantum Dot-Based Heterostructures for Enhanced Flexible Photodetection and Nonlinear Photonics. *ACS Appl. Nano Mater.* **2023**, *6*, 13629−13636.
(685) Selamneni, V.; Raghavan, H.; Hazra, A.; Sahatiya, P. MoS_2/Paper Decorated with Metal Nanoparticles (Au, Pt, and Pd) Based Plasmonic-Enhanced Broadband (Visible-NIR) Flexible Photodetectors. *Adv. Mater. Interfaces* **2021**, *8*, 2001988.
(686) Bube, R. H. Steady State Photoelectronic Analysis. In *Photoelectronic Properties of Semiconductors*; Cambridge University Press, 1992; pp 114−148.
(687) McGlynn, S. P. Concepts in Photoconductivity and Allied Problems. *J. Am. Chem. Soc.* **1964**, *86*, 5707.
(688) Liu, C.-H.; Chang, Y.-C.; Norris, T. B.; Zhong, Z. Graphene Photodetectors with Ultra-Broadband and High Responsivity at Room Temperature. *Nat. Nanotechnol.* **2014**, *9*, 273.
(689) Ma, Z.; Liu, D. 2-D Material-Based Photodetectors on Flexible Substrates. In *Inorganic Flexible Optoelectronics: Materials and Applications*; Ma, Z., Liu, D., Eds.; Wiley-VCH GmbH, 2019; pp 117−142.
(690) Xu, H.; Wu, J.; Feng, Q.; Mao, N.; Wang, C.; Zhang, J. High Responsivity and Gate Tunable Graphene-MoS_2 Hybrid Phototransistor. *Small* **2014**, *10*, 2300−2306.
(691) Liu, T.-J.; Xia, H.-Y.; Liu, B.; Jones, T. S.; Fang, M.; Yang, J.-L. Thin-Film Growth Behavior of Non-Planar Vanadium Oxide Phthalocyanine. *Chin. Phys. B* **2019**, *28*, 088101.
(692) Kim, H. M.; Lee, G. J.; Kim, M. S.; Song, Y. M. Fabrication of Flexible Image Sensor Based on Lateral NIPIN Phototransistors. *J. Vis. Exp.* **2018**, *136*, No. e57502.
(693) Kim, D.-H.; Lu, N.; Ghaffari, R.; Rogers, J. A. Inorganic Semiconductor Nanomaterials for Flexible and Stretchable Bio-Integrated Electronics. *NPG Asia Mater.* **2012**, *4*, No. e15.
(694) Sargent, E. H. Colloidal Quantum Dot Solar Cells. *Nat. Photonics* **2012**, *6*, 133−135.
(695) Sukhovatkin, V.; Hinds, S.; Brzozowski, L.; Sargent, E. H. Colloidal Quantum-Dot Photodetectors Exploiting Multiexciton Generation. *Science* **2009**, *324*, 1542−1544.
(696) Zhang, Y.; Peng, M.; Liu, Y.; Zhang, T.; Zhu, Q.; Lei, H.; Liu, S.; Tao, Y.; Li, L.; Wen, Z.; et al. Flexible Self-Powered Real-Time Ultraviolet Photodetector by Coupling Triboelectric and Photoelectric Effects. *ACS Appl. Mater. Interfaces* **2020**, *12*, 19384−19392.
(697) Yang, D.; Ma, H.; Li, J.; Fang, H.; Xie, H. Sunscreen-Inspired ZnO/PEG Composites for Flexible Ultraviolet Photodetectors with a Giant On-Off Ratio. *ACS Photonics* **2023**, *10*, 1320−1327.
(698) Lee, H.; Harden-Chaters, W.; Han, S. D.; Zhan, S.; Li, B.; Bang, S. Y.; Choi, H. W.; Lee, S.; Hou, B.; Occhipinti, L. G.; et al. Nano-to-Microporous Networks via Inkjet Printing of ZnO Nanoparticles/Graphene Hybrid for Ultraviolet Photodetectors. *ACS Appl. Nano Mater.* **2020**, *3*, 4454−4464.
(699) Arjun, K.; Karthikeyan, B. Flexible Ultraviolet Photodetector Based on Flower-Like ZnO/PEDOT:PSS Nanocomposites. *Appl. Phys. A: Mater. Sci. Process.* **2022**, *128*, 449.
(700) Klochko, N. P.; Klepikova, K. S.; Khrypunova, I. V.; Kopach, V. R.; Tyukhov, I. I.; Petrushenko, S. I.; Dukarov, S. V.; Sukhov, V. M.; Kirichenko, M. V.; Khrypunova, A. L. Solution-Processed Flexible Broadband ZnO Photodetector Modified by Ag Nanoparticles. *Sol. Energy* **2022**, *232*, 1−11.
(701) Ren, Z.; Sun, J.; Li, H.; Mao, P.; Wei, Y.; Zhong, X.; Hu, J.; Yang, S.; Wang, J. Bilayer PbS Quantum Dots for High-Performance Photodetectors. *Adv. Mater.* **2017**, *29*, 1702055.
(702) Zhou, W.; Shang, Y.; Garcia de Arquer, F. P.; Xu, K.; Wang, R.; Luo, S.; Xiao, X.; Zhou, X.; Huang, R.; Sargent, E. H.; et al. Solution-Processed Upconversion Photodetectors Based on Quantum Dots. *Nat. Electron.* **2020**, *3*, 251−258.
(703) Sun, Y.; Liu, Z.; Ding, Y.; Chen, Z. Flexible Broadband Photodetectors Enabled by MXene/PbS Quantum Dots Hybrid Structure. *IEEE Electron Device Lett.* **2021**, *42*, 1814−1817.
(704) Yin, X.; Zhang, C.; Guo, Y.; Yang, Y.; Xing, Y.; Que, W. PbS QD-Based Photodetectors: Future-Oriented Near-Infrared Detection Technology. *J. Mater. Chem. C* **2021**, *9*, 417.
(705) Oertel, D. C.; Bawendi, M. G.; Arango, A. C.; Bulovic, V. Photodetectors Based on Treated CdSe Quantum-Dot Films. *Appl. Phys. Lett.* **2005**, *87*, 213505.
(706) Lee, W.-Y.; Ha, S.; Lee, H.; Bae, J.-H.; Jang, B.; Kwon, H.-J.; Yun, Y.; Lee, S.; Jang, J. High-Detectivity Flexible Near-Infrared Photodetector Based on Chalcogenide Ag_2Se Nanoparticles. *Adv. Optical Mater.* **2019**, *7*, 1900812.
(707) Hu, J.; Yang, S.; Zhang, Z.; Li, H.; Veeramalai, C. P.; Sulaman, M.; Saleem, M. I.; Tang, Y.; Jiang, Y.; Tang, L.; et al. Solution-Processed, Flexible and Broadband Photodetector Based on $CsPbBr_3$/PbSe Quantum Dot Heterostructures. *J. Mater. Sci. Technol.* **2021**, *68*, 216−226.
(708) Hao, Q.; Tang, X.; Cheng, Y.; Hu, Y. Development of Flexible and Curved Infrared Detectors with HgTe Colloidal Quantum Dots. *Infrared Phys. Technol.* **2020**, *108*, 103344.
(709) Shen, K.; Xu, H.; Li, X.; Guo, J.; Sathasivam, S.; Wang, M.; Ren, A.; Choy, K. L.; Parkin, I. P.; Guo, Z.; et al. Flexible and Self-Powered Photodetector Arrays Based on All-Inorganic CsPbBr3 Quantum Dots. *Adv. Mater.* **2020**, *32*, 2000004.
(710) Lee, G. J.; Park, K.; Kim, M. S.; Chang, S.; Seok, T. J.; Park, H.-G.; Ju, G.; Kim, K.; Song, Y. M. Selective and Sensitive Photon Sieve Based on III-V Semiconductor Nanowire Forest Fabricated by Lithography-Free Process. *Adv. Optical Mater.* **2020**, *8*, 2000198.
(711) Chang, S.; Lee, G. J.; Song, Y. M. Recent Advances in Vertically Aligned Nanowires for Photonics Applications. *Micromachines* **2020**, *11*, 726.
(712) Dhanabalan, S. C.; Ponraj, J. S.; Zhang, H.; Bao, Q. Present Perspectives of Broadband Photodetectors Based on Nanobelts, Nanoribbons, Nanosheets, and the Emerging 2D Materials. *Nanoscale* **2016**, *8*, 6410.
(713) Wang, J.; Yan, C.; Kang, W.; Lee, P. S. High-Efficiency Transfer of Percolating Nanowire Films for Stretchable and Transparent Photodetectors. *Nanoscale* **2014**, *6*, 10734.
(714) Yan, R.; Gargas, D.; Yang, P. Nanowire Photonics. *Nat. Photonics* **2009**, *3*, 569−576.
(715) Shen, L.; Pun, E. Y. B.; Ho, J. C. Recent Developments in III-V Semiconducting Nanowires for High-Performance Photodetectors. *Chem. Front.* **2017**, *1*, 630.
(716) Fang, H.; Hu, W. Photogating in Low-Dimensional Photodetectors. *Adv. Sci.* **2017**, *4*, 1700323.
(717) Huang, J.-A.; Luo, L.-B. Low-Dimensional Plasmonic Photodetectors: Recent Progress and Future Opportunities. *Adv. Optical Mater.* **2018**, *6*, 1701282.
(718) Hossain, M.; Kumar, G. S.; Prabhava, S. N. B.; Sheerin, E. D.; McCloskey, D.; Acharya, S.; Rao, K. D. M.; Boland, J. J. Transparent, Flexible Silicon Nanostructured Wire Networks with Seamless Junctions for High-Performance Photodetector Applications. *ACS Nano* **2018**, *12*, 4727−4735.
(719) Aksoy, B.; Coskun, S.; Kucukyildiz, S.; Unalan, H. E. Transparent, Highly Flexible, All Nanowire Network Germanium Photodetectors. *Nanotechnology* **2012**, *23*, 325202.
(720) Liu, X.; Gu, L.; Zhang, Q.; Wu, J.; Long, Y.; Fan, Z. All-Printable Band-Edge Modulated ZnO Nanowire Photodetectors with Ultra-High Detectivity. *Nat. Commun.* **2014**, *5*, 4007.
(721) Yan, C.; Wang, J.; Wang, X.; Kang, W.; Cui, M.; Foo, C. Y.; Lee, P. S. An Intrinsically Stretchable Nanowire Photodetector with a Fully Embedded Structure. *Adv. Mater.* **2014**, *26*, 943−950.

https://doi.org/10.1021/acs.chemrev.3c00548
Chem. Rev. XXXX, XXX, XXX−XXX

(722) Zhao, L.; Gao, Z.; Zhang, J.; Lu, L.; Zou, D. Flexible Lateral-Bridged ZnO Nanowire UV Sensor for Focal-Plane Image Sensor Application. *Appl. Phys. Express* **2018**, *11*, 115001.
(723) Song, W.; Yang, D.; Qiu, Y.; Wang, Q.; Wu, B.; Zong, Y.; Feng, Q. ZnO Ultraviolet Photodetector Based on Flexible Polyester Fiber Substrates by Low-Temperature Hydrothermal Approach. *Micro Nano Lett.* **2019**, *14*, 215−218.
(724) Li, Y.; Li, Y.; Chen, J.; Sun, Z.; Li, Z.; Han, X.; Li, P.; Lin, X.; Liu, R.; Ma, Y.; et al. Full-Solution Processed All-Nanowire Flexible and Transparent Ultraviolet Photodetectors. *J. Mater. Chem. C* **2018**, *6*, 11666.
(725) Han, S.; Lee, S.-K.; Choi, I.; Song, J.; Lee, C.-R.; Kim, K.; Ryu, M.-Y.; Jeong, K.-U.; Kim, J. S. Highly Efficient and Flexible Photosensors with GaN Nanowires Horizontally Embedded in a Graphene Sandwich Channel. *ACS Appl. Mater. Interfaces* **2018**, *10*, 38173−38182.
(726) Han, S.; Choi, I.; Lee, C.-R.; Jeong, K.-U.; Lee, S.-K.; Kim, J. S. Fast Response Characteristics of Flexible Ultraviolet Photosensors with GaN Nanowires and Graphene. *ACS Appl. Mater. Interfaces* **2020**, *12*, 970−979.
(727) Han, S.; Noh, S.; Kim, J.-W.; Lee, C.-R.; Lee, S.-K.; Kim, J. S. Stretchable Inorganic GaN-Nanowire Photosensor with High Photocurrent and Photoresponsivity. *ACS Appl. Mater. Interfaces* **2021**, *13*, 22728−22737.
(728) Dai, Y.; Wang, X.; Peng, W.; Xu, C.; Wu, C.; Dong, K.; Liu, R.; Wang, Z. L. Self-Powered Si/CdS Flexible Photodetector with Broadband Response from 325 to 1550 nm Based on Pyro-Phototronic Effect: An Approach for Photosensing Below Bandgap Energy. *Adv. Mater.* **2018**, *30*, 1705893.
(729) Li, L.; Lou, Z.; Shen, G. Hierarchical CdS Nanowires Based Rigid and Flexible Photodetectors with Ultrahigh Sensitivity. *ACS Appl. Mater. Interfaces* **2015**, *7*, 23507−23514.
(730) Pei, Y.; Pei, R.; Liang, X.; Wang, Y.; Liu, L.; Chen, H.; Liang, J. CdS-Nanowires Flexible Photodetector with Ag-Nanowires Electrode Based on Non-Transfer Process. *Sci. Rep.* **2016**, *6*, 21551.
(731) Nawaz, M. Z.; Xu, L.; Zhou, X.; Shah, K. H.; Wang, J.; Wu, B.; Wang, C. CdS Nanobelt-Based Self-Powered Flexible Photodetectors with High Photosensitivity. *Mater. Adv.* **2021**, *2*, 6031.
(732) Li, D.; Yip, S.; Li, F.; Zhang, H.; Meng, Y.; Bu, X.; Kang, X.; Lan, C.; Liu, C.; Ho, J. C. Flexible Near-Infrared InGaSb Nanowire Array Detectors with Ultrafast Photoconductive Response Below 20μs. *Adv. Optical Mater.* **2020**, *8*, 2001201.
(733) Sa, Z.; Liu, F.; Liu, D.; Wang, M.; Zhang, J.; Yin, Y.; Pang, Z.; Zhuang, X.; Wang, P.; Yang, Z. Ag-Catalyzed GaSb Nanowires for Flexible Near-Infrared Photodetectors. *J. Semicond.* **2022**, *43*, 112302.
(734) Chen, G.; Wang, W.; Wang, C.; Ding, T.; Yang, Q. Controlled Synthesis of Ultrathin Sb_2Se_3 Nanowires and Application for Flexible Photodetectors. *Adv. Sci.* **2015**, *2*, 1500109.
(735) Tao, Y.-R.; Wu, X.-C.; Xiong, W.-W. Flexible Visible-Light Photodetectors with Broad Photoresponse Based on ZrS_3 Nanobelt Films. *Small* **2014**, *10*, 4905−4911.
(736) Zheng, Z.; Gan, L.; Li, H.; Ma, Y.; Bando, Y.; Golberg, D.; Zhai, T. A Fully Transparent and Flexible Ultraviolet-Visible Photodetector Based on Controlled Electrospun ZnO-CdO Heterojunction Nanofiber Arrays. *Adv. Funct. Mater.* **2015**, *25*, 5885−5894.
(737) Zhang, F.; Niu, S.; Guo, W.; Zhu, G.; Liu, Y.; Zhang, X.; Wang, Z. L. Piezo-Phototronic Effect Enhanced Visible/UV Photodetector of a Carbon-Fiber/ZnO-CdS Double-Shell Microwire. *ACS Nano* **2013**, *7*, 4537−4544.
(738) Liu, S.; Yang, D.; Ren, Y.; Song, J.; Hu, P.; Jiao, Y.; Fan, H.; Teng, F. Self-Powered, Flexible Ultraviolet Photodetector Based on ZnO/Te All Nanowires Heterojunction Structure. *Phys. Status Solidi A* **2023**, *220*, 2200612.
(739) Lee, G. J.; Kim, Y. J.; Song, H. S.; Yoo, D. E.; Lee, D.-W.; Kang, I.-S.; Song, Y. M. The Facile Implementation of Soft/Tunable Multiband Optical Filters by Stacking Vertical Silicon Nanowire Arrays for Smart Sensing. *Adv. Intell. Syst.* **2019**, *1*, 1900072.
(740) Kim, Y. J.; Yoo, Y. J.; Kang, M. H.; Ko, J. H.; Park, M. R.; Yoo, D. E.; Lee, D. W.; Kim, K.; Kang, I.-S.; Song, Y. M. Mechanotunable Optical Filters Based on Stretchable Silicon Nanowire Arrays. *Nanophotonics* **2020**, *9*, 3287−3293.
(741) Qu, Y.; Liao, L.; Li, Y.; Zhang, H.; Huang, Y.; Duan, X. Electrically Conductive and Optically Active Porous Silicon Nanowires. *Nano Lett.* **2009**, *9*, 4539−4543.
(742) Law, J. B. K.; Thong, J. T. L. Simple Fabrication of a ZnO Nanowire Photodetector with a Fast Photoresponse Time. *Appl. Phys. Lett.* **2006**, *88*, 133114.
(743) Babichev, A. V.; Zhang, H.; Lavenus, P.; Julien, F. H.; Egorov, A. Yu.; Lin, Y. T.; Tu, L. W.; Tchernycheva, M. GaN Nanowire Ultraviolet Photodetector with a Graphene Transparent Contact. *Appl. Phys. Lett.* **2013**, *103*, 201103.
(744) Dai, X.; Zhang, S.; Wang, Z.; Adamo, G.; Liu, H.; Huang, Y.; Couteau, C.; Soci, C. GaAs/AlGaAs Nanowire Photodetector. *Nano Lett.* **2014**, *14*, 2688−2693.
(745) Enrico, A.; Dubois, V.; Niklaus, F.; Stemme, G. Scalable Manufacturing of Single Nanowire Devices Using Crack-Defined Shadow Mask Lithography. *ACS Appl. Mater. Interfaces* **2019**, *11*, 8217−8226.
(746) Kiruthika, S.; Singh, S.; Kulkarni, G. U. Large Area Transparent ZnO Photodetectors with Au Wire Network Electrodes. *RSC Adv.* **2016**, *6*, 44668.
(747) Zheng, Z.; Gan, L.; Zhang, J.; Zhuge, F.; Zhai, T. An Enhanced UV-Vis-NIR and Flexible Photodetector Based on Electrospun ZnO Nanowire Array/PbS Quantum Dots Film Heterostructure. *Adv. Sci.* **2017**, *4*, 1600316.
(748) Kim, H.-J.; Oh, H.; Kim, T.; Kim, D.; Park, M. Stretchable Photodetectors Based on Electrospun Polymer/Perovskite Composite Nanofibers. *ACS Appl. Nano Mater.* **2022**, *5*, 1308−1316.
(749) Gu, L.; Tavakoli, M. M.; Zhang, D.; Zhang, Q.; Waleed, A.; Xiao, Y.; Tsui, K.-H.; Lin, Y.; Liao, L.; Wang, J.; et al. 3D Arrays of 1024-Pixel Image Sensors Based on Lead Halide Perovskite Nanowires. *Adv. Mater.* **2016**, *28*, 9713−9721.
(750) Gu, L.; Poddar, S.; Lin, Y.; Long, Z.; Zhang, D.; Zhang, Q.; Shu, L.; Qiu, X.; Kam, M.; Javey, A.; et al. A Biomimetic Eye with a Hemispherical Perovskite Nanowire Array Retina. *Nature* **2020**, *581*, 278−282.
(751) Cao, G.; Liu, D. Template-Based Synthesis of Nanorod, Nanowire, and Nanotube Arrays. *Adv. Colloid Interface Sci.* **2008**, *136*, 45−64.
(752) Pérez-Page, M.; Yu, E.; Li, J.; Rahman, M.; Dryden, D. M.; Vidu, R.; Stroeve, P. Template-Based Syntheses for Shape-Controlled Nanostructures. *Adv. Colloid Interface Sci.* **2016**, *234*, 51−79.
(753) Blagg, K.; Greymountain, T.; Kern, W.; Singh, M. Template-Based Electrodeposition and Characterization of Niobium Nanowires. *Electrochem. Commun.* **2019**, *101*, 39−42.
(754) Pan, W.; Liu, J.; Zhang, Z.; Gu, R.; Suvorova, A.; Gain, S.; Wang, H.; Li, Z.; Fu, L.; Faraone, L.; et al. Large Area Van der Waals Epitaxy of II-VI CdSe Thin Films for Flexible Optoelectronics and Full-Color Imaging. *Nano Res.* **2022**, *15*, 368−376.
(755) Su, T.-Y.; Medina, H.; Chen, Y.-Z.; Wang, S.-W.; Lee, S.-S.; Shih, Y.-C.; Chen, C.-W.; Kuo, H.-C.; Chuang, F.-C.; Chueh, Y.-L. Phase-Engineered $PtSe_2$-Layered Films by a Plasma-Assisted Selenization Process Toward All $PtSe_2$-Based Field Effect Transistor to Highly Sensitive, Flexible, and Wide-Spectrum Photoresponse Photodetectors. *Small* **2018**, *14*, 1800032.
(756) Yao, J.; Yang, G. Flexible and High-Performance All-2D Photodetector for Wearable Devices. *Small* **2018**, *14*, 1704524.
(757) Choi, J.-M.; Jang, H. Y.; Kim, A. R.; Kwon, J.-D.; Cho, B.; Park, M. H.; Kim, Y. Ultra-Flexible and Rollable 2D-MoS_2/Si Heterojunction-Based Near-Infrared Photodetector via Direct Synthesis. *Nanoscale* **2021**, *13*, 672.
(758) Zheng, Z.; Zhang, T.; Yao, J.; Zhang, Y.; Xu, J.; Yang, G. Flexible, Transparent, and Ultra-Broadband Photodetector Based on Large-Area WSe2 Film for Wearable Devices. *Nanotechnology* **2016**, *27*, 225501.
(759) Liu, Y.-L.; Yu, C.-C.; Lin, K.-T.; Yang, T.-C.; Wang, E.-Y.; Chen, H.-L.; Chen, L.-C.; Chen, K.-H. Transparent, Broadband, Flexible, and Bifacial-Operable Photodetectors Containing a Large-

https://doi.org/10.1021/acs.chemrev.3c00548
Chem. Rev. XXXX, XXX, XXX−XXX

Area Graphene-Gold Oxide Heterojunction. *ACS Nano* **2015**, *9*, 5093−5103.
(760) Kim, H.-S.; Chauhan, K. R.; Kim, J.; Choi, E. H. Flexible Vanadium Oxide Film for Broadband Transparent Photodetector. *Appl. Phys. Lett.* **2017**, *110*, 101907.
(761) Chen, Y.-Z.; Wang, S.-W.; Su, T.-Y.; Lee, S.-H.; Chen, C.-W.; Yang, C.-H.; Wang, K.; Kuo, H.-C.; Chueh, Y.-L. Phase-Engineered Type-II Multimetal-Selenide Heterostructures Toward Low-Power Consumption, Flexible, Transparent, and Wide-Spectrum Photoresponse Photodetectors. *Small* **2018**, *14*, 1704052.
(762) Sharma, M.; Aggarwal, P.; Singh, A.; Kaushik, S.; Singh, R. Flexible, Transparent, and Broadband Trilayer Photodetectors Based on MoS_2/WS_2 Nanostructures. *ACS Appl. Nano Mater.* **2022**, *5*, 13637−13648.
(763) Hwang, S.-W.; Tao, H.; Kim, D.-H.; Cheng, H.; Song, J.-K.; Rill, E.; Brenckle, M. A.; Panilaitis, B.; Won, S. M.; Kim, Y.-S.; et al. A Physically Transient form of Silicon Electronics. *Science* **2012**, *337*, 1640−1644.
(764) Wu, W.; Han, X.; Li, J.; Wang, X.; Zhang, Y.; Huo, Z.; Chen, Q.; Sun, X.; Xu, Z.; Tan, Y.; et al. Ultrathin and Conformable Lead Halide Perovskite Photodetector Arrays for Potential Application in Retina-Like Vision Sensing. *Adv. Mater.* **2021**, *33*, 2006006.
(765) Zhou, X.; Tian, Z.; Kim, H. J.; Wang, Y.; Xu, B.; Pan, R.; Chang, Y. J.; Di, Z.; Zhou, P.; Mei, Y. Rolling up $MoSe_2$ Nanomembranes as a Sensitive Tubular Photodetector. *Small* **2019**, *15*, 1902528.
(766) Fu, K. K.; Wang, Z.; Dai, J.; Carter, M.; Hu, L. Transient Electronics: Materials and Devices. *Chem. Mater.* **2016**, *28*, 3527−3539.
(767) Gao, Y.; Zhang, Y.; Wang, X.; Sim, K.; Liu, J.; Chen, J.; Feng, X.; Xu, H.; Yu, C. Moisture-Triggered Physically Transient Electronics. *Sci. Adv.* **2017**, *3*, No. e1701222.
(768) Han, W. B.; Lee, J. H.; Shin, J.-W.; Hwang, S.-W. Advanced Materials and Systems for Biodegradable, Transient Electronics. *Adv. Mater.* **2020**, *32*, 2002211.
(769) Jamshidi, R.; Taghavimehr, M.; Chen, Y.; Hashemi, N.; Montazami, R. Transient Electronics as Sustainable Systems: from Fundamentals to Applications. *Adv. Sustainable Syst.* **2022**, *6*, 2100057.
(770) Li, G.; Song, E.; Huang, G.; Pan, R.; Guo, Q.; Ma, F.; Zhou, B.; Di, Z.; Mei, Y. Flexible Transient Phototransistors by Use of Wafer-Compatible Transferred Silicon Nanomembranes. *Small* **2018**, *14*, 1802985.
(771) Chen, S.; Chen, J.; Zhang, X.; Li, Z.-Y.; Li, J. Kirigami/Origami: Unfolding the New Regime of Advanced 3D Microfabrication/Nanofabrication with 'Folding'. *Light: Sci. Appl.* **2020**, *9*, 75.
(772) Brooks, A. K.; Chakravarty, S.; Ali, M.; Yadavalli, V. K. Kirigami-Inspired Biodesign for Applications in Healthcare. *Adv. Mater.* **2022**, *34*, 2109550.
(773) Kim, G.-G.; Kim, Y.; Yoo, S.; Jang, H. S.; Ko, H. C. Hexahedral LED Arrays with Row and Column Control Lines formed by Selective Liquid-Phase Plasticization and Nondisruptive Tucking-Based Origami. *Adv. Mater. Technol.* **2020**, *5*, 2000010.
(774) Cheng, Y.-C.; Lu, H.-C.; Lee, X.; Zeng, H.; Priimagi, A. Kirigami-Based Light-Induced Shape-Morphing and Locomotion. *Adv. Mater.* **2020**, *32*, 1906233.
(775) Ta, T. D.; Chang, Z.; Narumi, K.; Umedachi, T.; Kawahara, Y. Printable Origami Bistable Structures for Foldable Jumpers. *2022 International Conference on Robotics and Automation (ICRA)*; IEEE, 2022; pp 7131−7137.
(776) Han, M.; Guo, X.; Chen, X.; Liang, C.; Zhao, H.; Zhang, Q.; Bai, W.; Zhang, F.; Wei, H.; Wu, C.; et al. Submillimeter-Scale Multimaterial Terrestrial Robots. *Sci. Robot.* **2022**, *4*, No. eabn0602.
(777) Evke, E. E.; Huang, C.; Wu, Y.-W.; Arwashan, M.; Lee, B.; forrest, S. R.; Shtein, M. Kirigami-Based Compliant Mechanism for Multiaxis Optical Tracking and Energy-Harvesting Applications. *Adv. Eng. Mater.* **2021**, *23*, 2001079.
(778) Li, H.; Wang, W.; Yang, Y.; Wang, Y.; Li, P.; Huang, J.; Li, J.; Lu, Y.; Li, Z.; Wang, Z.; et al. Kirigami-Based Highly Stretchable Thin Film Solar Cells That Are Mechanically Stable for More Than 1000 Cycles. *ACS Nano* **2020**, *14*, 1560−1568.
(779) Kim, D.-H.; Rogers, J. A. Bend, Buckle, and Fold: Mechanical Engineering with Nanomembranes. *ACS Nano* **2009**, *3*, 498−501.
(780) Kim, D.-H.; Xiao, J.; Song, J.; Huang, Y.; Rogers, J. A. Stretchable, Curvilinear Electronics Based on Inorganic Materials. *Adv. Mater.* **2010**, *22*, 2108−2124.
(781) Kim, J.; Lee, M.; Shim, H. J.; Ghaffari, R.; Cho, H. R.; Son, D.; Jung, Y. H.; Soh, M.; Choi, C.; Jung, S.; et al. Stretchable Silicon Nanoribbon Electronics for Skin Prosthesis. *Nat. Commun.* **2014**, *5*, 5747.
(782) Lee, E. K.; Baruah, R. K.; Leem, J. W.; Park, W.; Kim, B. H.; Urbas, A.; Ku, Z.; Kim, Y. L.; Alam, M. A.; Lee, C. H. Fractal Web Design of a Hemispherical Photodetector Array with Organic-Dye-Sensitized Graphene Hybrid Composites. *Adv. Mater.* **2020**, *32*, 2004456.
(783) Park, S. H.; Su, R.; Jeong, J.; Guo, S.; Qiu, K.; Joung, D.; Meng, F.; McAlpine, M. C. 3D Printed Masks and Transfer Stamping Process to Enable the Fabrication of the Hemispherical Organic Photodiodes. *Adv. Mater.* **2018**, *30*, 1803980.
(784) Gelinck, G. H.; Kumar, A.; Moet, D.; van der Steen, J.-L.; Shafique, U.; Malinowski, P. E.; Myny, K.; Rand, B. P.; Simon, M.; Rütten, W.; et al. X-ray Imager Using Solution Processed Organic Transistor Arrays and Bulk Heterojunction Photodiodes on Thin, Flexible Plastic Substrate. *Org. Electron.* **2013**, *14*, 2602−2609.
(785) Basiricò, L.; Ciavatti, A.; Fraboni, B. Solution-Grown Organic and Perovskite X-Ray Detectors: A New Paradigm for the Direct Detection of Ionizing Radiation. *Adv. Mater. Technol.* **2021**, *6*, 2000475.
(786) Xu, L.-J.; Lin, X.; He, Q.; Worku, M.; Ma, B. Highly Efficient Eco-Friendly X-Ray Scintillators Based on an Organic Manganese Halide. *Nat. Commun.* **2020**, *11*, 4329.
(787) Li, Z.; Chang, S.; Zhang, H.; Hu, Y.; Huang, Y.; Au, L.; Ren, S. Flexible Lead-Free X-ray Detector from Metal-Organic Frameworks. *Nano Lett.* **2021**, *21*, 6983−6989.
(788) Xu, M.; Zhu, M.; Zhao, D.; Chen, S.; Liu, S.; Zhang, Q.; Yuan, P.; Zhang, B.; Sellin, P.; Jie, W.; et al. Orientation and Mobility Control of 4HCB Organic Film for Flexible X-Ray Detectors with High Performance. *J. Mater. Sci. Technol.* **2023**, *135*, 46−53.
(789) Büchele, P.; Richter, M.; Tedde, S. F.; Matt, G. J.; Ankah, G. N.; Fischer, R.; Biele, M.; Metzger, W.; Lilliu, S.; Bikondoa, O.; et al. X-Ray Imaging with Scintillator-Sensitized Hybrid Organic Photodetectors. *Nat. Photonics* **2015**, *9*, 843−848.
(790) Zhang, L.; Pasthukova, N.; Yao, Y.; Zhong, X.; Pavlica, E.; Bratina, G.; Orgiu, E.; Samorì, P. Self-Suspended Nanomesh Scaffold for Ultrafast Flexible Photodetectors Based on Organic Semiconducting Crystals. *Adv. Mater.* **2018**, *30*, 1801181.
(791) Zhang, Y.; Qiu, Y.; Li, X.; Guo, Y.; Cao, S.; Gao, H.; Wu, Y.; Jiang, L. Organic Single-Crystalline Microwire Arrays Toward High-Performance Flexible Near-Infared Phototransistors. *Small* **2022**, *18*, 2203429.
(792) Park, Y.; Fuentes-Hernandez, C.; Kim, K.; Chou, W.-F.; Larrain, F. A.; Graham, S.; Pierron, O. N.; Kippelen, B. Skin-Like Low-Noise Elastomeric Organic Photodiodes. *Sci. Adv.* **2021**, *7*, No. eabj6565.
(793) Chen, L.; Cai, J.; Li, J.; Feng, S.-P.; Wei, G.; Li, W.-D. Nanostructured Texturing of $CH_3NH_3PbI_3$ Perovskite Thin Film on Flexible Substrate for Photodetector Application. *Org. Electron.* **2019**, *71*, 284−289.
(794) Ouyang, X.; Su, R.; Ng, D. W. H.; Han, G.; Pearson, D. R.; McAlpine, M. C. 3D Printed Skin-Interfaced UV-Visible Hybrid Photodetectors. *Adv. Sci.* **2022**, *9*, 2201275.
(795) Li, L.; Gu, L.; Lou, Z.; Fan, Z.; Shen, G. ZnO Quantum Dot Decorated Zn_2SnO_4 Nanowire Heterojunction Photodetectors with Drastic Performance Enhancement and Flexible Ultraviolet Image Sensors. *ACS Nano* **2017**, *11*, 4067−4076.

https://doi.org/10.1021/acs.chemrev.3c00548
Chem. Rev. XXXX, XXX, XXX−XXX

(796) Kim, M.; Kang, P.; Leem, J.; Nam, S. A Stretchable Crumpled Graphene Photodetector with Plasmonically Enhanced Photoresponsivity. *Nanoscale* **2017**, *9*, 4058.
(797) Kataria, M.; Yadav, K.; Haider, G.; Liao, Y. M.; Liou, Y.-R.; Cai, S.-Y.; Lin, H.; Chen, Y. H.; Inbaraj, C. R. P.; Bera, K. P.; et al. Transparent, Wearable, Broadband, and Highly Sensitive Upconversion Nanoparticles and Graphene-Based Hybrid Photodetectors. *ACS Photonics* **2018**, *5*, 2336−2347.
(798) Lee, D. J.; Ryu, S. R.; Kumar, G. M.; Cho, H. D.; Kim, D. Y.; Ilanchezhiyan, P. Piezo-Phototronic Effect Triggered Flexible UV Photodetectors Based on ZnO Nanosheets/GaN Nanorods Arrays. *Appl. Surf. Sci.* **2021**, *558*, 149896.
(799) Hwang, Y.; Hwang, Y. H.; Choi, K. W.; Lee, S.; Kim, S.; Park, S. J.; Ju, B.-K. Highly Stabilized Flexible Transparent Capacitive Photodetector Based on Silver Nanowire/Graphene Hybrid Electrodes. *Sci. Rep.* **2021**, *11*, 10499.
(800) Kolli, C. S. R.; Selamneni, V.; Martinez, B. A. M.; Carreno, A. F.; Sanchez, D. E.; Terrones, M.; Strupiechonski, E.; Bugallo, A. D. L.; Sahatiya, P. Broadband, Ultra-High-Responsive Monolayer MoS_2/SnS_2 Quantum-Dot-Based Mixed-Dimensional Photodetector. *ACS Appl. Mater. Interfaces* **2022**, *14*, 15415−15425.
(801) Shultz, A.; Liu, B.; Gong, M.; Alamri, M.; Walsh, M.; Schmitz, R. C.; Wu, J. Z. Development of Broadband PbS Quantum Dot/Graphene Photodetector Arrays with High-Speed Readout Circuits for Flexible Imagers. *ACS Appl. Nano Mater.* **2022**, *5*, 16896−16905.
(802) Heo, J. H.; Lee, D. S.; Shin, D. H.; Im, S. H. Recent Advancements in and Perspectives on Flexible Hybrid Perovskite Solar Cells. *J. Mater. Chem. A* **2019**, *7*, 888.
(803) Wang, Y.; Liu, Y.; Cao, S.; Wang, J. A Review on Solution-Processed Perovskite/Organic Hybrid Photodetectors. *J. Mater. Chem. C* **2021**, *9*, 5302.
(804) Thai, K. Y.; Park, I.; Kim, B. J.; Hoang, A. T.; Na, Y.; Park, C. U.; Chae, Y.; Ahn, J.-H. MoS_2/Graphene Photodetector Array with Strain-Modulated Photoresponse up to the Near-Infrared Regime. *ACS Nano* **2021**, *15*, 12836−12846.
(805) Nalwa, H. S. A Review of Molybdenum Disulfide (MoS_2) Based Photodetectors: from Ultra-Broadband, Self-Powered to Flexible Devices. *RSC Adv.* **2020**, *10*, 30529.
(806) Yu, H.; Xie, Y.; Wei, J.; Zhang, P.; Cui, Z. Highly-Bendable MoS_2/SnS Flexible Photodetector with Broadband Infrared Response. *Adv. Mater. Interfaces* **2022**, *9*, 2200896.
(807) Bao, Y.; Han, J.; Li, H.; Huang, K. Flexible, Heat-Resistant Photodetector Based on MoS_2 Nanosheets Thin Film on Transparent Muscovite Mica Substrate. *Nanotechnology* **2021**, *32*, 025206.
(808) Lopez-Sanchez, O.; Lembke, D.; Kayci, M.; Radenovic, A.; Kis, A. Ultrasensitive Photodetectors Based on Monolayer MoS2. *Nat. Nanotechnol.* **2013**, *8*, 497−501.
(809) Velusamy, D. B.; Haque, M. A.; Parida, M. R.; Zhang, F.; Wu, T.; Mohammed, O. F.; Alshareef, H. N. 2D Organic-Inorganic Hybrid Thin Films for Flexible UV-Visible Photodetectors. *Adv. Funct. Mater.* **2017**, *27*, 1605554.
(810) Lee, W.; Lee, J.; Yun, H.; Kim, J.; Park, J.; Choi, C.; Kim, D. C.; Seo, H.; Lee, H.; Yu, J. W.; et al. High-Resolution Spin-on-Patterning of Perovskite Thin Films for a Multiplexed Image Sensor Array. *Adv. Mater.* **2017**, *29*, 1702902.
(811) Dang, V. Q.; Trung, T. Q.; Duy, L. T.; Kim, B.-Y.; Siddiqui, S.; Lee, W.; Lee, N.-E. High-Performance Flexible Ultraviolet (UV) Phototransistor Using Hybrid Channel of Vertical ZnO Nanorods and Graphene. *ACS Appl. Mater. Interfaces* **2015**, *7*, 11032−11040.
(812) Lee, Y. H.; Park, S.; Won, Y.; Mun, J.; Ha, J. H.; Lee, J. H.; Lee, S. H.; Park, J.; Yeom, J.; Rho, J.; et al. Flexible High-Performance Graphene Hybrid Photodetectors Functionalized with Gold Nanostars and Perovskites. *NPG Asia Mater.* **2020**, *12*, 79.
(813) Li, N.; Wang, Q.; He, C.; Li, J.; Li, X.; Shen, C.; Huang, B.; Tang, J.; Yu, H.; Wang, S.; et al. 2D Semiconductor Based Flexible Photoresponsive Ring Oscillators for Artificial Vision Pixels. *ACS Nano* **2023**, *17*, 991−999.
(814) Ji, Z.; Liu, Y.; Zhao, C.; Wang, Z. L.; Mai, W. Perovskite Wide-Angle Field-Of-View Camera. *Adv. Mater.* **2022**, *34*, 2206957.
(815) Xiong, D.; Deng, W.; Tian, G.; Zhang, B.; Zhong, S.; Xie, Y.; Yang, T.; Zhao, H.; Yang, W. Controllable In-Situ-Oxidization of 3D-Networked $Ti_3C_2T_x$-TiO_2 Photodetectors for Large-Area Flexible Optical Imaging. *Nano Energy* **2022**, *93*, 106889.
(816) Kim, M. S.; Yeo, J.-E.; Choi, H.; Chang, S.; Kim, D.-H.; Song, Y. M. Evolution of Natural Eyes and Biomimetic Imaging Devices for Effective Image Acquisition. *J. Mater. Chem. C* **2023**, *11*, 12083−12104.
(817) Lee, G. J.; Nam, W. I.; Song, Y. M. Robustness of an Artificially Tailored Fisheye Imaging System with a Curvilinear Image Surface. *Opt. Laser Technol.* **2017**, *96*, 50−57.
(818) Kim, D. H.; Lee, G. J.; Song, Y. M. Compact Zooming Optical Systems for Panoramic and Telescopic Applications Based on Curved Image Sensor. *J. Optical Microsystems* **2022**, *2*, 31204.
(819) Xu, F.; Huang, W.; Liu, J.; Pang, W. Design of Lenses with Curved Petzval Image Surfaces. *J. Mod. Opt.* **2016**, *63*, 2211−2219.
(820) Land, M. F.; Nilsson, D.-E. The Origin of Vision. In *Animal Eye*; Oxford University Press, 2012; pp 1−22.
(821) Lee, L. P.; Szema, R. Inspirations from Biological Optics for Advanced Photonic Systems. *Science* **2005**, *310*, 1148−1150.
(822) Land, M. F. The Optics of Animal Eyes. *Contemp. Phys.* **1988**, *29*, 435−455.
(823) Lakshminarayanan, V.; Parthasarathy, M. K. Biomimetic Optics: Visual Systems. *J. Mod. Opt.* **2016**, 1.
(824) Lee, G. J.; Yoo, Y. J.; Song, Y. M. Recent Advances in Imaging Systems and Photonic Nanostructures Inspired by Insect Eye Geometry. *Appl. Spectrosc. Rev.* **2018**, *53*, 112−128.
(825) Rim, S.; Catrysse, P. B.; Dinyari, R.; Huang, K.; Peumans, P. The Optical Advantages of Curved Focal Plane Arrays. *Opt. Express* **2008**, *16*, 4965−4971.
(826) Dumas, D.; Fendler, M.; Baier, N.; Primot, J.; le Coarer, E. Curved Focal Plane Detector Array for Wide Field Cameras. *Appl. Opt.* **2012**, *51*, 5419−5424.
(827) Guenter, B.; Joshi, N.; Stoakley, R.; Keefe, A.; Geary, K.; Freeman, R.; Hundley, J.; Patterson, P.; Hammon, D.; Herrera, G.; et al. Highly Curved Image Sensors: A Practical Approach for Improved Optical Performance. *Opt. Express* **2017**, *25*, 13010−13023.
(828) Fan, D.; Lee, K.; forrest, S. R. Flexible Thin-Film InGaAs Photodiode Focal Plane Array. *Acs Photonics* **2016**, *3*, 670−676.
(829) Deng, W.; Zhang, X.; Huang, L.; Xu, X.; Wang, L.; Wang, J.; Shang, Q.; Lee, S.-T.; Jie, J. Aligned Single-Crystalline Perovskite Microwire Arrays for High-Performance Flexible Image Sensors with Long-Term Stability. *Adv. Mater.* **2016**, *28*, 2201−2208.
(830) Yoo, G.; Fung, T.-C.; Radtke, D.; Stumpf, M.; Zeitner, U.; Kanicki, J. Hemispherical Thin-Film Transistor Passive Pixel Sensors. *Sens. Actuator A-Phys.* **2010**, *158*, 280−283.
(831) Kim, M. S.; Lee, G. J.; Kim, H. M.; Song, Y. M. Parametric Optimization of Lateral NIPIN Phototransistors for Flexible Image Sensors. *Sensors* **2017**, *17*, 1774.
(832) Sanders, J. S.; Halford, C. E. Design and Analysis of Apposition Compound Eye Optical Sensors. *Opt. Eng.* **1995**, *34*, 222−235.
(833) Varela, F. G. The Vertebrate and the (Insect) Compound Eye in Evolutionary Perspective. *Vision Res.* **1971**, *11*, 201−209.
(834) Borst, A. Drosophila's View on Insect Vision. *Curr. Biol.* **2009**, *19*, R36−R47.
(835) Song, Y. M.; Xie, Y.; Malyarchuk, V.; Xiao, J.; Jung, I.; Choi, K.-J.; Liu, Z.; Park, H.; Lu, C.; Kim, R.-H.; et al. Digital Cameras with Designs Inspired by the Arthropod Eye. *Nature* **2013**, *497*, 95−99.
(836) Shin, G.; Jung, I.; Malyarchuk, V.; Song, J.; Wang, S.; Ko, H. C.; Huang, Y.; Ha, J. S.; Rogers, J. A. Micromechanics and Advanced Designs for Curved Photodetector Arrays in Hemispherical Electronic-Eye Cameras. *Small* **2010**, *6*, 851−856.
(837) Yu, H.; Zhao, X.; Tan, M.; Wang, B.; Zhang, M.; Wang, X.; Guo, S.; Tong, Y.; Tang, Q.; Liu, Y. Ultraflexible and Ultrasensitive Near-Infrared Organic Phototransistors for Hemispherical Biomimetic Eyes. *Adv. Funct. Mater.* **2022**, *32*, 2206765.
(838) Choi, C.; Choi, M. K.; Liu, S.; Kim, M.; Park, O. K.; Im, C.; Kim, J.; Qin, X.; Lee, G. J.; Cho, K. W.; et al. Human Eye-Inspired

https://doi.org/10.1021/acs.chemrev.3c00548
Chem. Rev. XXXX, XXX, XXX−XXX

Soft Optoelectronic Device Using High-Density MoS_2-Graphene Curved Image Sensor Array. *Nat. Commun.* **2017**, *8*, 1664.
(839) Atchison, D.; Smith, G. The Human Eye: An Overview. In *Optics of the Human Eye*; CRC Press, 2023; pp 3−14.
(840) Kim, M.; Chang, S.; Kim, M.; Yeo, J.-E.; Kim, M. S.; Lee, G. J.; Kim, D.-H.; Song, Y. M. Cuttlefish Eye-Inspired Artificial Vision for High-Quality Imaging under Uneven Illumination Conditions. *Sci. Robot.* **2023**, *8*, No. eade4698.
(841) Lee, M.; Seung, H.; Kwon, J. I.; Choi, M. K.; Kim, D.-H.; Choi, C. Nanomaterial-Based Synaptic Optoelectronic Devices for In-Sensor Preprocessing of Image Data. *ACS Omega* **2023**, *8*, 5209−5224.
(842) Ran, W.; Wang, L.; Zhao, S.; Wang, D.; Yin, R.; Lou, Z.; Shen, G. An Integrated Flexible All-Nanowire Infrared Sensing System with Record Photosensitivity. *Adv. Mater.* **2020**, *32*, 1908419.
(843) Wan, C.; Cai, P.; Guo, X.; Wang, M.; Matsuhisa, N.; Yang, L.; Lv, Z.; Luo, Y.; Loh, X. J.; Chen, X. An Artificial Sensory Neuron with Visual-Haptic Fusion. *Nat. Commun.* **2020**, *11*, 4602.
(844) Wang, Z.; Joshi, S.; Savel'ev, S.; Song, W.; Midya, R.; Li, Y.; Rao, M.; Yan, P.; Asapu, S.; Zhuo, Y.; et al. Fully Memristive Neural Networks for Pattern Classification with Unsupervised Learning. *Nat. Electron.* **2018**, *1*, 137−145.
(845) Wang, H.; Zhao, Q.; Ni, Z.; Li, Q.; Liu, H.; Yang, Y.; Wang, L.; Ran, Y.; Guo, Y.; Hu, W.; et al. A Ferroelectric/Electrochemical Modulated Organic Synapse for Ultraflexible, Artificial Visual-Perception System. *Adv. Mater.* **2018**, *30*, 1803961.
(846) Sun, F.; Lu, Q.; Liu, L.; Li, L.; Wang, Y.; Hao, M.; Cao, Z.; Wang, Z.; Wang, S.; Li, T.; et al. Bioinspired Flexible, Dual-Modulation Synaptic Transistors toward Artificial Visual Memory Systems. *Adv. Mater. Technol.* **2020**, *5*, 1900888.
(847) Zhou, F.; Zhou, Z.; Chen, J.; Choy, T. H.; Wang, J.; Zhang, N.; Lin, Z.; Yu, S.; Kang, J.; Wong, H.-S. P.; et al. Optoelectronic Resistive Random Access Memory for Neuromorphic Vision Sensors. *Nat. Nanotechnol.* **2019**, *14*, 776−782.
(848) Pradhan, B.; Das, S.; Li, J.; Chowdhury, F.; Cherusseri, J.; Pandey, D.; Dev, D.; Krishnaprasad, A.; Barrios, E.; Towers, A.; et al. Ultrasensitive and Ultrathin Phototransistors and Photonic Synapses Using Perovskite Quantum Dots Grown from Graphene Lattice. *Sci. Adv.* **2020**, *6*, No. eaay5225.
(849) Hou, Y.-X.; Li, Y.; Zhang, Z.-C.; Li, J.-Q.; Qi, D.-H.; Chen, X.-D.; Wang, J.-J.; Yao, B.-W.; Yu, M.-X.; Lu, T.-B.; et al. Large-Scale and Flexible Optical Synapses for Neuromorphic Computing and Integrated Visible Information Sensing Memory Processing. *ACS Nano* **2021**, *15*, 1497−1508.
(850) Choi, C.; Kim, H.; Kang, J.-H.; Song, M.-K.; Yeon, H.; Chang, C. S.; Suh, J. M.; Shin, J.; Lu, K.; Park, B.-I.; et al. Reconfigurable Heterogeneous Integration Using Stackable Chips with Embedded Artificial Intelligence. *Nat. Electron.* **2022**, *5*, 386−393.
(851) Vijjapu, M. T.; Fouda, M. E.; Agambayev, A.; Kang, C. H.; Lin, C.-H.; Ooi, B. S.; He, J.-H.; Eltawil, A. M.; Salama, K. N. A Flexible Capacitive Photoreceptor for the Biomimetic Retina. *Light: Sci. Appl.* **2022**, *11*, 3.
(852) Chen, S.; Lou, Z.; Chen, D.; Shen, G. An Artificial Flexible Visual Memory System Based on a UV-Motivated Memristor. *Adv. Mater.* **2018**, *30*, 1705400.
(853) He, Z.; Shen, H.; Ye, D.; Xiang, L.; Zhao, W.; Ding, J.; Zhang, F.; Di, C.-A.; Zhu, D. An Organic Transistor with Light Intensity-Dependent Active Photoadaptation. *Nat. Electron.* **2021**, *4*, 522−529.
(854) Kim, Y. C.; Kim, K. H.; Son, D.-Y.; Jeong, D.-N.; Seo, J.-Y.; Choi, Y. S.; Han, I. T.; Lee, S. Y.; Park, N.-G. Printable Organometallic Perovskite Enables Large-Area, Low-Dose X-Ray Imaging. *Nature* **2017**, *550*, 87−91.
(855) Liu, J.; Shabbir, B.; Wang, C.; Wan, T.; Ou, Q.; Yu, P.; Tadich, A.; Jiao, X.; Chu, D.; Qi, D.; et al. Flexible, Printable Soft-X-Ray Detectors Based on All-Inorganic Perovskite Quantum Dots. *Adv. Mater.* **2019**, *31*, 1901644.
(856) Demchyshyn, S.; Verdi, M.; Basiricò, L.; Ciavatti, A.; Hailegnaw, B.; Cavalcoli, D.; Scharber, M. C.; Sariciftci, N. S.; Kaltenbrunner, M.; Fraboni, B. Designing Ultraflexible Perovskite X-Ray Detectors through Interface Engineering. *Adv. Sci.* **2020**, *7*, 2002586.
(857) Gao, Y.; Ge, Y.; Wang, X.; Liu, J.; Liu, W.; Cao, Y.; Gu, K.; Guo, Z.; Wei, Y.-M.; Zhou, N.; et al. Ultrathin and Ultrasensitive Direct X-ray Detector Based on Heterojunction Phototransistors. *Adv. Mater.* **2021**, *33*, 2101717.
(858) van Breemen, A. J. J. M.; Simon, M.; Tousignant, O.; Shanmugam, S.; van der Steen, J.-L.; Akkerman, H. B.; Kronemeijer, A.; Ruetten, W.; Raaijmakers, R.; Alving, L.; et al. Curved Digital X-Ray Detectors. *NPG Flex. Electron.* **2020**, *4*, 22.
(859) Zhao, J.; Zhao, L.; Deng, Y.; Xiao, X.; Ni, Z.; Xu, S.; Huang, J. Perovskite-Filled Membranes for Flexible and Large-Area Direct-Conversion X-Ray Detector Arrays. *Nat. Photonics* **2020**, *14*, 612−617.
(860) Maltoni, D.; Maio, D.; Jain, A. K.; Prabhakar, S. Fingerprint Analysis and Representation. In *Handbook of Fingerprint Recognition*; Springer London, 2009; pp 97−166.
(861) Zhang, D.; Liu, F.; Zhao, Q.; Lu, G.; Luo, N. Selecting a Reference High Resolution for Fingerprint Recognition Using Minutiae and Pores. *IEEE Trans. Instrum. Meas.* **2011**, *60*, 863−871.
(862) van Breemen, A. J. J. M. V; Ollearo, R.; Shanmugam, S.; Peeters, B.; Peters, L. C. J. M.; van de Ketterij, R. L.; Katsouras, I.; Akkerman, H. B.; Frijters, C. H.; Giacomo, F. D.; et al. A Thin and Flexible Scanner for Fingerprints and Documents Based on Metal Halide Perovskites. *Nat. Electron.* **2021**, *4*, 818−826.
(863) Lochner, C. M.; Khan, Y.; Pierre, A.; Arias, A. C. All-Organic Optoelectronic Sensor for Pulse Oximetry. *Nat. Commun.* **2014**, *5*, 5745.
(864) Xu, H.; Liu, J.; Zhang, J.; Zhou, G.; Luo, N.; Zhao, N. Flexible Organic/Inorganic Hybrid Near-Infrared Photoplethysmogram Sensor for Cardiovascular Monitoring. *Adv. Mater.* **2017**, *29*, 1700975.
(865) Khan, Y.; Han, D.; Pierre, A.; Ting, J.; Wang, X.; Lochner, C. M.; Bovo, G.; Yaacobi-Gross, N.; Newsome, C.; Wilson, R.; et al. A Flexible Organic Reflectance Oximeter Array. *Proc. Natl. Acad. Sci. U. S. A.* **2018**, *115*, No. E11015-E11024.
(866) Lee, H.; Kim, E.; Lee, Y.; Kim, H.; Lee, J.; Kim, M.; Yoo, H.-J.; Yoo, S. Toward All-Day Wearable Health Monitoring: An Ultralow-Power, Reflective Organic Pulse Oximetry Sensing Patch. *Sci. Adv.* **2018**, *4*, No. eaas9530.
(867) Kim, J. H.; Liess, A.; Stolte, M.; Krause, A.-M.; Stepanenko, V.; Zhong, C.; Bialas, D.; Spano, F.; Würthner, F. An Efficient Narrowband Near-Infrared at 1040 nm Organic Photodetector Realized by Intermolecular Charge Transfer Mediated Coupling Based on a Squaraine Dye. *Adv. Mater.* **2021**, *33*, 2100582.
(868) Lee, H.; Lee, W.; Lee, H.; Kim, S.; Alban, M. V.; Song, J.; Kim, T.; Lee, S.; Yoo, S. Organic-Inorganic Hybrid Approach to Pulse Oximetry Sensors with Reliability and Low Power Consumption. *ACS Photonics* **2021**, *8*, 3564−3572.
(869) Liang, X.; Liu, Y.; Liu, P.; Yang, J.; Liu, J.; Yang, Y.; Wang, B.; Hu, J.; Zhang, L.; Yang, G.; et al. Large-Area Flexible Colloidal-Quantum-Dot Infrared Photodiodes for Photoplethysmogram Signal Measurements. *Sci. Bull.* **2023**, *68*, 698−705.
(870) Jiang, Z.; Yu, K.; Wang, H.; Rich, S.; Yokota, T.; Fukuda, K.; Someya, T. Ultraflexible Integrated Organic Electronics for Ultrasensitive Photodetection. *Adv. Mater. Technol.* **2021**, *6*, 2000956.
(871) Tran, M. H.; Hur, J. Ultrahigh Stability of Wearable Photodetector Using Zirconium Metal-Organic Framework Enabling In Situ and Continuous Monitoring of Ultraviolet Radiation Risk. *Adv. Optical Mater.* **2022**, *10*, 2101404.
(872) Cai, S.; Zuo, C.; Zhang, J.; Liu, H.; Fang, X. A Paper-Based Wearable Photodetector for Simultaneous UV Intensity and Dosage Measurement. *Adv. Funct. Mater.* **2021**, *31*, 2100026.
(873) Zhang, Z.; Geng, Y.; Cao, S.; Chen, Z.; Gao, H.; Zhu, X.; Zhang, X.; Wu, Y. Ultraviolet Photodetectors Based on Polymer Microwire Arrays toward Wearable Medical Devices. *ACS Appl. Mater. Interfaces* **2022**, *14*, 41257−41263.
(874) Bayan, S.; Pal, S.; Ray, S. K. Boron Carbonitride ($B_xC_yN_z$) Nanosheets Based Single Electrode Triboelectric Nanogenerator for Wearable UV Photodetectors. *Appl. Mater. Today* **2023**, *30*, 101686.

https://doi.org/10.1021/acs.chemrev.3c00548
Chem. Rev. XXXX, XXX, XXX−XXX

(875) Abid; Sehrawat, P.; Julien, C. M.; Islam, S. S. WS_2 Quantum Dots on e-Textile as a Wearable UV Photodetector: How Well Reduced Graphene Oxide Can Serve as a Carrier Transport Medium? *ACS Appl. Mater. Interfaces* **2020**, *12*, 39730−39744.
(876) Lee, D.; Seol, M.-L.; Motilal, G.; Kim, B.; Moon, D.-I.; Han, J.-W.; Meyyappan, M. All 3D-Printed Flexible ZnO UV Photodetector on an Ultraflat Substrate. *ACS Sens.* **2020**, *5*, 1028−1032.
(877) Polat, E. O.; Mercier, G.; Nikitskiy, I.; Puma, E.; Galan, T.; Gupta, S.; Montagut, M.; Piqueras, J. J.; Bouwens, M.; Durduran, T.; et al. Flexible Graphene Photodetectors for Wearable Fitness Monitoring. *Sci. Adv.* **2019**, *5*, No. eaaw7846.
(878) Li, H.; Ma, Y.; Liang, Z.; Wang, Z.; Cao, Y.; Xu, Y.; Zhou, H.; Lu, B.; Chen, Y.; Han, Z.; et al. Wearable Skin-Like Optoelectronic Systems with Suppression of Motion Artifacts for Cuff-Less Continuous Blood Pressure Monitor. *Natl. Sci. Rev.* **2020**, *7*, 849−862.
(879) He, J.; Qiao, K.; Gao, L.; Song, H.; Hu, L.; Jiang, S.; Zhong, J.; Tang, J. Synergetic Effect of Silver Nanocrystals Applied in PbS Colloidal Quantum Dots for High-Performance Infrared Photodetectors. *ACS Photonics* **2014**, *1*, 936−943.
(880) Wu, D.; Zhou, H.; Song, Z.; Zheng, M.; Liu, R.; Pan, X.; Wan, H.; Zhang, J.; Wang, H.; Li, X.; et al. Welding Perovskite Nanowires for Stable, Sensitive, Flexible Photodetectors. *ACS Nano* **2020**, *14*, 2777−2787.
(881) Wang, M.; Tian, W.; Cao, F.; Wang, M.; Li, L. Flexible and Self-Powered Lateral Photodetector Based on Inorganic Perovskite $CsPbI_3$-$CsPbBr_3$ Heterojunction Nanowire Array. *Adv. Funct. Mater.* **2020**, *30*, 1909771.
(882) Hu, P.; Wang, L.; Yoon, M.; Zhang, J.; Feng, W.; Wang, X.; Wen, Z.; Idrobo, J. C.; Miyamoto, Y.; Geohegan, D. B.; et al. Highly Responsive Ultrathin GaS Nanosheet Photodetectors on Rigid and Flexible Substrates. *Nano Lett.* **2013**, *13*, 1649−1654.
(883) Yin, j.; Tan, Z.; Hong, H.; Wu, J.; Yuan, H.; Liu, Y.; Chen, C.; Tan, C.; Yao, F.; Li, T.; et al. Ultrafast and Highly Sensitive Infrared Photodetectors Based on Two-Dimensional Oxyselenide Crystals. *Nat. Commun.* **2018**, *9*, 3311.
(884) Zhang, Y.; Huang, P.; Guo, J.; Shi, R.; Huang, W.; Shi, Z.; Wu, L.; Zhang, F.; Gao, L.; Li, C.; et al. Graphdiyne-Based Flexible Photodetectors with High Responsivity and Detectivity. *Adv. Mater.* **2020**, *32*, 2001082.
(885) An, S.; Wu, S.; Lee, K.-H.; Tan, C. S.; Tai, Y.-C.; Chang, G.-E.; Kim, M. High-Sensitivity and Mechanically Compliant Flexible Ge Photodetectors with a Vertical p-i-n Configuration. *ACS Appl. Electron. Mater.* **2021**, *3*, 1780−1786.
(886) Kuo, L.; Sangwan, V. K.; Rangnekar, S. V.; Chu, T.-C.; Lam, D.; Zhu, Z.; Richter, L. J.; Li, R.; Szydlowska, B. M.; Downing, J. R.; et al. All-Printed Ultrahigh-Responsivity MoS_2 Nanosheet Photodetectors Enabled by Megasonic Exfoliation. *Adv. Mater.* **2022**, *34*, 2203772.
(887) Shen, C.; Han, P.; Zheng, Z.; Jiang, W.; Gao, S.; Hua, C.; Chen, C. L.; Xia, F.; Zhai, T.; Liu, K.; et al. Spatially Confined Face-Selective Growth of Large-Area 2D Organic Molecular Crystals in a Supramolecular Gel for Highly Efficient Flexible Photodetection. *Adv. Sci.* **2022**, *9*, 2203662.
(888) Zou, Y.; Zhang, Z.; Yan, J.; Lin, L.; Huang, G.; Tan, Y.; You, Z.; Li, P. High-Temperature Flexible WSe_2 Photodetectors with Ultrahigh Photoresponsivity. *Nat. Commun.* **2022**, *13*, 4372.
(889) Wu, T.; Hamann, S. S.; Ceballos, A. C.; Chang, C.-E.; Solgaard, O.; Howe, R. T. Design and Fabrication of Silicon-Tessellated Structures for Monocentric Imagers. *Microsyst. Nanoeng.* **2016**, *2*, 16019.
(890) Chen, Y.; Lu, Y.; Liao, M.; Tian, Y.; Liu, Q.; Gao, C.; Yang, X.; Shan, C. 3D Solar-Blind Ga_2O_3 Photodetector Array Realized Via Origami Method. *Adv. Funct. Mater.* **2019**, *29*, 1906040.
(891) Lin, C.-H.; Tsai, D.-S.; Wei, T.-C.; Lien, D.-H.; Ke, J.-J.; Su, C.-H.; Sun, J.-Y.; Liao, Y.-C.; He, J.-H. Highly Deformable Origami Paper Photodetector Arrays. *ACS Nano* **2017**, *11*, 10230−10235.
(892) Ciavatti, A.; Capria, E.; Fraleoni-Morgera, A.; Tromba, G.; Dreossi, D.; Sellin, P. J.; Cosseddu, P.; Bonfiglio, A.; Fraboni, B. Toward Low-Voltage and Bendable X-Ray Direct Detectors Based on Organic Semiconducting Single Crystals. *Adv. Mater.* **2015**, *27*, 7213−7220.
(893) Castelvecchi, D. Quantum Technology Probes Ultimate Limits of Vision. *Nature* **2015**, DOI: 10.1038/nature.2015.17731.
(894) Qu, P.; Chen, F.; Liu, H.; Yang, Q.; Lu, J.; Si, J.; Wang, Y.; Hou, X. A Simple Route to Fabricate Artificial Compound Eye Structures. *Opt. Express* **2012**, *20*, 5775−5782.
(895) Wu, A.; Hammer, G. L.; Doherty, A.; von Caemmerer, S.; Farquhar, G. D. Quantifying Impacts of Enhancing Photosynthesis on Crop Yield. *Nat. Plants* **2019**, *5*, 380−388.
(896) Frey, S. T.; Haque, A. B. M. T.; Tutika, R.; Krotz, E. V.; Lee, C.; Haverkamp, C. B.; Markvicka, E. J.; Bartlett, M. D. Octopus-Inspired Adhesive Skins for Intelligent and Rapidly Switchable Underwater Adhesion. *Sci. Adv.* **2022**, *8*, No. eabq1905.
(897) Schweikert, L. E.; Fitak, R. R.; Johnsen, S. De Novo Transcriptomics Reveal Distinct Phototransduction Signaling Components in the Retina and Skin of a Color-Changing Vertebrate, the Hogfish (Lachnolaimus Maximus). *J. Comp. Physiol. A* **2018**, *204*, 475−485.
(898) Islam, M. M.; Newaz, A. A. R.; Song, L.; Lartey, B.; Lin, S.-C.; Fan, W.; Hajbabaie, A.; Khan, M. A.; Partovi, a.; Phuapaiboon, T.; Homaifar, A.; Karimoddini, A. Connected Autonomous Vehicles: State of Practice. *Appl. Stochastic Models Bus. Ind.* **2023**, *39* (5), 684−700.
(899) Carrivick, J. L.; Smith, M. W. Fluvial and Aquatic Applications of Structure from Motion Photogrammetry and Unmanned Aerial Vehicle/Drone Technology. *WIREs Water.* **2019**, *6*, No. e1328.
(900) Carlo, A. D.; Bonaccorso, F.; Kymakis, E. Outdoor Performance Evaluation of a 2D Materials-Based Perovskite Solar Farm. *Nat. Energy* **2022**, *7*, 580−581.
(901) Kim, H. M.; Kim, M. S.; Lee, G. J.; Yoo, Y. J.; Song, Y. M. Large Area Fabrication of Engineered Microlens Array with Low Sag Height for Light-Field Imaging. *Opt. Express* **2019**, *27*, 4435−4444.
(902) Gunther, J. E.; Jayet, B.; Sekar, S. K. V.; Kainerstorfer, J. M.; Andersson-Engels, S. Review of Optical Methods for Fetal Monitoring In Utero. *J. Biophotonics* **2022**, *15*, No. e202100343.
(903) Pakari, O.; Lopez, R.; Druckman, I.; Meng, E.; Zhou, E.; Wang, Z.; Clarke, S. D.; Pozzi, S. A. Real-Time Mixed Reality Display of Dual Particle Radiation Detector Data. *Sci. Rep.* **2023**, *13*, 362.
(904) Zhang, X.; Zheng, E.; Esopi, M. R.; Cai, C.; Yu, Q. Flexible Narrowband Ultraviolet Photodetectors with Photomultiplication Based on Wide Band Gap Conjugated Polymer and Inorganic Nanoparticles. *ACS Appl. Mater. Interfaces* **2018**, *10*, 28.
(905) Sim, K.; Chen, S.; Li, Z.; Rao, Z.; Liu, J.; Lu, Y.; Jang, S.; Ershad, F.; Chen, J.; Xiao, J.; et al. Three-Dimensional Curvy Electronics Created Using Conformal Additive Stamp Printing. *Nat. Electron.* **2019**, *2*, 471−479.
(906) Kanjee, Z.; Crowe, B.; Rodman, A. Accuracy of a Generative Artificial Intelligence Model in a Complex Diagnostic Challenge. *JAMA* **2023**, *330*, 78.
(907) Fujita, H. AI-Based Computer-Aided Diagnosis (AI-CAD): The Latest Review to Read First. *Radiol. Phys. Technol.* **2020**, *13*, 6−19.
(908) Mackanic, D. G.; Kao, M.; Bao, Z. Enabling Deformable and Stretchable Batteries. *Adv. Energy Mater.* **2020**, *10*, 2001424.
(909) Janssen, G. C. A. M.; Abdalla, M. M.; van Keulen, F.; Pujada, B. R.; van Venrooy, B. Celebrating the 100th Anniversary of the Stoney Equation for Film Stress: Developments from Polycrystalline Steel Strips to Single Crystal Silicon Wafers. *Thin Solid Films* **2009**, *517*, 1858−1867.
(910) Lu, N.; Yoon, J.; Suo, Z. Delamination of Stiff Islands Patterned on Stretchable Substrates. *Int. J. Mater. Res.* **2007**, *98*, 717.
(911) Han, D. Tautomeric Mixture Coordination Enables Efficient Lead-Free Perovskite LEDs. *Nature* **2023**, *622*, 493−498.
(912) Seo, G.; Jung, H.; Creason, T. D.; Yeddu, V.; Bamidele, M.; Echeverria, E.; Lee, J.; McIlroy, D.; Saparov, B.; Kim, D. Y. Lead-Free Halide Light-Emitting Diodes with External Quantum Efficiency

https://doi.org/10.1021/acs.chemrev.3c00548
Chem. Rev. XXXX, XXX, XXX−XXX

Exceeding 7% Using Host-Dopant Strategy. *ACS Energy Lett.* **2021**, *6* (7), 2584−2593.
(913) Wu, F.; Stark, E.; Ku, P. C.; Wise, K. D.; Buzsáki, G.; Yoon, E. Monolithically Integrated μLEDs on Silicon Neural Probes for High-Resolution Optogenetic Studies in Behaving Animals. *Neuron* **2015**, *88*, 1136−1148.
(914) Liu, C.; Zhao, Y.; Cai, X.; Xie, Y.; Wang, T.; Cheng, D.; Li, L.; Li, R.; Deng, Y.; Ding, H.; et al. A Wireless, Implantable Optoelectrochemical Probe for Optogenetic Stimulation and Dopamine Detection. *Microsyst. Nanoeng.* **2020**, *6*, 64.
(915) Arrenberg, A. B.; Stainier, D. Y. R.; Baier, H.; Huisken, J. Optogenetic Control of Cardiac Function. *Science* **2010**, *330*, 971−974.
(916) Raman, R.; Cvetkovic, C.; Uzel, S. G.; Platt, R. J.; Sengupta, P.; Kamm, R. D.; Bashir, R. Optogenetic Skeletal Muscle-Powered Adaptive Biological Machines. *Proc. Natl. Acad. Sci. U. S. A.* **2016**, *113*, 3497−3502.
(917) Sakar, M. S.; Neal, D.; Boudou, T.; Borochin, M. A.; Li, Y.; Weiss, R.; Kamm, R. D.; Chen, C. S.; Asada, H. H. Formation and Optogenetic Control of Engineered 3D Skeletal Muscle Bioactuators. *Lab Chip* **2012**, *12*, 4976−4985.
(918) Aydin, O.; Zhang, X.; Nuethong, S.; Pagan-Diaz, G. J.; Bashir, R.; Gazzola, M.; Saif, M. T. A.; et al. Neuromuscular Actuation of Biohybrid Motile Bots. *Proc. Natl. Acad. Sci. U. S. A.* **2019**, *116*, 19841−19847.
(919) Kim, Y.; Yang, Y.; Zhang, X.; Li, Z.; Vázquez-Guardado, A.; Park, I.; Wang, J.; Efimov, A. I.; Dou, Z.; Wang, Y. Remote Control of Muscle-Driven Miniature Robots with Battery-Free Wireless Optoelectronics. *Sci. Robot.* **2023**, *8*, No. eadd1053.
(920) *EXT 1036C, DRTECH*. https://www.drtech.co.kr/kr/sub/product/view.php?s_cate=2015&idx=226 (accessed 2023-11-15).
(921) Banach, M.; Markham, S.; Agaiby, R.; Too, P. 9−4: Low Leakage Organic Backplanes for High Pixel Density Optical Sensors. *SID Symposium Digest of Technical Papers* **2018**, *49*, 90−91.
(922) Patel, V.; Chesmore, A.; Legner, C. M.; Pandey, S. Trends in Workplace Wearable Technologies and Connected-Worker Solutions for Next-Generation Occupational Safety, Health, and Productivity. *Adv. Intell. Syst.* **2022**, *4*, 2100099.
(923) Waisberg, E.; Ong, J.; Masalkhi, M.; Zaman, N.; Sarker, P.; Lee, A. G.; Tavakkoli, A. The Future of Ophthalmology and Vision Science with the Apple Vision Pro. *Eye* **2023**, DOI: 10.1038/s41433-023-02688-5.
(924) Iqbal, S. M. A.; Mahgoub, I.; Du, E.; Leavitt, M. A.; Asghar, W. Advances in Healthcare Wearable Devices. *npj Flex Electron.* **2021**, *5*, 9.
(925) Moro, L.; Visser, R. J. Encapsulation of Flexible Displays: Background, Status, and Perspective. In *Flexible Flat Panel Displays*; Broer, D. J., Crawford, G. P., Eds.; John Wiley & Sons, 2023; pp 229−254.
(926) Flores-Vazquez, C.; Angulo, C.; Vallejo-Ramirez, D.; Icaza, D.; Pulla Galindo, S. Technical Development of the CeCi Social Robot. *Sensors* **2022**, *22*, 7619.
(927) Salamone, F.; Bellazzi, A.; Belussi, L.; Damato, G.; Danza, L.; Dell'Aquila, F.; Ghellere, M.; Megale, V.; Meroni, I.; Vitaletti, W. Evaluation of the Visual Stimuli on Personal Thermal Comfort Perception in Real and Virtual Environments Using Machine Learning Approaches. *Sensors* **2020**, *20*, 1627.
(928) Menon, L.; Yang, H.; Cho, S. J.; Mikae, S.; Ma, Z.; Zhou, W. Transferred Flexible Three-Color Silicon Membrane Photodetector Arrays. *IEEE Photonics Journal.* **2015**, *7*, 1.
(929) Yuan, H.-C.; Shin, J.; Qin, G.; Sun, L.; Bhattacharya, P.; Lagally, M. G.; Celler, G. K.; Ma, Z. Flexible Photodetectors on Plastic Substrates by Use of Printing Transferred Single-Crystal Germanium Membranes. *Appl. Phys. Lett.* **2009**, *94*, 013102.
(930) Guo, Q.; Fang, Y.; Zhang, M.; Huang, G.; Chu, P. K.; Mei, Y.; Di, Z.; Wang, X. Wrinkled Single-Crystalline Germanium Nanomembranes for Stretchable Photodetectors. *IEEE Trans. Electron Devices* **2017**, *64* (5), 1985−1990.
(931) Lei, Y.; Gu, L.; Yang, X.; Lin, Y.; Zheng, Z. Ductile-Metal Ag as Buffer Layer for Flexible Self-Powered Ag_2S Photodetectors. *Adv. Mater. Interfaces* **2021**, *8*, 2002255.
(932) Lian, Q.; Zhu, X.; Wang, X.; Bai, W.; Yang, J.; Zhang, Y.; Qi, R.; Huang, R.; Hu, W.; Tang, X.; et al. Ultrahigh-Detectivity Photodetectors with Van der Waals Epitaxial CdTe Single-Crystalline Films. *Small* **2019**, *15*, 1900236.
(933) Lei, Y.; Luo, J.; Yang, X.; Cai, T.; Qi, R.; Gu, L.; Zheng, Z. Thermal Evaporation of Large-Area SnS2 Thin Films with a UV-to-NIR Photoelectric Response for Flexible Photodetector Applications. *ACS Appl. Mater. Interfaces* **2020**, *12*, 24940−24950.
(934) Fazeli, N.; Oller, M.; Wu, J.; Wu, Z.; Tenenbaum, J. B.; Rodriguez, A. See, Feel, Act: Hierarchical Learning for Complex Manipulation Skills with Multisensory Fusion. *Sci. Robot.* **2019**, *4*, No. eaav3123.
(935) Clabaugh, C.; Matarić, M. Robots for the People, by the People: Personalizing Human-Machine Interaction. *Sci. Robot.* **2018**, *3*, No. eaat7451.
(936) van Eden, B.; Rosman, B. An Overview of Robot Vision. *Southern African Universities Power Engineering Conference/Robotics and Mechatronics/Pattern Recognition Association of South Africa* **2019**, 98−104.
(937) Ficuciello, F.; Migliozzi, A.; Laudante, G.; Falco, P.; Siciliano, B. Vision-Based Grasp Learning of an Anthropomorphic Hand-Arm System in a Synergy-Based Control Framework. *Sci. Robot.* **2019**, *4*, No. eaao4900.
(938) Kim, D.; Kang, B. B.; Kim, K. B.; Choi, H.; Ha, J.; Cho, K.-J.; Jo, S. Eyes Are Faster Than Hands: A Soft Wearable Robot Learns User Intention from the Egocentric View. *Sci. Robot.* **2019**, *4*, No. eaav2949.
(939) Zhang, H.; Rogers, J. A. Recent Advances in Flexible Inorganic Light Emitting Diodes: From Materials Design to Integrated Optoelectronic Platforms. *Adv. Opt. Mater.* **2019**, *7*, 1800936.
(940) Visintin, F. Photocopier Industry: At the Forefront of Servitization. In *Servitization in Industry*; Lay, G., Eds.; Springer, Cham., 2014; pp 23−43.

https://doi.org/10.1021/acs.chemrev.3c00548
Chem. Rev. XXXX, XXX, XXX−XXX